Vrije Universiteit Brussel

Faculteit van de Wetenschappen

A Study of the Z^0 Lineshape at LEP through the reaction $e^+e^- \rightarrow \mu^+\mu^-$

Cao Fang

December 1993

Promotor: Prof. J. Lemonne

Vrije Universiteit Brussel
Pleinlaan 2
1050 Brussel

Proefschrift ingediend
met het oog op het behalen
van de graad van
Doctor in de Wetenschappen

Acknowledgements

It is a pleasure to thank all the persons who made this thesis possible in one way or another. First, I express my profound gratitude to the promoter of this work, Prof. Jacques Lemonne, for kindly accepting me at the Inter-University Institute for High Energies (IIHE) as a Ph.D. student and introducing me to the exciting field of particle physics. I especially acknowledge the many enriching discussions, constructive comments and suggestions on the manuscript of this thesis as well as all the physics I learnt from him over the last five years.

I am very much indebted to my supervisor Dr. Catherine De Clercq for all advice on matters of scale large or small. From the begining to the end of this work she has always been available for constructive and stimulating discussions. Her friendship and support during the progress of this thesis are much appreciated.

I am grateful to Prof. Jean Sacton for the experienced advice concerning this work.

I enjoyed working with Dr. Walter Van Doninck on the drift velocity monitoring chambers. His insight of the chamber operation and his elegant ideas were very helpful as well as his comments and suggestions on the drift velocity monitoring chapter.

I also owe a lot to the innumerable fruitful discussions I had with Prof. Stefaan Tavernier with whom I shared the same office during the last five years.

For a better understanding of the theoretical framework I highly appreciated the helpful discussions with Prof. D. Bardin. I also thank him and Dr. Alexander Olchevsky for the discussions about the ZFITTER program. I thank Dr. Peter Kluit, Dr. Frederic Stichelbaut, Dr. Peter Renton and Dr. Vladimir Nikolaenko for all the useful discussions about the muon analysis. I also thank Dr. Catherine Vander Velde for her help and comments on the trigger part and from Dr. John Wickens for the DELANA program.

I acknowledge all my DELPHI colleagues who contributed to the achievement of

the results presented in this thesis.

It is really a pleasure working in the Belgian DELPHI group. The hard work and friendly cooperation from every member of this group made the forward muon systems together with other DELPHI system a big success. I thank every member.

I am thankful to Dr. Mark Goldberg for the help in English formulation and for the useful suggestions. I thank Ms. Myriam Pins for her care and patience in drawing some of the figures.

I wish to acknowledge all these years of encouragement and unqualified support from my parents and family. They have been pillars of support I could rely on at all times. I thank my father for my first lesson of physics and my mother for my first philosophy lesson. I also thank my brother for all his loving care from my early naughty childhood until now. I sincerely thank my wife, Zhang Shuping, for her love, patience and support during all these years. I am grateful for all the wonderful discussions we had in physics and life in general. In addition she is the first reader of this thesis. Her comments are very much welcomed.

Contents

List of Figures

List of Tables

Chapter 1

Introduction

The Standard Model of electroweak interactions, developed in the sixties by Glashow, Weinberg and Salam, is one of the key theories to explain the fundamental structure of the universe, unifying the electromagnetic and weak forces. The electromagnetic force is the result of virtual photon exchange between charged particles, the weak force acts between all types of fundamental particle and is mediated by the exchange of massive, intermediate $W^{\pm}$ and Z^0 vector bosons. The relative strength of the electric and weak forces can be expressed in function of the Weinberg mixing angle which can be defined as:

$$sin^2\theta_w = 1 - \frac{m_W^2}{m_Z^2} \tag{1.1}$$

where m_W and m_Z are the mass of W and Z^0 bosons.

The model includes "families" of point like spin 1/2 particles which make up matter. In each family, there are two types of quarks (up-type and down-type) and two types of leptons (an electron-type particle and an associated neutrino). The theory does not predict the number of such fundamental fermion families. Although the Standard Model has already been subjected to a wide variety of detailed tests, no discrepancy between theory and experiments has yet been found. In 1983, the UA1 and UA2 experiments at CERN first observed the production of Z^0 bosons in $p\overline{p}$ collisions. In order to perform detailed studies of the decays of the Z^0 and of the weak neutral current interaction, the Large Electron Positron (LEP) Collider Ring was built at CERN, the European particle physics laboratory, close to Geneva in Switzerland. Since 1989, LEP is operated at energies near 91 GeV around the Z^0-mass and opened up the possibility of carrying out detailed investigations of the physics of the Z^0 intermediate boson with four large detectors: ALEPH, DELPHI, L3 and OPAL. By 1995, the center of mass energy of LEP will be extended up to and beyond the W^+W^- pair production threshold.

The work presented in this thesis was carried out in the framework of the DELPHI (Detector for Lepton, Photon and Hadron Identification) collaboration, and describes one of the important projects of LEP, namely: the measurement of the $e^+e^- \rightarrow Z^0/\gamma \rightarrow \mu^+\mu^-$ line shape. The partial width of the process $Z^0 \rightarrow \mu^+\mu^-$ will be measured and used to check lepton universality. In addition, the Z^0 mass, M_Z, the Weinberg angle $sin^2\theta_w$ as well as the ratio of the hadronic to muon partial decay width are also determined on the base of the muon line shape. These measurements allow direct checks of the validity of the Standard Model. They also permit the extraction of the number of families of light neutrinos and hence inferentially, the number of quark and lepton generations. The replication of fermion families is one of the outstanding questions in particle physics. Three generations of fermions have been discovered so far (although the top quark has not been observed and the evidence for the existence of the ν_τ is only indirect). There is no convincing theoretical reason why there could not be a larger number of fermion generations. As will be shown, the data clearly demonstrate that there are only three generations. This result is one of the most interesting obtained to date at the new e^+e^--colliders.

The data used in this analysis was collected from April 23th to August 29th of 1990, at seven center of mass energy points ranging from 88.22 to 94.24 GeV.

The DELPHI detector is a multi-purpose detector with a total volume of about $10 \times 10 \times 10$ m^3, consisting of a barrel part with a superconducting coil, tracking chambers, electromagnetic and hadronic calorimeters and a muon detector, and two end caps of a similar configuration. In these endcaps, the Forward Muon Chambers cover the polar angle regions $9^o < \theta < 43^o$ and $137^o < \theta < 171^o$. They were built by a consortium of Belgium laboratories: the IIHE (ULB-VUB), of Brussels, the U.I. Antwerpen and the U. Mons-Hainaut.

The theoretical background needed for the analysis is presented in chapter 2. In chapter 3 the experimental setup is described, including an overview of the LEP collider and a description of the DELPHI detector, its data acquisition and trigger system. In order to determine the position of the muons passing trough the muon chambers, one needs to have a precise knowledge of the drift velocity of ionisation electrons in the muon chambers. The drift velocity depends on external parameters like temperature, pressure etc. An on-line controlled drift velocity monitoring system for the Forward Muon Chambers has been built. The performance of the drift velocity monitoring system and the muon chambers will be discussed in detail in chapter 4. The data analysis used to obtain a sample of $e^+e^- \rightarrow Z^0/\gamma \rightarrow \mu^+\mu^-$ events is presented in chapter 5. In chapter 6, the parameters of the Z^0 resonance and the resulting number of the light neutrino species are determined. These results are compared to the 'world average' results. A *résumé* of the main results of this thesis is given in the 'Summary and Conclusions'.

Chapter 2

Theoretical Background

2.1 Families of Leptons and Quarks in the Standard Model of Electroweak Interactions

The Standard Model of electroweak interactions [2, 3, 4] together with Quantum Chromodynamics (QCD) have hitherto been remarkably successful in describing the interactions between the elementary constituents of matter. The basic constituents of matter are six leptons and six quarks and their antiparticles. The forces between these constituents are the electroweak force and the colour force. The leptons are the electron (e), the muon (μ), the tau (τ) and the associated neutrinos (ν_e, ν_μ, ν_τ). Leptons carry no colour charge and are thus insensitive to strong interactions. The quarks are labelled as up (u), down (d), charm (c), strange (s), top (t) and beauty (b). Each quark has three colour states and is hence sensitive to the strong interaction. So far, the top quark has not been observed (the top mass is expected to be m_t = 141 ± 27 GeV[5]) and the evidence for the existence of the ν_τ is only indirect.

Leptons and quarks can be grouped into three identical families containing left handed (L) doublets and right (R) handed singlet representations of the SU(2) group of "weak isospin". The 'weak hypercharge' Y (generator of the $U_Y(1)$ group), satisfies the following relation Q = I_3 + Y/2 for all particles, where Q is the charge and I_3 is the third component of the weak isospin. For charged leptons and their assumed zero mass partners ν_e, ν_μ, ν_τ the singlet and doublet assignments are:

$$\begin{pmatrix} \nu_e \\ e \end{pmatrix}_L \quad \begin{pmatrix} \nu_\mu \\ \mu \end{pmatrix}_L \quad \begin{pmatrix} \nu_\tau \\ \tau \end{pmatrix}_L \quad \left(e \right)_R \quad \left(\mu \right)_R \quad \left(\tau \right)_R$$

The corresponding assignments for quarks are:

$$\begin{pmatrix} u \\ d' \end{pmatrix}_L \begin{pmatrix} c \\ s' \end{pmatrix}_L \begin{pmatrix} t \\ b' \end{pmatrix}_L \quad \begin{pmatrix} u \end{pmatrix}_R \begin{pmatrix} d' \end{pmatrix}_R \begin{pmatrix} c \end{pmatrix}_R \begin{pmatrix} s' \end{pmatrix}_R \begin{pmatrix} t \end{pmatrix}_R \begin{pmatrix} b' \end{pmatrix}_R$$

The d', s' and b' states are related to the physical quark states by the Kobayashi-Maskawa matrix:

$$\begin{pmatrix} d' \\ s' \\ b' \end{pmatrix} = \begin{pmatrix} U_{ud} & U_{us} & U_{ub} \\ U_{cd} & U_{cs} & U_{cb} \\ U_{td} & U_{ts} & U_{tb} \end{pmatrix} \begin{pmatrix} d \\ s \\ t \end{pmatrix}$$

Table 2.1 summarises the corresponding quantum numbers for the first family.

	ν_L^e	e_L^-	e_R^-	u_L	d_L	u_R	d_R
I_3	$\frac{1}{2}$	$-\frac{1}{2}$	0	$\frac{1}{2}$	$-\frac{1}{2}$	0	0
Y	-1	-1	-2	$\frac{1}{3}$	$\frac{1}{3}$	$\frac{4}{3}$	$-\frac{2}{3}$
Q	0	-1	-1	$\frac{2}{3}$	$-\frac{1}{3}$	$\frac{2}{3}$	$-\frac{1}{3}$

Table 2.1: SU(2) and U(1) weak quantum numbers of the first family.

Leptons interact with each other and with the quarks through the electromagnetic and the weak forces, which are unified in a single gauge theory based on the SU(2)×U(1) symmetry. The gauge bosons mediating the electroweak force are the photon and the heavy intermediate bosons $W^{\pm}$ and Z^0. They acquire masses by spontaneous breaking of the gauge symmetry. The simplest way to achieve this breaking is by introducing a field of scalar Higgs particle. In 1983, the $W^{\pm}$ and Z^0 particles were discovered in $p\bar{p}$ collisions by the UA1 and UA2 experiments at CERN [6, 7], but the Higgs particle remines hitherto undetected. The detailed studies of the Z^0 interactions and decays only became possible by 1989 when the LEP (CERN) and SLC (Standford) e^+e^--colliders came into operation.

2.2 The e^+e^- Annihilation Cross Section, the Z^0 Width and Branching Ratios

The present work concerns the basic process $e^+e^- \rightarrow f\bar{f}$, where f represents a fundamental fermion of mass m_f, either a quark or a lepton. If $f \neq e$, there are two basic diagrams shown in fig. 2.1 which contribute in the lowest order perturbation theory of electroweak interactions to the e^+e^- annihilation cross section around the Z^0 peak. These are $e^+e^- \rightarrow \gamma \rightarrow f\bar{f}$ and $e^+e^- \rightarrow Z^0 \rightarrow f\bar{f}$ in s-channel exchange.

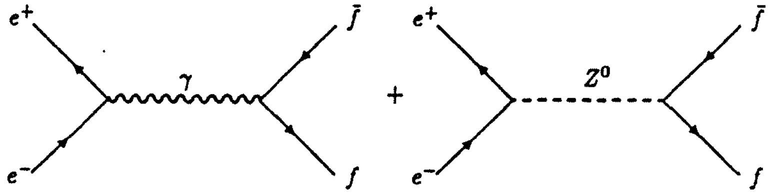

Figure 2.1: The lowest order diagrams for the processes $e^+e^- \rightarrow Z^0/\gamma \rightarrow \mu^+\mu^-$.

In the lowest order, the differential cross section for the reaction $e^+e^- \rightarrow f\bar{f}$, where f is any fundamental fermion ($f \neq e$) is given by the spin averaged square of the sum of the matrix elements $\mathcal{M}_\gamma$ and $\mathcal{M}_Z$ for the exchange of γ and Z^0 respectively:

$$< |\mathcal{M}|^2 > = < |\mathcal{M}_\gamma + \mathcal{M}_Z|^2 > \tag{2.1}$$

It can be written in the following way[8]:

$$\frac{d\sigma}{d\Omega} = \frac{\alpha^2}{4s} N_c^f \sqrt{1-4\mu_f}[G_1(s)(1+cos^2\theta) + G_2(s)4\mu_f sin^2\theta + G_3(s)2\sqrt{1-4\mu_f}cos\theta] \tag{2.2}$$

where s is the center of mass energy squared, $N_c^f = 1$ and $N_c^f = 3$ for $f =$ lepton and $f =$ quark respectively, $\mu_f = m_f^2/s$, α is the fine structure constant and

$$G_1(s) = Q_e^2Q_f^2 + 2Q_eQ_fv_ev_fReX_0(s) + (v_e^2 + a_e^2)(v_f^2 + a_f^2 - 4\mu_f a_f^2)|X_0(s)|^2$$

$$G_2(s) = Q_e^2 Q_f^2 + 2Q_e Q_f v_e v_f Re X_0(s) + (v_e^2 + a_e^2) v_f^2 |X_0(s)|^2$$
$$G_3(s) = 2Q_e Q_f a_e a_f Re X_0(s) + 4v_e a_e v_f a_f |X_0(s)|^2$$

where the Q_f denotes the electric charge of a given fermion species f and the Z propagator is:

$$X_0(s) = \frac{s}{s - M_Z^2 + iM_Z\Gamma_Z} \tag{2.3}$$

the real part of which can be written as:

$$Re X_0(s) = \frac{s(s - M_Z^2)}{(s - M_Z^2)^2 + M_Z^2\Gamma_Z^2} \tag{2.4}$$

The vector (v_f) and axial vector (a_f) neutral current coupling constants are given by:

$$v_f = \frac{I_3^f - 2Q_f sin^2\theta_w}{2sin\theta_w cos\theta_w}, \quad a_f = \frac{I_3^f}{2sin\theta_w cos\theta_w} \tag{2.5}$$

where I_3^f denotes the third isospin component of a given fermion species f.

The total Z width in lowest order is:

$$\Gamma_Z = \sum_f \Gamma_f = \sum_f N_c^f \frac{\alpha}{3} M_Z \sqrt{1 - 4\mu_f}(v_f^2(1 + 2\mu_f) + a_f^2(1 - 4\mu_f)) \tag{2.6}$$

Near the Z peak, μ_f tends to zero, and the following simplified expressions hold to a very good approximation:

$$\frac{d\sigma}{d\Omega} = \frac{\alpha^2}{4s} N_c^f [G_1(s)(1 + cos^2\theta) + G_3(s) 2cos\theta] \tag{2.7}$$

and the Z width becomes:

$$\Gamma_Z = \sum_f N_c^f \frac{\alpha}{3} M_Z (v_f^2 + a_f^2) \tag{2.8}$$

The total cross section is[15]:

$$\sigma_0(s) = \frac{4\pi\alpha^2}{3s} N_c^f G_1(s) \tag{2.9}$$

or

$$\sigma_0(s) = \frac{4\pi Q_f^2 \alpha^2 N_c^f}{3s} + \frac{s N_c^f}{(s - M_Z^2)^2 + M_Z^2\Gamma_Z^2}[\frac{12\pi\Gamma_e\Gamma_f}{M_Z^2 N_c^f} - (2Q_f v_e v_f)\frac{4\pi\alpha^2 N_c^f}{3}\frac{(s - M_Z^2)}{s}] \tag{2.10}$$

The first term in eq. 2.10 is the pure QED cross section, the second term is the Breit-Wigner form for a spin 1 resonance and the last term represents the $Z - \gamma$ interference.

Eq. 2.10 reduces to the pure Breit-Wigner formula in the case of ν pair production:

$$\sigma_0(s) = \frac{12\pi\Gamma_e\Gamma_\nu}{M_Z^2}\frac{s}{(s-M_Z^2)^2+M_Z^2\Gamma_Z^2} \tag{2.11}$$

which reaches its maximum value of σ_{max}:

$$\sigma_{max} = \frac{12\pi\Gamma_e\Gamma_f}{M_Z^2\Gamma_Z^2}(1+\frac{1}{4}\gamma^2) \tag{2.12}$$

for

$$\sqrt{s} = M_Z(1+\gamma^2)^{1/4} \tag{2.13}$$

with

$$\gamma = \frac{\Gamma_Z}{M_Z} \tag{2.14}$$

Note that the cross section reaches its maximum at a centre of mass energy slightly higher than M_Z, where $\sigma(M_Z^2)$ is:

$$\sigma(M_Z^2) = \frac{12\pi\Gamma_e\Gamma_f}{M_Z^2\Gamma_Z^2} \approx \sigma_{max} \tag{2.15}$$

If one neglects the higher order terms in γ^2, the right and left half maxima positions for the cross section are:

$$\sqrt{s}_\pm = M_Z(1+\frac{3}{8}\gamma^2) \pm \frac{\Gamma_Z}{2}(1-\frac{1}{8}\gamma^2) \tag{2.16}$$

When one photon exchange is present, the full width at half maximum becomes slightly larger because the pure QED term changes only marginally over the FWHM range but contributes to the peak cross section.

2.3 Radiative Corrections

The lowest order results discussed above are significantly modified if higher order terms in the perturbation expansion are included. Diagrams corresponding to some

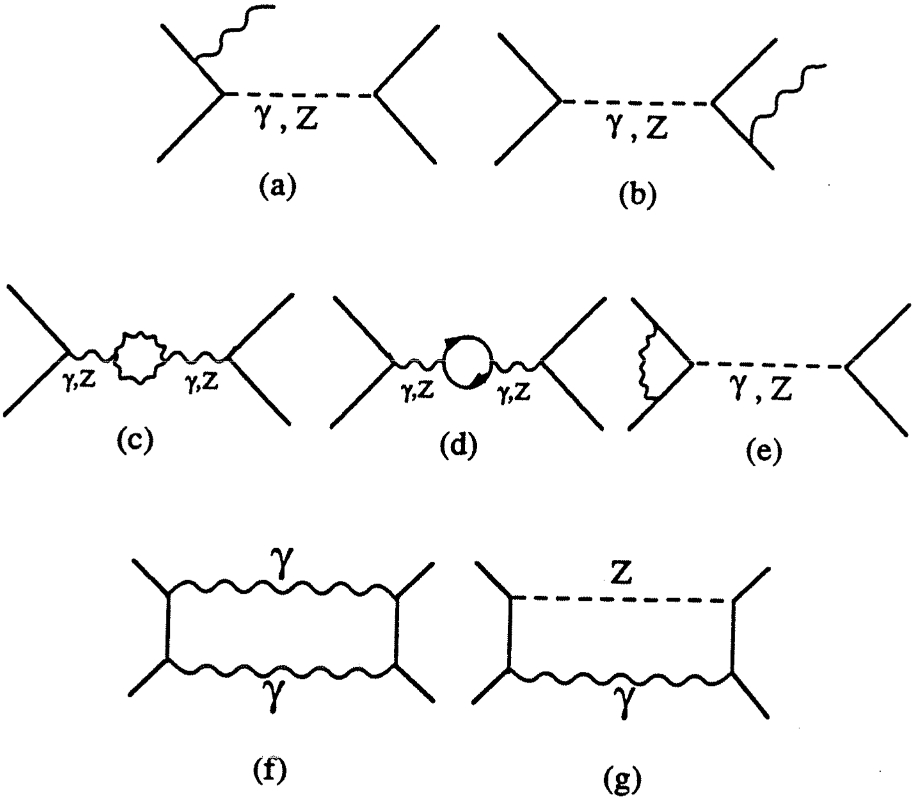

Figure 2.2: Some radiative correction diagrams.

higher order terms are shown in fig. 2.2. These diagrams all fall in one of the following categories:

1. **Initial and Final State Bremsstrahlung Corrections:** (e.g. diagrams shown in fig. 2.2(a)(b)) Of these, the initial state bremsstrahlung correction (a) is the dominant one. It is also the largest among all the electroweak corrections. At the Z^0 peak the initial state bremsstrahlung effect reduces the peak cross section by about 30%. All other radiative effects together reduce the peak cross section only by about 3%. This can be understood intuitively as follows: if the initial electron or positron emits a photon the centre of mass energy between the electron and positron is reduced, and the cross section off-resonance is much lower. They are the only radiative corrections changing the collision energy.

2. **Self Energy (propagator) Corrections:** (e.g. diagrams shown in fig. 2.2(c)(d)) If these corrections modify the photon propagator, they are called "vacuum polarisation corrections" and if the corrections modify the weak gauge bosons, they are called "oblique corrections".

3. **Vertex Corrections:** (e.g diagram shown in fig. 2.2(e)) This kind of radiative correction does not change the collision energy, and therefore does not distort the line shape. It enters as an overall scale correction factor to the cross section.

4. **Box Corrections:** (e.g. diagrams shown in fig. 2.2(f)(g)) The effect of such diagrams on the line shape is negligible.

A complete treatment of these effects can be found in [9],[10].

2.3.1 Correction to the Z^0 Line Shape

All the radiative corrections to the Z^0 line shape used in this analysis are estimated by the program ZFITTER[11]. This program is based on a theoretical formulation ref. [13] in which radiative corrections can be computed at the level of the differential cross-sections, which are subsequently integrated to obtain the line-shape. The QED corrections to the differential cross section are introduced as follows:

$$\frac{d\sigma}{dcos\theta} = \sum_{m,n} \sum_{A=T,FB} \sum_{a=e,i,f} Re[\sigma_A^{a,0}(s,s;m,n) R_A^a(cos\theta,m,n)] \tag{2.17}$$

The summations over m and n include photon and Z-boson exchange, (m,n = γ,Z). The values of the index A = T and A = FB refer to even and odd cross section parts. As the total cross section is obtained by an integration over the scattering angle θ, only the even terms are relevant in this discussion.

The indexes $a = e, f$ and i refer to the initial (e^+e^-) and final state ($f\bar{f}$) radiation and their interference.

The functions $R^a_A(\cos\theta, m, n)$ represent the QED corrections to the Born like cross section $\sigma^{a,0}_A(s, s'; m, n)$ (when the energy squared of the created fermion pair $s' = s$, $\sigma^{a,0}_A(s, s'; m, n)$ becomes a pure Born cross section). They depend only on the mass and width of the Z^0, and on kinematic variables like s, $\cos\theta$ and on a cut-off value Δ on the variable $v = \frac{s-s'}{s}$. These functions can be expressed by semi-analytic formulae for the soft $S^a_A(\cos\theta, \epsilon; m, n)$ and hard $H^a_A(v, cos\theta)$ part of QED bremsstrahlung radiator functions ref. [13].

$$R^a_A(cos\theta, m, n) = \int_0^{\Delta} dv \frac{\sigma^{a,0}_A(s, s'; m, n)}{\sigma^{a,0}_A(s, s; m, n)} [\delta(v) S^a_A(cos\theta, \epsilon; m, n) + \theta(v - \epsilon) H^a_A(v, cos\theta)] \tag{2:18}$$

where $\delta(v)$ is a Dirac function, $\theta(v - \epsilon)$ is a step function and the cut-off Δ can vary from 0 up to the kinematic limit: 1 - $4m_f^2$/s. The energy squared of the created fermion pair is s' = (1 - v)s and ϵ is the parameter which discriminates between soft and hard photons. The functions R^a_A(cosθ,m,n) are the result of a sum of real and virtual photon corrections. They are obtained by lengthy Feynman diagram calculations described in ref. [13]

The inclusion of non-QED weak loop effects is performed using a form factor approach [12]. This procedure makes the electroweak coupling constants v_f and a_f (see eq. 2.5) in the Born-like cross section $\sigma^{a,0}_A(s, s'; m, n)$ complex and s-dependent.

Fig. 2.3 taken from ref. [13] shows (a) symmetric and asymmetric contributions due to Z^0 exchange, γ exchange and γ, Z^0 interference for the cut-off $\Delta = 1$, (b) the Born cross section and initial-state radiation cross section with the photon energy

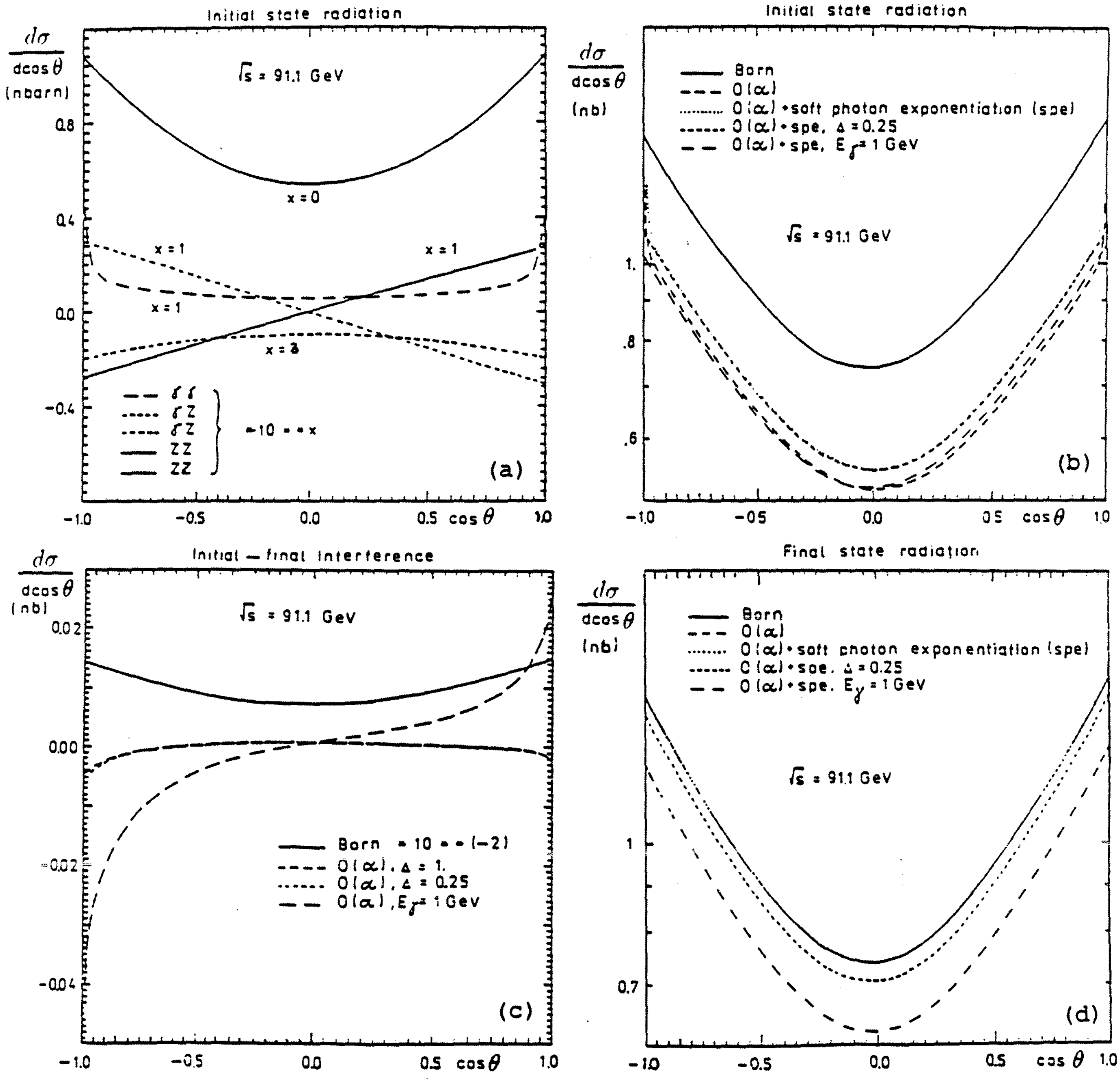

Figure 2.3: The QED corrections to the differential cross section as function of the scattering angle. (a)The symmetric and asymmetric contributions due to Z^0 exchange, γ exchange and γZ^0 interference. (b)Born and initial-state radiation contributions. (c)initial-final state radiation interference. (d)final-state radiation corrections.

cut-off Δ as a parameter, (c) initial-final interference and (d) the final-state correction to the differential cross section $d\sigma/d\cos\theta$ in nb as a function of the scattering angle at an energy $\sqrt{s} = 91.1$ GeV (close to the Z-boson mass value), for $\Gamma_Z = 2.5$ GeV, $sin^2\theta_w = 0.23$.

From fig. 2.3 (a), one can deduce that the Z-boson exchange is absolutely dominant near the Z^0 peak as expected. Moreover, the A=T and A=FB contributions are clearly separated. The initial state radiation (shown in fig. 2.3 (b)) is the largest correction and it affects the cross section by about 30%. In comparison, the contributions from the initial-final state radiation interference of the photon radiation and the final state photon radiation (shown in fig. 2.3 (c) and (d)) are very small.

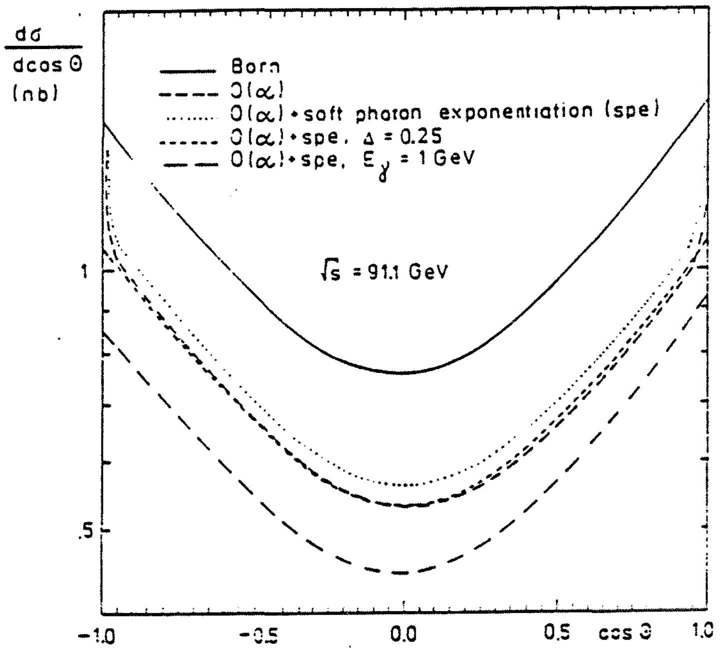

Figure 2.4: The differential cross section with complete electroweak corrections as a function of the scattering angle with the value of parameters $M_Z = 91.1, m_t = 100, M_H = 100$ (all masses in GeV) and $\alpha_s = 0.12$.

Fig. 2.4 shows the differential cross section with complete electroweak corrections as a function of the scattering angle, and fig. 2.5 taken from [10] illustrates the effect of initial state bremsstrahlung on the $e^+e^- \longrightarrow \mu^+\mu^-$ line shape near the Z^0 resonance.

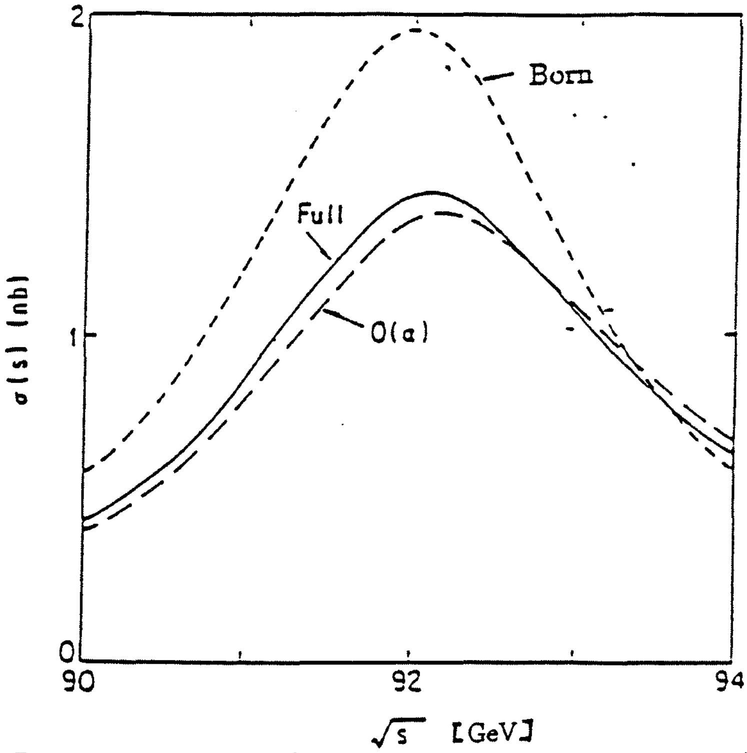

Figure 2.5: The effects of initial state bremsstrahlung on the process $e^+e^- \longrightarrow \mu^+\mu^-$ near the Z^0 resonance. M_Z was assumed to be $M_Z = 92$ GeV for the graph.

2.3.2 The Modified Born-Cross Section

In the modified Born approximation, non QED-radiative corrections to the Born cross section near the Z^0 pole are parameterised in terms of s-dependent effective coupling constants. The Born cross section formula eq. 2.10 becomes the modified Born cross-section given below:

$$\sigma_0(s) = \frac{4\pi Q_f^2 \bar{\alpha} N_c^f}{3s} + \frac{s}{(s-M_Z^2)^2 + s^2\Gamma_Z^2/M_Z^2} \times \left[\frac{12\pi\Gamma_e\Gamma_f}{M_Z^2}\frac{1}{(1+\frac{3\alpha}{4\pi})(1+\frac{3\alpha}{4\pi}Q_f^2)} - (2Q_f v_e v_f)\frac{4\pi\bar{\alpha}}{3}N_c^f\frac{(s-M_Z^2)}{s}\right] \qquad (2.19)$$

where α is the fine structure constant and $\bar{\alpha}$ stands for the value of the running QED coupling constant at $s = M_Z^2$ and Q_f=-1 for leptonic (e, μ, τ) final states. The introduction of an s-dependent width term $s^2\Gamma_Z^2/M_Z^2$ also accounts for radiative correction effects. Factors of the type $(1 + \frac{3\alpha}{4\pi})$ are due to the final state pure QED radiative correction to the leptonic partial widths, which must be divided out in eq. 2.19 in view of the QED corrected definition of Γ_l given below (see eq. 2.20). The leptonic width Γ_l in terms of the effective vector and axial vector couplings $\overline{v}_l$ and $\overline{a}_l$ of the Z^0 to charged leptons is given by:

$$\Gamma_l = \frac{G_\mu M_Z^3}{6\pi\sqrt{2}}(\overline{v}_l^2 + \overline{a}_l^2)(1 + \frac{3\alpha}{4\pi}) \tag{2.20}$$

Alternatively, it can be expressed in terms of effective weak mixing angle $sin^2\theta_w^{eff}$ and an effective ρ parameter (ρ_{eff}) via the relations[12, 13]:

$$\overline{a}_l^2 = \frac{1}{4}\rho_{eff} \tag{2.21}$$

$$\overline{v}_l^2 = \frac{1}{4}\rho_{eff}(1 - 4sin^2\theta_W^{eff})^2 \tag{2.22}$$

and eq. 2.20 can be reformulated as:

$$\Gamma_l = \frac{G_\mu M_Z^3}{6\pi\sqrt{2}}\frac{\rho_{eff}}{4}[1 + (1 - 4sin^2\theta_w^{eff})^2](1 + \frac{3\alpha}{4\pi}) \tag{2.23}$$

This can in turn be written as:

$$(1 - 4sin^2\theta_w^{eff}) = \pm\sqrt{\frac{4\Gamma_l}{\rho_{eff}(1 + \frac{3\alpha}{4\pi})(\frac{G_\mu M_Z^3}{6\pi\sqrt{2}})} - 1} \tag{2.24}$$

In order to have real results for eq. 2.24, one requires that:

$$\Gamma_l \geq \frac{G_\mu M_Z^3}{6\pi\sqrt{2}}\frac{\rho_{eff}}{4}(1 + \frac{3\alpha}{4\pi}) \tag{2.25}$$

Taking the dependence of the running Veltman parameter ρ_{eff} on the mass m_t of the top quark into account [16],

$$\rho_{eff} = \rho_0(1 + \frac{3\sqrt{2}G_F}{16\pi^2}m_t^2) \tag{2.26}$$

This implies that $\Gamma_l \geq 83.3$ MeV by taking the lower limit on $m_t > 91$ GeV/c^2[18] from the CDF experiment, and putting ρ_0=1 as predicted by the standard model.

With eq. 2.26, eq. 2.24 becomes[1]:

$$\Gamma_l = \frac{G_\mu M_Z^3}{6\pi\sqrt{2}}\frac{\rho_0}{4}(1 + \frac{3\sqrt{2}G_F}{16\pi^2}m_t^2)[1 + (1 - 4sin^2\theta_w^{eff})^2](1 + \frac{3\alpha}{4\pi}) \tag{2.27}$$

Hence, if $\Gamma_l \geq 83.3$ MeV, $sin^2\theta_w^{eff}$ can be computed in a straight forward way as:

$$sin^2\theta_w^{eff} = \frac{1}{4}[1 \pm \sqrt{\frac{4\Gamma_l}{\rho_{eff}(1 + \frac{3\alpha}{4\pi})(\frac{G_\mu M_Z^3}{6\pi\sqrt{2}})} - 1}\ ] \tag{2.28}$$

2.4 Neutrino Counting

Experiments at the LEP and SLC e^+e^- colliders provided the first non cosmological information concerning the number of light neutrino ($m_\nu < 1/2M_Z$) species. The study of the Z^0 resonance at LEP allows a precise determination of the number of light neutrino species which can be extracted from the data in two distinct ways:

1. through a study of the Z^0 lineshape using one or more of the decay channels of the Z^0.
2. through the direct measurement of the cross section for single photon production from the reaction $e^+e^- \rightarrow \nu\bar{\nu}\gamma$, where the photon is used as the tag on the production of $\nu\bar{\nu}\gamma$, otherwise unobservable.

The first method has the advantage that it can be carried out during a scan of the Z^0 and requires less integrated luminosity, but relies quite heavily on a detailed understanding of the standard model. The second method is less model-dependent, but requires running LEP at energies above the Z^0 resonance and in addition requires greater integrated luminosity for a measurement of comparable precision and it is limited by the understanding of the relative contributions of signal and background processes.

From the Z^0 line shape measurement one can extract the number of light neutrino species belonging to an SU(2) doublet present in the standard model, and hence the number of elementary fermion generations. If there is an additional generation, it

---

^{0}1. Same formula can also be found as a very good approximation from the ref. [20]

will contribute additional channels for the decay of the Z^0 and thus will increase its total width.

There are several ways (see Chapter 6) to determine the number of neutrino species from a study of the Z^0-line shape. Here we will briefly discuss two of them.

2.4.1 The Method of Comparison of the Total and Expected Widths

If the partial Z^0 widths are known, the number of neutrino species is given by N_ν assuming only neutrinos contribute to the total invisible width. The number of neutrino species N_ν is then given by:

$$N_\nu = 3 + \frac{\Gamma_Z - \Gamma_Z^{SM}}{\Gamma_\nu^{SM}} \tag{2.29}$$

where Γ_Z is the total measured width of the Z^0 and Γ_Z^{SM} is the standard model prediction for the width of the Z^0 assuming 3 generations.

$$\Gamma_Z^{SM} = \Gamma_e + \Gamma_\mu + \Gamma_\tau + \Gamma_{hadronic} + N_\nu \Gamma_\nu \tag{2.30}$$

The standard model predictions for the individual partial widths are:

$$\Gamma_e = \Gamma_\mu = \Gamma_\tau = 83.64^{+0.27}_{-0.22} \text{ MeV}$$
$$\Gamma_{hadronic} = 1735^{+6.3}_{-5.6} \text{ MeV}$$
$$\Gamma_\nu = 166.69^{+0.45}_{-0.35} \text{ MeV}$$

So that $\Gamma_Z^{SM} = 2485.99^{+6.37}_{-5.65}$ MeV for $N_\nu = 3$.

where the uncertainties arise from those on the Z boson mass ($M_Z = 91.187 \pm 0.007$ GeV), the top quark mass ($m_t = 141 \pm 27$ GeV), the Higgs mass ($50 < m_H < 1000$ GeV) and the strong coupling constant ($\alpha_s = 0.120 \pm 0.006$) which are based on [19].

In this work, only the $e^+e^- \to Z^0/\gamma \to \mu^+\mu^-$ channel will be analysed. It is not very sensitive to Γ_Z as compared to the hadronic channel, therefore an alterative approach is more adapted to the present analysis and discussed in next section.

2.4.2 The Method of the Peak Cross Section

The total width Γ_Z and the pole muon cross section are related by:

$$\Gamma_Z = 3\Gamma_l + \Gamma_{hadronic} + N_\nu \Gamma_\nu \tag{2.31}$$

with

$$\sigma_{\mu\mu}^{pole} = \frac{12\pi\Gamma_e\Gamma_\mu}{M_Z^2\Gamma_Z^2} \tag{2.32}$$

and

$$\Gamma_l = \sqrt{\Gamma_e\Gamma_\mu} \tag{2.33}$$

Keeping N_ν and M_Z free and taking the total width Γ_Z from the DELPHI measurements or world average, one can fit the $e^+e^- \rightarrow Z^0/\gamma \rightarrow \mu^+\mu^-$ cross section to obtain the value of N_ν. This method is the most precise one but requires a precise knowledge of the luminosity L in order to have a small error on σ_μ^{pole}.

As will be discussed in Chapter 6, this method turns out to be well suited to study the number of neutrino species via the $e^+e^- \rightarrow Z^0/\gamma \rightarrow \mu^+\mu^-$ channel.

Chapter 3

The Description of the Experimental Setup

In this chapter a brief overview of the LEP collider and the DELPHI detector are presented. The design and operation of the DELPHI subdetectors, trigger and offline system used for the $e^+e^- \rightarrow Z^0/\gamma \rightarrow \mu^+\mu^-$ analysis are described in detail.

3.1 The LEP Collider

LEP, the Large Electron-Positron storage ring (circumference $\simeq$ 26.6 km) at CERN, is a quasi circular collider designed to accelerate beams of electrons and positrons circulating in opposite directions. In the present first phase of operation, bunches of electrons and positrons can be made to undergo head-on collisions at centre of mass energies $\sqrt{s} < 100$ GeV, around the Z^0 rest mass energy. In a second phase, which should be accomplished by the year 1994, $\sqrt{s}$ values up to almost 200 GeV will be reached, allowing for W^+W^- pair production. There were four bunches per beam before October 1992 and since then there are eight bunches per beam. Four interaction points have been equipped with experiments named: ALEPH, DELPHI, L3 and OPAL. A partial view of the LEP collider is shown in Fig. 3.1. The injector complex, which delivers to LEP electrons and positrons of 20 GeV, comprises:

- a 200 MeV LINAC which delivers electrons onto a converter target to produce positrons;
- a LINAC which accelerates the positrons and electrons to 600 MeV;

- a 600 MeV storage ring (the EPA, or Electron Positron Accumulator ring);
- the Proton Synchrotron(PS) which accelerates electrons and positrons to 3.5 GeV;
- the Super Proton Synchrotron (SPS) which accelerates electrons and positrons to 20 GeV and injects them into the LEP ring.

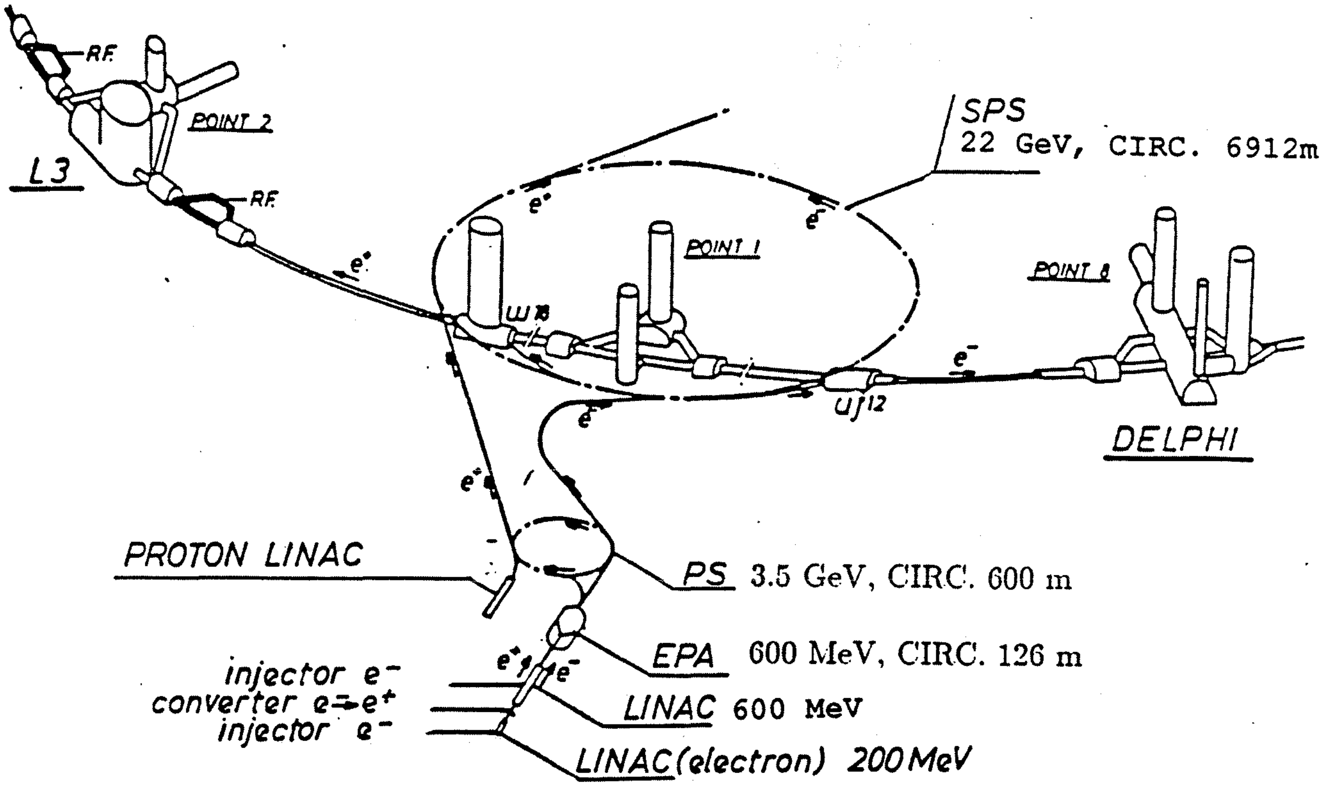

Figure 3.1: An overview of LEP and its injector complex.

A summary of the main parameters of the first phase of LEP is given in Table 3.1. Further details on the design of LEP can be found in [21].

An important machine parameter is the luminosity $\mathcal{L}$. It is a measure of the useful flux of beam particles for interactions. If a reaction with cross-section σ leads to an event rate dn/dt, by definition one has:

$$\frac{dn}{dt} = \mathcal{L}\sigma \tag{3.1}$$

LEP 100 MACHINE PARAMETERS	
Injection energy	20 GeV
Maximum beam energy	55 GeV
Total number of dipole magnets	3368
Dipole field	0.0645 Tesla
Total number of quadrupoles	816
Radio frequency System	
RF frequency	352 MHz
Revolution time	88.92446μs
Length of 128 cavities	212 m
Peak power per klystrons	1.1 MW
Interaction Region	
RMS beam radii	$\sigma_x = 300\mu$m, $\sigma_y = 10\mu$m
RMS bunch length	$\sigma_z = 12$ mm
Number of bunches per beam	4
Number of interaction points	$4 + 4$
Equipped experimental areas(P2,P4,P6,P8)	4
RMS energy spread	6×10^{-4}
Performance	
Current in 4 bunches	3 mA
Nominal luminosity	$1.6 \times 10^{31} cm^{-2} s^{-1}$

Table 3.1: The Main LEP Parameters (phase 1).

The luminosity is given by:

$$\mathcal{L} = \frac{N^+ N^- k f}{4\pi\sigma_x\sigma_y} \quad [cm^{-2}s^{-1}] \tag{3.2}$$

where N^+ and N^- are the number of e^+ or e^- in a bunch, k is the number of bunches of each type of particle, f is the revolution frequency and σ_x and σ_y are the horizontal and vertical r.m.s. beam radii transverse to the beam at the collision points. A Gaussian density distribution in all three directions is assumed.

According to Eq. 3.2, in order to obtain high luminosity one needs large number of particles per bunch and small beam size. However, the number of particles in a bunch N is limited by the interaction between the beams and the electromagnetic fields created by them in the beam pipe. The mean energy loss of an electron per turn is given by the formula [22]:

$$\delta E(keV) = \frac{88.47 \times E^4(GeV)}{R(m)}, \tag{3.3}$$

where E is the bunch energy and R is the bending radius of the dipole magnets. Therefore, synchrotron radiation imposes sharp upper limits on the energy. For a beam energy of 45 GeV nearly 90 MeV per orbit , or 0.2% of the total beam energy is lost due to the synchrotron radiation. In fact the real figure is higher because of the addition of straight sections near the experimental halls (to prevent synchrotron radiation flooding the experiments) and the klystrons galleries, implying a reduced radius of curvature in the bending sections.

During the year 1990, the luminosity was about $\mathcal{L}= 5\times10^{30}cm^{-2}s^{-1}$ which is lower than the design value, $\mathcal{L}=1.6\times10^{31}cm^{-2}s^{-1}$ on the Z^0 peak. The luminosity has reached its design value at end of 1992.

3.2 The DELPHI Detector

DELPHI(Detector with Lepton, Photon and Hadron Identification) is one of the four detectors surrounding an interaction point of LEP. DELPHI is a general purpose detector with emphasis on particle identification. Its characteristics are:

- hadron and lepton identification over approximately 90% of the full solid angle;
- fine spatial granularity of all the components;
- three dimensional information on every track and energy deposition.

The particle identification is partly achieved by combining conventional methods, for example the use of electromagnetic and hadronic calorimeters and muon chambers, as well as ionization measurements in the Time Projection Chamber(TPC). Use is however also made of the particle velocity measurements based on Ring-Imaging Ćerenkov Counters(RICH). These methods mentioned above also provide a fine granularity and the three-dimensional information of the collected tracks. The magnetic field of DELPHI is about 1.23 Tesla and is created by a large superconducting solenoid. The solenoid has a length of 7.4 m and an inner diameter of 5.2 m. The following two confining requirements mainly dictate the size of the beam pipe:

1. The smaller the diameter the better short lived particles can be measured with a high resolution tracking detector (vertex detector).
2. The larger the diameter, the lower background rates due to particle-wall interactions.

During the year 1990, the inner diameter of the aluminium beam pipe at the interaction point was 156 mm.

DELPHI can be divided in sets of subdetectors performing specific tasks:

- Tracking chambers
- Calorimeters
- Muon chambers
- Luminosity monitoring detectors
- Scintillators
- Ring Imaging Ćerenkov Detectors(RICH)

A full list of the DELPHI detectors and a brief summary of their structure and purpose is given in the following subsections. It is worth notice that the detectors are split into three major parts: *a barrel* and *two end caps.* Fig. 3.2 shows an overview of the DELPHI detector. All the technical details are fully described in [23, 24]. The numbers in the fig. 3.2 stand for the following detectors: 1: Vertex detector(VD) 2: Inner Detector(ID) 3: Time Projection Chamber(TPC) 4: Barrel Ring Imaging Ćerenkov Counter(RICH) 5: Outer Detector(OD) 6: High Density Projection Chamber(HPC) 7: Superconducting Solenoid 8: Time of Flight Counters(TOF) 9: Hadron Calorimeter(HCAL) 10: Barrel Muon Chambers(MUB) 11: Forward Chamber A(FCA) 12: Small Angle Tagger(SAT) 13: Forward RICH(FRICH) 14: Forward Chamber B(FCB) 15: Forward Electromagnetic Calorimeter(FEMC) 16: Forward

Muon Chambers(MUF) 17: Forward Scintillator Hodoscope(HOF). The Very Small Angle Tagger(VSAT) is mounted outside the view shown in fig. 3.2

The DELPHI z-axis is coincident with the electron beam, the x direction is towards the centre of the LEP ring and y is in the vertical direction. In polar coordinates θ is the angle with the positive z axis and ϕ is the angle in the x-y plane measured anti-clockwise(seen from a position of positive z) with the positive x-axis; R is the absolute distance from the z axis.

Fig. 3.3 shows an approximate geometrical layout, as seen in the Y-Z plane, of the detectors used in the $e^+e^- \rightarrow Z^0/\gamma \rightarrow \mu^+\mu^-$ study.

DELPHI Collaboration / The DELPHI detector

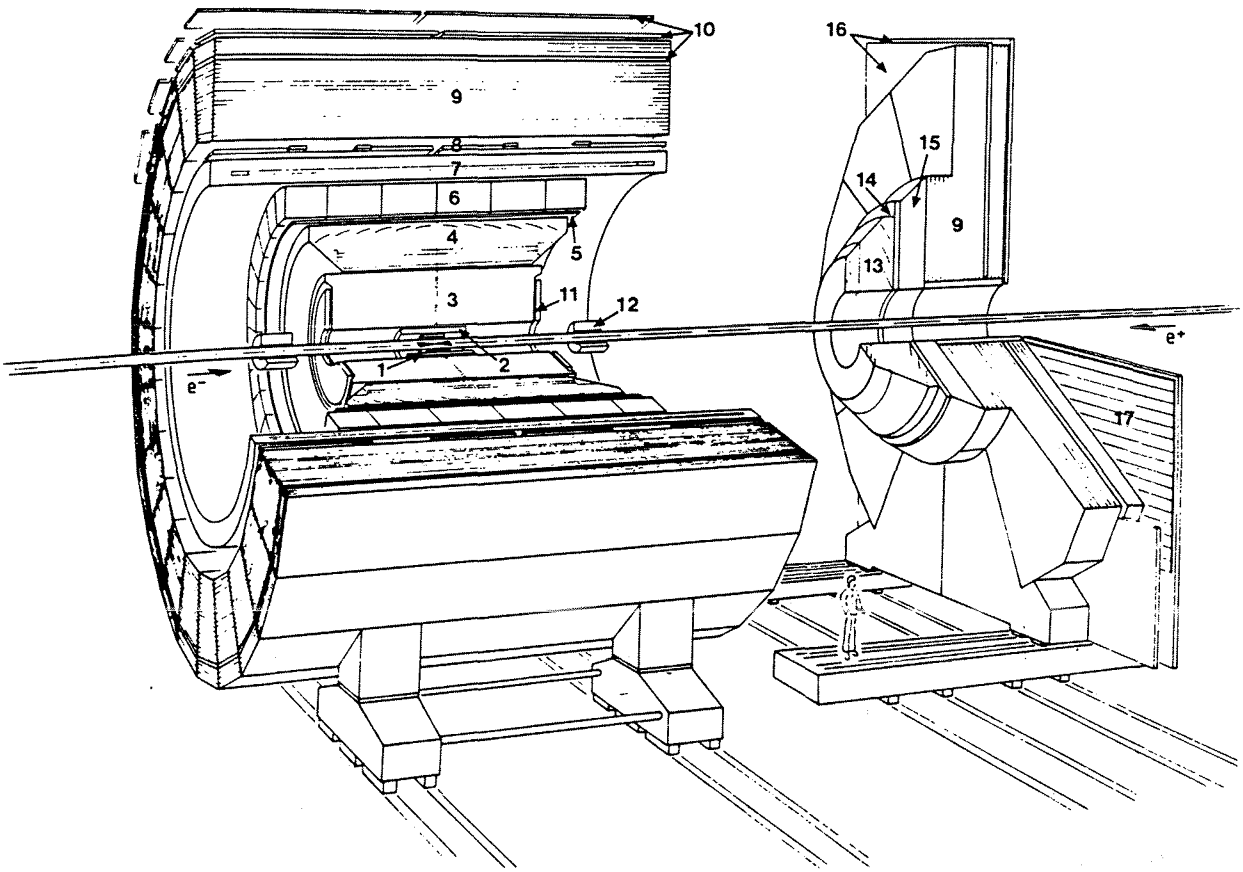

Figure 3.2: The DELPHI detector.

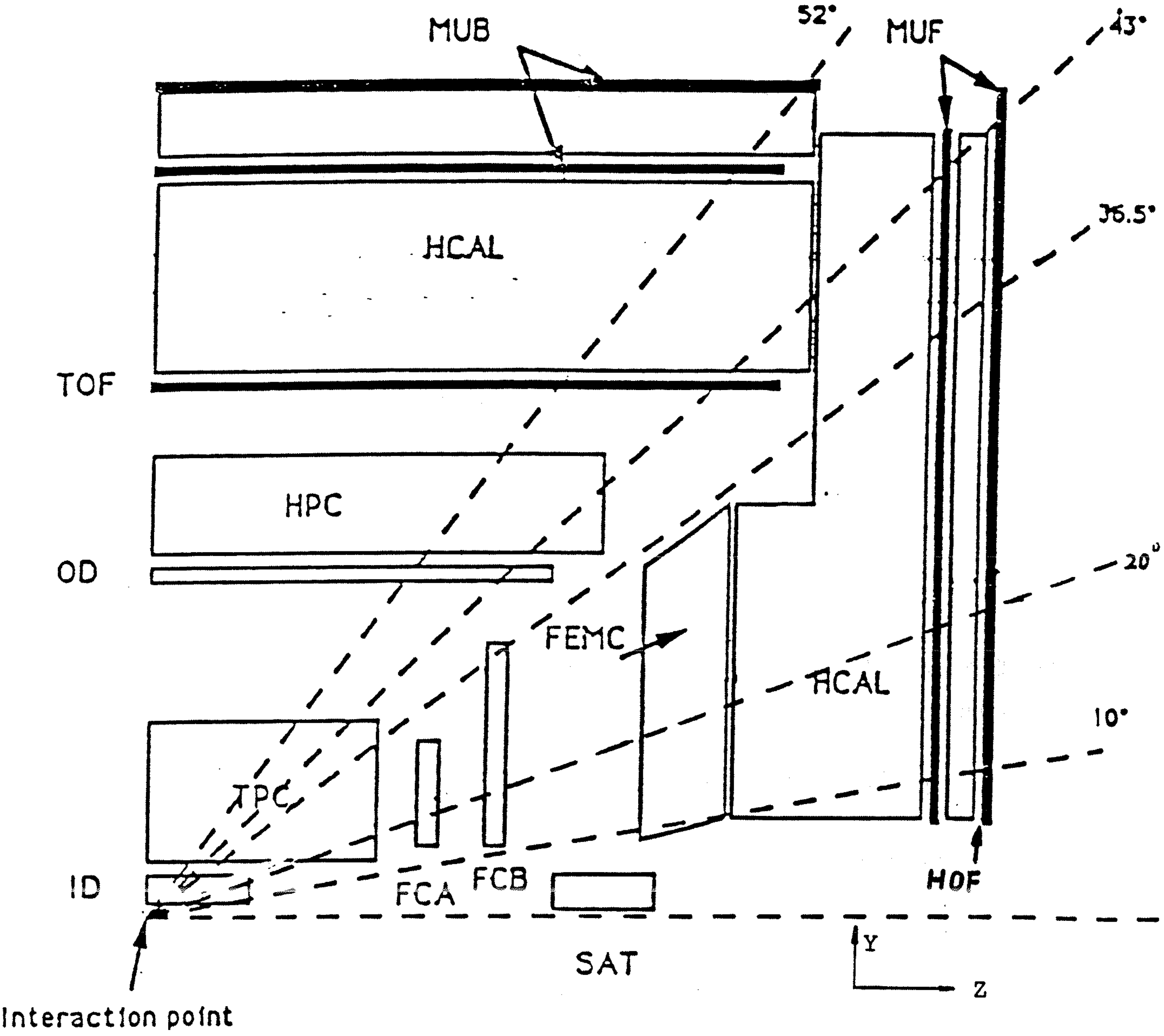

Figure 3.3: DELPHI subdetectors used in this analysis as seen in the Y-Z plane. Only one quarter of the detector is shown.

Detector	R(cm)	$\mid Z \mid$(cm)	$\theta(^o)$	points along track	Resolution per point σ(mm)
Vertex	9/11	$\leq$ 12	37-143	2*	Rϕ: 0.007
ID: jet-s	11.8-22.3	$\leq$ 40	17-163	24	Rϕ: 0.09
trigger-s	23-28	$\leq$50	30-150	5	Z: $<$ 1
TPC	35-111	$\leq$134	20-160	16	Rϕ: 0.23
				192	Z: 0.9
OD	198-206	$\leq$ 232	43-137	5*Rϕ	Rϕ:0.11
				3*Z	Z: 44
MUB	$\sim$ 445	$\leq$ 365	52-138	2(+2)	Rϕ: 1.5
	$\sim$ 485				Z: 10
FCA	30-103	155-165	11-33	2*(x,u,v)	x,u,v: 0.3
FCB	53-195	267-283	11-35	4*(x,u,v)	x,u,v: 0.25
MUF	70-460	463	9-43	(2+2)*(x,y)	x,y: 5.0
		500			
SAT	10-23.8/27.6	203,216,230	2.5-6.8	2(3)	R: 0.3
					ϕ: 0.5^o

Table 3.2: Specifications and performance of tracking detectors. The * refers to the 1990 configuration.

3.3 Tracking Detectors

The tracking detectors include the following detectors: Vertex Detector (VD); Inner Detector (ID); Time Projection Chamber (TPC); Outer Detector (OD); Forward Chamber A (FCA) and Forward Chamber B (FCB). A summary of the principal parameters and the performance of these tracking detectors is given in Table 3.2.

3.3.1 Vertex Detector (VD)

The Vertex Detector directly surrounds the beam pipe and consists of three concentric polygons of silicon strip detectors of length 24.0 cm at average radii of 63, 90 and 110 mm. For the 1990 data taking only two layers were installed at 90 and 110 mm. It covers an angular region in θ between 37^o and 143^o and it is segmented in 24 modules in ϕ, with about 10 % overlap between the modules, parallel to the beam pipe. Each module contains 4 microstrip silicon detectors along Z. This detector is capable of measuring very precisely the transverse (Rϕ) coordinates of the tracks from the charged particles close to the beam pipe. The Rϕ resolution for a single track is about 7 μm and about 100 μm for two tracks separation in 1990.

3.3.2 Inner Detector (ID)

The Inner Detector provides high redundancy for vertex reconstruction and trigger information. It contains:

- An inner drift chamber with jet-chamber geometry, giving 24 Rϕ-points per track.
- 5 cylindrical MWPC (Multi-Wire Proportional Chambers) layers. The wires provide fast trigger information and resolve left/right ambiguities from the jet section. The Z coordinate is read out by circular cathode strips.

Up to typically 20 points per track in the jet chamber and 95 % efficiency per layer in the outer section has been reached during LEP operation. The average single wire resolution is $\sigma_{R\phi} = 90$ μm in the jet chamber and $\sigma_z < 1$mm in the outer layers.

3.3.3 Time Projection Chamber (TPC)

The TPC is a cylindrical drift chamber with an inner radius of 35 cm, an outer radius of 111 cm and a length of 2 × 134 cm. It is segmented in 6 identical azimuthal sectors. When the particles traverse the sensitive gas volume, they will create electrons by ionization. These electrons drift under the influence of an uniform electric field parallel to the z axis to one of the end plates where they can induce signals on 16 circular pad rows and 192 sense wires, providing dE/dX information. The ϕ, z coordinates are given by the readout pads and the measured drift times respectively (at atmospheric pressure and at T = 22°C, the typical electron drift velocity value is 66.94 ± 0.07mm/μs). The track elements (see section 3.9.1) found by the TPC are used as starting point for the track reconstruction in the angular region of $22^o \leq \theta \leq 158^o$.

The TPC has the following specification: good two track separation with three-dimensional localization; efficient e/π separation (complemented by hadron identification with the RICH); and good momentum measurement (by combining TPC, vertex, inner and outer detectors' information. See section 3.3.6). Its resolution derived from operation at LEP is:

$$\sigma_{R\phi} \simeq 230\ \mu\text{m}; \qquad \sigma_z = 0.9\ \text{mm};$$

Two-track separation: 1 ~ 2 cm.

The TPC is the principal tracking device of DELPHI.

3.3.4 Outer Detector (OD)

The Outer Detector is composed of 24 modules mounted on the barrel RICH, each 4.7 m long and consisting of 145 drift tubes in 5 layers. It covers θ angles between 43^o to 137^o, the layers are staggered and overlap with the adjacent modules thereby providing full azimuthal coverage.

The outer detector provides fast trigger information in both Rϕ and z coordinates. The Rϕ coordinate is derived from the drift time in each tube and the Z coordinate reconstructed by the delay time measured at the end of the wires. The resolutions are:

$$\sigma_{R\phi} \simeq 110\ \mu\text{m}, \qquad \sigma_z \simeq 44\ \text{mm}.$$

3.3.5 Forward Chamber A & B (FCA, FCB)

The Forward Chambers are drift chambers which provide triggering and tracking information in the End-Cap regions $11^o \leq \theta \leq 33^o$ and $147^o \leq \theta \leq 169^o$ respectively. The FCA chambers are mounted on both ends of the TPC. Each side consists of 3 chambers, each of them with two staggered layers split into half-disks with an outer radius of 103 cm. Each half-disk has 3 chambers, each with two staggered layers and split into half-discs with an outer radius of 103 cm. The chambers are turned with respect to each other by 120°. This provides 2×3 coordinates: xx′, uu′, vv′, where x′ is staggered with respect to x. The resolutions measured at LEP are:

$$\sigma_{x,y} \simeq 150\ \mu\text{m}. \qquad \sigma_\phi \simeq 25\ \text{mrad}.$$

The FCB chambers are placed between the Forward RICH and the Forward Electromagnetic Calorimeter. It is located at region $|Z| \simeq 267$ - 283 cm and covers the angular regions $11^o \leq \theta \leq 35^o$ and $145^o \leq \theta \leq 169^o$, respectively. It affords a precise track element using 4×3 coordinates x, u, v for tracking and pattern recognition and it substantially improves the momentum resolution in the forward arms. The resolution at LEP is estimated to be:

$$\sigma_{x,y} = 130\ \mu\text{m}.$$

3.3.6 Combined Tracking Detectors

The high momentum resolution is provided essentially by combining the information from the above independent tracking devices. By using the forward chambers, DELPHI has the potentiality for a quite unique resolution for a LEP detector in the forward region. For the 1990 data the following results have been obtained for muon pairs at 45.6 GeV:

$\sigma_p/\text{p} = 7$ %	Using ID, TPC, OD.	in Barrel region.
$\sigma_p/\text{p} = 17$ %	Using ID, TPC, FCB.	in Forward region ($20^o \sim 35^o$).

3.4 Calorimeters

Calorimeters are detectors that measure the energy of traversing charged and neutral particles. They are positioned outside the tracking detectors and are made of high density materials (e.g. lead, iron) in which the traversing particles deposit all or a large part of their energy.

3.4.1 Electromagnetic Calorimeter

The supports for detectors like the TPC, the FCB and the RICH and the complex structure of cable ducts cause a gap in the electromagnetic coverage of DELPHI in the regions $35^o \leq \theta \leq 42^o$ and $138^o \leq \theta \leq 145^o$ (see fig. 3.3). One electromagnetic calorimeter (HPC) covers the barrel region and another (FEMC) covers the two end cap regions of the detector.

The aim of the electromagnetic calorimeters is to measure the charge distribution induced by electromagnetic showers and hadrons with high granularity in all coordinates. Electrons loss nearly all their energy in the calorimeter and generate large and distinctive showers, while pions and muons only deposit comparatively little energy.

High Density Projection Chamber (HPC)

The High Density Projection Chamber is the barrel electromagnetic calorimeter, covering the angular region $43^o \leq \theta \leq 137^o$ (fig. 3.4(a)). It is one of the first large scale calorimeters to use the time-projection technique. The HPC is divided in 6 rings along the z-axis. Each ring is azimuthally divided in 24 modules. Each module extends radially from 208 cm up to 260 cm. The electrons and positrons in the electromagnetic showers ionise the gas between the walls of lead converter material. The ionisation charge of showers and tracks is extracted onto a single proportional wire plane at one end of each HPC module. Their arrival time is used to determine the position of their formation along the drift channel. Thus the three-dimensional charge distribution induced by electromagnetic showers and by hadrons is measured with a very high granularity in all coordinates.

Typical values for the granularity of this device are:

$$\mathrm{Z} \simeq 4.0 \text{ mm}, \qquad \mathrm{R} \simeq 4.5 \text{ cm}, \qquad \mathrm{R}\phi \simeq 4.0 \text{ cm}.$$

The achieved resolutions in the shower direction are:

$$\sigma_\theta \simeq 25 \text{ mrad} \qquad \sigma_\phi \simeq 50 \text{ mrad}$$

Two showers are separated if:

$$\Delta(\mathrm{z}) > 2 \text{ cm} \qquad \Delta(\mathrm{R}\phi) > 4 \text{ cm}$$

The achieved fractional energy resolution, in the reconstruction of 45.5 GeV showers from Bhabha events, is:

$$\frac{\sigma_E}{E} \simeq 10\%.$$

Forward Electromagnetic Calorimeter (FEMC)

The forward electromagnetic calorimeter covers the end-cap angular regions $10^o \leq \theta \leq 36.5^o$ and $143.5^o \leq \theta \leq 170^o$ (fig. 3.4(b)). The FEMC consists of 4500 lead-glass blocks in each end-cap with a projective 'pyramidal' geometry pointing to the interaction region. The lead-glass blocks are read out by vacuum phototriodes. The lead-glass has a radiation length (X_0) of 2 cm. This calorimeter

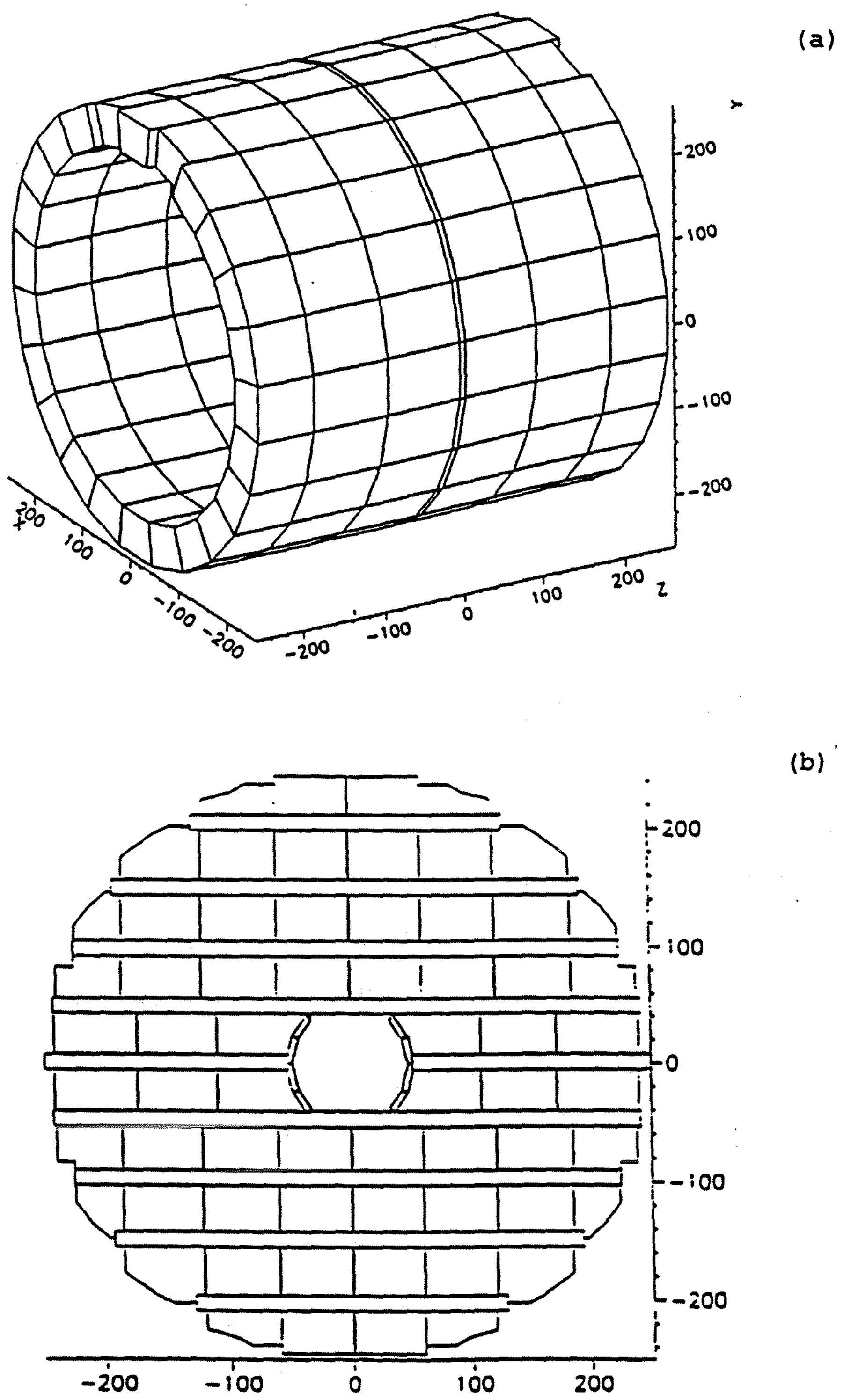

Figure 3.4: View of the electromagnetic calorimeters (a) for barrel (HPC), at 208 cm from the central point of DELPHI in the radial coordinate, and about 4 m long. The 6 z-ring segmentation is exhibited, with 24 RΦ modules in each of these rings. (b) Front view of one of the end caps (FEMC). It consists of about 4500 lead glass blocks.

operates in the difficult region after the end-wall of the TPC ($0.45X_0$) and other thick materials where the showering of electrons, the conversion of photons and other phenomena affect the accuracy of the energy measurement.

The accuracy in the energy resolution and shower position reconstruction is: (E in GeV)

$$\frac{\sigma_E}{E} \simeq [(0.35 + \frac{5}{\sqrt{E}})^2 + (\frac{6}{E})^2]^{1/2}\ (\%)$$

$$\sigma_{X,Y} \simeq \frac{8.2}{\sqrt{E}}\ (\mathrm{mm})$$

The fractional energy resolution in the reconstruction of 45.5 GeV showers from Bhabha events is:

$$\frac{\sigma_E}{E} \simeq 9\%.$$

3.4.2 Hadron Calorimeter (HCAL)

The hadron calorimeter is a sampling gas detector incorporated in the magnet yoke. The polar angle coverage is from 42.6° to 137.4° in the barrel area, and from 11.2° to 48.5° and from 131.5° to 168.8° in end-caps (fig. 3.5 and fig. 3.6).

HCAL consists of 20 layers of plastic streamer tubes. The tubes are inserted into 2 cm slots between the 5 cm thick iron plates of the segmented magnet return yoke in both the barrel and end-caps. The detectors are wire chambers which consist of a plastic cathode forming 8 cells of 9×9 mm^2 with a central anode wire in each tube. Hadronic showers are generated when incoming particles impact on the iron, and the streamer tubes sample the deposited energy in the layers between the modules. The performance of the detector has been studied using hadron and dimuon events from Z^0 decay. For the hadronic analysis, tracks measured in the TPC and penetrating through to interact in the hadron calorimeter were used. Good performance results have been achieved [24, 25].

The energy resolution is:

$$\frac{\sigma_E}{E} \simeq \frac{120}{\sqrt{E}}\ (\%).$$

with a granularity of about 10 cm.

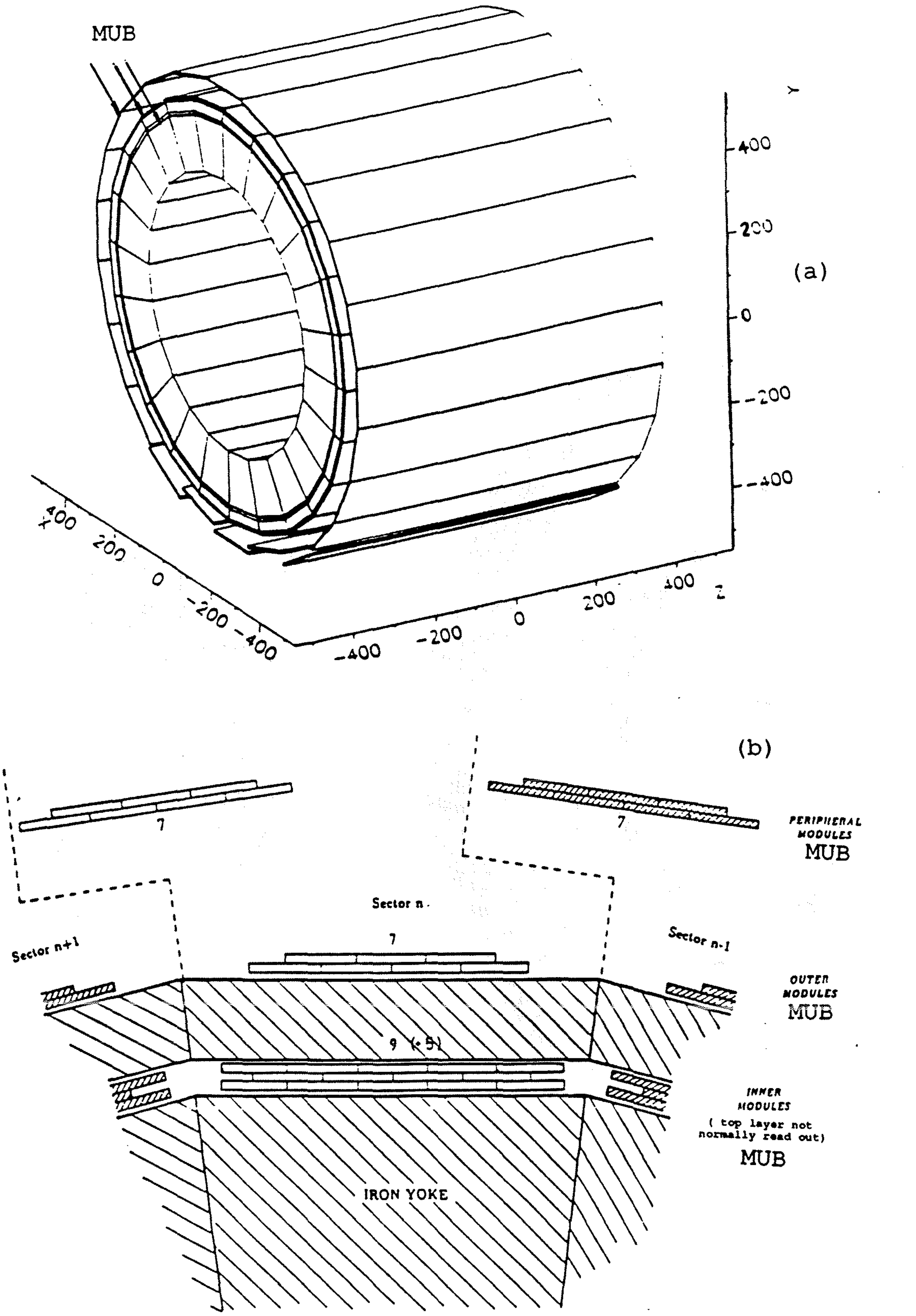

Figure 3.5: The barrel hadronic calorimeter (HCAL) and muon chambers (MUB): (a) perspective; (b) partial transverse section. The Rϕ segmentation (24 modules) of both detectors, and the three layers of MUB are visible.

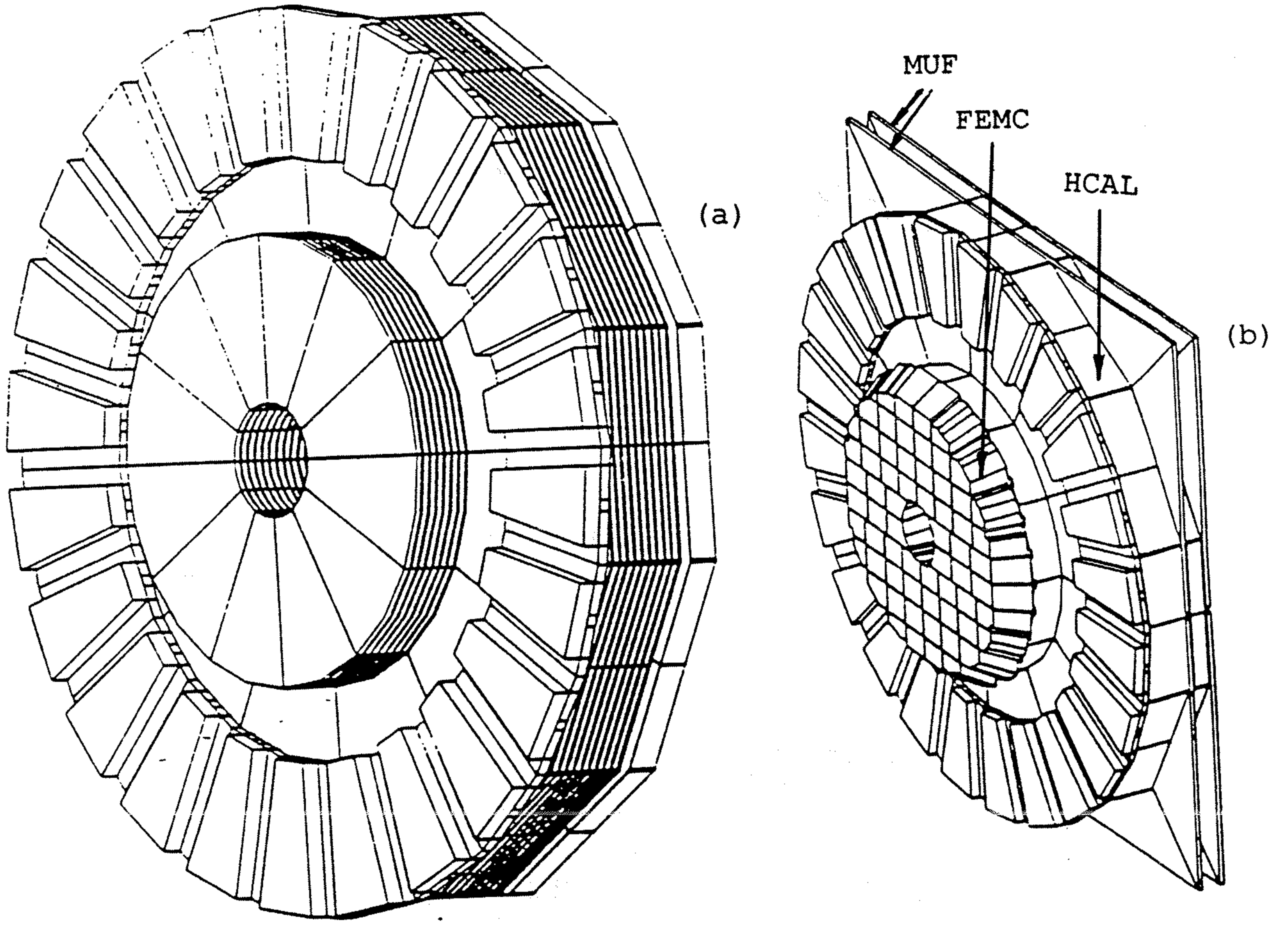

Figure 3.6: (a) Forward hadronic calorimeter components (inner and outer disk). (b) combination between FEMC, HACL and MUF in one end cap.

3.5 Muon Chambers

The muon chambers provide muon identification. The muon chamber angular coverage is not complete. Beside the inevitable low angle dead zones there are the regions $43^o \leq \theta \leq 53^o$ and $127^o \leq \theta \leq 137^o$ which are not covered by muon chambers (fig. 3.3 for the muon chambers coverage). The Barrel Muon Chambers (MUB) cover the barrel region and the Forward Muon Chambers (MUF) cover the two end-cap regions. Fig. 3.5 shows the relative position between the HACL and MUB and fig. 3.6 shows the relative position between the FEMC, HACL and MUF.

The Muon Chambers will be described in detail in chapter 4.

3.6 Luminosity Monitoring Detectors

The luminosity monitors: Small Angle Tagger (SAT) and Vary Small Angle Tagger (VSAT) are small detectors very close to the beam pipe. They are used to measure the luminosity by detecting Bhabha events (t-channel $e^+e^- \longrightarrow e^+e^-$). They are also used to perform a precise survey of the beam position and the interaction point.

During the year 1990, the SAT was the principal luminosity monitor. Each of its two arms consists of an electromagnetic calorimeter. The calorimeter covers the polar angles from 43 (3^o) to 135 mrad (7.7^o) placed about 250 cm from the interaction point and is aligned parallel to the beam. It consists of alternating layers of lead sheet (0.9 mm thick) and plastic scintillating fibres (ϕ=1 mm). Scintillating fibres were chosen because of their excellent radiation hardness and also because they can easily be fitted into a cylindrical geometry. The total thickness of the calorimeter is 28 radiation lengths. The calorimeter is divided in 2 half cylinders. In the vertical plane, there is a 2 cm wide dead zone between these two half cylinders. Behind each calorimeter the fibres are collected into 288 bundles per half cylinder, each read out by a photodiode.

The segmentation of the SAT is shown in Fig. 3.7(a). In each arm the calorimeter was foreseen to be complemented by a silicon layer track detector. As these tracking detectors were only partly installed in one arm in 1990, a lead mask (10 radiation lengths thick) was used on other arm (Fig. 3.7(c)). Its conical outer surface defines the acceptance radius to < 100 μm. Zones of 15^o from the vertical have also been excluded

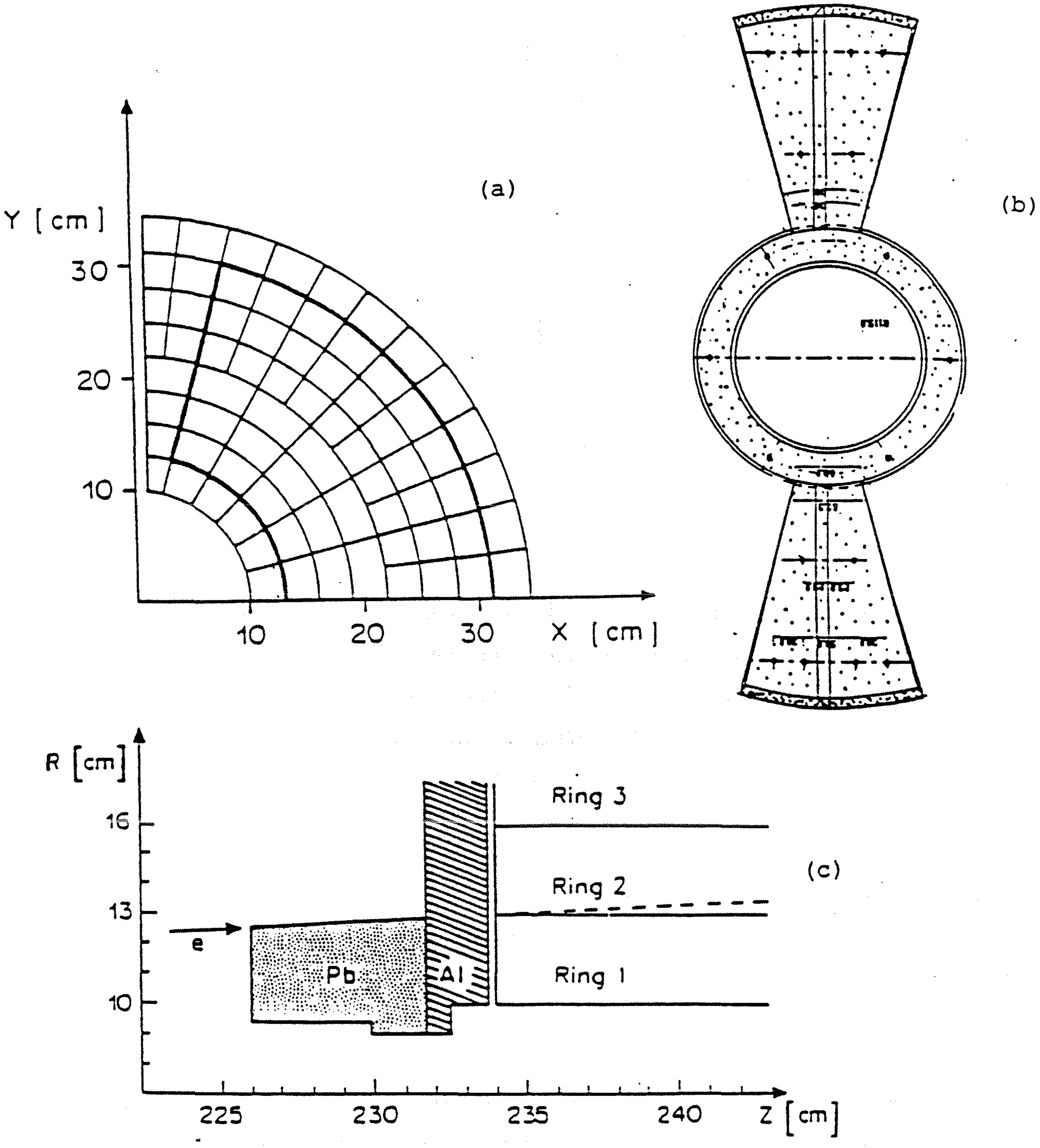

Figure 3.7: (a) Segmentation of the SAT calorimeter in one quadrant. The border of the acceptance in the calorimeter with the mask is indicated by a thick line (dashed line for the 12 cm mask). (b) Front view of the 'butterfly' wings and lead mask. (c) Longitudinal (partial) view of SAT and the 13 cm lead mask in front of it, covering completely the first ring.

from the fiducial volume. (Fig. 3.7(a)). So called "butterfly" wings are added to the lead mask described above to cover the vertical dead zones (Fig. 3.7(b)). They allow an accurate definition of the fiducial region close to the vertical dead zones and hence reduce the associated systematic uncertainty.

3.7 Scintillator Counters

The barrel Time Of Flight (TOF) system and the Forward Hodoscopes (HOF) in the end caps, consist of scintillation counters. They cover the barrel and end-cap regions respectively. The main function is to participate in fast trigger decisions, to measure the time of flight of particles (barrel scintillator) and to provide information about cosmic particles and the cosmic trigger.

TOF consists of scintillator strips equipped with photomultipliers at both ends allowing Time Of Flight measurement. They are mounted between the Solenoid and the iron return yoke, covering polar angles $41^o \leq \theta \leq 139^o$ (with a dead zone around $\theta = 90^o$). HOF consists of two planes of scintillator counters (one per end-cap) mounted between the end-cap yoke and the second layer of the Forward Muon Chambers. HOF is the only detector giving an independent muon trigger in the 1st level (see 3.8.2 about the trigger level) at the end cap regions, extending and improving the muon detection and trigger efficiency down to the very low angle region.

3.8 The Trigger System

The trigger system is one of the fundamental parts of the data taking chain of an experiment. It decides whether the Data Acquisition System (DAS) has to record a certain event on the permanent data storage (tape, cassette) or that it has to clear the buffers and wait for a next event.

3.8.1 Trigger Rate and Limitations

Trigger Rate and Total Events

At LEP, bunch crossings at the collision points of the beams occur about every 22 μs. If the data recorded by the detector at each bunch crossing would be registered, the typical event rate would be about 45 kHz.

For the designed machine luminosity $L \sim 10^{31}\ cm^{-2}s^{-1}$ and the Z^0 peak cross-section, $\sigma_z \simeq 30$ nb, the Z^0 production rate would be:

$$\frac{dN_{Z^0}}{dt} = L\sigma \simeq 0.3 H_Z \tag{3.4}$$

Besides $e^+e^- \rightarrow Z^0$ interactions, there are other processes occurring during the collision time, such as $\gamma\gamma$ interactions, beam gas interactions, cosmics, noise etc. Therefore the total rate of events recorded in the detector has the following components[1]:

- The rate of produced γ, Z^0 events which is dependent on the centre of mass energy of the annihilation process $\sim$ 0.3 Hz on the peak of the resonance, diminishing off peak.
- The Bhabha event rate in the small angle luminosity detectors which is approximately constant in the resonance range. It is of the same order of magnitude as the Z^0 event rate at the peak: 0.3 Hz.
- The rate of events from $\gamma\gamma$ interactions (about 0.04 Hz) which has a sizable cross-section within the detector acceptance.
- The contribution from the machine background events (off-momentum beam particles, scattered photons, beam gas collisions, etc.).
- The rate of cosmic events crossing the detector volume. Such rate can be estimated and controlled to rather low levels. It is less than 0.001 Hz.
- Noisy detector components can generate signals faking real interactions and contribute to the total rate of recorded events.

The aim of the trigger system is to take as many good events as possible and to reduce as much as possible the background. If the trigger can make a decision within 22 μs, no interesting events will be lost due to the trigger decision. However, there are two main factors which limit the trigger decision time. They are the detector limitations and the electronics limitations.

---

[1] These rates correspond to a value of $L \sim 10^{31}\ cm^{-2}s^{-1}$. In reality, during the 1990 data taking period, the LEP peak luminosity was about $5\times 10^{30}\ cm^{-2}s^{-1}$.

Detector Limitations

The detector dimension and the physical processes used to obtain the final signal often limit the use of a detector in the trigger. There are three slow subdetectors in DELPHI. They are:

- TPC: has a long drift distance of up to 1.2 m with a typical electron drift velocity of 6 cm/μs. It can take 20 μs before the detector produces any signal.
- HPC: mainly participates in the electromagnetic energy subtrigger. Its average read-out time is about 12 μs. Scintillators are inserted in the HPC modules to provide information for the fast energy trigger.
- The maximum drift time from the forward muon chambers can be as long as 14 μs. Therefore MUF is prohibited from participating in the fast muon trigger.

Electronics Limitations

The electronic limitations are mainly caused by the minimum time needed by the front-end electronics to be ready to accept a new event after a reset. It is due to event buffer clearing and initialization of the electronics. Most of the DELPHI partitions need less than 1 μs to be ready before the next Beam Cross Over (BCO) signal, some subdetectors need a few μs. The time needed to transfer an event and record it in the data storage medium also slows down the trigger system.

3.8.2 DELPHI Trigger for the year 1990

In the year 1990, the DELPHI trigger system was organized in two levels (fig. 3.8): the *first level trigger* (T1) and the *second level trigger* (T2). The trigger data from the subtriggers contain multiplicity information on the number of tracks (0, 1, 2 and more than 2), or number of energy clusters above a given threshold for the calorimeters. The muon subtrigger will be studied in detail in chapter 5.

- **First Level Trigger(T1):**

  The first level trigger was introduced to provide a fast background rejection and allowed to minimise the space charge in the TPC. Its processing time was

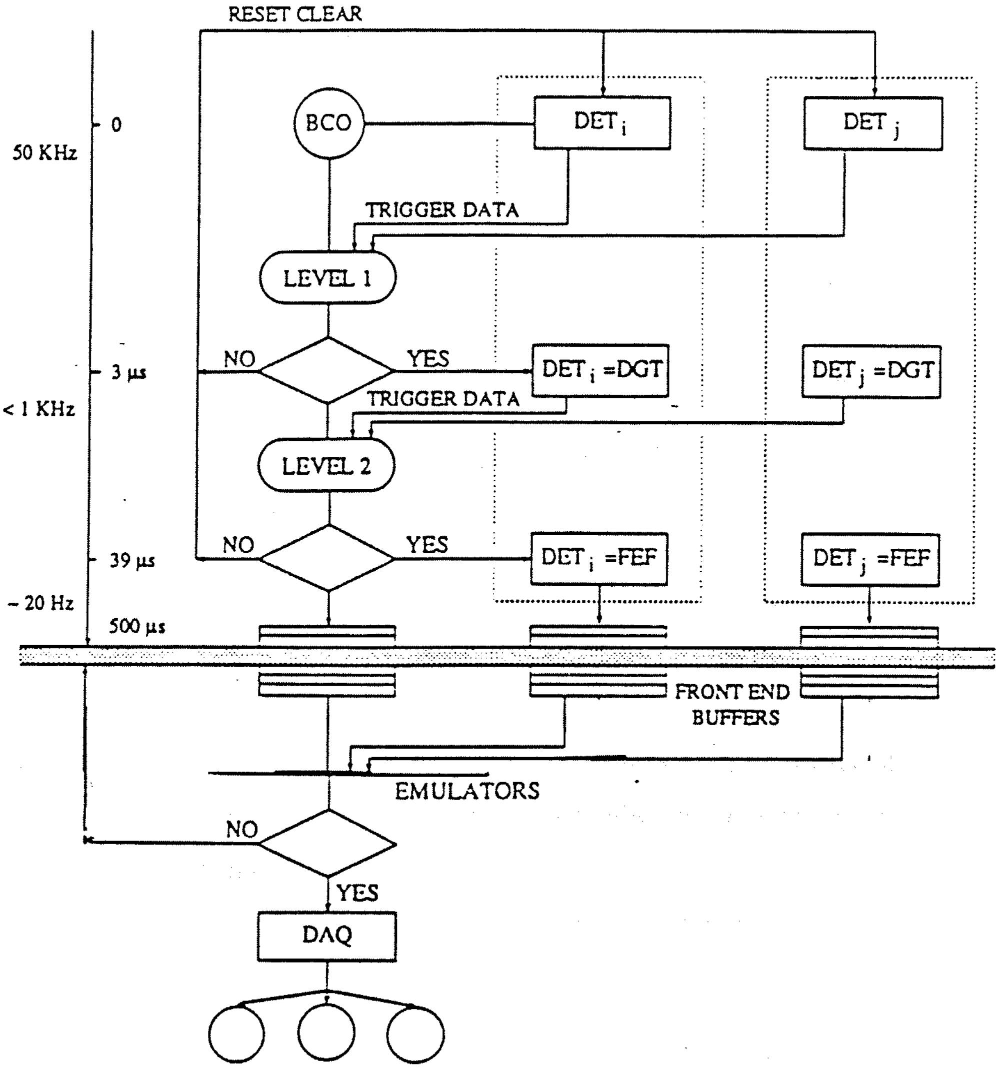

Figure 3.8: The two levels of the DELPHI trigger system and the rates, timings of each level.

limited to 3.5 μs after BCO. If the decision at this level was negative the front-end electronics was reset and TPC gas amplification would be gated off until the next BCO. The rate was about 500 Hz.

- **Second Level Trigger (T2):**

  In case of a positive T1 decision, the system takes the next 35 μs to perform the second level trigger decision. It used the information from the drift detectors like the TPC, HPC and MUF, which was available only 10 $\sim$ 20 μs after the BCO. If the second level decision was negative the front-end electronics was reset and ready to take the next BCO. Thus one BCO was lost in case of a reject at the second level. If the second level decision was positive, another 500 μs to 7 ms were needed to free the Front End Buffers (FEBs) and to prepare for a new event. The rate of the second level was about 2 Hz.

The Trigger Decision System

The trigger decisions were based on the information obtained from the different detectors. The following information was given by the participating detectors to the first and second level trigger.

- **the number of tracks (Track Subtrigger)**: the first level barrel track trigger uses data from the ID and OD and looks for a correlation between the two detectors in the R-ϕ plane. The TPC provides a second level track trigger using an 'OR' of the ID and OD signals as first level trigger. The forward/backward track trigger uses data from Forward Chambers A and B.
- **muon's (Muon Subtrigger)**: the participating detectors are HOF and muon chambers.
- **total energy (Total Energy Subtrigger)**: this trigger looks for electromagnetic showers in the FEMC. The threshold was 4 GeV per shower. The HPC gives a back to back trigger where signals in at least two opposite HPC scintillator sectors are required.
- **Bhabha's (SAT Subtrigger)**: it is the e^+e^- trigger at small angles used for the luminosity monitoring. The threshold was 13 GeV in both back-to-back arms of the SAT.

- **other triggers:** apart from the triggers described above, several other triggers are available. They include a TOF back-to-back trigger, a TOF majority trigger, ID/OD majority trigger, the SCOD trigger which combined information from the TOF and OD, and the majority 2 trigger which has the following components: HOF, FEMC, FCA/B, ID and OD.

3.9 DELPHI Offline System

The DELPHI offline system consists of the following main components:

- a data analysis program (DELANA)
- a Monte Carlo simulation program (DELSIM)
- an interactive graphics system (DELGRA, DELTOP and COPA)

DELANA calls a set of routines named as PXTAGxx.CAR containing tagging code used to flag events specific to each physics analysis team.

3.9.1 DELANA

The DELPHI data analysis and event reconstruction program is called DELANA ([27]).

For each event, a steering routine checks the validity period of the database information for each detector and updates the constants which are in memory if necessary. For each detector module, steering routines are called to control the stand alone 'local pattern recognition'.

In the first stage, the data is analysed to produce space points, track elements, energy deposits etc., without using any information from other subdetectors. Track search processors group the track elements into candidate tracks. These candidate tracks are then submitted to the full track fit to resolve ambiguities and to provide fitted track parameters. The resulting tracks are extrapolated throughout the detector, giving impact points and track parameters and their errors (including extrapolated measurement errors and multiple Coulomb scattering errors) at the entry to each of the detectors.

In the second stage, tracking detectors are called to complete their pattern recognition using predictions supplied by the first stage. A further pass of the track search and fit processors is made, using as input those track elements not so far included in a fitted track. All rebuilt and newly found tracks are then extrapolated and the results are added to those from the first stage pattern recognition. Second stage calorimeter processing is called, and whenever a calorimeter can connect an energy deposit to an extrapolated charged track, this information is added to the track bank information.

The next step is to call all detectors with separate mass identification processors and to include the results in the data for the appropriate track. The mass information provided by the individual detectors, is then collected and analysed by a global processor to give a final mass assignment to the tracks.

Finally, primary and secondary vertices are fitted from among the charged particle tracks. Neutral particle trajectories are constructed from the calorimeter data and added to the primary vertex.

Data management inside DELANA is based on the Track Analysis and Graphics Package, TANAGRA[33]. This package provides a well defined data structure (VETBAS - Vertex and Track Basic Structure) for storing vertex and track information in a module independent format. At the end of each event processing, DELANA also provides a summary (DST) of the data contained in the VETBAS. The output of the reconstruction program can be chosen to be the complete VETBAS structure, the DST only or both data structures.

TANAGRA

TANAGRA is organised as a library of routines built on top of the memory management package ZEBRA([28]), and consists of:

- a data structure called VETBAS (Vertex and Track Basic Structure) containing track, vertex and space point information in a defined format. The form is almost independent of the detector from which the information originated;

- a package of routines to transfer, retrieve or modify the VETBAS information. The data are carefully protected; a scheme is provided to test if an intervention is allowed, given a set of privileges depending on the user and the nature of the intervention;

- some application software, referred to as DAST (Direct Application Software of TANAGRA).

Event Data Tree

Several levels of data exist in the VETBAS structure (see fig. 3.9). They reflect the different data reduction steps during the event analysis:

- **TD (Detector data)**: the detector data, TD, are saved in a detector dependent form. The data stored at the TD level are mainly space points, drift time and pulse heights, hence they are not the raw data themselves but require some preprocessing (calibration) by the detector dependent analysis modules. The TD data are the input to the local pattern recognition modules.

- **TE (Track Elements)**: the pattern recognition is first done locally for the various detector components. The results of this local pattern recognition are transformed to the global DELPHI reference frame and stored at the TE level in the form of space points, track positions and directions independent of the originating detector component. The TE data will be used by the global pattern recognition to build track strings.

- **TS (Track Strings)**: the global track search tries to connect track elements together, creating strings of track elements, by a fast string search algorithm. The results of the string search are stored at the TS level in the form of lists of track elements belonging to a candidate charged particle track. If there is some ambiguity, TANAGRA has the facility to keep all concurrent solutions and to specify that they are mutually exclusive.

- **TK (Tracks)**: The candidate track strings are submitted to the full track fitting procedure which solves all ambiguities and contradictions. The results are stored in TK banks, which thus represent a clean and consistent set of tracks.

- **TB (Bundles of tracks)**: when the tracks have been formed they will be scanned to find common origins. A list of tracks, possibly originating from the same vertex, is stored as a track bundle at the TB level.

- **TV (Vertices)**: starting from one bundle or several bundles of tracks, a global vertex fit can be performed in order to determine both the vertex position and the track parameters at the vertex.

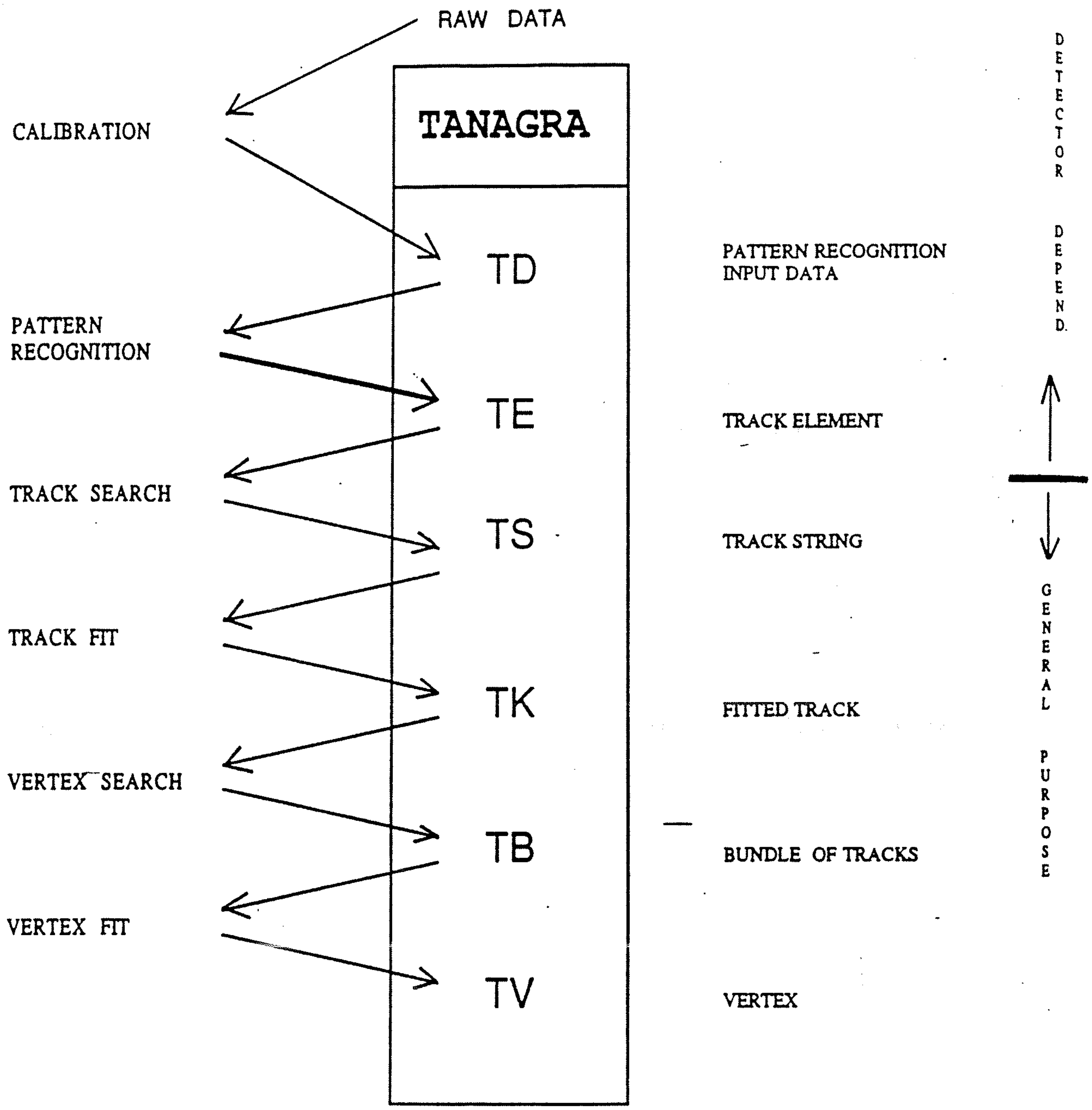

Data reduction and TANAGRA entities at each processing step

Figure 3.9: The different data levels of the VETBAS data structure.

There is a general DELANA extrapolation package, giving intersection points of extrapolated tracks on various surfaces throughout the detector which are stored in TKX banks.

The analysis of the channel $e^+e^- \rightarrow Z^0/\gamma \rightarrow \mu^+\mu^-$ described in this thesis is based on TANAGRA TE and TK information.

DELANA Leptonic Tagging

For the dimuon channel analysis the important tagging in DELANA is the leptonic tagging.

The aim of this tagging is to separate leptonic channels from background events (due to beam gas, beam wall, cosmic events) and hadronic events (which normally should have a large number of charged particle tracks).

Events were tagged as likely leptonic candidates if they satisfied at least one of the following 2 sets of conditions:

1) Total multiplicity of charged particle tracks ≤ 8.

AND

- at least one charged particle track with impact parameter at the normal beam crossing point < 8 cm in the xy-plane and < 10 cm from z=0.

AND

- ESUM $= \Sigma E_{charged\,particles} + \Sigma E_{electromagnetic\,showers} > 8$ GeV.

2) Total multiplicity of charged particle tracks ≤ 8.

AND at least one of the three conditions:

- at least 2 showers in HPC with E > 5 GeV

OR

- at least 1 shower in each end cap of FEMC with E > 4 GeV.

OR

- at least 1 shower with E > 10 GeV.

'Team 2' Tagging

In addition to the DELANA leptonic tagging, events were tagged which had no charged particle tracks but which had roughly back-to-back muonic signals in the MUF, HCAL, FEMC or TEs in the forward tracking chambers. This tagging is called the 'Team 2' tagging named after the DELPHI physics team 2 which coordinates the analysis of the $e^+e^- \rightarrow \mu^+\mu^-$ data. The team 2 tagging is mainly designed for the dimuon analysis in the forward region where the tracking efficiency is slightly lower than that in the barrel region.

3.9.2 DELSIM

DELSIM[29] is the Monte Carlo simulation program used by DELPHI. It includes event generators for e^+e^- interactions (and some background events) and the tracking of the produced particles through the DELPHI detector.

The generation part of DELSIM contains generators for all $e^+e^- \rightarrow Z^0/\gamma \rightarrow f\bar{f}$ processes, and Z^0H^0, H^+H^- and 2γ processes. DELSIM can easily be interfaced with external generators like MUSTRAAL, WOROJET, KORALZ, DYMU3, etc. which including all radiative corrections to Z^0 production. The full generation history and all particle relationships are saved by DELSIM and can be used for physics analysis studies. DYMU3[30], KORALZ[31] and BABAMC[32] generators are used to generate $\mu^+\mu^-$, $\tau^+\tau^-$ and e^+e^- events to study the detection efficiencies and the background.

After the generation, the final state particles are tracked through the detector. At each tracking step, the simulation code of the detector module located at the current particle position is called. Each module has two objectives:

- to determine space points for display purposes and for checking track finding algorithms;
- to simulate the pulses on electronic channels.

During the particle tracking the following processes are taken into account:

- Bending in the magnetic field
- Multiple scattering

- Energy loss
- Bremsstrahlung
- Photon conversion
- Compton scattering
- Nuclear interaction and absorption

For each detector, the inefficiencies are taken into account and realistic electronic noise and background is added.

In the detector dependent software, the output is converted into the form in which it appears as raw data in a real data taking situation.

Chapter 4

The Muon Chambers and the Slow Control System for the Monitoring of the Drift Velocity of the Forward Muon Chambers

The DELPHI muon detector system consists of two parts: the barrel and end cap chambers. In each of the two end caps of DELPHI, behind 85 cm of iron of the magnet return yoke, the Forward Muon detector (MUF) consists of two planes of drift chambers separated by another 20 cm of iron.

The slow control system of the MUF chambers has been developed to monitor several parameters among which the detector high voltages, the gas pressure, the anode thresholds, and the drift velocity. The first part of this chapter briefly describes the principles of operation of drift chamber in general and of the DELPHI muon chambers in particular, while the second part is devoted to the details of the monitoring of the drift velocity.

4.1 Principles of Operation of Drift Chambers

The principles of operation of drift chambers are very well described in detail by Sauli[34]. A basic drift chamber arrangement is shown in fig. 4.1. In its basic form, a single-cell gas filled drift chamber consists of a drift region of moderate electric field, followed by a high field region around an anode wire providing avalanche multiplica-

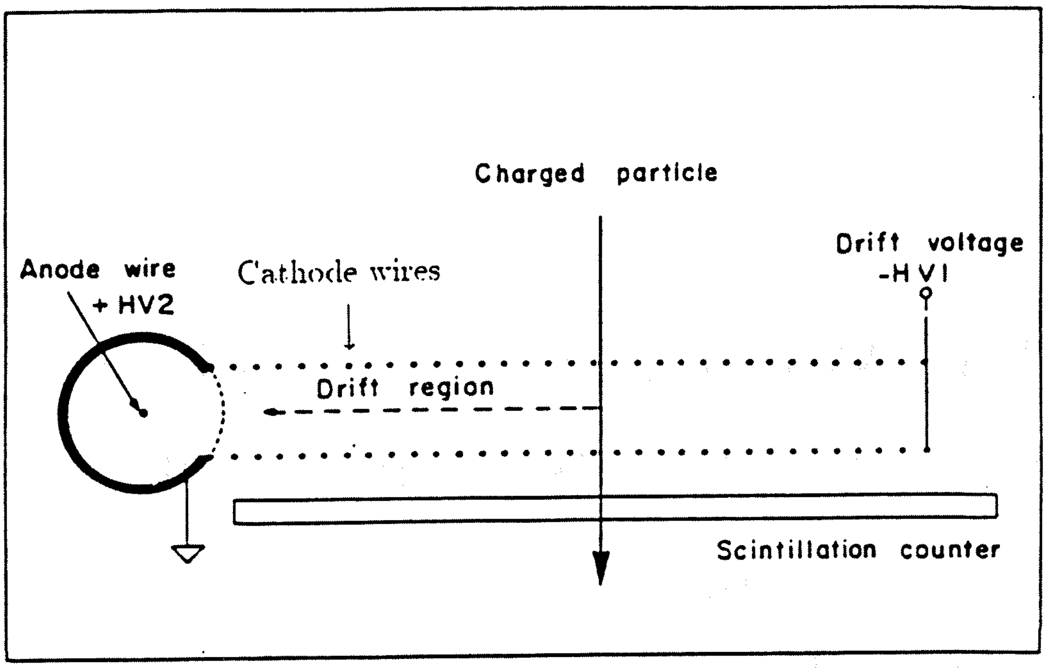

Figure 4.1: Principle of operation of a drift chamber.

tion of the number of electrons reaching the wire. A region of approximately uniform field is set up between the anode and cathode wires. A charged particle traversing the gas filling of the chamber liberates electrons that drift towards the anode. After a time Δt, the electrons are collected at the anode, and a signal is recorded indicating that a charged particle has passed. The position of the particle's traversal is then given by:

$$x = \int_{t_0}^{t_0+\Delta t} V_d(t)dt \tag{4.1}$$

where V_d(t) is the electron drift velocity. The initial time t$_0$ is defined by a fast externally generated pulse. In the DELPHI experiment t_0 is given by the Beam Cross Over time.

For a constant drift velocity as expected in an uniform electric field, relation Eq. 4.1 becomes

$$x = V_d \bigtriangleup t \tag{4.2}$$

4.1.1 Primary Ionization

A charged particle, traversing a gaseous medium, can interact with it in many ways. However, only the electromagnetic interaction is used as a basis for the detection. By incoherent Coulomb interactions, a fast charged particle excites the gas atoms and ionises them along its path. The resulting positive ions and free electrons are the basic constituent of the electrical signal developed by the gas chambers. For several kinds of gases at atmospheric pressure and for minimum ionising particles, the energy loss and the produced number of ion pairs are given in [34]. The contribution of other electromagnetic processes, such as Ćerenkov and transition radiation, to the total energy loss are negligible in gases.

4.1.2 Drift of Electrons

Due to their small mass, the ionisation electrons can substantially increase their speed between subsequent collisions with the gas molecules and gain significant kinetic energy under the influence of the applied electric field. They move along the field direction with the average drift velocity V_d. The value of V_d is essentially a function of the applied electric field E and is given by the following formula, due to Townsend as referred by Sauli[34]:

$$V_d = \frac{e}{2m} E \tau \tag{4.3}$$

where τ is the mean time between collisions and e and m are the charge and mass of the electron respectively. The drift velocity of the electron is smaller than its non-directional velocity v, for an electron of mean free path $\lambda(\varepsilon)$ at thermal erengy ε one has:

$$\tau = \frac{\lambda(\varepsilon)}{v} = \frac{1}{v} \frac{1}{N\sigma(\varepsilon)}, \tag{4.4}$$

where N is the number of molecules per unit gas volume and $\sigma(\varepsilon)$ is the collision cross section. Since N is proportional to the pressure P divided by the temperature T, we expect the drift velocity to be dependent on the so-called *reduced electric field* E/P, that is:

$$V_d \sim \frac{ET}{P} \tag{4.5}$$

Thus for a given chamber geometry, the major factors which can influence the drift velocity are:

- the applied electric field
- the gas pressure
- the gas composition
- the temperature of the chamber

In a realistic system it is possible to take all these factors into account by proper monitoring and to set definite limits to the tolerable variations as function of the desired final accuracy.

In a drift chamber, the electric field is shaped to be as uniform as possible throughout the chamber. Electrons very quickly reach a stable drift velocity and maintain it over most of the drift path, thus giving rise to a simple linear relationship between drift time and drift distance (see Eq. 4.2). Therefore one can obtain the space coordinates of an ionising particle traversal from the measurement of the drift time.

4.1.3 Avalanche Multiplication

At a low value of the electric field, the electrons and the positive ions created by the ionising particles simply drift to their respective collecting electrodes. Along their migration path, many collisions normally occur between the ions or electrons and the neutral gas molecules. If the energy of electrons is greater than the ionization potential of the medium, an additional ion pair may be created in the collision. The electrons liberated by this secondary ionization process will also be accelerated by the electric field. During their subsequent drift, they undergo collisions with other molecules and thus can also contribute to additional ionization. Near the anode wire where strong electric fields are present, this gas multiplication process therefore takes the form of a cascade, called *avalanche formation.*

Consider an electron liberated in a region of uniform electric field. After about one mean free path of amplification λ_p, one electron-ion pair will be produced, and two electrons will continue the drift. Again after about one mean free path, two other ion pairs will be produced, and so on. The avalanche multiplication factor M is given by the following formula:

$$n = n_0 e^{\frac{x}{\lambda_p}}, \qquad M = \frac{n}{n_0} = e^{\frac{x}{\lambda_p}} \tag{4.6}$$

where n_0 is the number of electrons at a given position. After a path x, the increase in the number of the electrons will be *M*.

In the vicinity of the anode formed by a thin metal wire, the electric field in the system is maximum at the surface of the wire and rapidly decreases as r^{-1}, the inverse of the radial distance to the wire. In most of the region where the charges are produced by the primary ionisation process, the electric field only makes electrons drift towards the anode and positive ions towards the cathode. But very close to the anode, normally at a distance of a few wire radii, the field is strong enough so that multiplication starts; a typical drop-like avalanche develops with all electrons in the front and ions behind.

Fig. 4.2 shows the time development of an avalanche around the anode wire. A single primary electron proceeds towards the anode (a), experiencing ionising collisions in regions of increasingly high fields (b). Due to the lateral diffusion, a drop-like avalanche develops surrounding the wire (c)(d). Electrons are collected in a very short time (about 1 nsec) and a cloud of positive ions is left behind, slowly migrating towards the cathodes (e). The consequence of this avalanche formation is that the drift velocity is no longer constant near the anode wire.

Depending on the voltage difference between anode and cathode, on the working gas etc., the chamber can be operated in different modes: for example the proportional mode (like in the DELPHI Barrel Muon detector case), and the limited streamer mode (in the DELPHI Forward Muon chambers case).

The main features of the limited streamer mode in which the DELPHI MUF detector operates can be summarized as [35, 39]:

1) Thick anode wires (100 μm stainless steel in MUF case) which are normally robust enough to be directly stretched through the chamber without supporting spacers (or with few supporting spacers), allowing the use of extruded Al tubes

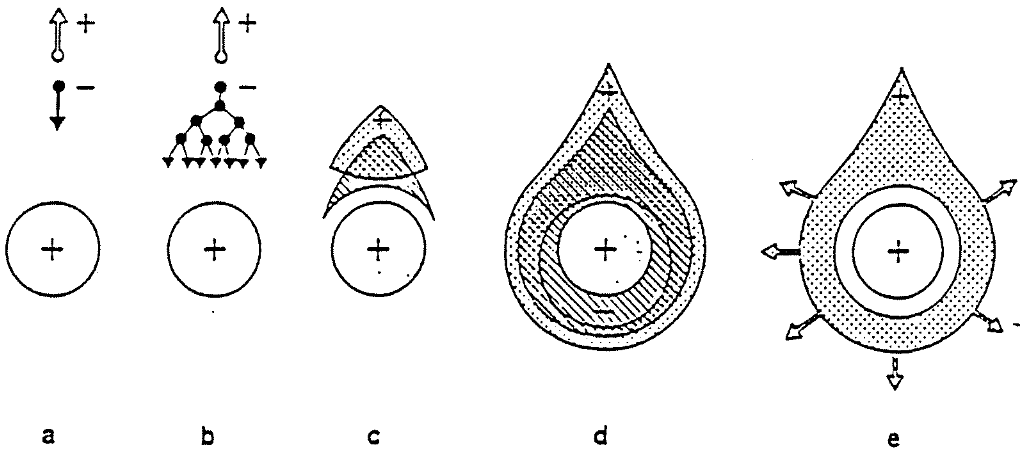

Figure 4.2: Time development of an avalanche in a proportional counter. From (a) to (e) are the different steps of the avalanche.

as unit drift cells. This ensures not only an easy construction but also gas tightness.

2) Large pulse height of the streamer signal (> 50 mV into 50 Ω) making anode preamplifiers unnecessary. Sizeable pulses are induced by capacitive coupling on the delay lines oriented parallel to the anode wires used to sense the avalanche position along the anode wires. The large pulse height of the streamers makes the attenuation problem of such transmission lines less critical.

3) Very fast rise time of the streamer signal leading to small anode time slewing.

4) Increased dead time with respect to proportional pulses but this is not a limitation for a muon detector where a low counting rates (less than 100 Hz for MUF case) are expected.

5) Large amounts of inflammable "quencher" gas are required for streamer mode operation which may lead to ageing. Again it is not a problem for a muon detector with a low counting rate.

6) Large amounts of "quencher" gas used in a big system require a special treatment. In DELPHI, the MUF system is surrounded by an aluminium container serving as gas buffer filled with CO_2.

4.2 The DELPHI Muon Chambers

In this section the conception and emphasis of the DELPHI muon detector are discussed and a detailed presentation of the Forward Muon Chambers is given.

4.2.1 The Barrel Muon Detector (MUB)

The Barrel Muon Chambers [38] consist of 3 layers of drift chambers (inner layer, outer layer and peripheral layer) covering the polar angular region $52^o < \theta < 132^o$. Each layer is segmented in 2×24 azimuthal sectors (planks), with drift chambers of 3.65 m length operated in the proportional mode. The drift tubes are 20.8 cm wide and 2.6 cm thick.

The Inner Layer is inserted inside the return yoke of the magnet behind 90 cm of iron. Each azimuthal sector contains 14 drift chambers (5+4+5) in three staggered layers. Of these three staggered layers of drift tubes, only two are read out which leaves the third one as spare.

The Outer Layer is mounted on the outer surface of the iron yoke behind a further 20 cm of iron. Each plank is 83 cm wide and consists of two staggered layers of (4+3) drift tubes.

The Peripheral Layer is placed 50 cm outside the iron yoke. Each plank is 83 cm wide, covers the dead zones left by the inner and outer layers, and consists of two staggered layers of (4+3) drift tubes.

For the inner and outer layers, each sector of chambers partially covers the corresponding yoke sector of the hadron calorimeter. For the peripheral layer, each sector overlaps partially with the two adjacent sectors of the inner and outer layers and the corresponding adjacent yoke sectors. Fig 3.5 in section 3.5 clearly shows the overlaps. The RΦ coordinate is determined from the drift time to the central anode wire. The Z coordinate is determined by measuring the time difference of the pulse arrival at each end of the delay line.

The barrel muon chambers are operated in proportional mode with a gas mixture consisting of 85.5% Ar, 8.5% CH_4 and 6.0% CO_2.

The drift velocity is: 4.90 ± 0.10 cm/μsec. The pulse delay along the delay line is about 1.8 ns/cm.

The RΦ and Z resolutions obtained from data taken at LEP are:

$\sigma_{R\Phi} \simeq 4\ mm \qquad \sigma_Z \simeq 25\ mm.$

4.2.2 The Forward Muon Chambers (MUF)

The Forward Muon detector is one of the end cap components of the DELPHI detector [38, 42]. It covers the polar angular regions $9^o < \theta < 43^o$ and $137^o < \theta < 171^o$. In each of the two end caps, the Forward Muon detector consists of two detection planes as shown in fig. 4.3. One plane is located inside the yoke behind 85 cm of iron, and the other plane is 30 cm further out, behind another 20 cm of iron and the Forward Scintillators (see section 3.7).

The dimension of each plane is about 9×9 m^2. Each plane is composed of four identical detector modules called 'quadrants' as shown in fig. 4.4. Each quadrant is composed of two orthogonally crossed layers of 22 drift tubes and covers a sensitive area of approximately 4.35×4.35 m^2. To ensure gas tightness, each quadrant is surrounded by an Al container serving as gas buffer and filled with CO_2. A total of 16 quadrants constitutes the entire Forward Muon detector.

The basic detector cell is a drift chamber [39, 40] with a sensitive volume of 4.354 m long, 18.8 cm wide and 2.0 cm thick. A cross section of such a cell is shown in fig. 4.5. The chamber body consists of an extruded aluminium tube profile. The drift field electrode configuration is assembled from PVC profiles into which copper strips have been coextruded. A 100 μm diameter stainless steel anode wire is strung along the chamber axis and supported by two nylon spacers at 180 cm from either end. One of the earthed cathodes facing the anode consists of a flat solenoidal delay line [41] glued into a specific PVC profile. Injection moulded plugs seal the chamber at both ends and contain the gas feed through, the anode holder and the copper-berylium contact springs that distribute the drift field potentials to the electrodes. At one end, the plug also contains the resistor chain for the voltage grading. The drift field can be achieved with this type of structure is show by fig. 4.6.

The detector is operated in the limited streamer mode using a gas mixture of 70% CO_2, 14% Ar, 14% iC_4H_{10} and 2% of isopropylic alcohol vapour [42]. At the operation drift field of about 700 V/cm, the drift velocity is around 7 mm/μsec, which is fast enough to cope with the LEP beam crossing period and slow enough to be insensitive to the magnetic stray field in the DELPHI end caps. The delay line has a characteristic impedance of about 620 Ω and a pulse delay of approximately 580 ns/m. In DELPHI, the x and y coordinates are measured alternatively by the drift time to the anode wire and by the delay line propagation times to both ends.

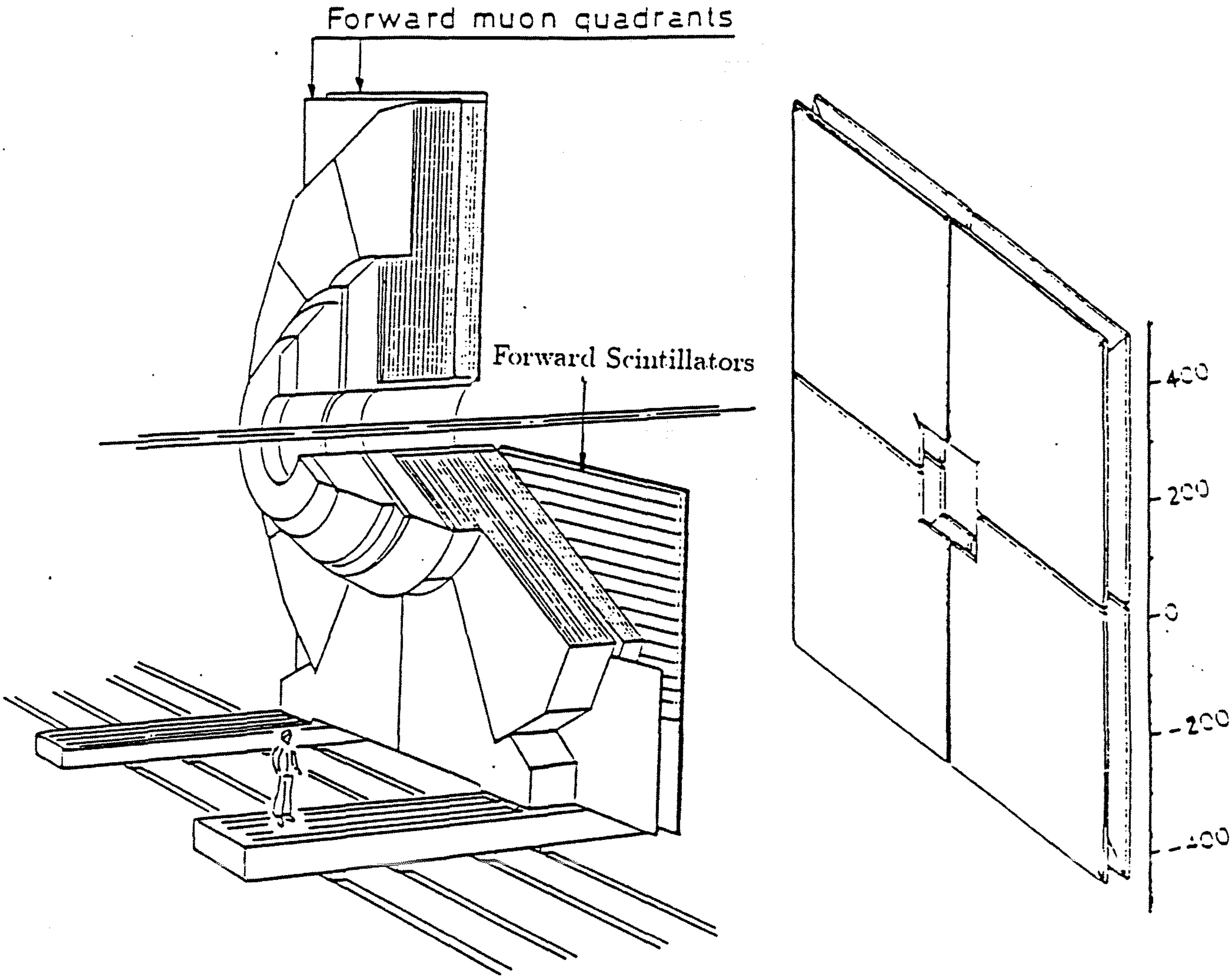

Figure 4.3: The profile of the forward muon detector.

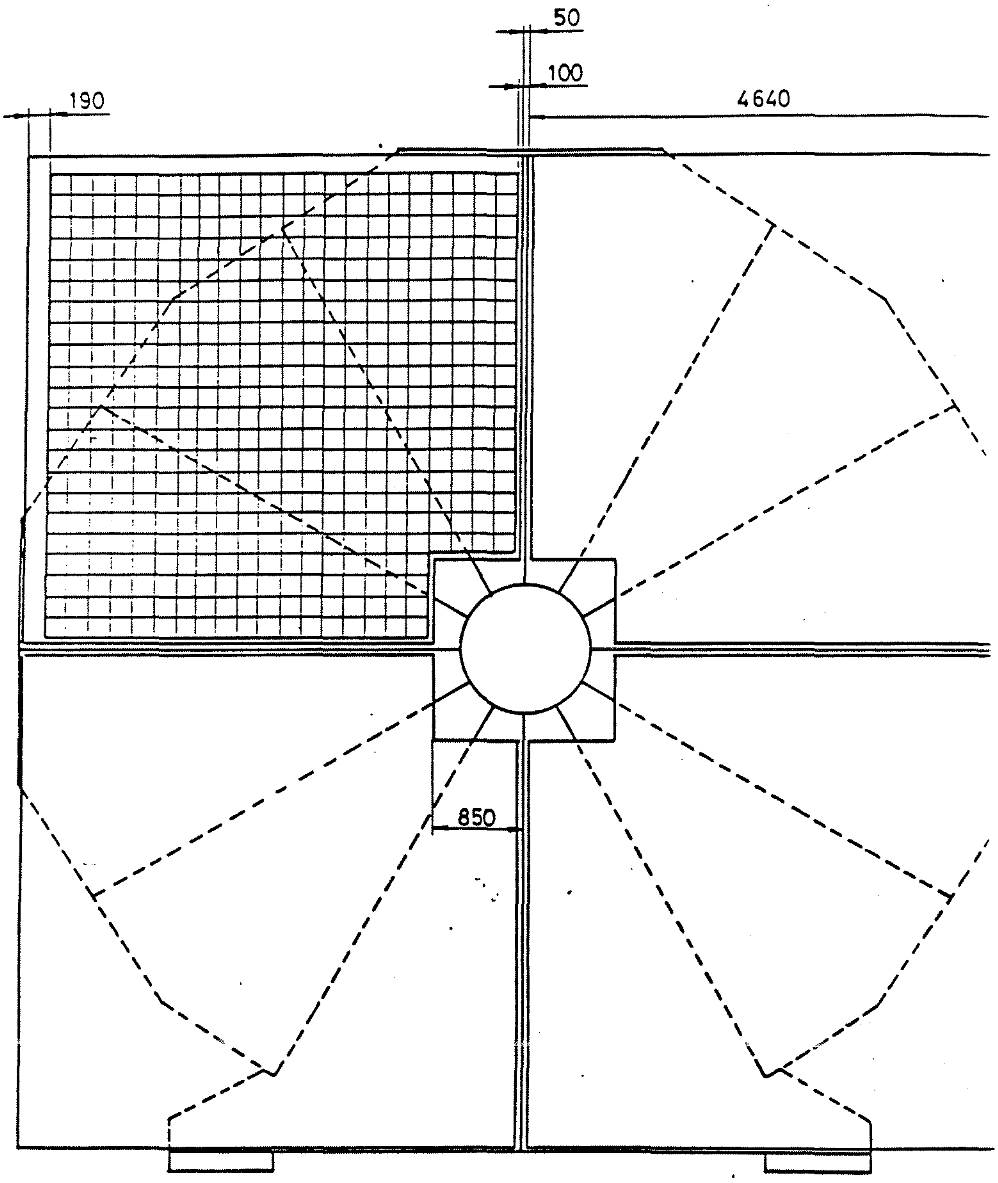

Figure 4.4: Schematic view of the MUF quadrants.

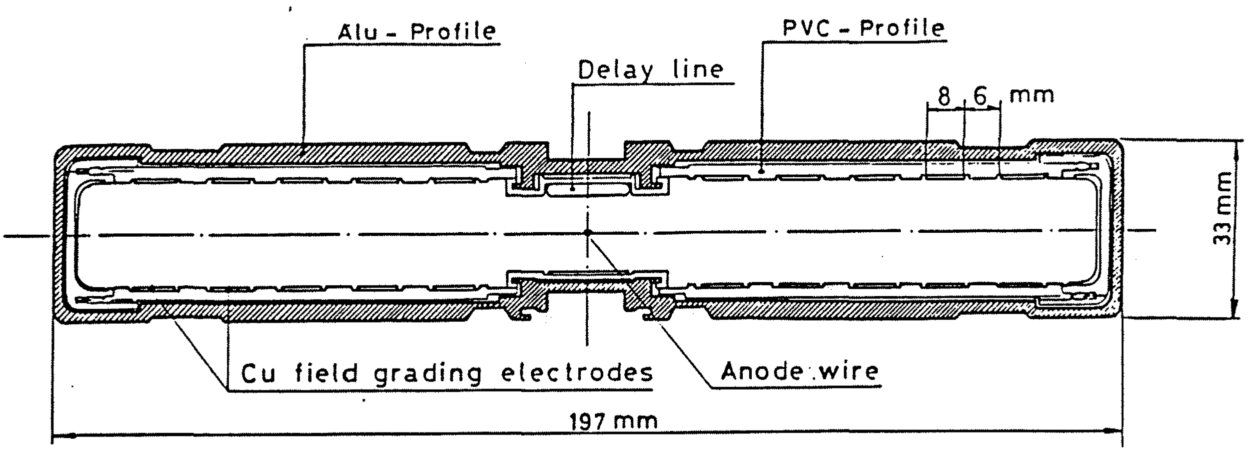

Figure 4.5: The basic detector cell of the Forward Muon chamber.

The intrinsic resolution along the drift distance of such drift chambers is found to be better than 1 mm. The position resolution of the delay lines is between 1.5 and 2.5 mm i.e. about 0.06% over a total length of 4.35 m. The muon identification efficiency exceeds 99% by requiring at least two hits associated to a muon track out of the four possible from all 4 layers. The delay line efficiency, requiring the signal of at least one end to be recorded, is found to be in excess of 99% for all lines.

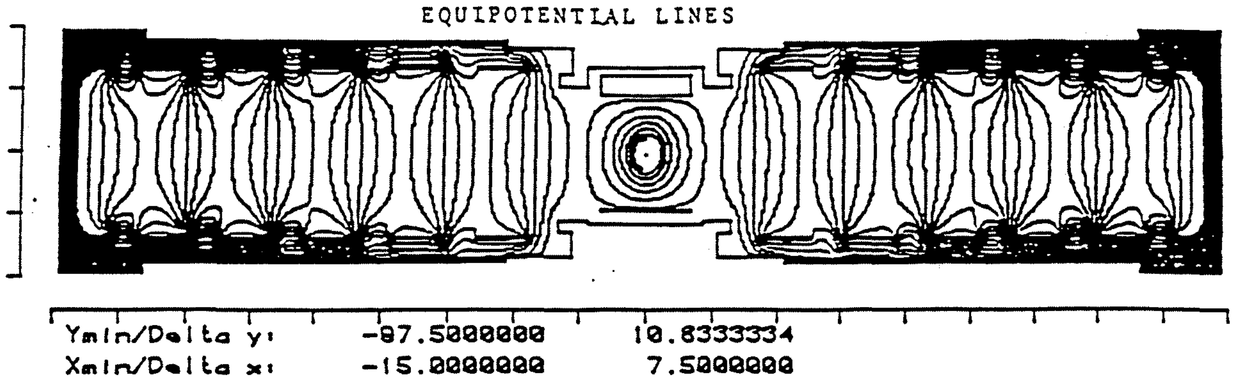

Figure 4.6: The equipotential line achieved with the type of the structure of the chambers used by MUF.

The 22 different chambers of one layer in one quadrant share the same gas input. The drift velocity in the different chambers of one layer of a quadrant is shown in fig. 4.7 and was determined from the analysis of data recorded in a cosmic hodoscope before the DELPHI experiment was assembled. An average drift velocity of 7.14±0.02 mm/μsec is found. The difference between the drift velocity from the

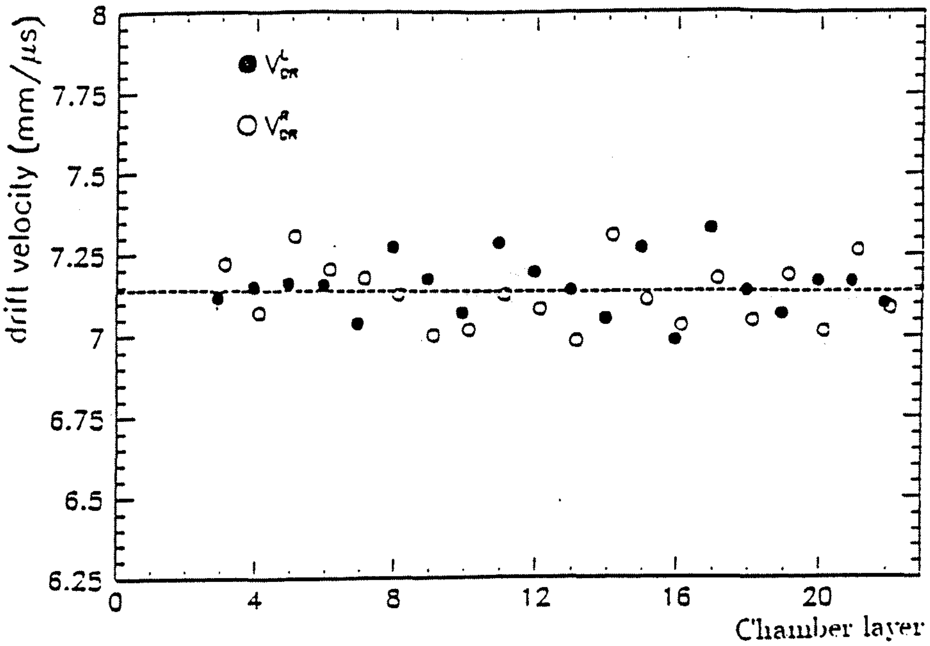

Figure 4.7: Drift velocities in the 22 chambers of one quadrant layer. $V^L_{DR}(V^R_{DR})$ are the drift velocities from the left(right) side to the anode. Measurements errors are of the order of 0.1 mm/μs.

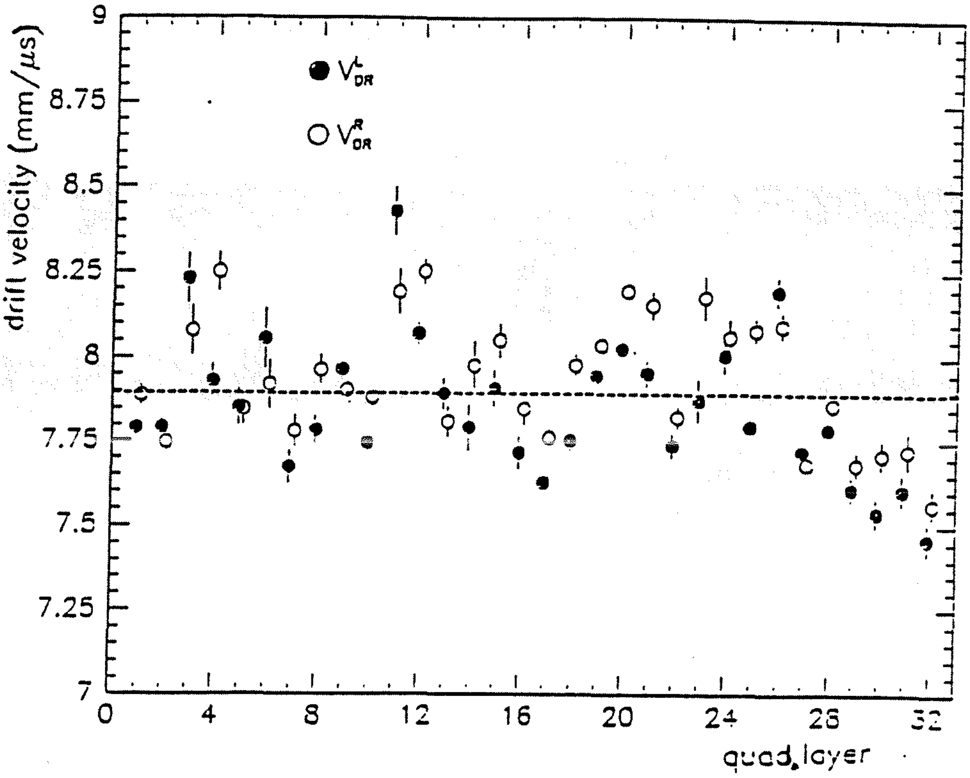

Figure 4.8: Drift velocities in quadrant layers. $V^L_{DR}(V^R_{DR})$ are the drift velocities from the left(right) side to the anode.

different chambers of the same layer is about 1% [51]. As described in eq. 4.5, the drift velocity V_d is proportional to ET/P. Since the applied field grading voltage, the temperature T, the gas pressure P and the gas composition are the same for all the chambers of one layer, possible differences in drift velocities are due to the differences in the chambers themselves such as mechanical tolerances or electric field shaping.

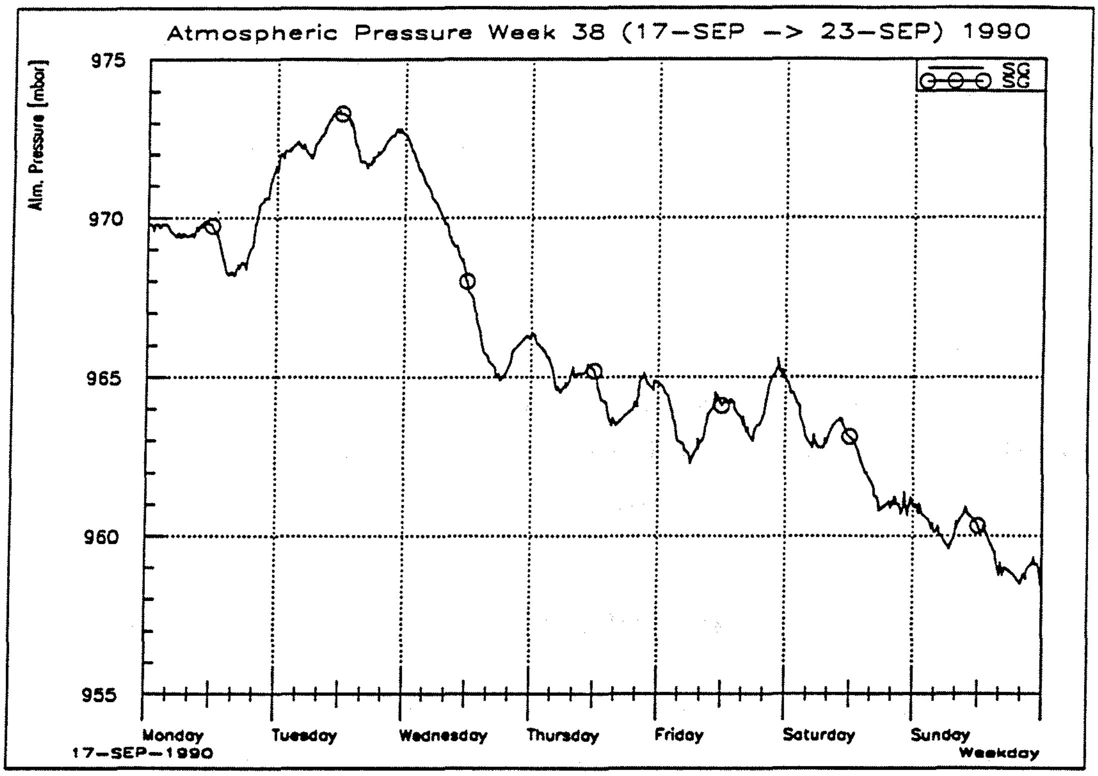

Figure 4.9: Atmospheric pressure variation within one week.

The average drift velocity per detector layer of the 16 quadrants of the Forward Muon detector was determined from the analysis of the data from beam halo muons from some runs over months during 1991 and are shown in fig. 4.8. An average drift velocity of 7.90±0.03 mm/μsec with a variation among the different layers of about 0.2 mm/μsec [51] is found. From the plot one can see that the drift velocity can vary from about 7.46 mm/μsec to 8.43 mm/μsec, which is a variation of (12.3±0.4)%, much greater than the differences due to mechanical or electrical tolerances. In order to give precise position measurements, the drift velocity should therefore be measured layer by layer.

As mentioned before (eq. 4.5), the drift velocity V_d varies approximate linearly with the reduced field E/P. Since the drift field potential is kept constant to be better than 1% in each quadrant layer and the temperature in the underground area of DELPHI is regulated and stable within one degree, only the changes in the gas mixture and its pressure could be responsible for sizeable variations in such an open gas flow system, hence requiring a continuous monitoring of the atmospheric pressure or alternatively of the drift velocity. The gas mixture is monitored and iteratively corrected by a microprocessor giving a mixture stability of ±0.1% [38]. During the 1990 data taking period, for instance, the atmospheric pressure varied by more than 40 mb, which corresponds to about 6% drift velocity difference (see section 4.5). Fig. 4.9 shows the atmospheric pressure variation during one week of a data taking period in 1990.

To avoid systematic errors in the position sensing and to achieve 1 mm of resolution on the drift distance, one needs to have a 1% resolution on the drift velocity which is the mechanical limitation of the MUF drift tubes as shown in fig. 4.7. To obtain this, an on line systematic drift velocity monitoring system has been developed and will be described in the next paragraphs.

4.3 The Drift Velocity Monitoring Chambers

In this section the monitoring chambers themselves are described. Next, a discussion of the feasibility to use them to monitor the drift velocity of the MUF chambers in DELPHI is given. Finally the hardware connections of the monitoring chambers to the MUF detector are described.

4.3.1 The Monitoring Chambers

The measurement of the drift velocity is performed by a drift tube, schematically presented in fig. 4.10. It is identical to the detector cell used in the Forward Muon detector but only 30cm long (see section 4.2.2 for a description of the drift tube). Two entrance windows of 8 mm diameter have been installed at 32.0 and 73.2 mm drift distance respectively. The distance between the two windows is precisely determined to be 41.2±0.1 mm. Opposite to the entrance windows, at the bottom of the drift tube, two small reservoirs filled with cotton wool, doped with Ethyl Ferrocene, have been installed. This allows the evaporation of small amounts of Ethyl Ferrocene as a photo-sensitive agent. Flash tubes have been chosen as ultraviolet light source to ionize the detector gas. They consist of a spark gap of 1 mm between cylindrical tungsten electrodes which are inside a blown glass bulb filled with H_2 gas at 200 Torr. The advantage to use the flash tube rather than a radioactive source is not only the price but also the ease to provide a trigger. The glass bulb is equipped with a 8 mm diameter MgF_2 window of 1.2 mm thickness, allowing UV photons with a wavelength down to about 110 nm to escape the flash lamp. The MgF_2 window pressed against an O-ring seals the entrance window of the drift chamber. The arc discharge is obtained by discharging a capacitor across the spark gap, while the flash rate is given by the characteristic time of the RC chain. Using a capacitor of 0.01 μF, a series resistor of 47 MΩ and an electrode potential difference of about 1.5 KV, a repetition rate of a few Hz is obtained. Under these conditions the flash duration, measured with a photo-multiplier, is of the order of 40 ns. These operation conditions were found to suit our application. The UV photons are collimated through a small hole of 2 mm diameter under each entrance window. The produced photoelectrons migrate to the anode of the chamber, where avalanche multiplication occurs. The drift time is measured precisely by a Time to Digital Converter (TDC). The trigger signal starting the TDC is provided by a small pick-up loop around one of the electrodes of the spark gap of the lamps.

Fig. 4.11 shows a typical drift time versus drift distance relationship taken from ref. [51]. Over the major part of the drift path, i.e. between about 2 and 8 cm drift distance, the relationship between the drift time and drift distance is linear and its slope is referred to as the drift velocity V_d. Therefore one can use the fixed distance between the lamps and the measured drift times to calculate the drift velocity. In the monitoring chambers case, the drift velocity is obtained by:

$$V_d = \frac{r}{\Delta t} \tag{4.7}$$

where the Δt is the drift time difference between the lamp two and lamp one and r is the distance between the two lamps.

4.3.2 Feasibility Studies

To answer the question whether it is possible to use such monitoring chambers to monitor the drift velocity in the DELPHI Forward Muon chambers, the following tests were carried out.

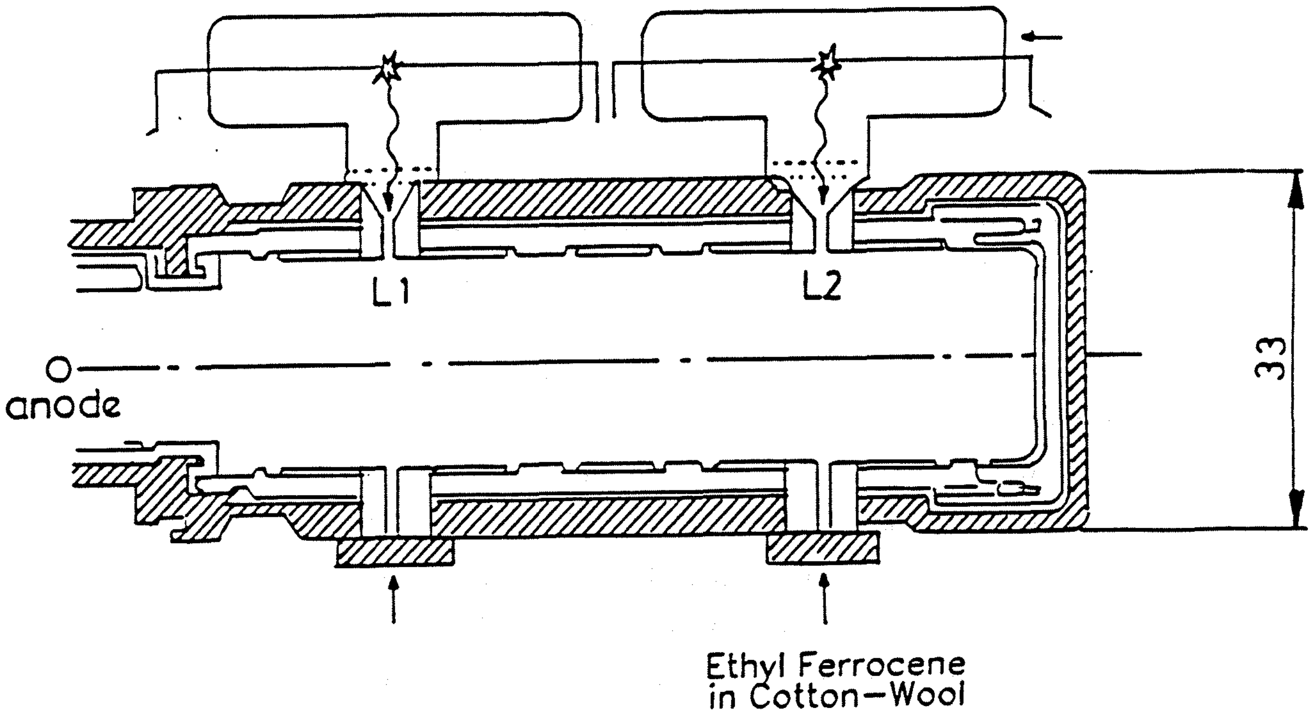

Figure 4.10: Schematic view of the monitoring chamber. a: The MgF_2 window. The symbols L1 and L2 refer to lamp one and lamp two respectively.

The monitoring chamber, equipped with H_2 flash tubes, was connected to the gas mixture downstream of a stack of three full size drift chambers situated in a cosmic hodoscope as shown in fig. 4.12. The drift chambers were chosen at the limit of the accepted tolerances from three different production batches. The hodoscope provided tracking of cosmic particles, allowing a prediction of the impact coordinates in the three full size drift chambers with a precision of 0.5 mm. The drift velocities in these drift chambers could hence be measured. The monitoring chamber was flushed with the exit gas of the three drift chambers and its exhaust to the open air went through a microvalve and an exit bubbler. The microvalve allowed an overpressure to be applied to the entire system. The overpressure was measured between the full size chambers and the monitoring chamber using a mercury manometer. In this way the drift velocities measured in the full size chambers and in the monitoring chamber respectively, could be compared as a function of the applied overpressure. The gas mixture of 70% CO_2, 14% Ar, 14% iC_4H_{10} and 2% of isopropilic alcohol vapour was produced via a mass flow meter system delivering a flow of about 10 l/hour. The gas filling of the monitoring chamber was therefore renewed about 8 times every hour.

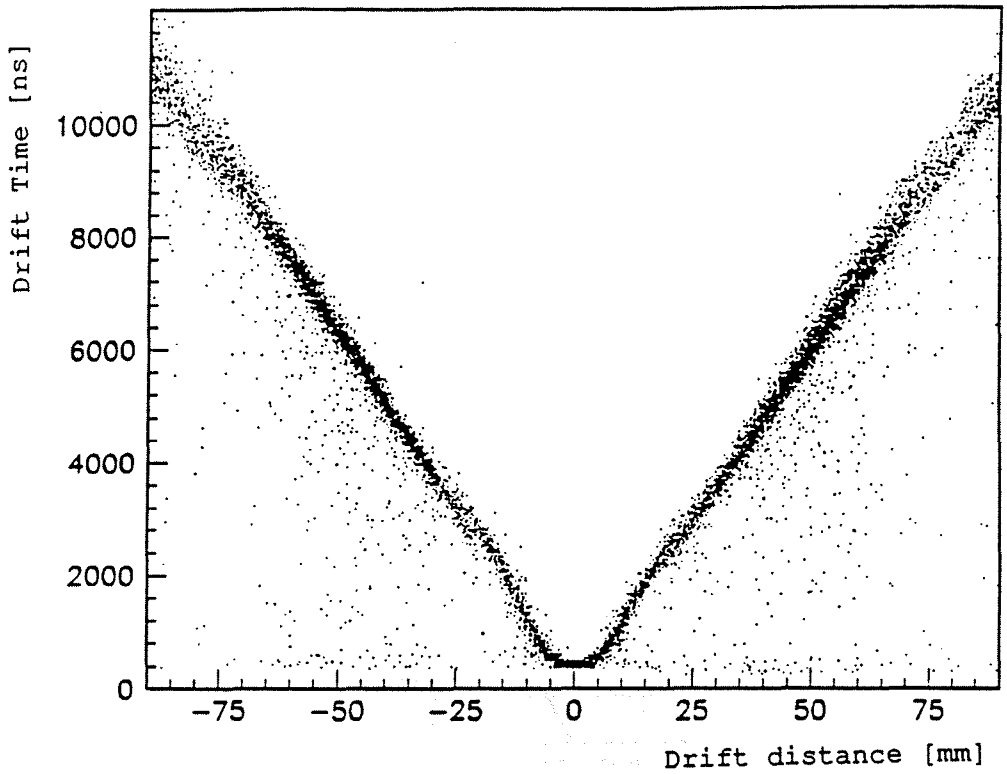

Figure 4.11: Typical drift time versus drift distance. The relationship between the drift time and drift distance is linear between 1 and 8 cm drift distance.

The drift velocity has been measured at several pressures in the full size drift chambers situated inside the cosmic hodoscope. The latter triggered on a cosmic particle via the coincidence of the signals from the scintillators situated at either side of the drift chambers, the lower counter being covered by 10 cm of lead. The reconstruction of the cosmic tracks was obtained from 2 × 6 drift chambers operated in proportional mode. A premixed gas composed of 90% Argon and 10% Methane was used in these chambers. The drift field was set to 300 V/cm in order to operate these tracking chambers at a saturated drift velocity of 4 cm/μs. In this way the reconstruction of the cosmic particle trajectories was essentially insensitive to atmospheric pressure variations. To minimise possible systematic errors in the track reconstruction, the hodoscope was recalibrated using a subset (all layers hit) of the recorded data at each pressure value.

The data acquisition was based on NIM and CAMAC read out by a personal computer. The drift time measurements were performed with LECROY TDC's (2280A).

From the reconstructed tracks, the coordinates of the cosmic particle trajectory inside the three full size drift chambers was predicted with a precision of about

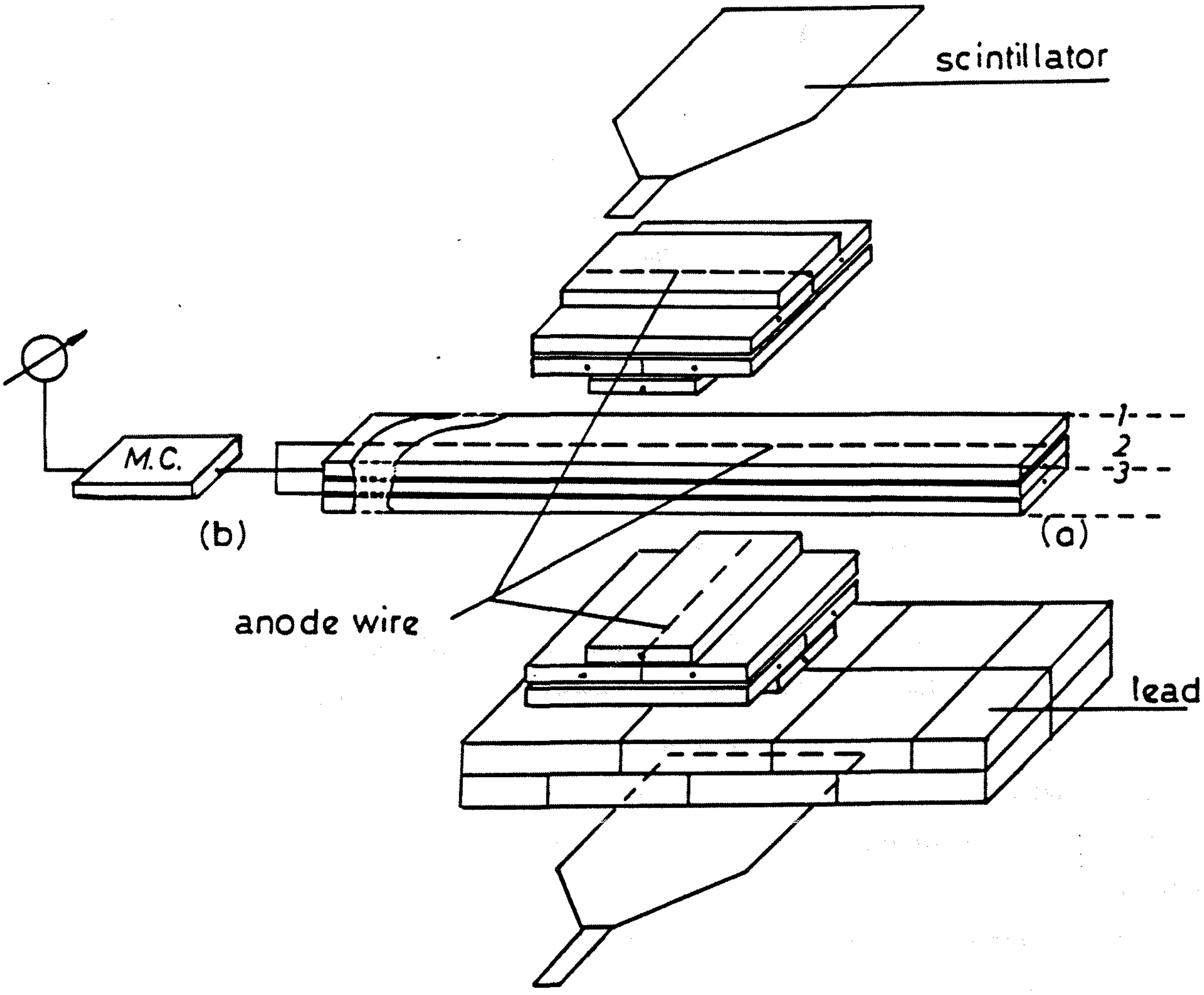

Figure 4.12: The feasibility study experimental set-up. a: Full size drift chambers; (b) Monitoring chambers.

0.5 mm. It is worth mentioning that the geometrical acceptance of the hodoscope was limited to about 20° around the vertical. Uncertainties arising from the track inclination are therefore small with respect to the accuracy of the predictions.

In fig. 4.11 departures from linearity are observed near the anode wire and close to the chamber edges. The linear part of this plot, situated approximately between 2 cm and 8 cm drift distance, was used to determine the drift velocities at either side of the anode wire for the three full size drift chambers exposed to cosmic rays for different values of the pressure measured with the mercury manometer. Fig. 4.13 shows the drift velocities determined at either side of the anode wire of the three drift chambers exposed to cosmic rays at different values of the pressure as measured with the mercury manometer. The same pattern is observed in all data indicating that the variations of the order of a few percent are systematic and probably due to the tolerances in the mechanical construction of the drift chambers.

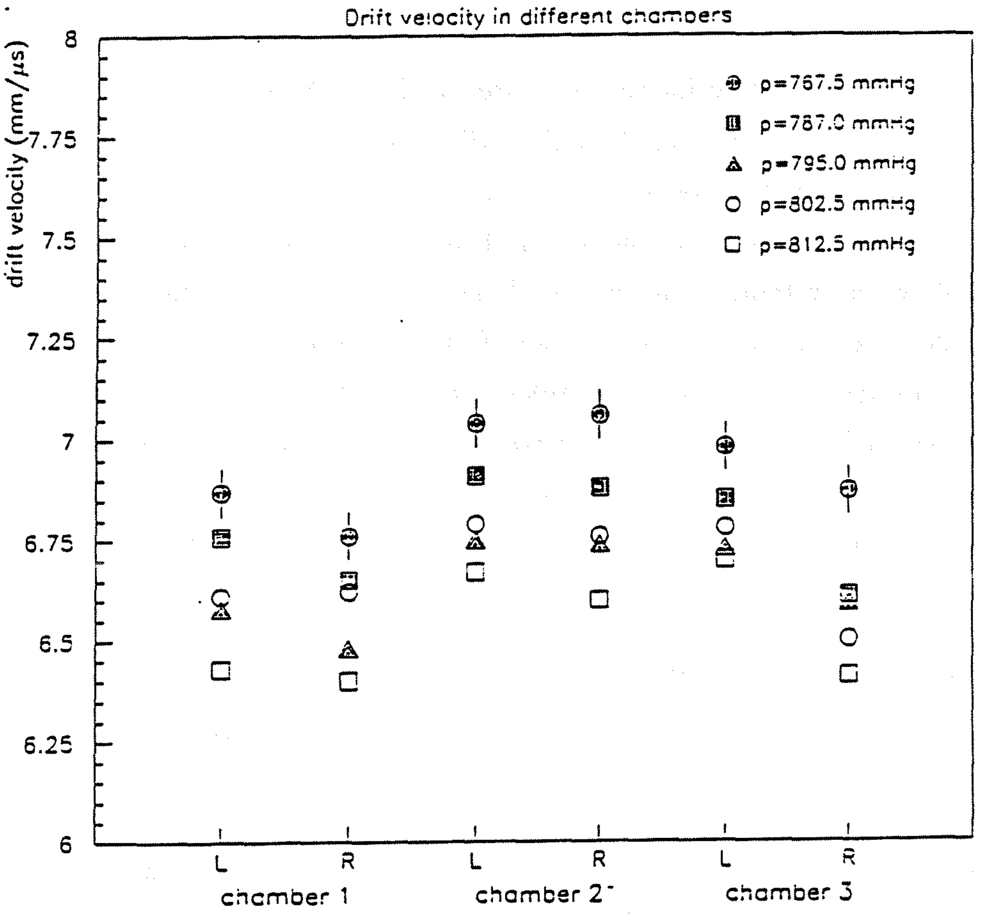

Figure 4.13: Drift velocities in the three full size chambers at different values of the gas pressure. L and R refer to the drift velocity left and right of the anode wires.

Before and after each period of data taking with the cosmic hodoscope, the drift velocity was measured in the monitoring chamber. Whereas a cosmic run took about 20 hours and is mostly performed over night, the measurement of the drift velocity using the H_2 flash tubes only takes a few minutes. The pick-up signal from the arc discharge started the time digitizer whereas the anode signal from the drift chamber stopped it. The RMS values of these time distributions are about 200 ns, consistent with the standard deviation expected from the dimension of the entrance window (diameter=2 mm) and the flash duration ($t_f \approx 40$ ns).

Fig. 4.14 shows the drift velocity measured with the H_2-flash tubes in the monitoring chamber at different values of the pressure as measured with the mercury manometer. The data show an approximately linear decrease of the drift velocity with increasing pressure within the narrow pressure interval investigated. The slope yields a 0.1 mm/μsec velocity change for a pressure variation of 10 mmHg in our gas mixture.

The average of the drift velocities measured with the H_2-flash tubes, before and after each cosmic run, is compared to the drift velocities determined in the three full size chambers from the cosmic data in fig. 4.15. The ratio of drift velocities is compatible with unity for two out of the three full size drift chambers, whereas chamber 2 shows a systematic departure of the order of 2%. As mentioned before systematic effects of that order are expected from construction tolerances especially since the 3 chambers represent extreme tolerances from different production batches. Such systematic effects can easily be corrected for after calibration. In all cases the results are compatible with a constant ratio to better than 1%, justifying the monitoring procedure.

4.3.3 Hardware Connections of the Monitoring Chamber with the DELPHI Forward Muon Chambers

As mentioned before, the whole Forward Muon detector system consists of 32 quadrant layers (16 for each end cap). The gas mixture is provided to each end cap by two independent but identical distribution systems. In each such system, the 16 channels of a differential manifold distribute the gas mixture to the 16 quadrant layers at an overpressure of about 3.5 mb (one channel per layer which contains 22 drift tubes) . The gas from the 16 quadrant layers then reaches the exhaust via another

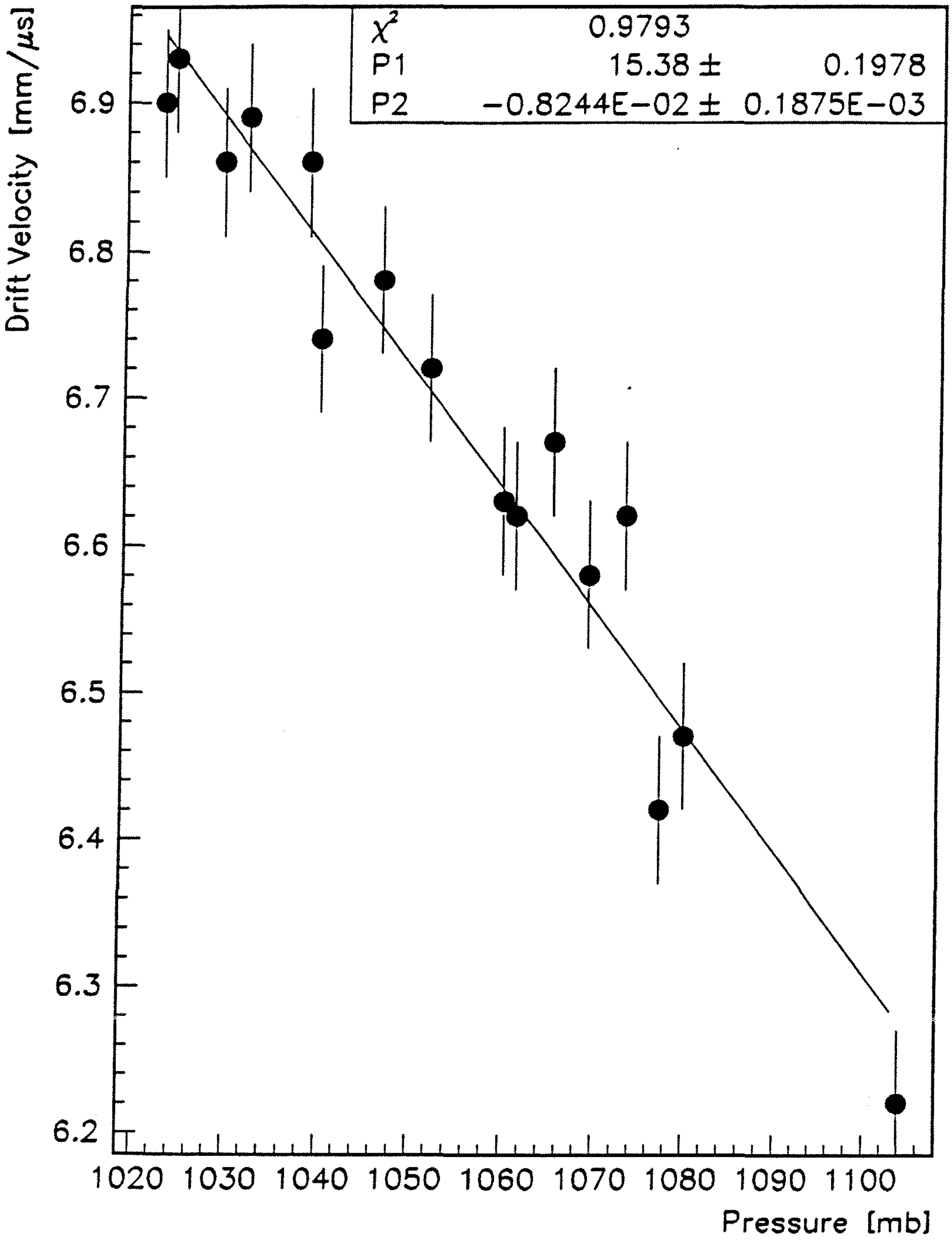

Figure 4.14: The drift velocity versus pressure measured by the monitoring chamber. The line is the fitted V_d-Pressure function.

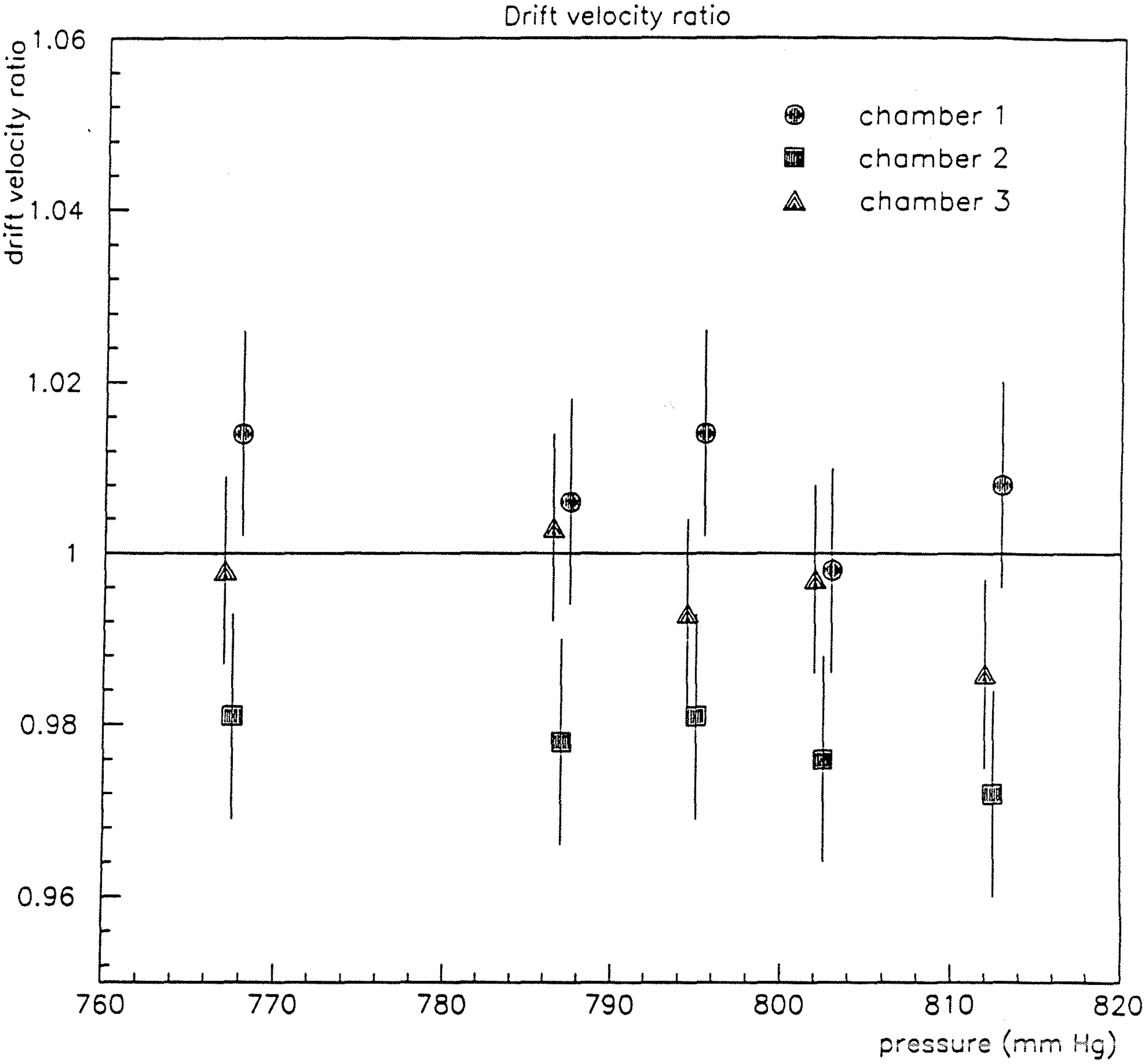

Figure 4.15: The drift velocity ratio between the full size drift chambers and the monitoring chamber.

16 channel manifold and a common bubbler setting an over pressure of about 2 mb. Each of these 16 independent gas channels is connected to a single "analysis channel" via electric sampling valves numbered 1-16. The input gas is also connected to the monitoring channel via sampling valve 0. The monitoring chamber is installed in this analysis channel and fed alternately by the input gas and the 16 detector exit gas channels, its exhaust to the open air goes through an exit bubbler. The monitoring chamber equipped with the flash tubes is installed in a gas tight box flushed with CO_2 gas, which is the main component of the working gas mixture.

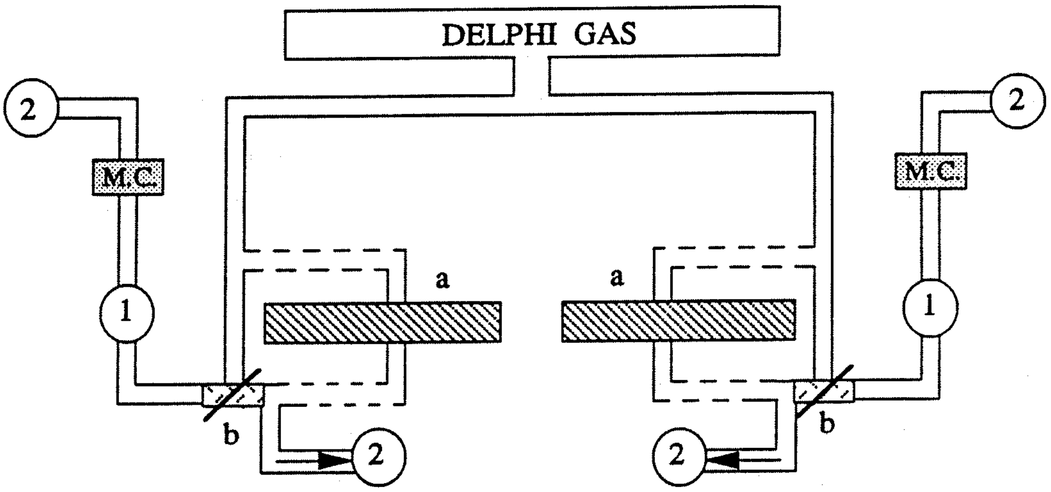

Figure 4.16: The connection of the monitoring chambers with quadrants. (a) Quadrants; (b) Sampling values; m.c: Monitoring Chamber; 1. Gas flow meter; 2. Gas bubbler

Fig. 4.16 shows schematically the connection of the monitoring chambers with the quadrants and the gas system.

4.4 The Slow Control System For the Drift Velocity Monitoring

In order to continuously monitor the drift velocity, it was decided to integrate the measurement of the drift velocity in the DELPHI slow control system.

To monitor and control the DELPHI subdetectors, a slow control system based on G64 bus and VAX computers has been developed. The lower level of the monitoring and control is done by a PASCAL program in permanent loop on the G64 microprocessor. The graph plotting and user interaction are performed via VAX computers. These equipment computers are linked to the G64 crates by the ethernet or cheapernet local area networks. A detector typically has one equipment computer servicing several G64 crates. In this section, the DELPHI and MUF slow control system are very briefly described, followed by the description of the software developed specifically for the drift velocity monitoring.

4.4.1 The DELPHI Slow Control System

The slow control system of the DELPHI detector[38, 47] monitors the entire apparatus, allows an operator to control the experiment, takes automatic action if required in the event of an alarm and records the slowly-varying values of parameters required for data analysis. This system can interface to the different subdetector hardware, as well as to other systems such as those controlling gas supplies and monitoring safety.

The slow control software consists of three layers:

- **State Model** This is the top layer. It is a hierarchically ordered state model in which subdetectors are treated as objects which must be in one of a set of pre-defined states. Below this, each subdetector is similarly treated until a set of elementary objects is reached, each of which corresponds to a subsystem of the subdetector.

- **Elementary Processes (EP)** One elementary process controls and monitors the hardware of each subsystem of a subdetector and sets the state of the corresponding elementary object in the state model description.

- **G64 crates** These form the interface between the VAX-based elementary process and the hardware. They receive commands from the elementary processes and return information back to them. The G64 skeleton program runs on the G64 crates and receives Remote Procedure Calls (RPC) from the elementary processes to read or set the hardware. The program loop continuously monitors the apparatus, reporting changes via RPC to the EPs.

More detailed information about the DELPHI slow control system and software can be found in the appendix A and the references referred therein.

4.4.2 Slow Control Hardware Used for the Monitoring of the Drift Velocity

There is one MUF G64 crate mounted in each side of the end caps. Both of them are connected with a G64 TDC created specially for the purpose of monitoring the drift velocity. The G64 TDC contains 256 channels each with 50 nsec channel width, the full scale of the G64 TDC being 12.8 μsec. The lamp flash rate is about 2 Hz. Fig. 4.17 shows the schematic electronic set-up and the timing diagram. The 'total' efficiency (chamber and lamp efficiency) can be calculated as:

$$eff = \frac{number\ of\ events\ of\ counter\ II}{number\ of\ events\ of\ counter\ I} \tag{4.8}$$

where counter I counts the total number of trigger pick-up signals and the counter II totalizes the number of the coincidence signals between the anode wire signal of the chamber and the pick-up signal.

4.4.3 Slow Control Software Used for the Monitoring of the Drift Velocity

Besides the elementary process (EP) controlling for high voltage, low voltage and fastbus for both end-caps, there are drift velocity monitoring EPs controlling the MUF G64 crates, four EPs per end-cap in total. Both G64 systems run the same skeleton. It is the standard DELPHI skeleton with special modifications for the G64 TDC handling.

Each drift velocity monitoring EP is uniquely identified by the detector and subsystem names. Knowing these names, the EP is able to obtain all other information from the slow control database. Given the detector name and subsystem name, the EP can obtain a list of all channels to be controlled or monitored, the channel types, and the physical addresses of each channel. Whenever there is a State Management Interface (SMI) command to START, the EP reads values from a database and sends them to the hardware. One should note that a single EP software program runs independently for both end-caps.

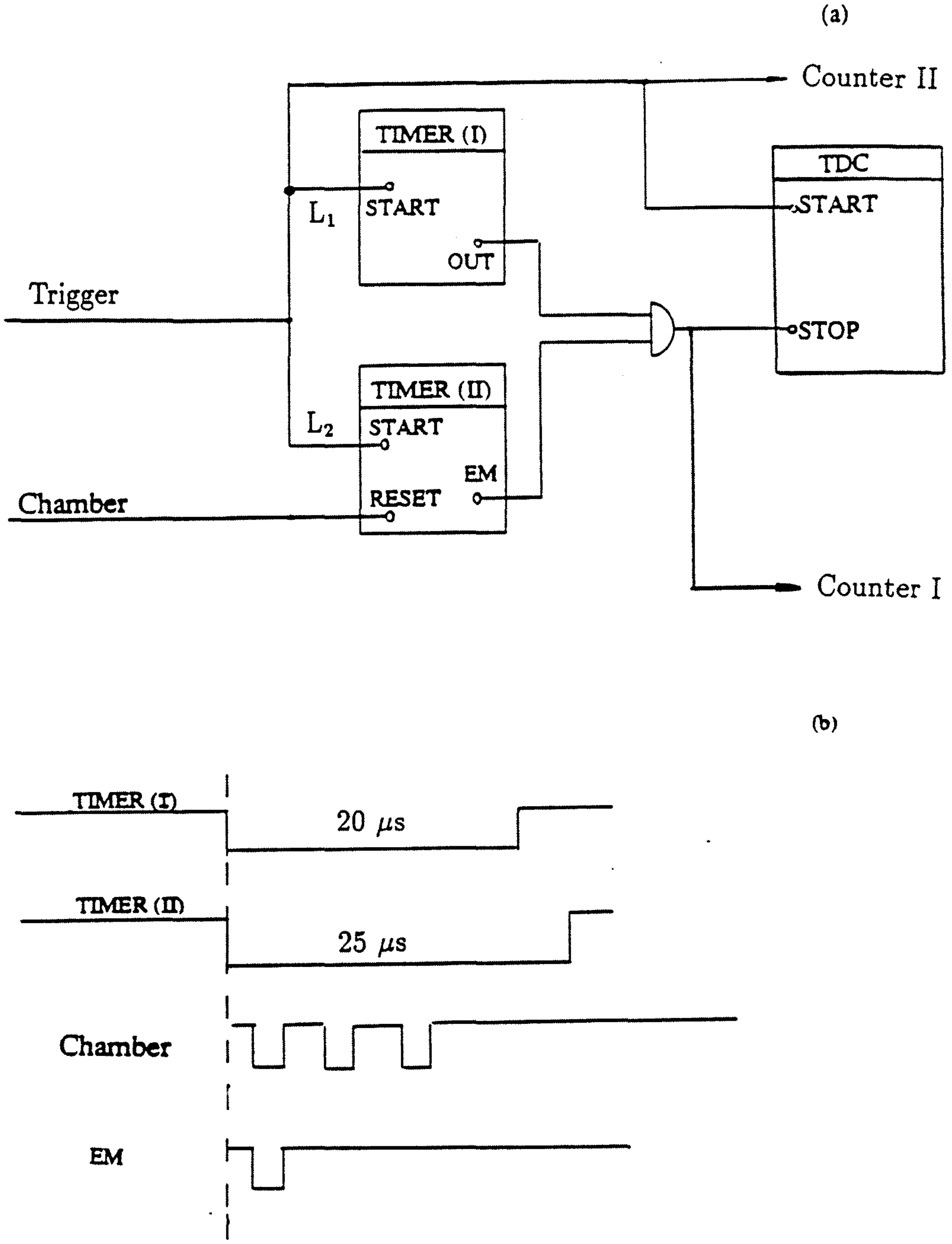

Figure 4.17: (a) Schematic electronic set-up of the drift velocity monitoring. L_1 and L_2 are same length. (b) Timing diagram.

The G64 skeletons send possible alarm messages to the elementary process. There are two special alarm conditions for the drift velocity monitoring:

1. The number of events accumulated is compared to a preset limit. When this limit is reached, an "alarm message" is sent to the elementary process telling that the data taking is finished (See next section about the data taking).
2. An error limit is set for all channels using the Time-to-Digital Converters (TDC). The error limit is reached if during 10 consecutive attempts to read the TDC no start signal has been seen (corresponding to a start rate dropped below 1% as compared to the normal start rate) or if after 100 consecutive attempts to read the TDC no stop signal has been seen (corresponding to a data taking efficiency below 10%). In this case, an alarm message will also be sent to the EP to stop the data collection. In this extreme case, either the lamp is broken, the chamber has a hardware problem or the TDC is not functioning properly.

The control of the high voltage on the flash lamps and of the data taking time are also executed by the elementary process without changing the database.

In order to monitor the drift velocity through the DELPHI slow control system, a series of functions had to be added to the EP. Since the flash rate is lamp dependent, one has to separate the data taking for both lamps in order to have about the same statistics for each.

The major functions of the elementary process for the drift velocity monitoring chambers are: (fig. 4.18)

- The Elementary Process first checks the high voltage states on the monitoring chambers and on the H_2 flash tubes. If they are on, the EP will switch them off. This is mainly to prevent the chamber from tripping while the gas is being changed.
- Next, the EP tries to switch on the desired gas sampling channel by a Remote Procedure Call (RPC) to the DELPHI gas system EP. In case of failure after 50 attempts the EP is switched off. This condition could arise if either the gas system G64 is off or the link between the VAX and the gas G64 skeleton is off.

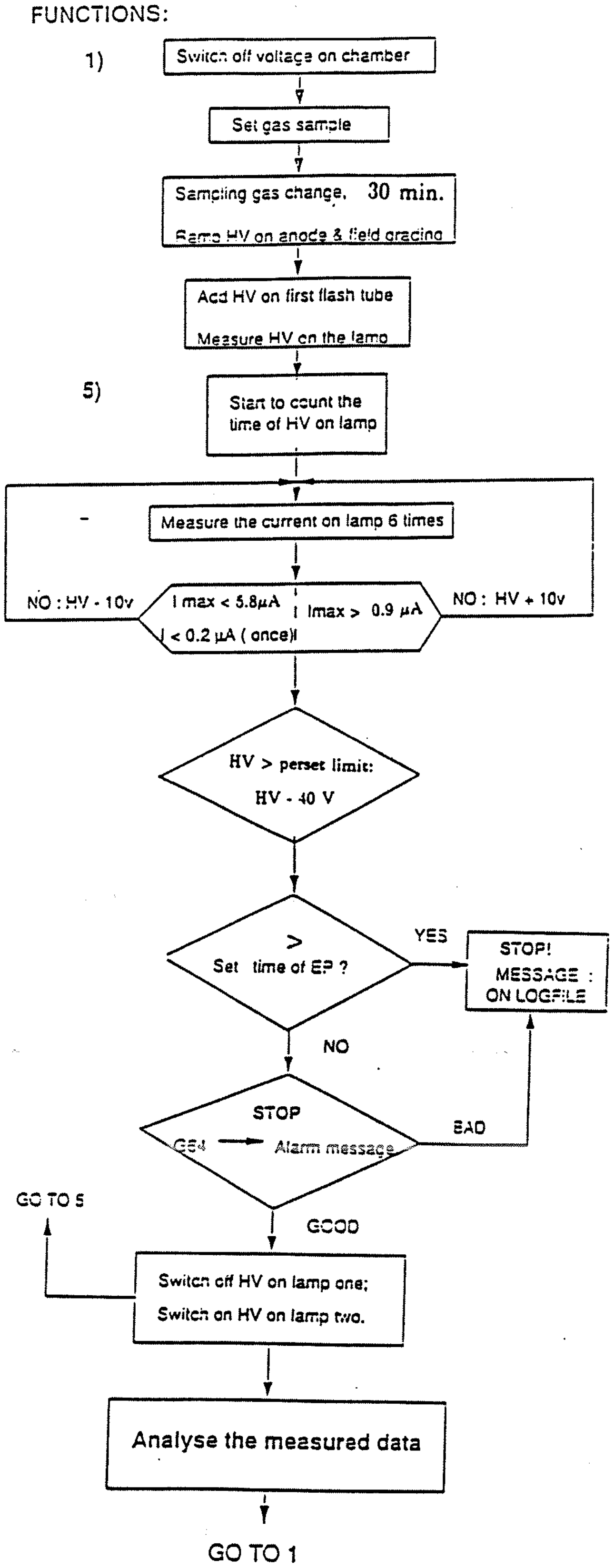

Figure 4.18: Main functions of the Elementary Process for the drift velocity monitoring.

- After 30 minutes of gas flushing, the gas in the monitoring chamber has been refreshed more than 3 times, and therefore should be the same as the input gas. The anode and field grading voltages of the monitoring chambers are then ramped up to the preset values by the elementary process.

- As soon as the anode and field grading voltages of the monitoring chamber reach the preset values, the high voltage on the first flash tube (the tube close the anode wire) is turned on by the EP.

- The EP then properly tunes the high voltage on the lamp. The optimal high voltage value is derived from six consecutive measurements of the electric current of the lamp (within a few seconds). The high voltage value tuning is performed in the following way: For these six measurements of the current

  1. **if** $I_{max} < 0.9$ mA **or** $I_i < 0.2$ mA all six times:

     then $V_{lamp} = V_{lamp} + 10$ V.

     if $V_{lamp} \geq V_{limit}$, **then** $V_{lamp} = V_{lamp}$ - 40 V.

  2. **if** $I_{max} > 5.8$ mA **or** only once $I_i \leq 0.2$ mA:

     then $V_{lamp} = V_{lamp}$ - 10 V.

  I_{max} is the maximum value of the current that occurred during the six measurements. V_{limit} is a preset high voltage safety value for the lamp. The current value for I_{max} and V_{limit} are chosen by experience considering the efficiency and the flash rate of the lamp. It is found empirically that the voltage applied to the lamp may vary over months, reflecting presumably slowly changing microscopic conditions of the electrode tips.

- The EP writes the proper high voltage value for the lamp to a data file for the next start of run and sends the command to the G64 skeleton to start data taking.

- After receiving the data collection finish 'alarm' message from the G64 skeleton, the high voltage is reset to 0 for the first lamp and switched on for the second lamp (the one far away from the anode wire). The same data taking procedure is started as for the first lamp. At the end, the EP will send a requirement to the gas G64 skeleton to read the atmospheric pressure. The EP will then send a message to ask the MUF G64 skeleton to transfer the collected data to the EP and store it in memory. These data consist of TDC counts of required number of events and the corresponding total number of TDC readings.[1]

- In case the data taking is longer than the EP preset time, the high voltage of the lamp and the chamber will be turn off and an alarm will be sent out, the message will be written in the log file. This condition could arise if either the lamp is broken or the G64 TDC is not functioning properly.
- After the data collection is finished for both lamps (300 events for each lamp) an analysis subroutine is called from the EP to analyse the data. If the drift velocity value is outside the preset window an alarm is issued. The EP will then send an alarm message to EMU (Error Message Utility) and write down a message in the error log file and display an alarm message on VAX computer terminals. This tells the operators that the drift velocity has suddenly changed due to an unknown reason.
- The whole procedure is restarted for the next gas sample channel.

4.4.4 Drift Time Analysis Subroutine

Fig. 4.19 shows one of the measured time histograms, fitted with a Gaussian distribution with a linear background for each lamp. Each histogram contains 300 measurements of the drift time for a given lamp and a given gas analysis channel.

For a given run, the average drift time of the electrons is calculated by a method of successive approximations in terms of the confidence intervals around the mean value.

For an ideal normal distribution, the peak position is at the mean of the distribution. Therefore, for the first step of the calculation, the mean T_1 and variance σ_1 are computed from the data sample contained within ± 10 TDC (1 TDC channel is 50 ns) channels around the apparent peak position X_{peak}. The peak position X_{peak} is found as the median channel of the cell determined by 3 TDC channels and overlaps of one TDC channel between adjacent cells, which contains the maximum number of

---

[1] The 'efficiency' obtained by (total number of stop times)/(total number of start times) is compatible with the one obtained with the NIM counters.

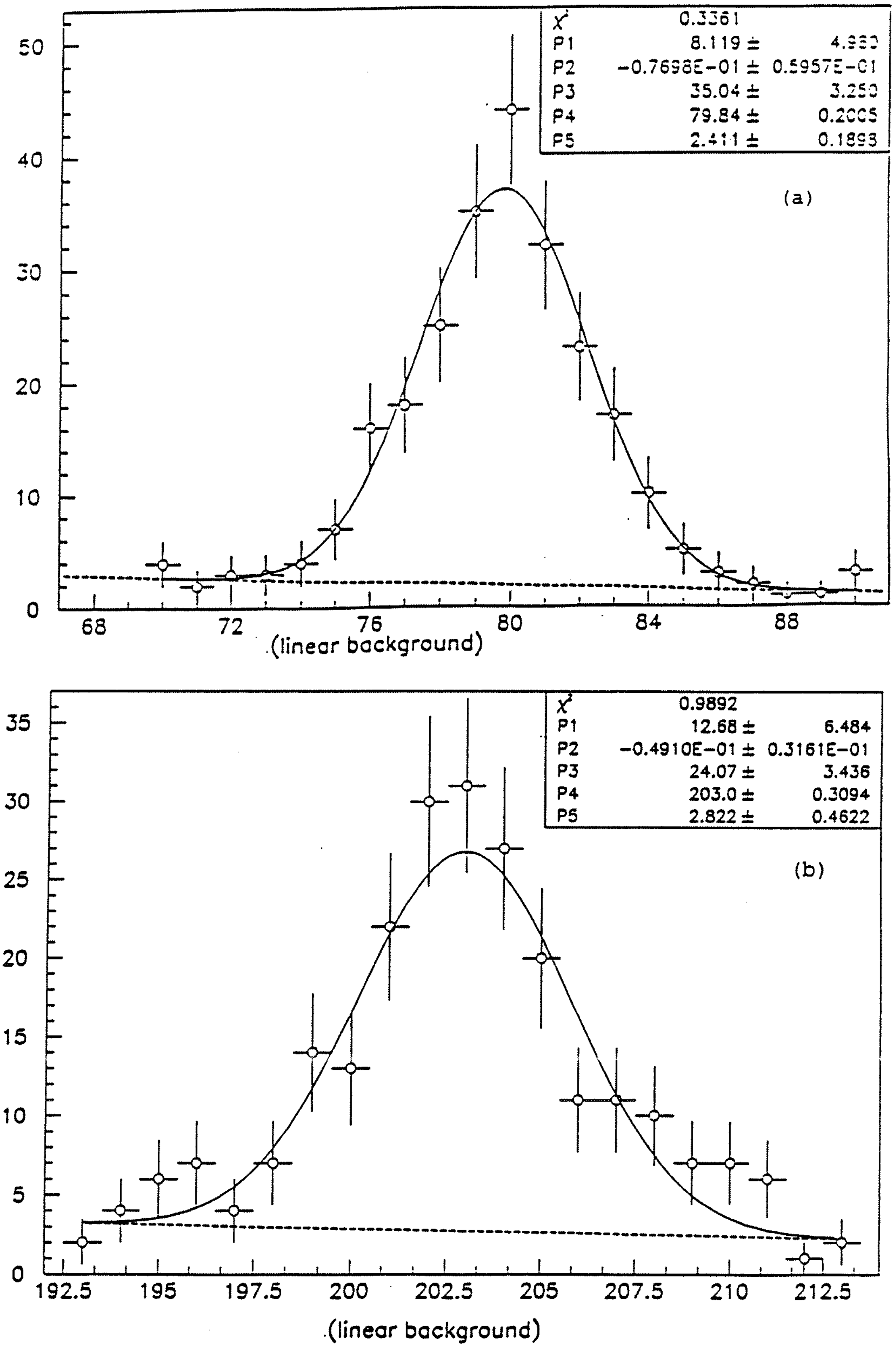

Figure 4.19: The time histogram of the monitoring chambers. They are fitted to a Gaussian distribution with a linear background. (a) for window one and (b) for window two.

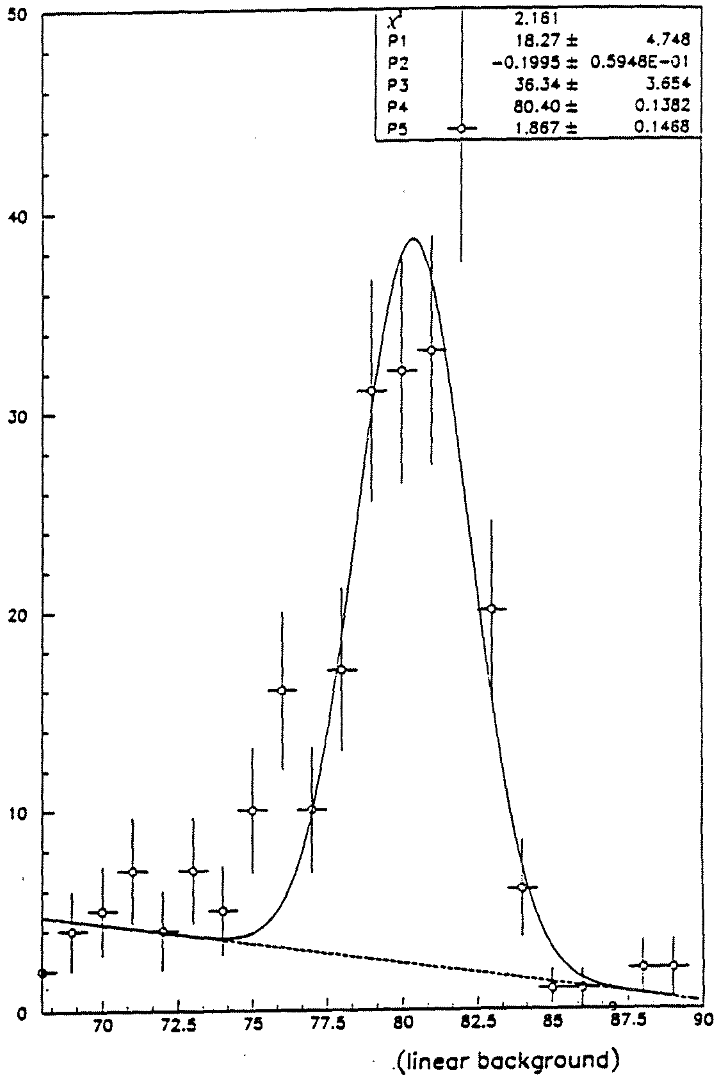

Figure 4.20: An extreme asymmetric drift time distribution.

events. The mean and the variance calculated in this way are used to determine the confidence interval for the second step and the calculations are reiterated according to following procedure:

$$
\begin{array}{ll}
X_{peak}\text{-10ch.} \leq X_{peak} \leq X_{peak}\text{+10ch.} & \Longrightarrow T_1,\ \sigma_1, \\
T_1\text{-}2\sigma_1 \leq T_1 \leq T_1\text{+}2\sigma_1 & \Longrightarrow T_2, \sigma_2, \\
\dots\ \dots & \\
T_{n-1}\text{-}2\sigma_{n-1} \leq T_{n-1} \leq T_{n-1}\text{+}2\sigma_{n-1} & \Longrightarrow T_n, \sigma_n
\end{array}
$$

...till:

$$\frac{|T_n - T_{n-1}|}{\sigma_n} < 2.5 \times 10^{-4} \tag{4.9}$$

where T_1 ... T_N are the mean values at each step and σ_1 ... σ_n are the corresponding dispersions. The value 2.5 $\times 10^{-4}$ is chosen to make sure that $T_n - T_{n-1}$ is less than 0.01 ns and this requirement is normally achieved after less than 3 iterations. The typical final sigma of the drift time histogram is about 2.5 TDC channels (1 TDC channel is 50 ns). The final drift time and its dispersion are thereby determined as T_n and σ_n.

The drift time distribution sometimes appears with an asymmetry due to some unknown reasons. Fig. 4.20 shows an extreme case of an asymmetric distribution yielding a mean value of the drift time which is about 100 ns apart from the peak. The influence on the drift velocity determination from the asymmetry of the drift time distribution is found to be less than 2%.

4.5 Results from the Measurements Made in DELPHI

The two monitoring chambers were installed in DELPHI and started monitoring the drift velocity in July of 1990 and stopped at the end of 1991 for reasons of calibration which will be explained below. The drift velocity monitoring is continually carried on with the DELPHI physics data taking. The chamber monitoring the drift velocity of end cap A is called Chamber A and the one monitoring the drift velocity of end cap C is called Chamber C.

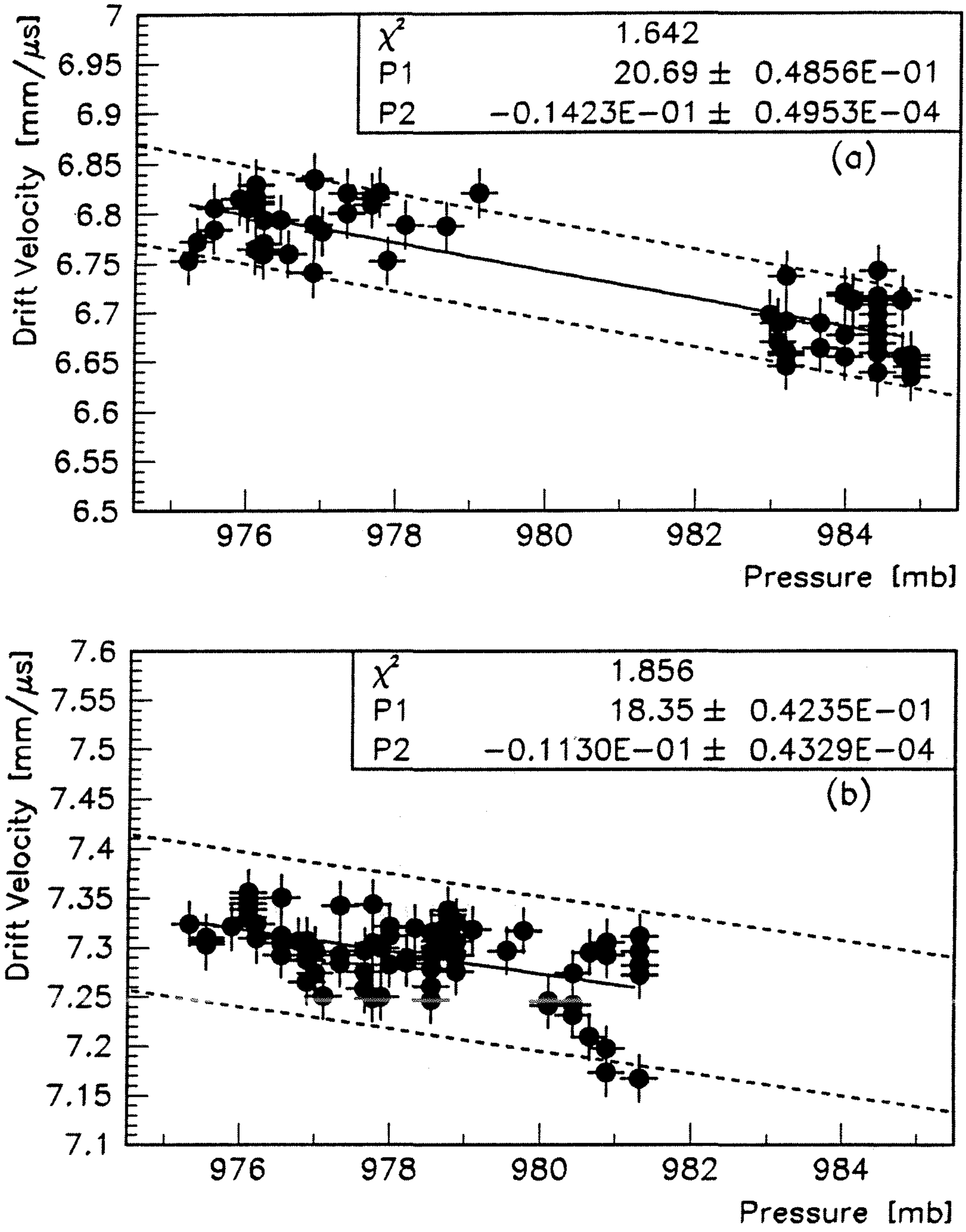

Figure 4.21: Distribution of the drift velocity as function of pressure. The two dotted lines determine a band for the drift velocity. The error is statistical only. (a) for End Cap A and (b) for End Cap C.

In these initial investigations of the performance of the monitoring chambers, the monitoring chambers were only connected to the input gas of the MUF quadrants.

The variation of the pressure in the DELPHI underground area is small compared to the variation of the pressure investigated during the feasibility study (see sec 4.3.2). In fact, the pressure changes in the pit are so small that it rules out the possibility to use the drift velocity and the pressure values to obtain the slope of the V_d-P function from the measurements in DELPHI (The ratio of the variation of the pressure during the initial investigations in DELPHI and the during the feasibility study is 12.87 mb/101.32 mb, which is only about 13%). Therefore the V_d-P relation obtained in the feasibility study was used to analyse the DELPHI data.

The slope obtained in the feasibility study is (see section 4.3.2):

$S_{Feas.}$=$-0.824\times10^{-2}\pm$ 0.188×10^{-3} (mm$\cdot\mu$sec$^{-1}\cdot$mb^{-1})
The errors are statistical only.

Fig. 4.21 shows the distribution of the measured drift velocities as a function of the recorded pressure where the errors are due to statistics only. It is seen that essentially all the drift velocity values are inside the bands determined by the dotted lines. The widths of the band are:

$$Width^{A}_{band} = 0.1 \text{ mm}/\mu\text{sec.}$$
$$Width^{C}_{band} = 0.15 \text{ mm}/\mu\text{sec.}$$

The half band widths are obtained by the following procedure:

1. plot all the data as function of pressure
2. within each ΔP = 0.5 mb interval assume that the data distribution is gaussian
3. calculate the variance of the drift velocity in each ΔP = 0.5 mb interval
4. (average the above variances) × 2.

The half band widths divided by the drift velocity have the values:
0.05/6.76 = 0.74% for chamber A and
0.075/7.31 = 1.01% for chamber C respectively.

This just suits the requirement of the drift velocity monitoring, i.e. to vary less than 1% of the drift velocity. It also shows that a monitoring of the drift velocity better than 1% is not possible as discussed before.

If one only selects those runs obtained in DELPHI where the pressure varies less than 2 mb around 978 mb, the following drift velocities are obtained for the input gas to the MUF quadrants:

$V_a = 6.77 \pm 0.03$ mm/μsec

$V_c = 7.30 \pm 0.04$ mm/μsec.

The difference is:

$$V_{dif} = \frac{V_c - V_a}{V_a} = \frac{T_a - T_c}{T_c} = (7.83 \pm 0.74)\% \tag{4.10}$$

where T_a and T_c are the drift times between the two windows for chamber A and C respectively.

This difference exceeds the 1% precision which was obtained before. When interchanging the roles of the two monitoring chambers, keeping the values of all external parameter fixed, this difference persisted and the individual drift velocities remained the same in each chamber. Thus, it has been conclusively shown that this difference is intrinsic to the chambers and not to the external connection and signal processing units.

Further studies and a discussion are given in the next section.

4.6 Calibration of the Monitoring Chamber with a Nitrogen Laser Beam

In order to investigate the origin of the difference in drift velocity measured in the two monitoring chambers in DELPHI, these chambers were recalibrated with a nitrogen laser beam.

There are several possible sources of systematic uncertainties in the monitoring chamber setup. The uncertainty on the drift distance is related directly to the exact lamp position. In an attempt to remove this uncertainty, a nitrogen laser system[50] is used. In this section a brief discussion of the laser system, the calibration setup and the calibration results will be given.

4.6.1 The Nitrogen Laser System

The nitrogen laser, used for the calibration of the monitoring chamber, pulses UV light at a wave length of 337 nm. One of the advantages of the nitrogen laser is that it can produce a light pulse of very short duration (≈ 1 ns) which is sufficiently short compared to the drift time of the electrons in the drift chamber. This light pulse is able, for a moderate pulse energy, to produce a track of sufficient ionization clusters in the chamber gas. The nitrogen laser can produce straight and reproducible ionization tracks over an area which is limited by the aperture of the entrance window of the chambers.

The electrical and optical setup of the laser system can be found in the Appendix B and the references refered therein.

4.6.2 Setup of the External Beam Optics

Fig. 4.22 shows schematically the external optical bench for the calibration system. The laser light passes a Beam Width Adapter (BWA) which converts the beam diameter to the required value and focuses the beam slightly. The lenses used in the BWA have focal lengths of 25 mm and 100 mm respectively. A focusing lens F is placed behind the BWA. The distance between F and the BWA can be chosen rather free to enable accurate beam positioning along the beam axis. The focusing lens is placed at the point x = 0 and has a focal length of 300 mm. All the lenses are made of the optical glass BK 7 ensuring a transparency of about 90% per lens.

Calculations of the Beam Width

For a nitrogen laser with a beam width $\sigma_0 = 0.35$ mm, the beam width after the BWA σ_b is 1.4 mm.

Taking the place where the focusing lens is placed as x = 0, if the diffraction is not taken into account, the width of the beam decreases linearly to zero as a function of the distance x according to:

$$\sigma = \frac{(f - x)\sigma_b}{f} \tag{4.11}$$

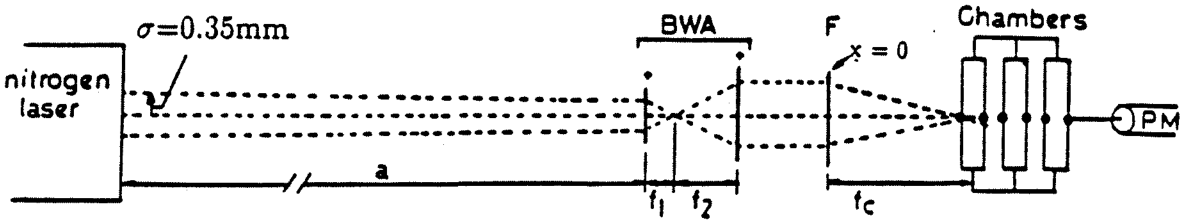

Figure 4.22: Setup of the external beam optics

where f is the focal length and σ_b is the beam width at x = 0. The width of the Gaussian diffraction pattern at a position x is given by[50]:

$$\sigma = \frac{x\sigma_f}{f} \tag{4.12}$$

where σ_f is the width at x = f.

For the focused beam it is important to know how well the ionization is confined along the focal point. If a certain fraction τ of total ionization is located in the range f - δ < x < f + δ, then the length of this range as a function of τ is given by:

$$l = 2\delta = tg(\frac{\tau\pi}{2})\frac{f^2}{k\sigma_b^2} \tag{4.13}$$

where f is the focal length, k is the wavelength number: $2\pi/\lambda$, $\sigma_b = 1.4$ mm. With f = 300 mm, λ = 337 nm and taking τ = 90%, one obtains l = 15.54 mm which corresponds to δ = 7.77 mm.

At the point x = f ± δ, taking diffraction part into account, one can obtain to a good approximation the width σ_x at the point x as:

$$\sigma^2_{(x=f\pm\delta)} = \sigma_f^2[1 + \frac{(\delta/f)^2\sigma_b^2}{\sigma_f^2}] \tag{4.14}$$

where σ_f is the beam width at the focal point and is given by:

$$\sigma_f = \frac{f}{2\sigma_b k} \tag{4.15}$$

Even taking δ =7.77 mm, which is an extreme case for the focal point far away from the central point of the chamber (where normally the focal point should be), one obtained σ_x = 0.037 mm which is about 0.09% of the drift distance. The corresponding error in the drift distance due to the ionization dispersion will thus be neglected for the purpose of this analysis.

4.6.3 Chamber Test Setup

In order to use the laser beam to calibrate the monitoring chambers, the reservoirs filled with cotton wool doped with Ethyl Ferrocene were replaced by quartz exit windows to let the laser beam pass through the chambers. The chambers were put one behind the other with entrance and exit windows aligned so that the laser beam could pass through the chambers without changing the chamber position. A quartz fibre connected to a photo-multiplier provided a trigger on the passage of the laser light. The delayed PM signal started the TDC, which was stopped in turn by the coincidence signal between the PM (with the delay) and the chamber. The PM signal delay was needed in order to record the drift time in a TDC of 1 μsec full range. In order to minimise systematic errors during the laser calibration, the identity and settings of all electronic modules were kept fixed, with the exception of the value of the PM delay if the change is absolutely necessary. The schematic electronic setup and the timing diagram are shown in fig. 4.23.

4.6.4 Experimental Results

The measurements were carried out for two different settings of the Field Grading high voltage -6200 V and -7500 V. Since the important parameter to be determined is the difference between the drift velocities of the two chambers, all the conditions must be kept the same for the same windows of the two chambers. The results are shown in table 4.1.

The drift times were measured as the time differences:

$$T_{drift} = (t_{delay} + t_{TDC})_{II} - (t_{delay} + t_{TDC})_{I}$$

here I and II refer to the windows close and far from the anode wire respectively. The relative difference between the drift times of the two chambers is:

chamber window	Delay time $t_{delay}[\mu\text{sec}]$	TDC measured time $t_{TDC}[\text{nsec}]$
Field Grading = -6200 V:		
Cham. A Wind. 1	$3.5050 \pm 0.0105 \pm 0.0002$	807.6 ± 1.012
Cham. C Wind. 1	$3.5050 \pm 0.0105 \pm 0.0002$	488.4 ± 0.915
Cham. A Wind. 2	$12.0250 \pm 0.0361 \pm 0.0006$	218.2 ± 1.110
Cham. C Wind. 2	$11.0250 \pm 0.0331 \pm 0.0006$	273.7 ± 0.593
Field Grading = -7500 V:		
Cham. A Wind. 1	$3.1340 \pm 0.0094 \pm 0.0002$	581.4 ± 0.334
Cham. C Wind. 1	$3.1340 \pm 0.0094 \pm 0.0002$	302.5 ± 0.833
Cham. A Wind. 2	$8.6000 \pm 0.0258 \pm 0.0004$	881.4 ± 0.561
Cham. C Wind. 2	$8.6000 \pm 0.0258 \pm 0.0004$	199.0 ± 1.078

Table 4.1: Results of the drift time measurement. The first part of the delay time error comes from the oscilloscope measurement and the second comes from the time delay generator.

$$\Delta T = \frac{T_a - T_c}{T_c} \tag{4.16}$$

where $T_{a,c}$ is the drift time between the two windows for chamber A or C. For the field grading values at -6200 V and -7500 V, we obtained:

$$\Delta T_{6200} = (8.560 \pm 0.686)\ \%$$

$$\Delta T_{7500} = (7.524 \pm 0.047)\ \%$$

The values of ΔT_{6200} and ΔT_{7500} are in agreement with each other as expected (the difference between ΔT_{7500} and ΔT_{6200} is 1.5 σ).

The error of ΔT_{7500} is considerably smaller than that of ΔT_{6200} because during the measurement of ΔT_{7500}, the delay time is left unaltered. Therefore, there is a strict cancellation of the larger error of the delay time measurement from the oscilloscope, so that only the small error from the time generator contributes. In contrast, for the field grading value of -6200 V the delay time had to be altered. The reason is that when switching the measurement from chamber A to chamber C, the drift time difference between the two chambers was greater than 1 μs, which is the full-scale of the TDC.

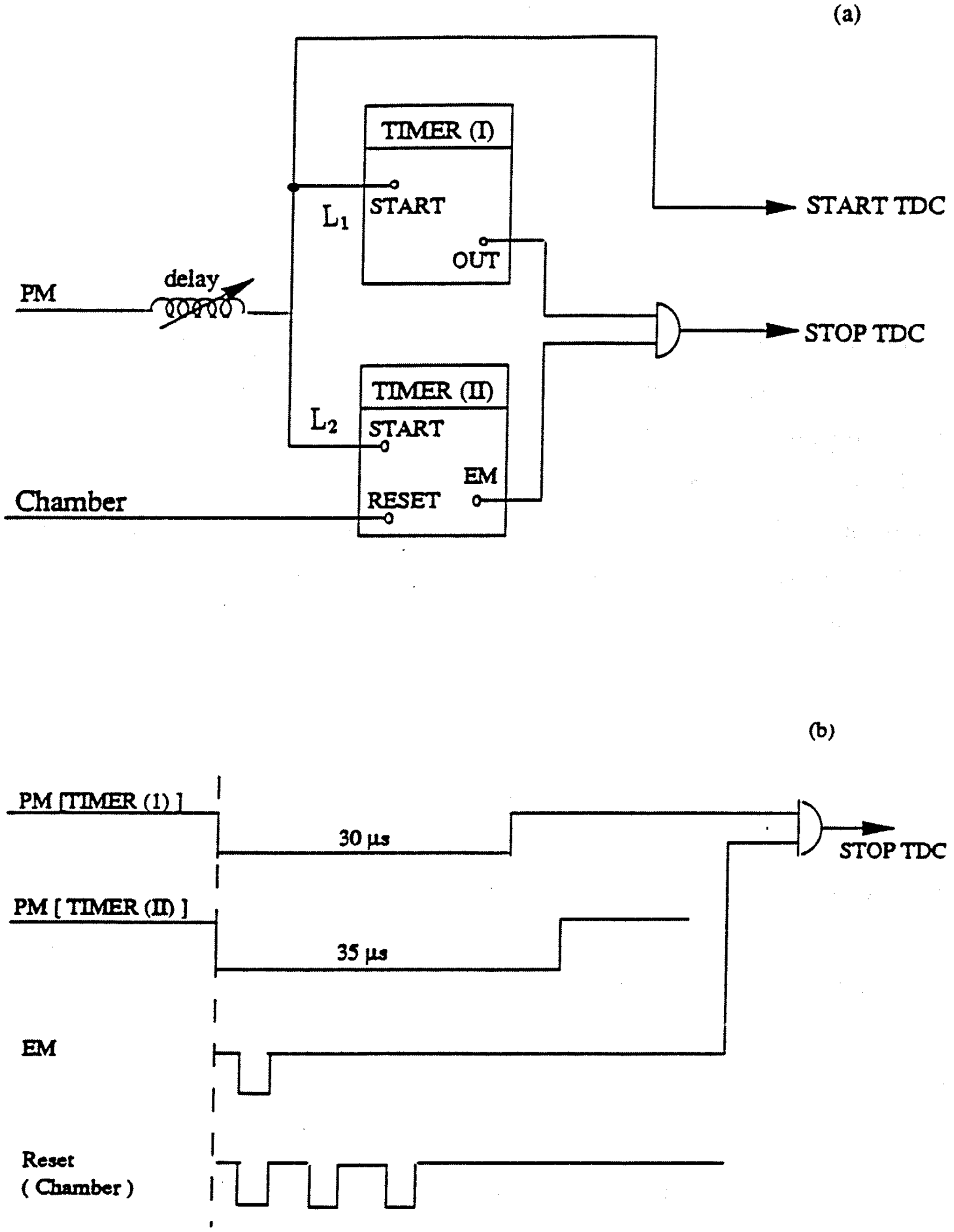

Figure 4.23: (a) Schematic electronic setup of the chamber test with a laser beam. L_1 and L_2 have the same length. (b) Timing diagram.

4.6.5 Discussion and Conclusions

The electron drift velocity is given by:

$$V = k\frac{E}{P} \tag{4.17}$$

where k is constant for a certain gas, E and P are the electric field and gas pressure. Whereas the quantity ΔT:

$$\Delta T = \frac{T_a - T_c}{T_c} = \frac{V_c - V_a}{V_a} = \frac{V_c}{V_a} - 1 = \frac{E_c}{E_a} - 1 \quad (for\ P_a = P_c)$$

is independent of the pressure and slope k and depends only on the electric fields. Therefore we conclude that the electric fields in the two chambers are not identical even when the same field grading and anode high voltages are applied. So, one can use the ΔT obtained by the laser beam calibration to correct the difference of the drift velocities measured in DELPHI for this effect. The value $\Delta T_{7500} = (7.524\ \pm 0.047)$ % is compatible with the result $V_{dif} = (7.83 \pm 0.74)\%$ obtained in DELPHI (see eq. 4.10, the difference being 0.41σ).

In conclusion, the difference between the drift velocities from the two monitoring chambers A and C used for the MUF monitoring in DELPHI is:

$$V_{dif} = \frac{V_c - V_a}{V_a} = \frac{T_a - T_c}{T_c} = (7.524 \pm 0.047)\%$$

and is explained entirely by the difference of the electric field E in the chambers. The mostly likely explanation of the electric field difference is that the resistances used in the two chambers are different. In fact the monitoring chambers were built by material rejected for the MUF construction and this could lead to this rather large systematic discrepancy.

4.7 Study of the Ratios of the Drift Velocities Measured in the Monitoring Chambers to those Measured in the MUF Quadrants

In order to use the monitoring chambers to monitor the drift velocities of the MUF chambers of DELPHI, a further calibration has to be performed to determine the ratio of the drift velocities in the MUF chambers of each layer to those measured with the monitoring chambers. This can be done by using parallel muons. Parallel muons consist of a halo of high momentum muons simultaneous with and approximately parallel to the e^+e^- beams and produced in upstream beam elements. These halo muons usually cross 8 muon chamber layers. The drift velocities are fitted from the "drift time-distance to anode" relationships derived from the track fit to the parallel muon data. From the off-line analysis of parallel muons we obtained the average drift velocity $V_{pa}(V_{pc})$ of each MUF-layer of side A(C) by the following procedure. The ratio of the drift velocity of each layer to that of one specific layer from side A, for which the parallel muon study produced high statistics, was measured. The latter measurements were combined with a measurement of the ratio of the drift velocity derived from the parallel muon study for the specific layer to that (V_{ma}) simultaneously measured by the monitoring chamber on side A. The same procedure could not be applied independently to estimate V_{mc} for end-cap C as the G64 TDC card used for the time measurements with the monitoring chamber was too noisy during the period in which the parallel muon data were collected. However, as the ratio V_{ma}/V_{mc} as measured by both monitoring chambers is known, an on line monitoring by those chambers of the average drift velocities in each quadrant layer still remains possible.

The data actually used to study these ratios are the following. Data were taken with monitoring chamber A connected to gas channel A1, to measure the drift velocity in the output gas of quadrant layer Q11 X, a layer giving high statistics for parallel muons. A sample of parallel muon data was taken with the complete MUF detector at the same time as the above measurements were done. During 13 days of data taking at the end of the physics run in 1993, a total of 60468 parallel muons have been selected in the whole MUF detector and 214,800 events (358 runs) were recorded for the monitoring chamber A.

The drift velocity obtained from the monitoring chamber is:

$$V_{ma} = (6.452 \pm 0.031)\ \mathrm{mm}/\mu\mathrm{sec}.$$

and the drift velocity obtained by the analysis of the parallel muon data for the specific layer Q11 X is [52]:

$$V_{pa} = (7.929 \pm 0.026)\ \mathrm{mm}/\mu\mathrm{sec}.$$

Therefore the ratio of both drift velocities is:

$$R_{ma1} = \frac{V_{pa}}{V_{ma}} \doteq 1.229 \pm 0.007$$

As the ratio of the drift velocities in all quadrant layers inside end-cap A to that of layer Q11 X are known from the parallel muons analysis, one can obtain the ratio of the drift velocity in each layer in end-cap A to that in the monitoring chamber A. The results are displayed in Table 4.2.

From the knowledge of V_{mc}/V_{ma} and the ratio of the average drift velocities V_{pc} in all layers on side C to that measured in Q11 X, we obtained the ratios V_{pc}/V_{mc} displayed in Table 4.2 as well.

A gas channel (MUF layer)	V_{pa}/V_{ma}	C gas channel (MUF layer)	V_{pc}/V_{mc}
1 (Q11 X)	1.229 ± 0.006	1 (Q31 X)	1.164 ± 0.015
2 (Q11 Y)	1.217 ± 0.010	2 (Q31 Y)	1.196 ± 0.015
3 (Q12 X)	1.309 ± 0.017	3 (Q32 X)	1.173 ± 0.009
4 (Q12 Y)	1.286 ± 0.014	4 (Q32 Y)	1.233 ± 0.013
5 (Q13 X)	1.269 ± 0.023	5 (Q33 X)	1.195 ± 0.031
6 (Q13 Y)	1.323 ± 0.035	6 (Q33 Y)	1.138 ± 0.015
7 (Q14 X)	1.229 ± 0.014	7 (Q34 X)	1.191 ± 0.028
8 (Q14 Y)	1.236 ± 0.013	8 (Q34 Y)	1.256 ± 0.027
9 (Q21 X)	1.230 ± 0.010	9 (Q41 X)	1.184 ± 0.015
10 (Q21 Y)	1.232 ± 0.010	10 (Q41 Y)	1.235 ± 0.019
11 (Q22 X)	1.325 ± 0.017	11 (Q42 X)	1.232 ± 0.013
12 (Q22 Y)	1.289 ± 0.013	12 (Q42 Y)	1.292 ± 0.015
13 (Q23 X)	1.290 ± 0.024	13 (Q43 X)	1.165 ± 0.032
14 (Q23 Y)	1.287 ± 0.031	14 (Q43 Y)	1.166 ± 0.032
15 (Q24 X)	1.228 ± 0.012	15 (Q44 X)	1.204 ± 0.030
16 (Q24 Y)	1.222 ± 0.012	16 (Q44 Y)	1.199 ± 0.028

Table 4.2: Ratio of the drift velocity $V_{pa}(V_{pc})$ in each MUF layer of side A(C) to the result $V_{ma}(V_{mc})$ of the measurements with the corresponding monitoring chambers A(C).

4.7.1 Discussion

There are about 23% and 17% differences in the drift velocities measured by the monitoring chambers and by the MUF detectors for end-cap A and C, respectively. The following questions have to be understood:

1. What is the source for such a large difference in drift velocity?
2. Is this difference constant with time?

This drift velocity difference must be somehow due to pressure differences inside the chambers. To answer the second question, one needs further calibration with parallel muons.

4.8 Conclusions

The drift velocity monitoring system described was built in order to provide a fast on line monitoring of the drift velocities in the MUF chamber layers. During 1990 and 1991, simultaneously with most of the DELPHI physics runs, the drift velocity monitoring system was developed and optimised in DELPHI. The results showed that with the on-line drift velocity monitoring system, the uncertainty in the drift velocity of the Forward Muon Chambers can be reduced to about 1%, representing the limitation from the mechanical and electrical tolerances of these chambers.

However, a rather large systematic discrepancy (7.52 ±0.05)%) was found between the two monitoring chambers, presumably due to the differences of the geometry and the drift fields of the chambers. There is further evidence for this from the studies using a nitrogen laser system.

Calibration measurements to determine the ratio of the drift velocity obtained by the analysis of the parallel muons with the MUF detector and that measured with the monitoring chambers have started. However, further calibration is needed to cross-check and improve the results and check whether these ratios are constants in time.

Chapter 5

Analysis of Dimuon Decay of the Z^0

The channel studied here is $e^+e^- \rightarrow Z^0/\gamma \rightarrow \mu^+\mu^-$ around the Z^0-pole. For incident electrons and positrons of exactly the same energy, muon pairs from Z^0 decay are produced back-to-back in the laboratory frame, each with the energy E_{beam} of the beam particles and coming from the interaction region at the time the beams cross (BCO). Radiative effects, both from initial and final states, lead to muons having energies slightly less than E_{beam} and not exactly back-to-back. Due to photon radiation leading to pair creation into the beam pipe or into the material of TPC, events with more than two tracks are produced as well. The muons penetrate all the detector material without undergoing strong interactions and deposit only a small fraction of their energy in the calorimeters. Fig. 5.1 shows an example of a clean back to back dimuon event. The schematic view of the various DELPHI subdetectors is presented in fig.3.3. The muons originate from the centre of DELPHI and pass through the Electromagnetic Calorimeters (EMCAL) and Hadron Calorimeters (HCAL) producing minimal ionization. In addition, signals are generated in the Forward Muon Chambers (MUF) on the outside of DELPHI.

In this chapter, the selection of muon pair candidate events and the techniques used to estimate backgrounds and efficiencies are presented. The luminosity and the normalised dimuon cross section are studied. In the sections 5.2 up to 5.5, the data collection, data reduction, run selection and events selection are described. The calculation of efficiencies and background are presented in sections 5.6 to 5.10 and 10000 $\mu^+\mu^-$ and 9000 $\tau^+\tau^-$ simulated events generated by the programs described in Sec-

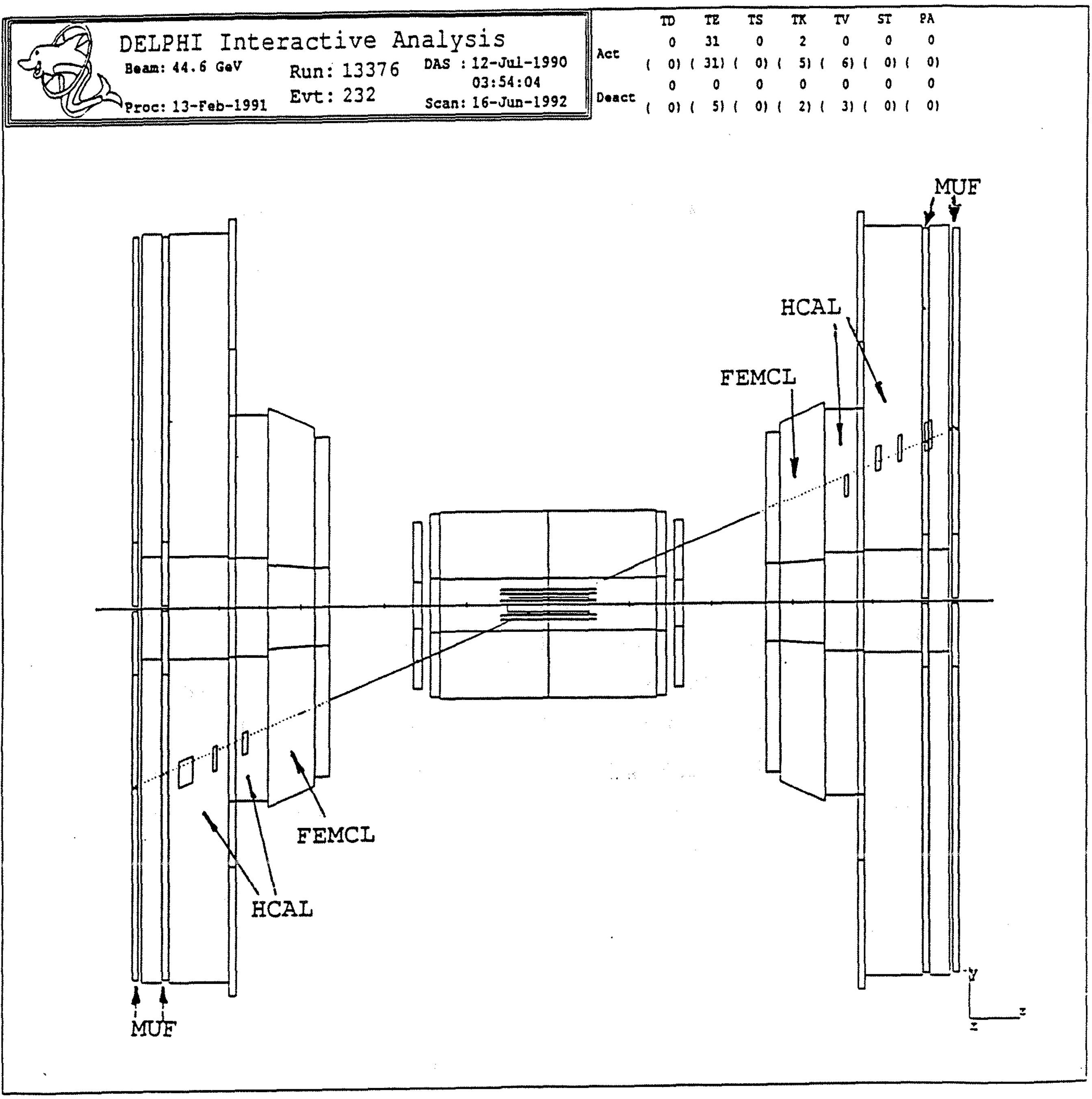

```
DELPHI Interactive Analysis
Beam: 44.6 GeV        Run: 13376   DAS : 12-Jul-1990
                                         03:54:04
Proc: 13-Feb-1991     Evt: 232     Scan: 16-Jun-1992

           TD     TE     TS     TK     TV     ST     PA
Act         0     31      0      2      0      0      0
        (   0) (  31) (   0) (   5) (   6) (   0) (   0)
Deact       0      0      0      0      0      0      0
        (   0) (   5) (   0) (   2) (   3) (   0) (   0)
```

Figure 5.1: A dimuon event in DELPHI. 'Points' on EMCAL and MUF and the 'squares' on HCAL are the signals generated by the muons. The dotted lines mark the extrapolated track positions.

tion 3.9.2 are used. Finally, the luminosity measurement is described in section 5.12 and determination of the dimuon cross section is presented in section 5.13.

5.1 Description of Muon Identification Methods

The methods of muon identification rely on the differences between the interactions of muons and other particles with matter. Hadrons have strong interactions with matter, producing a typical cascade. Electrons cause electromagnetic cascades when they pass through matter mainly due to bremsstrahlung and pair-production processes. Muons do not interact strongly and do not emit any significant bremsstrahlung. The high momentum muons studied in this work are minimum ionising particles which deposit little energy when passing through matter.

There are two methods for discriminating between muons and electrons or hadrons:

1) Muons can be recognised in a calorimeter as isolated, minimum ionising particles with small energy deposition. In contrast, hadrons and electrons produce hadronic cascades or electromagnetic showers.

2) Muons can be identified by their ability to penetrate matter almost without deflection. In DELPHI, the typical value of the lateral r.m.s. deviation of a 45 GeV/c muon penetrating through the entire iron yoke is about 5 mm. Muon chambers are placed at the external edge of the iron yoke of the magnet, acting as an absorber. If the extrapolation of a track recorded in detector layers situated in front of the absorber can be matched with hits in the muon detectors, then the track is likely to result from a muon.

5.2 Data Collection

The analysis described in this chapter is based on the data taken during 1990. In that year, the LEP physics runs started on April 23th and ended on August 29th. The corresponding LEP fills and DELPHI DAS runs are 185 to 415 and 7419 to 15829 respectively.

The data are derived from a scan around the Z^0 peak at seven centre-of-mass energies ranging from 88.22 to 94.22 GeV.

During most of this running period, the efficiencies of the tracking chamber in the very forward region (polar angle $\theta < 20^o$ and $\theta > 160^o$) were so low that any further extension of this polar angle interval was judged to be unsafe.

Therefore, the data for this analysis is restricted to the polar angle range

$$20^o \leq \theta \leq 160^o$$

where θ is the polar angle with respect to the incident e^- direction (DELPHI z-axis).

The detectors (See Chapter 3) used for collecting the data in this analysis are:

- The Inner Detector (ID), the Time Projection Chamber (TPC), the Outer Detector (OD), Forward Chamber A (FCA) and Forward Chamber B (FCB). They are used for track reconstruction.
- The barrel electromagnetic calorimeter (HPC), the Forward Electromagnetic Calorimeter (FEMC), the Hadron Calorimeter (HCAL) (both in barrel region and forward region), the Barrel Muon Chambers (MUB), and the Forward Muon Chambers (MUF) are used for muon identification.
- The Small Angle Tagger (SAT) is used for the luminosity measurements.
- The Time of Flight Counters (TOF) and the end cap scintillators (HOF) are used in the trigger.

The trigger on muon candidates is based on positive signals from at least one of the following trigger components (see chapter 3):

A) First Level (T1) Triggers:

1. **TOMJ**: signals in at least two sectors of TOF are required.
2. **IOMJ**: a majority trigger where at least one signal in ID combined with signals in at least two sectors of OD are required.
3. **SCOD**: a combination of TOF and OD. It requests at least one signal in TOF and one in OD.
4. **HOF**: HOF single-arm signal from at least one of the end cap.
5. **FCAB**: at least one signal in forward or backward FCA/FCB chambers.

B) Second Level (T2) Triggers:

1. **TPC**: The TPC single track trigger.
2. **HOBB**: a back-to-back trigger where signals in at least two sectors of HOF opposite in θ and ϕ are required.
3. **MAJORITY 2**: The 'majority 2' trigger :

   It requires a coincidence of at least two of the following 6 conditions:

   - (1) HOF trigger from one of the end-caps.
   - (2) At least one signal in forward FCA/FCB chambers.
   - (3) At least one signal in backward FCA/FCB chambers.
   - (4) At least one signal in forward EMF with energy deposition of at least 3.0 GeV.
   - (5) At least one signal in backward EMF with energy deposition of at least 3.0 GeV.
   - (6) A coincidence of one OD quadrant with any ID signal.

C) **FWMU** The "Forward Muon" trigger:

- It contains HOF at 1st level and forward muon chamber information at 2nd level. When collecting the muon chamber information for the MUF trigger, the entire forward region is divided into 8 octants. One octant is fired if at least 3 out of the 4 muon chamber layers of an octant are hit.

5.3 Data Reduction

During the data taking of 1990, the raw data were written to IBM cassettes. These cassettes were processed by the DELANA program in which a leptonic tagging routine labelled events as leptonic candidates. After the DELANA[1] leptonic tagging, all the leptonic candidates with some background from hadronic, cosmic and beam gas events, remained.

---

[1] For DELANA , TK, TE see section 3.9.1

In DELANA, a "leptonic event" was accepted if the total number of charged particles was not more than 8 and at least one of the following conditions was fulfilled [53]:

1) the total energy $E_{tot} > 8$ GeV. (see formula (5.1) for the definition of E_{tot})
2) at least one charged particle track with momentum P > 2 GeV/c and impact parameter at the origin < 10 cm in z and < 8 cm in the XY plane.

The total energy is computed as :

$$E_{tot} = E_{track} + E_{HPC} + E_{EMF} \tag{5.1}$$

$$E_{track} = maximum(\sum E_{TPC,TE} \qquad or \qquad \sum E_{TK}) \tag{5.2}$$

which is the maximum energy value between total TEs from TPC or total tracks.

$$E_{EMF} = \sum E_{EMF,TE}; \qquad E_{HPC} = \sum E_{HPC,TE} \qquad (if\ E\ >\ 1\ GeV) \tag{5.3}$$

which are the sum of all those TEs with energy larger than 1 GeV from EMF or HPC respectively.

It was checked that no simulated di-muon events were lost due to the leptonic tagging. After the event passed the DELANA leptonic tagging, a program named P2ANA was used. This created a MINI_DST data file containing all the essential information about the event, such as momentum, θ and ϕ value, trigger bits, tracking information, etc. There are 207 variables per event.

5.4 Run Selection

It is impossible for a big detector such as DELPHI to work at 100% efficiency over extensive running periods. The status of each subdetector changes from day to day. For the data analysis it is obviously very important to know the working status of each subdetector. DELPHI has a detector situation log book file, RUNSEL90[54], to record the working condition of every subdetector on a run by run basis. For the muon pair analysis the following conditions are imposed before accepting a run:

- The detectors SAT, TPC, MUB, MUF, HPC, FEMC and HCAL are in good working conditions.

- For the trigger, the TPC, SAT and HOBB trigger hardware are in good working condition.

For the other detectors, such as FCA, FCB, ID, OD, TOF, it is found that for $20^o \leq \theta \leq 160^o$ (see section 5.5.8) the detector situation has no essential influence on the results of the analysis when the former conditions are already fulfilled.

5.5 Selection of Dimuon Events

A summary of the cuts for the dimuon event selection is described in this section followed by a detailed discussion of each cut. The calculation of the efficiencies is given in section 5.6 to section 5.9.

A sample of **4002** muon pair candidates are selected using the following criteria:

- **Cut on the Total Number of Tracks:** The number N_{TK} of tracks (TK's) produced by charged particles should be larger than 1 and less than 6 (see section 5.5.1).

- **Acollinearity Cut:** The acollinearity angle between the two highest momentum particle tracks should be less than 10^o (see section 5.5.2).

- **Cut on "the Total Number of Tracks N_{TK} Greater than Two" events:** To reduce the background from τ-decays with the number of tracks greater than two, we either require that acollinearity angle between the two highest momentum particle tracks should be less than 1^o or that at least one of the two highest momentum particles should be identified as a muon by the muon chambers (see section 5.5.3).

- **Momentum Cut on Charged Particles:** The two highest momentum particles should both have a momentum greater than 15 GeV/c (see section 5.5.4).

- **Vertex Cut:** The two highest momentum particle tracks should come from the vertex region. The vertex region is defined by $r < 1.5$ cm and $|z| < 4.5$ cm, where r and $|z|$ are the projected distances in the xy-plane and on the Z axis respectively between the interaction point and the point of closest approach of the track (see section 5.5.5).

- **Muon Identification:** Both highest momentum particles should be identified as muons by at least one of the muon identification chambers (e.g. MUB or MUF, or HPC or FEMC, or HCAL.) (see section 5.5.6).
- **Tau Veto:** Those events with the acolinearity angle between the tracks of the two highest momentum particles of leptonic events greater than 1^o and the deposited energy in HCAL greater than E_{cut} will be cut as tau background. (see section 5.5.7).
- **Polar Angle Acceptance:** Of the two highest momentum particles, the track of the negative particle should have a polar angle between 20^o and 160^o (see section 5.5.8).

5.5.1 Cut on the Total Number of Tracks

The dimuon decay from the Z^0 should produce at least two charged particles. Considering radiative effects, the total number of tracks (N_{TK}) is required to be $1 < N_{TK} < 6$. This may remove some dimuon events by total track reconstruction inefficiency (including the working condition of tracking chambers and the dead space effects). The track losses are studied (in section 5.7) as function of the working condition efficiency of the tracking chambers and inefficiencies (in section 5.9) due to the tracking chamber dead space are examined.

Fig. 5.2 shows the distribution of the total number of charged particle tracks for those events which passed all muon cuts apart from that on the total number of tracks. To enhance the purity of this test sample, the momenta of the two highest energetic charged particles are required to be both greater than 25 GeV/c and the acollinearity angle has to be less than 1^o. From the figure one can see that the number of the events with more than two tracks compared to the number of events with just two tracks is very small and that there should be a negligible number of genuine dimuon events with $N_{TK} > 5$.

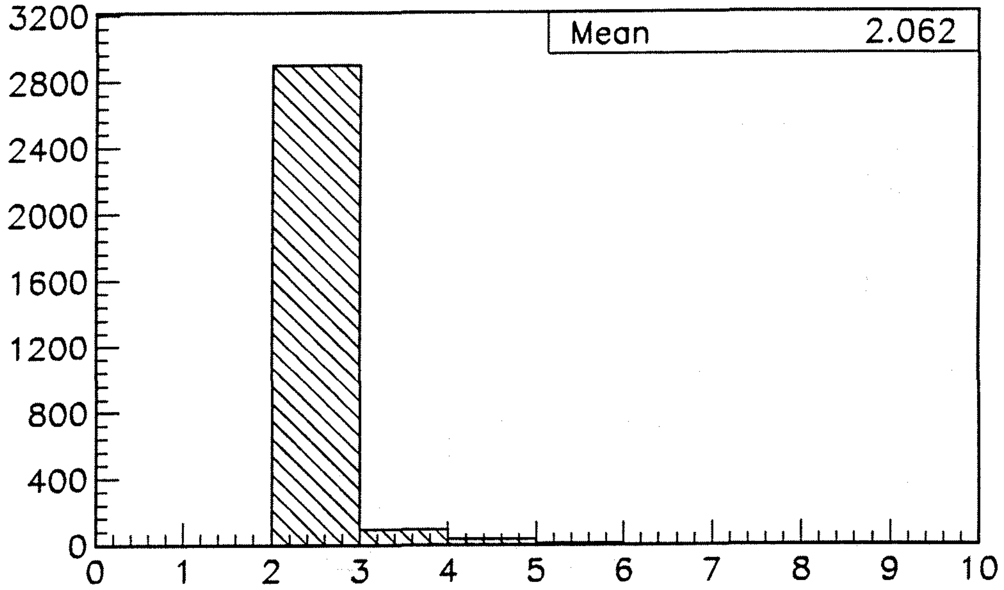

Figure 5.2: The distribution of the total number of tracks produced by charged particles. No event of N_{TK}=6 has been found on the plot.

5.5.2 Acollinearity Cut

For the events with 2 charged particles with measured momenta $\vec{P}_1$ and $\vec{P}_2$ in the Z^0 decay final state, the acollinearity angle is defined as :

$$\cos\theta_{acol} = -\frac{\vec{P}_1 \cdot \vec{P}_2}{|\vec{P}_1||\vec{P}_2|} \tag{5.4}$$

The acollinearity of the $\mu^+\mu^-$ events is mainly caused by the initial and the final state radiation processes. Fig. 5.3 shows the acollinearity angle distributions, based on simulated $\mu^+\mu^-$ and $\tau^+\tau^-$ events and all real data for tagged leptonic events respectively (see section 5.3 about the lepton tag conditions).

Fig. 5.3 clearly indicates that:

- For the $\mu^+\mu^-$ events, about 87% of the μ pairs have the acollinearity angle $\theta_{acol} < 1°$.
- For the $\tau^+\tau^-$ events, about 92% of the τ pairs have acollinearity angle $\theta_{acol} > 1°$.

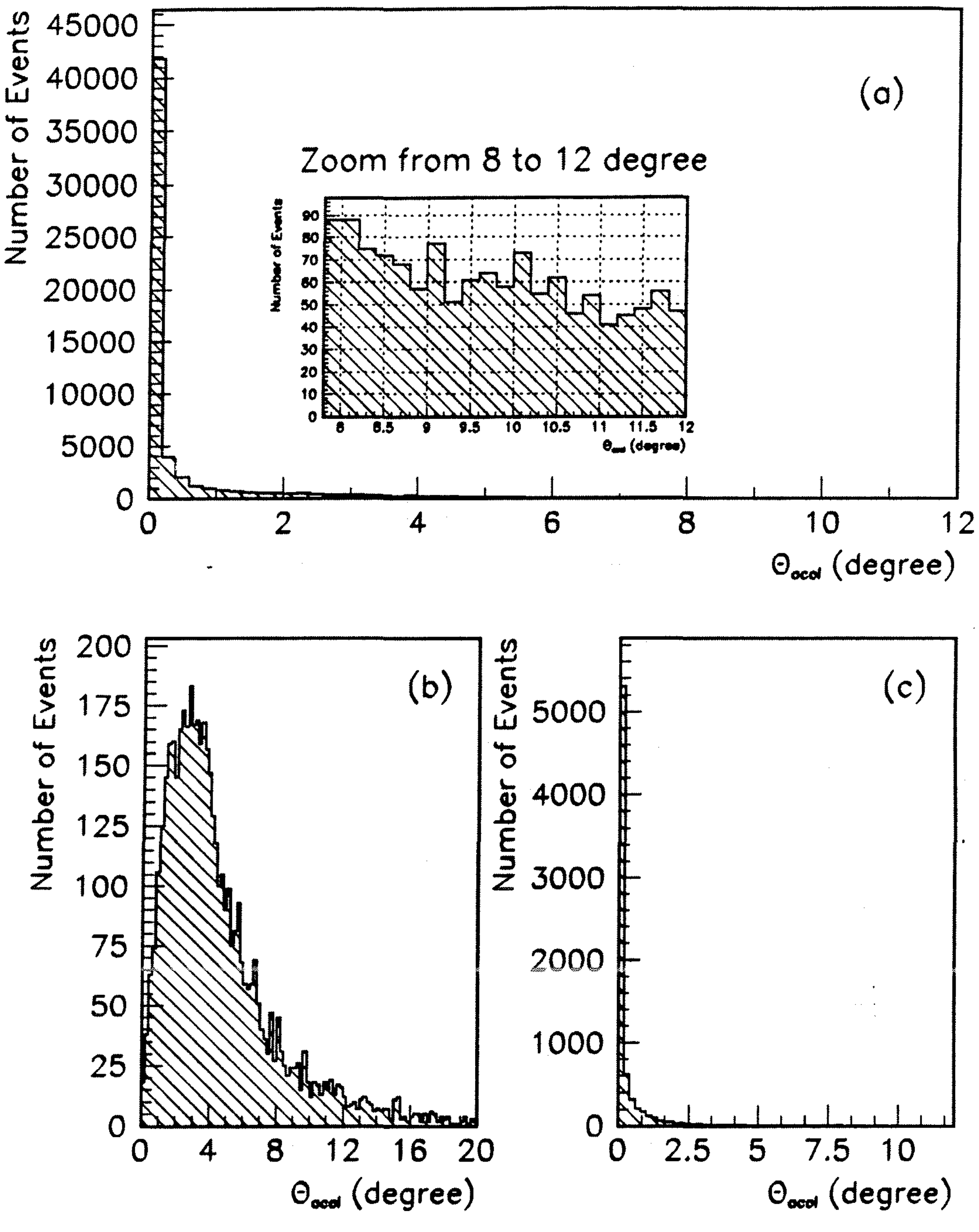

Figure 5.3: The acollinearity angle distribution (a) for all events tagged as leptonic; (b) simulated $\tau^+\tau^-$ events; (c) simulated $\mu^+\mu^-$ events.

Table 5.1 summarises the fraction of $\mu^+\mu^-$ and $\tau^+\tau^-$ events with different acollinearity angles. For the most of the muon-pair events the acollinearity angle is less than 1^o, while for most tau-pair events the acollinearity angle is greater than 1^o. Applying the constraint that the acollinearity angle should be $\leq 1^o$, in addition to the other events selection criteria, a 'clean muon' or a 'background enriched' sample can be obtained. Such samples will be used to study different efficiencies in the following sections.

LEPTON PAIR	$\theta_{acol} > 1^o$	$\theta_{acol} > 2^o$	$\theta_{acol} > 3^o$
$\mu^+\mu^-$	$(12.96 \pm 0.35)\%$	$(7.04 \pm 0.27)\%$	$(2.73 \pm 0.71)\%$
$\tau^+\tau^-$	$(92.38 \pm 0.37)\%$	$(78.32 \pm 0.57)\%$	$(61.97 \pm 0.67)\%$

Table 5.1: Fraction of $\mu^+\mu^-$ and $\tau^+\tau^-$ events with acollinearity angle θ_{acol} great than 1^o, 2^o and 3^o respectively.

In order to avoid the loss of dimuon events a conservative acollinearity cut: $\theta_{acol} \leq 10^o$ is imposed on the experimental sample.

This cut, whose efficiency and background effects will be examined in section 5.9 and section 5.10 respectively, will however be tightened for events with more than two tracks.

5.5.3 Cut on "the Total Number of Tracks Greater than Two" Events

Table 5.1 shows that for $Z^0 \longrightarrow \mu^+\mu^-$ decays producing more than 2 tracks, the acolinearity angle between the two highest momentum particles is less than one degree in more than 87% of the cases. For $Z^0 \longrightarrow \tau^+\tau^-$ decays, the conclusion is just the opposite. More than 92% of the $\tau^+\tau^-$ final states have acolinearity angle between the two highest momentum particles is greater than one degree.

Fig. 5.4(a) and (b) show that the acolinearity angle between the two highest momentum particles for simulated $\mu^+\mu^-$ and $\tau^+\tau^-$ final states with more than two tracks is greater than 1^o in $(29.52\pm2.57)\%$ and $(93.57\pm0.84)\%$ of the cases respectively.

Considering that the percentage of $Z^0 \longrightarrow \mu^+\mu^-$ events with more than two tracks is small (see Fig. 5.2), events with $N_{TK} > 2$ are unlikely to be of the di-muon type when the acollinearity angle is greater than one degree and neither of the two highest momentum particles was identified as a muon by the muon chambers. The cut on "total number of tracks greater than two events" is then defined as follows:

- If the total number of tracks is greater than two, we either require that the acollinearity angle between the two highest momentum particle tracks should be less than 1^o or that at least one of the two highest momentum particles should be identified as a muon by the muon chambers.

The effect of this cut is further examined in sections 5.9 and 5.10.

5.5.4 Momentum Cut on Charged Particles

The momentum of the muons in the dimuon decay from the Z^0 decay should be comparable to the momentum of the beam particles.

The accuracy of the momentum measurement is related to the precision with which the track curvature in the magnetic field can be estimated. The radius of curvature R of the tracks in the magnetic field is given by:

$$R[m] = P_T[GeV/c]/0.29979B[Tesla] \tag{5.5}$$

where P_T is the momentum of the particles in the plane transverse to the magnetic field. The magnetic field in DELPHI is along the z axis and the value is 1.23 Tesla.

For each of the two highest momentum particles we define the quantity $\triangle P^*$ as the difference between the inverse momentum $|1/P_{track}|$ [1] and the inverse momentum from the beam particles $1/P_{beam}$, divided by the latter:

$$\triangle P^* = \frac{|\frac{1}{P_{track}}| - \frac{1}{P_{beam}}}{\frac{1}{P_{beam}}} \tag{5.6}$$

This quantity $\triangle P^*$, whose distribution should be approximately gaussian, was computed after applying all the muon selection cuts but lowering the momentum cut on charged particles from 15 to 5 GeV/c, and taking account of the fact that the energy of the incident particles varied around the Z^0 peak at seven centre-of-mass energies from 88.22 GeV to 94.22 GeV. The distribution of $\triangle P^*$ is displayed in fig. 5.5(a). The mean value of the distribution = 0.024 ± 0.002 and the RMS = 0.272 ± 0.003.

The inverse momentum has also been plotted for the two highest momentum particles in each event (See Fig. 5.5(b)). The inverse momentum value equal to

---

[1] P_{track} carries the sign of the charge of the particle.

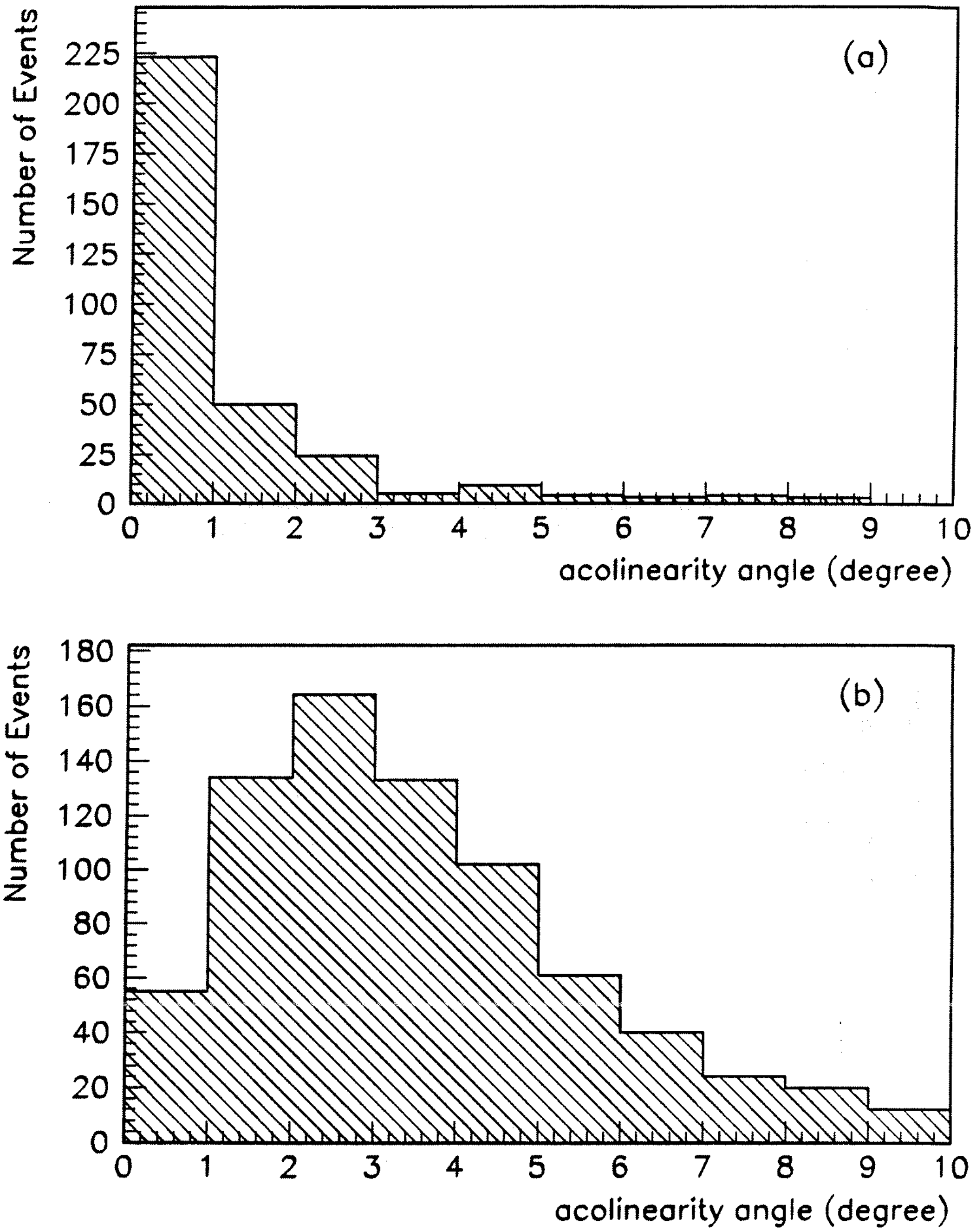

Figure 5.4: Distribution of the acollinearity angle between the two highest momentum particles in events with more than two tracks. (a) for the simulated $\mu^+\mu^-$ events. (b) for the simulated $\tau^+\tau^-$ events.

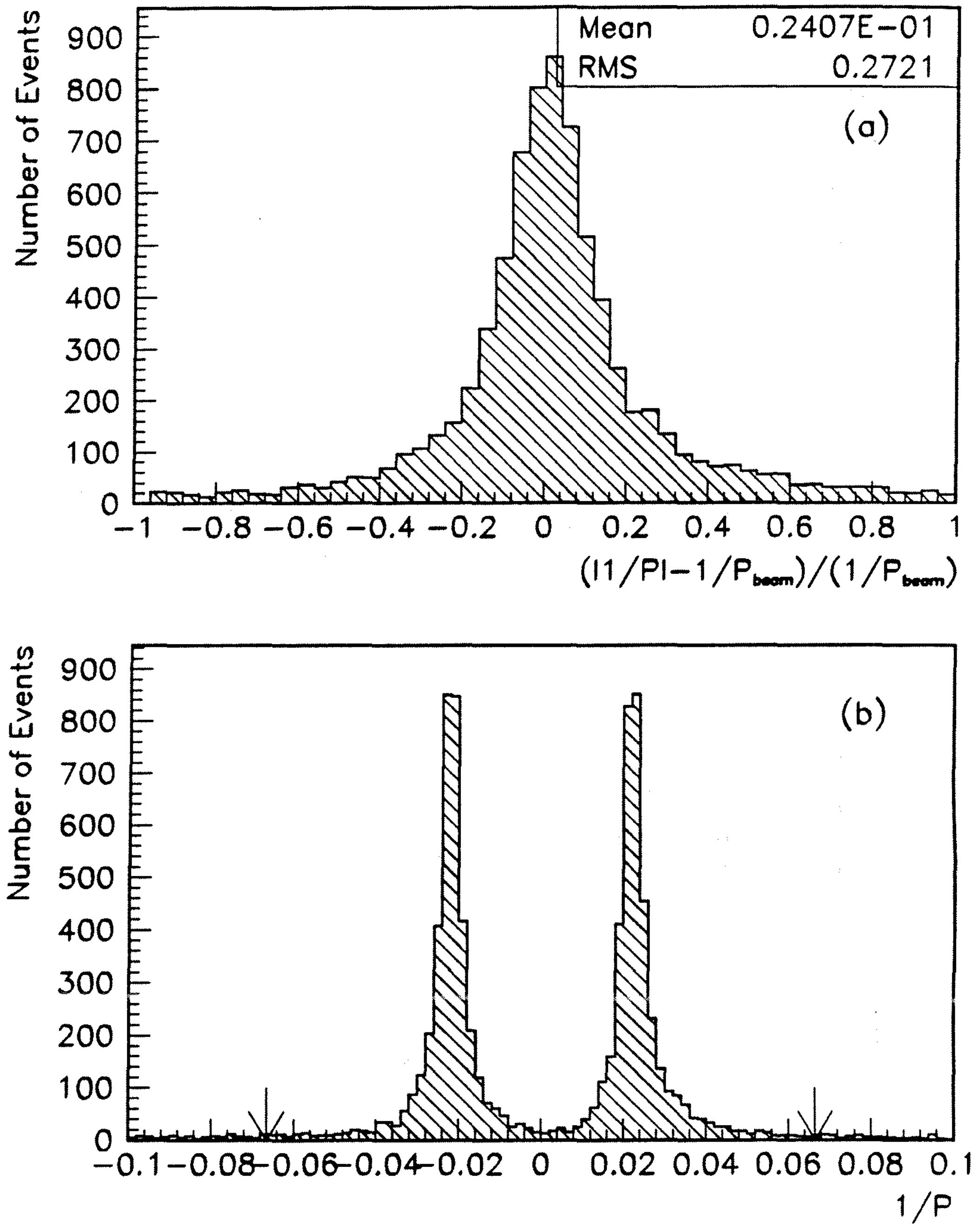

Figure 5.5: Inverse momentum resolution for the muon pair candidate events: (a) The difference between the inverse momenta of muons and the inverse beam particle momenta divided by the latter. (b) Inverse momentum of the particle track in unit of $(GeV/c)^{-1}$.

0.067 $(GeV/c)^{-1}$ corresponds to a momentum value of 15 GeV/c and figure 5.5(b) shows that the dimuon peaks lie well within this limit.

The non Gaussian tails of both distributions are mainly due to the radiative effects and the contamination of the $\tau^{+}\tau^{-}$ background.

We conclude that a safe momentum cut on charged particles is applied by demanding that:

- each of the two highest momentum particles has a momentum greater than 15 GeV/c.

The effect of this cut on selection efficiency and background is further examined in sections 5.9 and 5.10.

5.5.5 The Vertex Cut

In order to remove cosmic ray background from the muon sample, a vertex cut is applied. One checks that the track is produced in the bunch crossing region in order to distinguish muon-pairs from cosmic muons. Fig. 5.6 shows the distribution of the distance of the closest approach of the muon tracks to the beam spot in the transverse (Rmin) and the longitudinal (Zmin) direction after applying all the muon selection cuts except the vertex cut. On this basis the interaction region is conservatively defined as a cylinder parallel to the beam having half length 4.5 cm and radius 1.5 cm with the interaction point of the beams as the central point.

The average beam spot position is determined for each LEP fill from the reconstruction of hadronic Z^0 event vertices using the software package CORPUS11[59]. It is known with a precision which depends on that of the alignment of the tracking detectors. The tracks which are used to determine the beam spot, are fitted using the information from all detectors including the vertex detector. Typically the mean beam position in a fill was reconstructed to be better than 20 μm in both x and y. For the z coordinate value the precision is however not better than 2 cm [64]. Fig. 5.7 shows the measured average position and the width of the interaction region for each LEP fill, (a) for x and (b) for y.

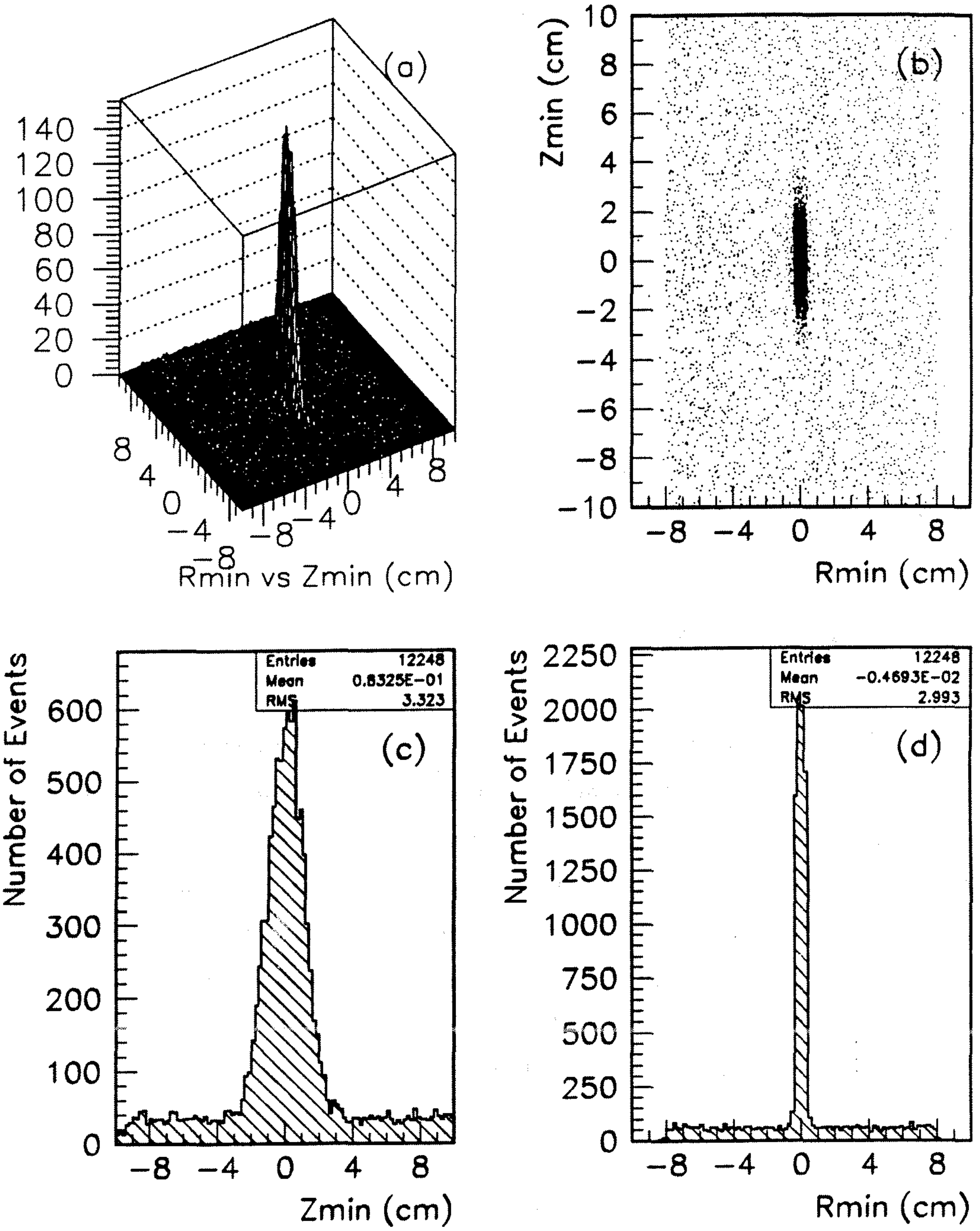

Figure 5.6: The distribution of the distance of the closest approach of muon tracks to the e^+e^- interaction point in the transverse (Rmin) and the longitudinal (Zmin) direction.

As the cosmic background appears everywhere with the same probability density, the background appears as a uniform distribution in Fig. 5.6. The remaining cosmic background after the vertex cut will be studied in detail in section 5.10.

The origin of a track is obtained by its interpolation towards the centre of DELPHI. For the analysis of the 1990 $\mu^+\mu^-$ data, the vertex detector results were not yet taken into account in the reconstruction program DELANA, so that the ID and TPC are the key subdetectors for the reconstruction of the origin of a track. If one of these two subdetectors can not provide TEs for the track (see section 3.9.1), its origin will be poorly determined from the interpolation and the allowed interaction region is increased by a factor 2 in both Z and R for those tracks whose ID or TPC TE is missing.

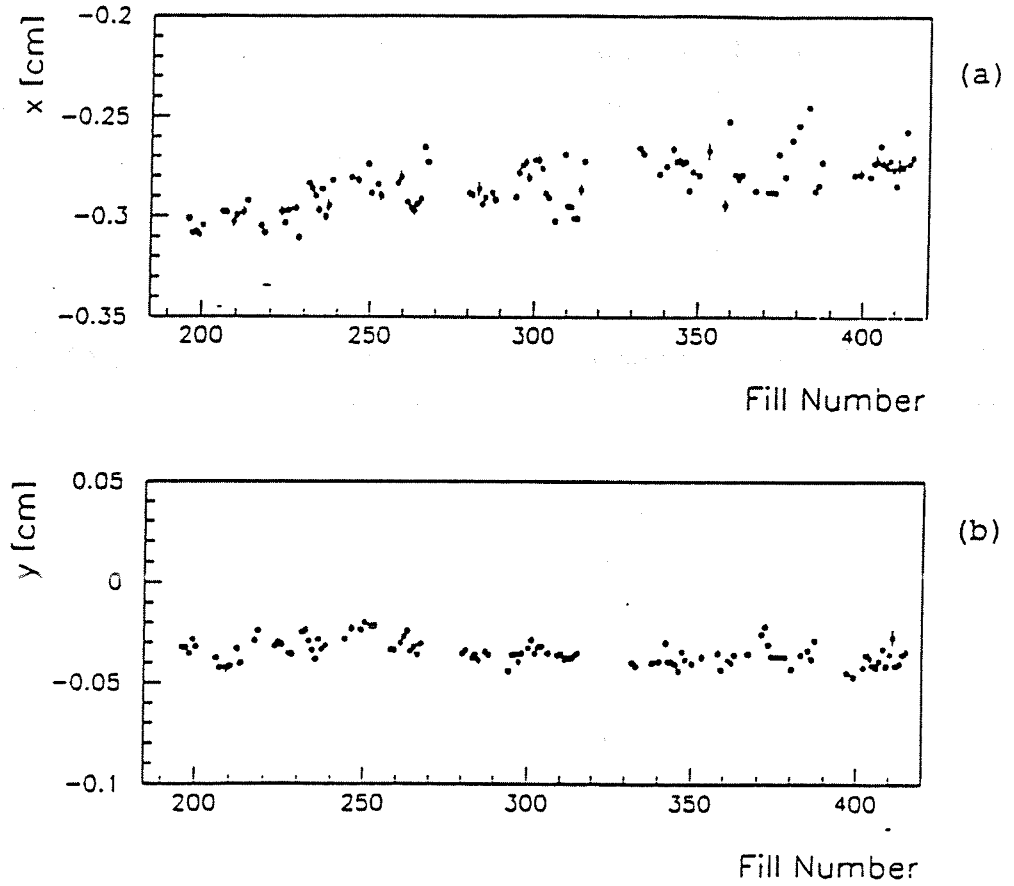

Figure 5.7: Average beam position as a function of the LEP fill number, determined by reconstructing the event vertices. (a) for x and (b) for y. Only the larger error bars are visible.

With this provision, the vertex cut normally used in this analysis is:

$$R_{min} < 1.5 \text{ cm} \qquad \textbf{And} \qquad |Z_{min}| < 4.5 \text{ cm}$$

No event loss due to the vertex cut is expected in view of its conservative definition.

5.5.6 Muon Identification

In this analysis the information from muon chambers, electromagnetic calorimeters and hadron calorimeters is used to identify the muons. The identification criteria are described in this section, while the efficiencies are discussed in section 5.8.

Identification From the Muon Chambers

For the identification based on muon chambers data, the general idea is to match space points reconstructed in the muon chambers with the tracks seen by the central tracking detectors of DELPHI. This is done by extrapolating muon candidate tracks through the electromagnetic and hadron calorimeters towards the planes of the muon chambers, taking into account energy loss and the propagation of measurement errors on the track. The predicted impact points are then combined in the EMMASS routine[60] with the hit points found in the muon chambers by the DELANA detector specific modules MUBANA and MUFANA (see chapter 3 about DELANA and MUB(F)ANA), taking into account the full error matrix on the predicted hit and the detector measurement errors on the measured hit. For dimuon events a high identification efficiency can be achieved by merely requiring at least one hit close to the track.

The muon identification is performed in the following way.

1) There is a loop over all the tracks (TKR's) that are extrapolated to the muon chambers and all the space points (TE's) of the muon chambers are associated to each of these tracks within a region defined by:

$$R = \left(\frac{T1_{\mathrm{ex}} - T1_{\mathrm{muc}}}{\delta T1_{\mathrm{ex}}}\right)^2 + \left(\frac{T2_{\mathrm{ex}} - T2_{\mathrm{muc}}}{\delta T2_{\mathrm{ex}}}\right)^2 \qquad (5.7)$$

with

$$R < 50 \text{ (for MUB)}$$
$$R < 200 \text{ (for MUF)}$$

where the coordinates T1 and T2 denote $R\phi$ and Z in the barrel region and X and Y in the end-cap region. The subscript 'ex' refers to the extrapolation and the 'muc' refers to the muon chambers measured space points. The errors $\delta T1_{ex}$ and $\delta T2_{ex}$ on the extrapolated point are given by the extrapolation package used in DELANA. For 45 GeV muons, δT_{ex} is of the order of 7 mm for MUB and 7 mm ($\theta \sim 25^o$) to 20 mm ($\theta \sim 42^o$) for MUF.

2) Only the space points that have the best match with the extrapolated track are retained. The best match is defined in terms of the lowest χ^2 per degree of freedom. The χ^2 and the fitting method are described in ref. [60]. If the $(\chi^2/\ d.f.) > 100$ one layer is dropped, the fitting procedure is performed again. If no improvement is obtained another layer is dropped and the procedure is reiterated. The best of the previous results is kept if no more layers can be dropped.

If at least one space point is found in the region R, the track is identified as coming from a muon by the muon chambers.

Following this procedure, the level of 'noise' hits in the chambers is found to be totally negligible (see ref. [60]).

Identification by Electromagnetic Calorimeters (EMCAL)

In the High Density Projection Chamber (HPC) and the Forward Electromagnetic Calorimeter (FEMC), the identification of muons is based on the energy deposited in the calorimeters by the particle. Due to bremsstrahlung and pair-production processes the high energy electrons will lead to the production of electromagnetic showers in the electromagnetic calorimeters. The minimum ionising particles can be distinguished from those electrons in the electromagnetic calorimeters by their comparatively small energy deposition.

At the track entry point in the HPC a cone like solid angle, with half opening angle with respect to the track direction of 10^o in θ and 20^o in ϕ, is defined. Fig. 5.8 (a) shows the energy deposited in this angular region for those events which passed all the muon selection cuts except the identification by the muon chambers, EMCAL or

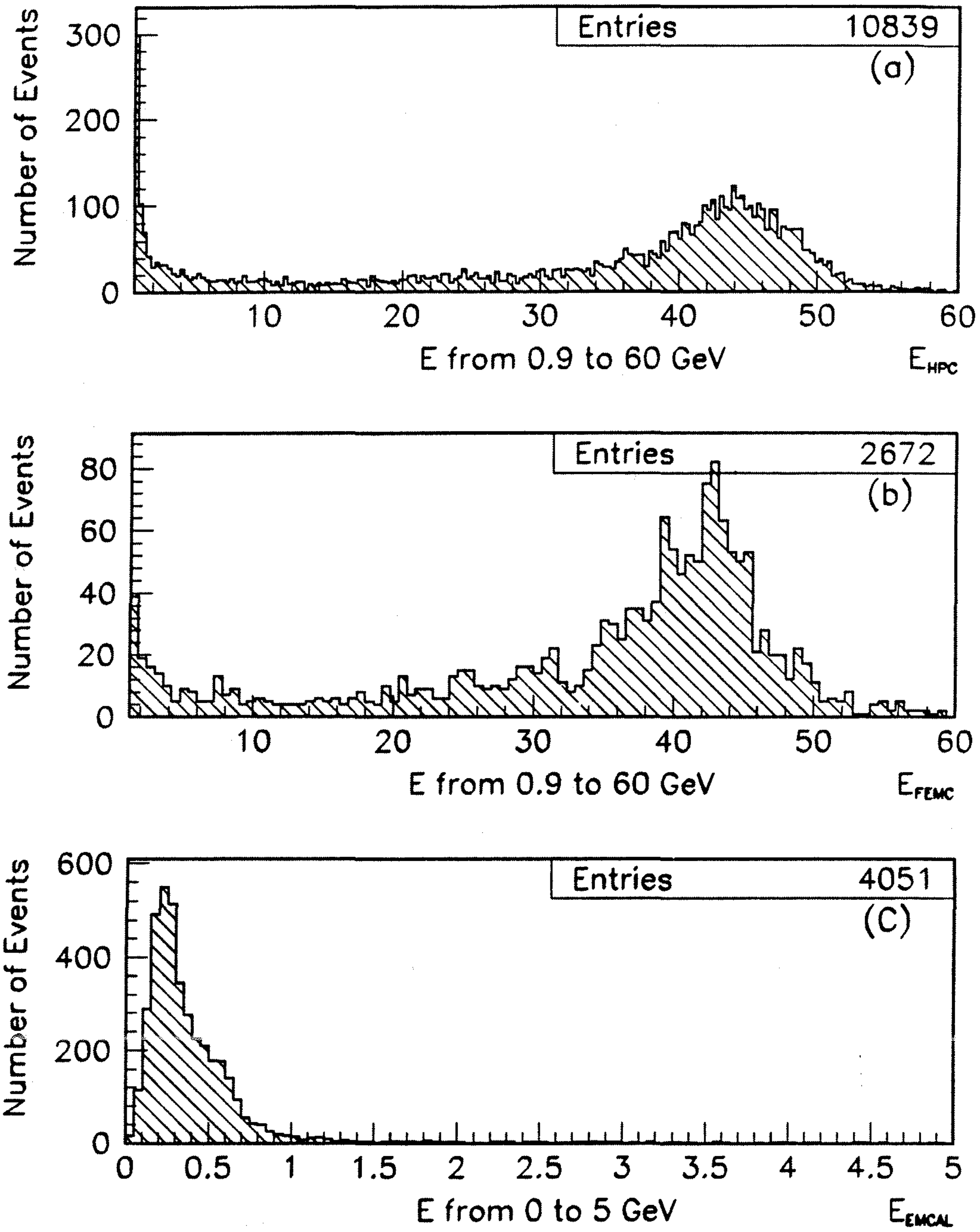

Figure 5.8: Deposited energy E_{EMCAL} in the electromagnetic calorimeters by particles from leptonic events; (a) In the HPC (b)In the FEMC (c) In both the HPC or the FEMC for 'clean muon' events (see text). Notice that the figures only show the events with E_{EMCAL} greater than 0.9 GeV for (a), (b). The noise at E_{EMCAL}=0 is removed from (c).

HCAL. The energy deposition in the FEMC situated in the forward region is presented in fig. 5.8 (b). Fig. 5.8 (c) shows the energy deposition in the HPC or FEMC of the 'clean muon' events which passed all the muon selection cuts, the particles being identified as muons by the muon chambers. In addition, they are required to satisfy the tightened cuts, which are: the momentum of each of the two highest momentum particles is greater than 25 GeV/c and the acollinearity angle is less than 1°. In both electromagnetic calorimeters the muons from $\mu^+\mu^-$ events deposit an energy $E_{EMCAL} < 1$ GeV where $E_{EMCAL} \simeq 40$ GeV for e^+e^- final states. The intermediate region is mostly populated by $\tau^+\tau^-$ events.

Fig. 5.8 shows that almost no 'clean muon' deposit an energy greater than 1 GeV and that only a small fraction of 'non muon' events, such as electrons or the tau decay products, could possibly deposit energies below that value.

In conclusion, we classify tracks as coming from muons in the electromagnetic calorimeters HPC and FEMC if:

$$E_{EMCAL} < 1.0 \text{ GeV}$$

Identification by Hadron Calorimeters (HCAL)

Muons can pass through all the iron of the hadron calorimeters, depositing small amounts of energy in all four layers. Hadrons, on the contrary, will have strong interactions with the iron of the hadron calorimeters and should deposit most of their energy in the first two layers. If some electrons passed through the electromagnetic calorimeter, the shower should mainly be contained in the first two layers as well.

Fig. 5.9 shows the total deposited energy E_{dep} in all four layers in HCAL as a function of θ. Fig. 5.9 (a) (b) are related to those 'clean muon' events which satisfy all the muon selection cuts and the particles are identified as muons by the muon chambers and where, in addition:

$$P_1 > 25 \text{ GeV/c}; \qquad P_2 > 25 \text{ GeV/c}; \qquad \theta_{acol} < 1^o.$$

The non linear distribution is due to the fact that the effective thickness of the iron as seen by the particles passing through the hadron calorimeters is θ-dependent. Figs. 5.9 (c) (d) are related to those 'non muon' events which are not identified as muons by the muon chambers, $\theta_{acol} > 1^o$ and are not in the region $42^o < \theta < 52^o$ or $128^o < \theta < 138^o$ (not covered by muon chambers).

Fig. 5.10 (a) (b) show that in the barrel region the distribution of $\mathrm{E}\sin^2\theta$ is less θ-dependent for the 'clean muon' sample. Fig. 5.10 (c) (d) show the same distribution for the 'non muon' sample.

The total number, NLAY, of the layers in which particles from leptonic events deposit energy is studied in fig. 5.11 for 'clean muon' and 'non muon' events respectively. NLAY is the sum of the number of layers in which $E_{ilay}\sin^2\theta < 6.0$ GeV; where E_{ilay} is the deposited energy in layer 'ilay' and θ is the polar angle of the track to which this energy was associated by DELANA.

Fig. 5.11 (a) presents the plot of NLAY as a function of θ for the 'clean muon' events and fig. 5.11 (c) shows the same distribution, but related to those 'non muon' events which are neither identified as muons by the muon chambers nor by EMCAL in the muon chamber hole region, $42^o < \theta < 52^o$ or $128^o < \theta < 138^o$. Fig. 5.11 shows that for the most of the 'muon events' NLAY is greater than 2, independent of the value of θ.

Consequently, particles traversing HCAL will be identified as muon candidates if:

$$\mathrm{NLAY} \geq 2$$

AND

$$E_{cut} = E_{HCAL} \times \sin^2\theta < 10 \text{ GeV} \qquad (55^o < \theta < 125^o)$$

$$E_{cut} = E_{HCAL} < 15 \text{ GeV} \qquad (\text{if } \theta \leq 55^o \text{ or } \theta \geq 125^o)$$

where E_{HCAL} is the total deposited energy in HCAL.

The muon identification, whose efficiency and background effects will be examined in section 5.8 and section 5.10 respectively.

5.5.7 Tau Veto

Those events in which the acolinearity angle between the tracks of the two highest momentum particles of leptonic events is greater than 1^o and the deposited energy in HCAL is greater than E_{cut} will be cut as tau background. The E_{cut} is defined as above (in section 5.5.6).

The efficiency of the tau veto will be examined in section 5.9 and the background effects will be examined in section 5.10.

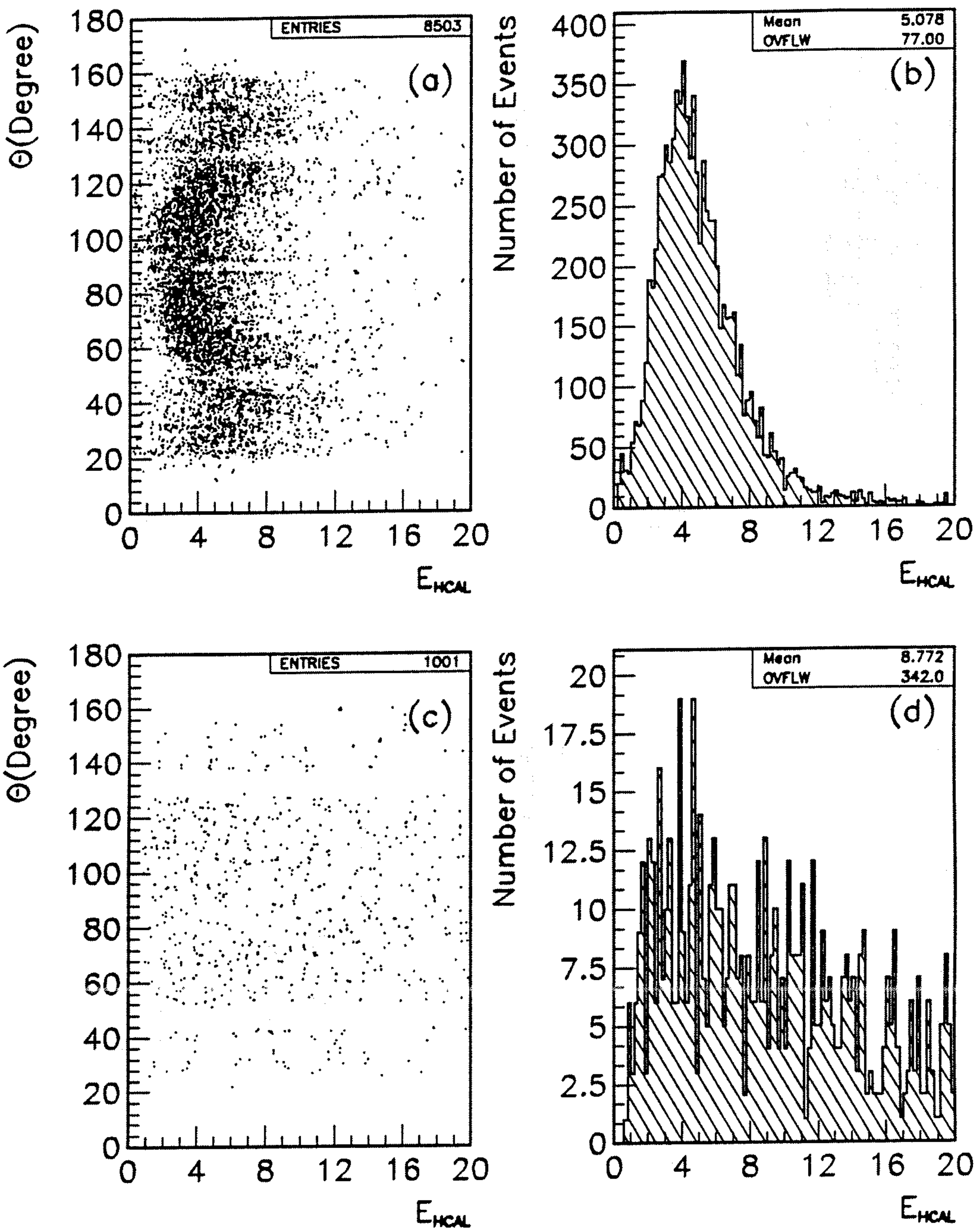

Figure 5.9: Total deposited energy E_{HCAL} [GeV] in Hadron Calorimeters: (a)(b) for 'clean muon' and (c) (d) for 'non muon' events (see text). Figures (a) (c) show θ vs E_{HCAL}; (b) (d) show the projections of (a) and (c) on the E_{HCAL} axis.

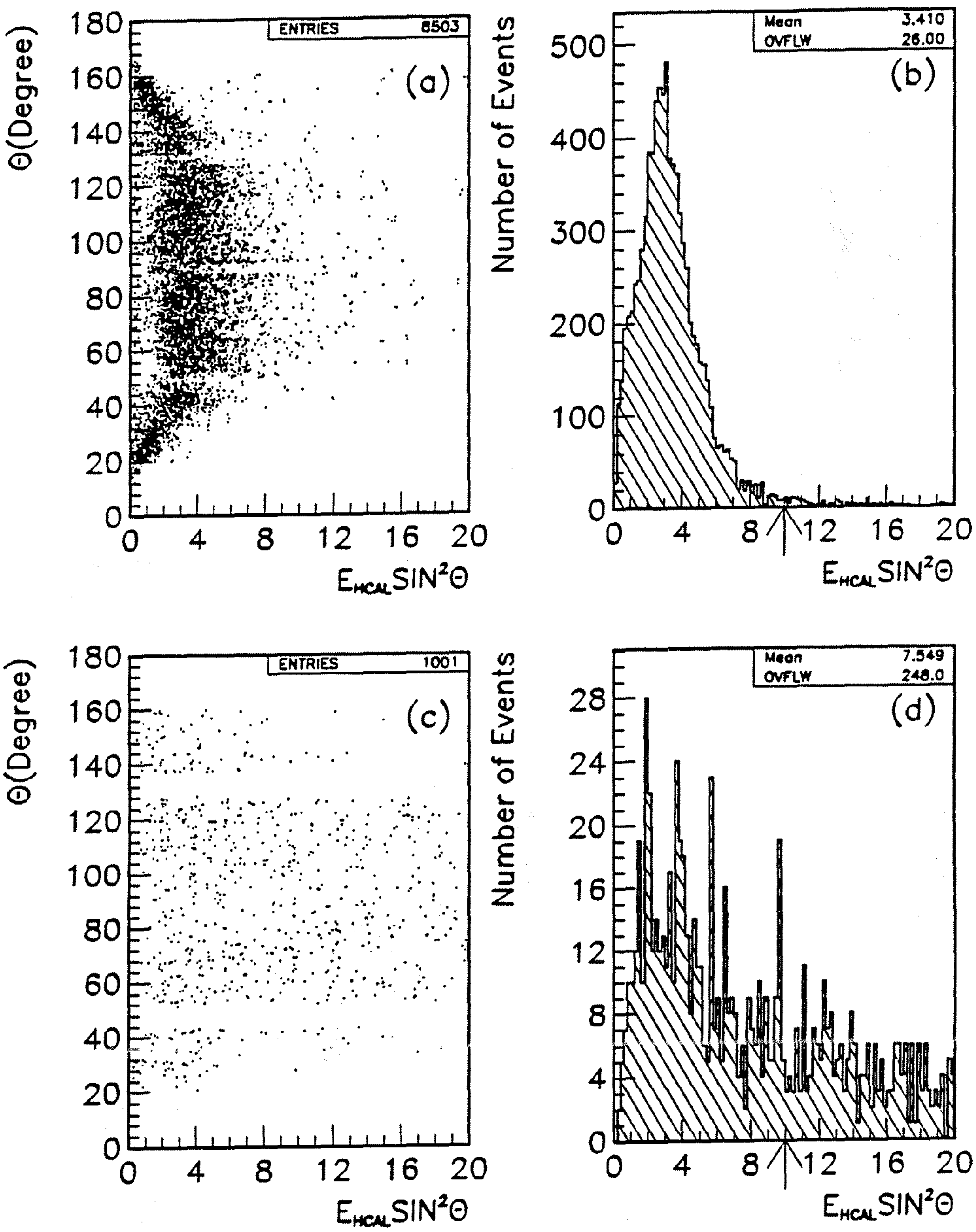

Figure 5.10: $E^* = E_{HCAL}\sin^2\theta$ in Hadron Calorimeters: (a)(b) for 'clean muon' and (c)(d) for 'non muon' events (see text); figure (a)(c) show θ versus E^* and (b)(d) show projections of (a) and (c) on the E^* axis.

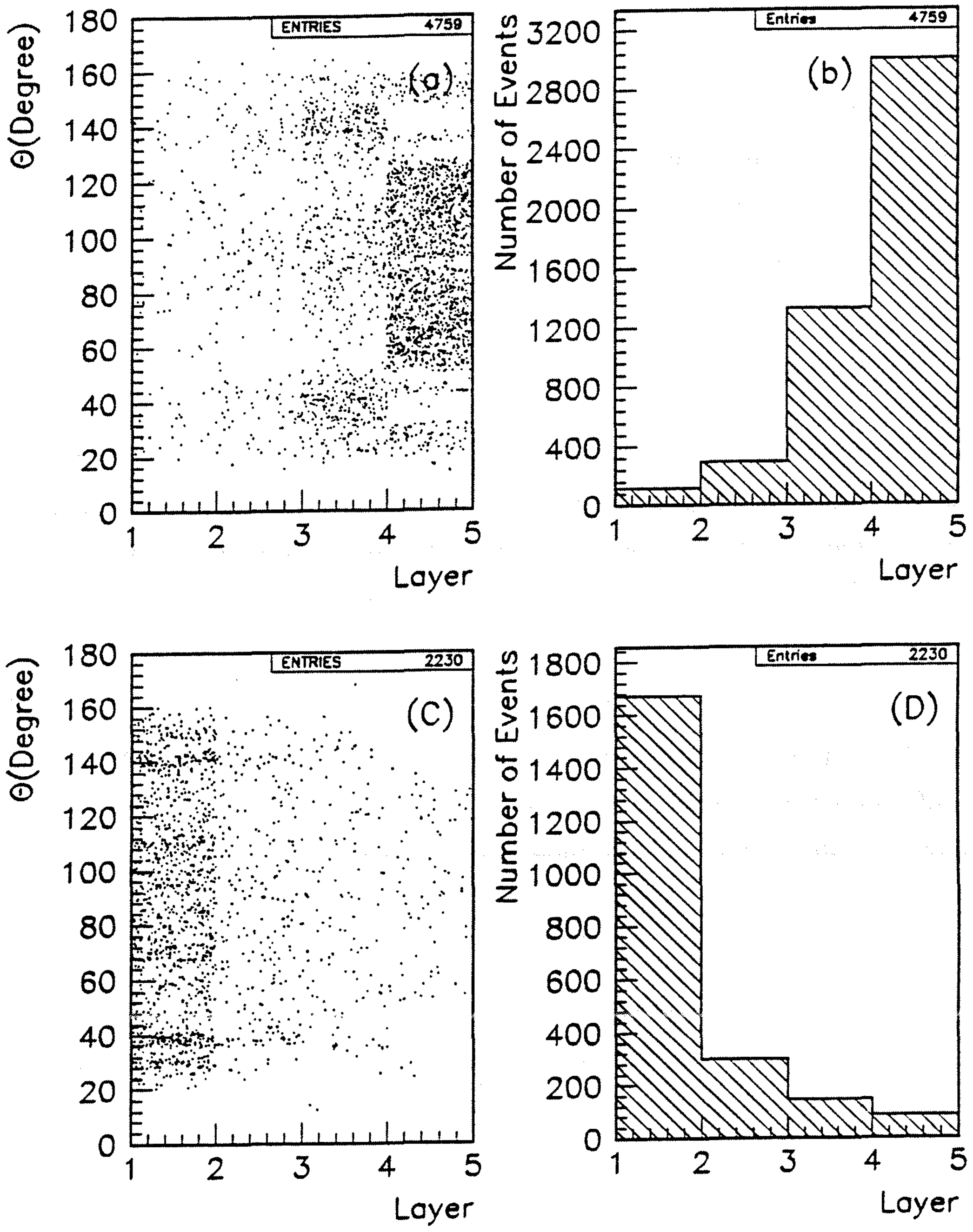

Figure 5.11: NLAY distribution in Hadron Calorimeters vs θ: (a) for 'clean muon' events; (b) projection of (a) on NLAY axis; (c) for 'non muon' events; (d) projection of (c) on NLAY axis.

5.5.8 Polar Angle Acceptance

The event is accepted if the polar angle of the negative charged particle from the two highest momentum particles is in the acceptance region of:

$$20^o \leq \theta \leq 160^o.$$

The correction to the total $\mu^+\mu^-$ cross section for this polar angle acceptance, together with the acollinearity and momentum cut for the two highest momentum particles is obtained from the ZFITTER[61] program (see section 5.11 in which electroweak radiative corrections are calculated).

5.6 Trigger Efficiency

In this analysis, the calculation of the trigger efficiency is based on the fact that there are at least two independent triggers in the same polar angle θ region. The data sample used here consists of events considered to be di-muon candidates in this analysis. The definition of the efficiencies of those triggers are given as the following:

$$\epsilon_1 = \frac{N_{12}}{N_2}; \qquad \epsilon_2 = \frac{N_{12}}{N_1} \tag{5.8}$$

where N_{12} is the number of events that fired both triggers, N_1 and N_2 are those number of events that fired at least trigger 1 and at least trigger 2 respectively.

The overall efficiency of the two independent triggers is :

$$\epsilon = \epsilon_1 + \epsilon_2 - \epsilon_1 \times \epsilon_2 \tag{5.9}$$

Fig. 5.12 shows each muon subtrigger efficiency respectively, averaged over the whole year 1990 (For more information concerning trigger definition see also sections 3.8.2 and 5.2). Fig. 5.13 presents the average muon trigger efficiencies for the data taken in the year 1990 subdivided in three periods determined by DELPHI run number.

During 1990, the DELPHI trigger was gradually improved. Therefore it is indeed difficult to use one trigger efficiency for the whole year. Three periods were distinguished for the year 1990 in order to get a more precise correction factor. In the third period the DELPHI muon trigger was flat in almost the whole θ angle region and reached a very high value (> 0.9992). The trigger efficiencies in these three periods are shown in table 5.2.

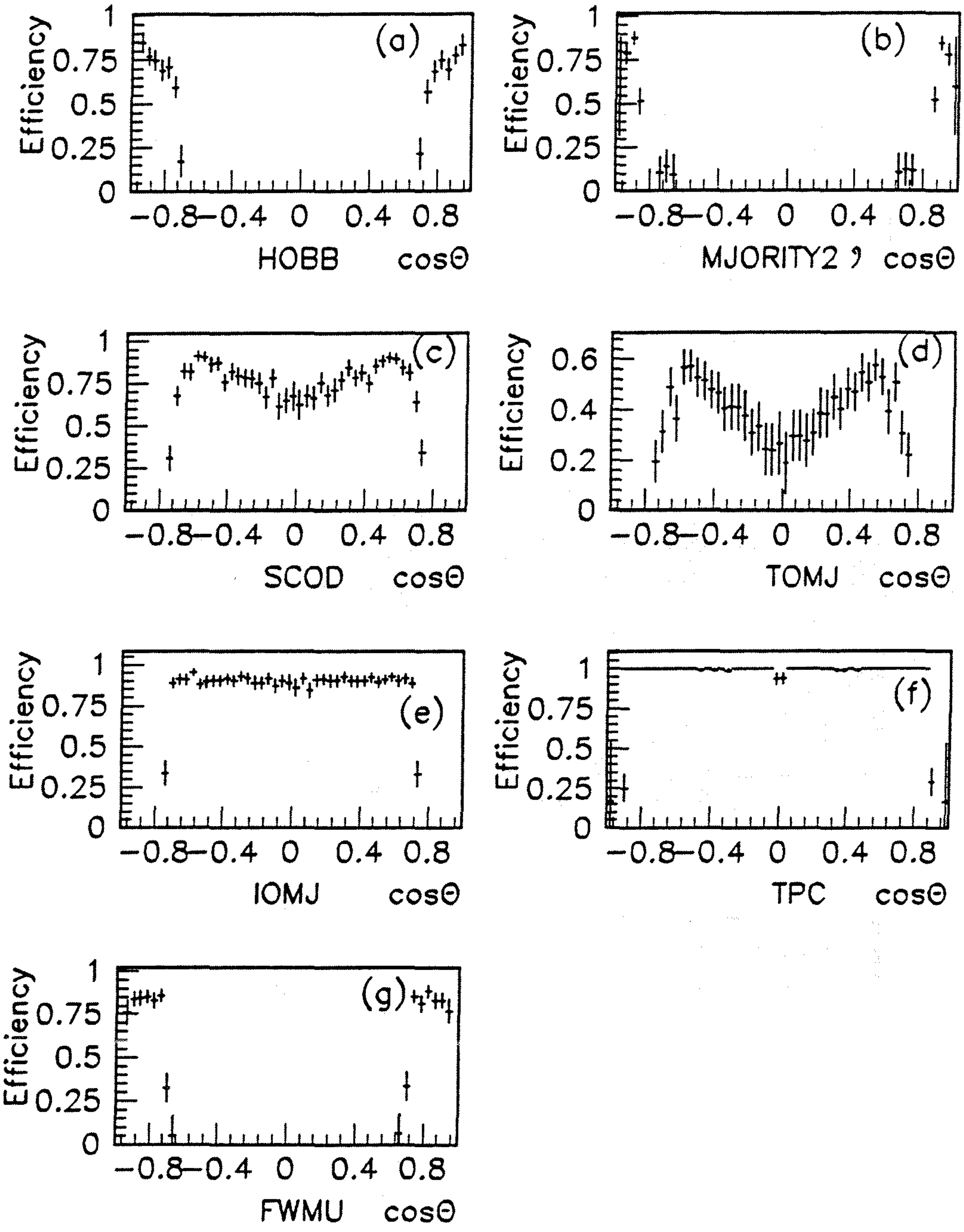

Figure 5.12: Distributions of all the muon subtriggers (defined in Section 5.2); (a) HOBB; (b) majority 2 without HOF; (c)SCOD; (d) TOMJ; (e) IOMJ; (f) TPC; (g) FWMU.

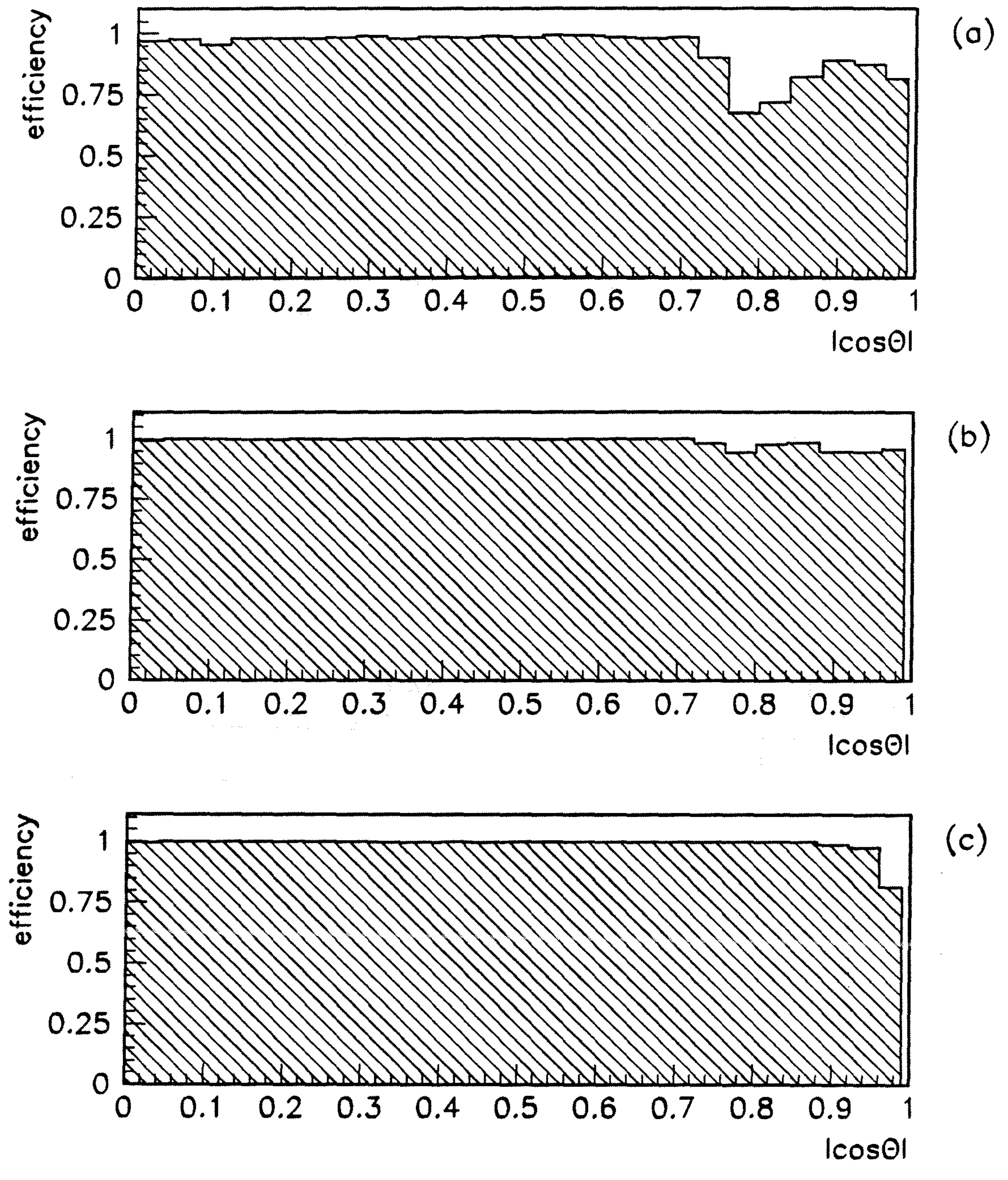

Figure 5.13: The average trigger efficiency of the three different periods. (a) DELPHI run ♯ ≤ 10265; (b) 10266 ≤ DELPHI run ♯ ≤13829; (c)13830 ≤ DELPHI run ♯ ≤15829.

LEP Fill	$185 \leq$ Fill ≤ 294	294< Fill≤ 357	357 < Fill ≤ 415
DELPHI RUN #	7495≤ RUN# ≤10265	10265< RUN# ≤13828	13828 ≤RUN# ≤15829
EFFICIENCY	0.909±0.009	0.989±0.004	0.9992±0.0006

Table 5.2: Trigger efficiencies for three separate periods.

5.7 Track Reconstruction Efficiency

The track reconstruction efficiency is degraded by two kind of sources: the dead space and the working condition of the tracking chambers. They are studied in the following two subsections.

The predominant parts of the dead space are: the gaps in ϕ between the six 60^o read-out sectors of the TPC and the plate between the two halves of the TPC at $Z = 0$ or $\theta = 90^o$.

5.7.1 Geometrical Efficiencies

Fig. 5.14 shows the ϕ distribution for the muon candidates. The holes due to the TPC dead space and the suspension crosses of the forward muon chamber quadrants are clearly visible. One can still see tracks in the 'dead' TPC tracking space as the trajectory of a particle emitted in the dead space can be sufficiently curved to leave it further downstream, or the track can be determined by using tracking information obtained from other detectors such as ID, OD, FCA, or FCB. Possible correction of the tracking efficiency in the dead space, with other effects seen in the data are implicitly taken into account by calculating an overall efficiency factor, called ϵ_{cor} which will be discussed in section 5.9.

5.7.2 Tracking Chamber Efficiencies

Outside dead space, the track reconstruction efficiency ϵ_{2TK} related to the working condition of the tracking chambers can be calculated by using the number of observed one track candidate events (N_{1TK}) compared to the number of two tracks candidate events (N_{2TK}) with two highest momentum tracks in opposite direction in θ and ϕ.

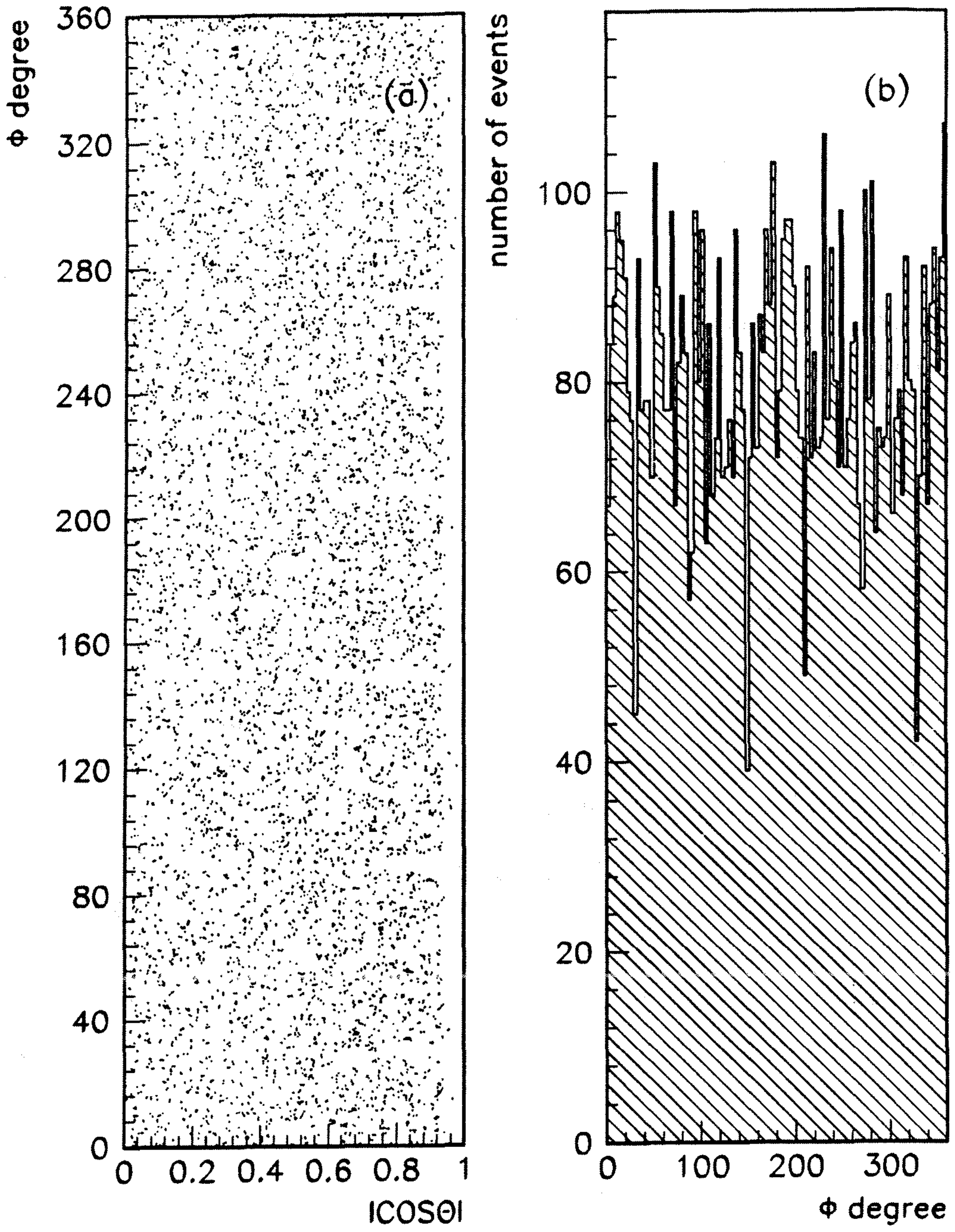

Figure 5.14: The ϕ distribution of muon candidates.

This is easily quantified as:

$$\epsilon_{2TK} = \frac{N_{2TK}}{N_{2TK} + N_{1TK}} \tag{5.10}$$

The analysis of this thesis is based on the use of 2 TK events. The 1 TK events are only used to establish the 2 TK efficiency. To avoid spurious events from 1 TK, which are mainly contamination background coming from electronic noise, beam gas, beam pipe wall events, etc., only events which satisfy the following conditions are accepted as 1 TK candidates:

- The particle momentum as measured from the TK is greater than 15 GeV/c.
- On the "no track" side, the radius of curvature R' in the x,y plane of the particle producing no identified track is determined by the following three points: the point from the TE(see 3.9.1) on the no track side which is the furthest away from the beam spot and situated in an angular region opposite to the track, the end point of the TK on the track side, and the beam spot. The angular region is determined as the follows: ± 10^o in θ and ± 20^o in ϕ relative to the opposite direction of the track. The momentum of the particle is computed from the radius of curvature R' and the polar angle of the reconstructed TK and is required to be greater than 10 GeV/c.
- The angle between the tangent of the TK at the beam spot and the line determined by connecting the point of the furthest TE of the non reconstructed track and the beam spot is less than 10^o.
- Both particles should be identified as muons in one of the muon identification subdetectors (Muon chambers, HCAL, EMCAL)

Fig. 5.15 shows the relation between the measured momentum of the reconstructed track and the momentum determined by the radius of the circle computed from the 3 points on these tracks for the above-defined 2 track events which are identified as muons by this analysis. In most cases good agreement is achieved between the two methods, but large deviations can exceptionally occur.

The 0 TK efficiency is found to be negligible ($\sim 3.6\times10^{-6}$).

The track reconstruction efficiency ϵ_{2TK} is found to be:

$$\epsilon_{2TK} = 0.9962 \pm 0.0009$$

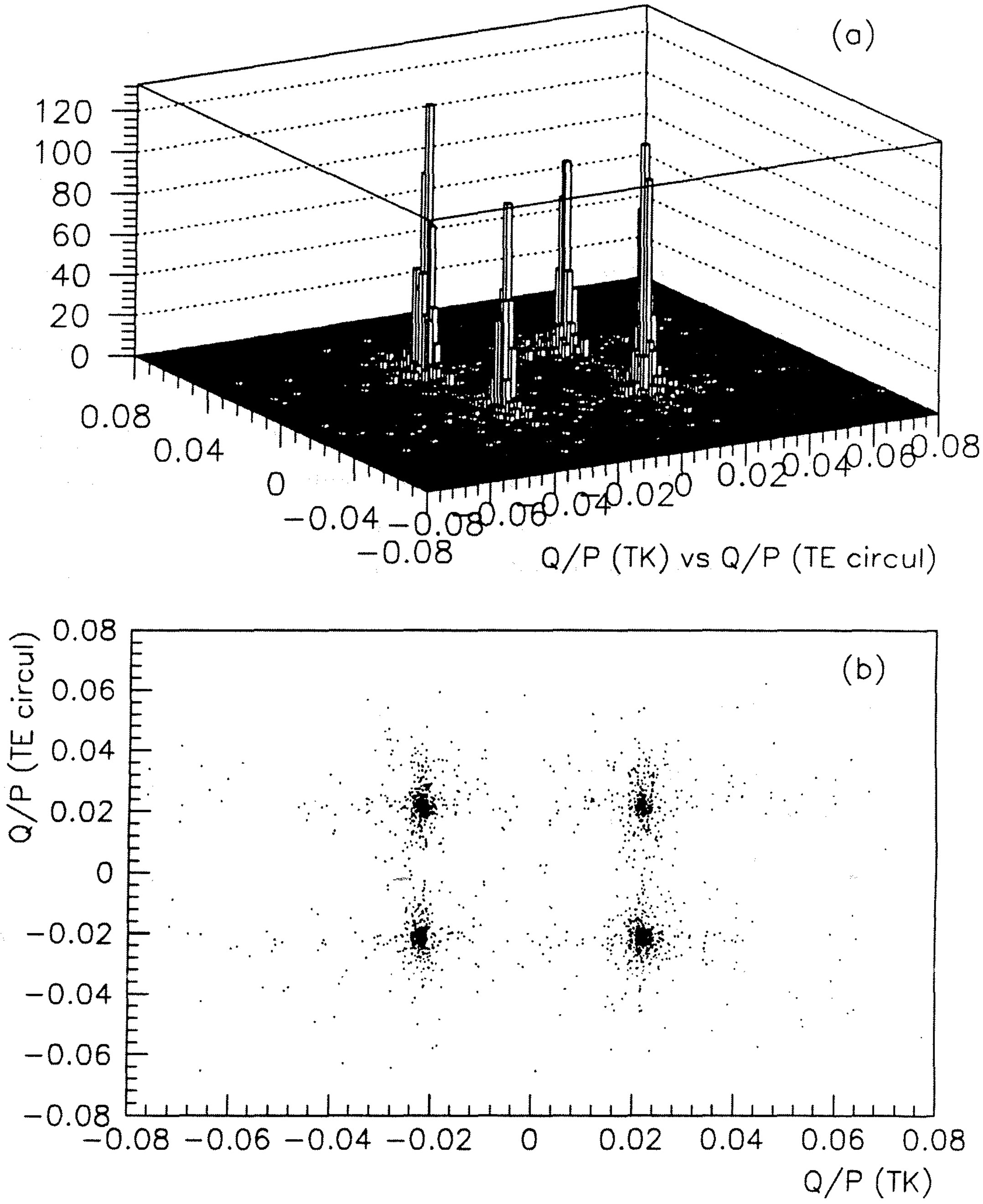

Figure 5.15: The relation between the inverse momentum multiplied by the measured charge from track and the inverse momentum multiplied by the measured charge obtained from the calculated circle: (a) lego plot; (b)histogram plot.

5.8 Muon Identification Efficiencies

In this section the muon identification efficiencies of each subdetector, i.e. muon chambers, hadron calorimeters and electromagnetic calorimeters, will be studied. The overall muon identification efficiency of these three subdetectors is studied as well.

In order to get the correct muon identification efficiency, a clean dimuon sample is selected by the following restrictive cuts, mainly to diminish the influence from the τ background:

- All the standard cuts
- Minimum momentum of each of the two highest momentum charged particles is greater than 25 GeV/c.
- The acollinearity angle is less than 1^o.

The way to calculate the muon identification efficiency of one of the subdetectors is as follows: among the three "muon identification" subdetectors A, B, C , if either A or B or both identifies the particles as muons, the subdetector C can give one of the following responses:

- N_{yes} : the number of such particles which are identified as muons by subdetector C
- N_{no} : the number of such particles which are not identified as muons by subdetector C

The muon identification efficiency of the subdetector C is defined by the following expression:

$$\epsilon_{\mu id} = \frac{N_{yes}}{N_{yes} + N_{no}} \tag{5.11}$$

Fig. 5.16 shows the muon identification efficiencies as a function of cosθ for EMCAL, HCAL, and MUC (MUB or MUF) respectively.

Fig. 5.17 shows the logical "OR" of these three efficiencies which is almost equal to 1 at all polar angles.

The total muon identification efficiency using the three subdetectors is:

$\epsilon_{\mu id} = 0.9943 \pm 0.0012$

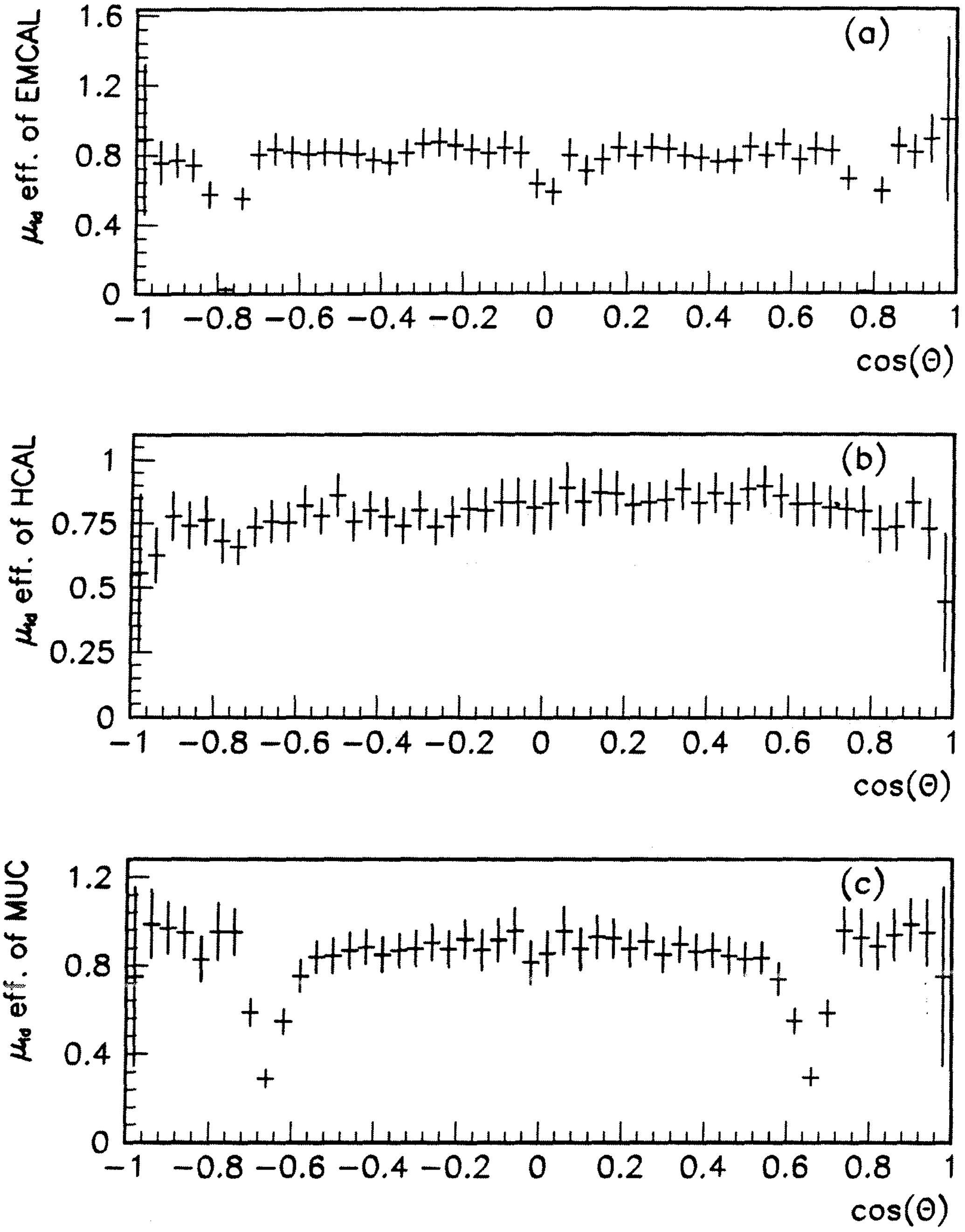

Figure 5.16: The muon identification efficiencies for EMCAL, HCAL and MUC.

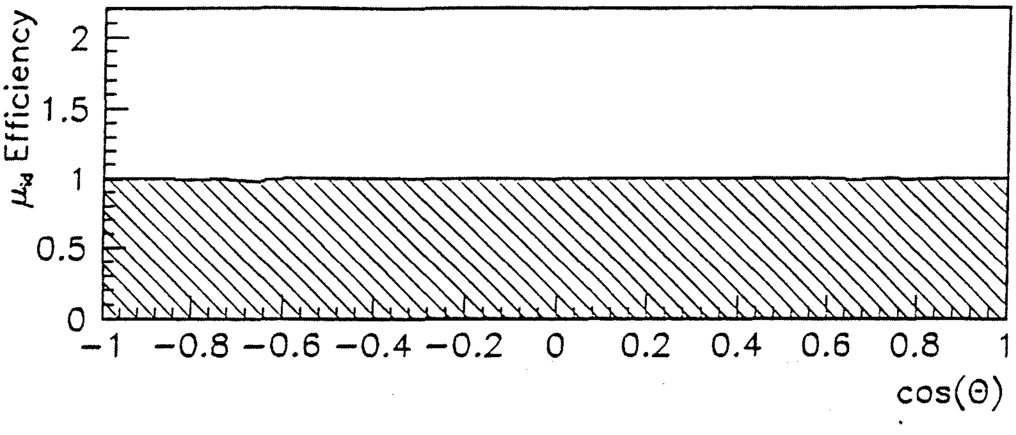

Figure 5.17: Logical "OR" of EMCAL, HCAL, MUC muon identification efficiencies.

5.9 Combined Efficiencies

The efficiencies related to the "total number of track" cut and to the cut on "the total number of tracks greater than two" events should also be accounted for. Moreover, the following factors can introduce a loss of muon events: the non-muon event background veto (see sections 5.10.1 and 5.5.7), the tracking reconstruction in the dead space of the tracking chamber and the muon loss in the forward muon chambers cross, etc., the latter being clearly correlated. An overall efficiency factor ϵ_{cor} for all these combined effects has been calculated using a sample of 9224 simulated dimuon events, of which 481 are eliminated by the above cuts.

This efficiency is thus found to be:

$$\epsilon_{cor} = 0.9479 \pm 0.0023$$

The estimate of the number of muon events lost due to the two highest particle momentum cut, the acollinearity cut and the θ angle acceptance has been implemented in the ZFITTER program. This efficiency called ϵ_{pac} takes radiative corrections of the Z^0 decay into consideration. It is:

$$\epsilon_{pac} = 0.8840 \pm 0.0051 \text{ for } \sqrt{s} = 91.21 \text{ GeV}.$$

5.10 Backgrounds

Most of the e^+e^- and $\tau^+\tau^-$ background is removed from the muon candidates by applying all the cuts described above. Two additional background vetoes are introduced and will be described in the following subsections in which the cosmic background is also studied.

5.10.1 Electron Background

Those events for which the energy deposited in the HPC or the FEMC by each of the two highest momentum particles is greater than 10 GeV are considered to be non-muon background events and are removed.(see fig. 5.8).

The following cuts are applied to leptonic events in order to select e^+e^- final states and to evaluate the remaining e^+e^- background in the muon-pair sample :

- $1 < N_{TK} < 6$
- The momenta of the two highest momentum particles are greater than 25 GeV/c.
- The acolinearity angle is less than 1°.
- The deposited energies of these two particles in the electromagnetic calorimeters should both be greater than 25 GeV.

After these cuts, a clean e^+e^- sample of 1991 events is selected. Amongst these events, no one is misidentified as a muon by the other two muon identification subdetectors. So, at a 95% confidence level, the possibility that the muon chambers and hadron calorimeters misidentify an electron as a muon is 0.15%.

The possibility of misidentification of the electron as a muon by the muon identification subdetectors is also investigated in the following way:

On events with two back-to-back tracks, the following cuts are applied to define a second clean e^+e^- sample:

- The momentum of each of the two highest momentum particles is greater than 25 GeV/c.
- The acolinearity angle is less than 1°.
- on the $Z > 0$ side the deposited energy of the particle in the electromagnetic calorimeters is greater than 40 GeV.

In the $Z < 0$ hemisphere, the possibility for the second track particle to be misidentified as a muon is then studied.

Among 1574 selected e^+e^- events, 20 tracks in the Z $<$ 0 hemisphere are misidentified by the muon identification subdetectors (2 by the muon chambers, 13 by the hadron calorimeters and 7 by the electromagnetic calorimeters). One should notice that there is some overlap in the misidentification between the three kinds of subdetectors. This gives the maximum single particle misidentification rate in the Z $<$ 0 hemisphere P_2=(1.27 ± 0.28)%, if all of these 1574 events are electrons.

Applying the same procedure to the Z $<$ 0 hemisphere, 1609 e^+e^- events are selected of which 18 tracks are misidentified by the muon identification subdetectors on the Z $>$ 0 side (12 by the hadron calorimeters and 6 by the electromagnetic calorimeters). This gives the maximum single particle misidentification rate in the Z $>$ 0 hemisphere P_1=(1.12± 0.26)%, if all these 1609 events are electrons.

Therefore the maximum misidentification rate for an electron pair as a muon pair is:

$$P=(0.014\pm 0.005)\%.$$

The e^+e^- background will hence be neglected for the purpose of this analysis.

5.10.2 Tau Background

The remaining τ background after the τ veto cut is studied by using the simulated τ events. From 9000 simulated $\tau^+\tau^-$ events, 141 events passed all the muon identification cuts and all background vetoes. After normalisation of the number of simulated $\tau^+\tau^-$ to the simulated $\mu^+\mu^-$, the τ background is found to be:

$$(1.76\pm 0.14)\%.$$

5.10.3 Cosmic Background

A large fraction of the cosmic ray background can be removed by timing measurements using the Outer Detector (OD) (see chapter 3). If the muons come from the Z^0 decay, one expects that the time difference between the two muons is 0± 1.9 nsec. However, if the muon is of cosmic origin, the time difference will be about 10 ± 1.9 nsec.

A total of 42 cosmic rays are removed from the sample of 4044 $\mu^+\mu-$ events by the timing measurements.

The remaining contamination by cosmic events is studied in the following way:

One notices that the cosmic flux density is same inside and outside the vertex region (see fig. 5.6). If the events passed all the muon identification cuts and lie in the expanded vertex region (see below) excluding the original vertex region, they are considered to be cosmic background events. The number of cosmic background events in the original vertex region can be estimated by comparing the ratio between the surface of the original and the expanded vertex region and the number of cosmic background events in both regions.

The cosmic muon density is defined as follows:

$$Density_{cosmic} = N_{exp}/S_{exp} \tag{5.12}$$

where the N_{exp} and S_{exp} are the number of cosmic background events and the surface of the expanded vertex region respectively (see fig. 5.6.(b) and 5.18)).

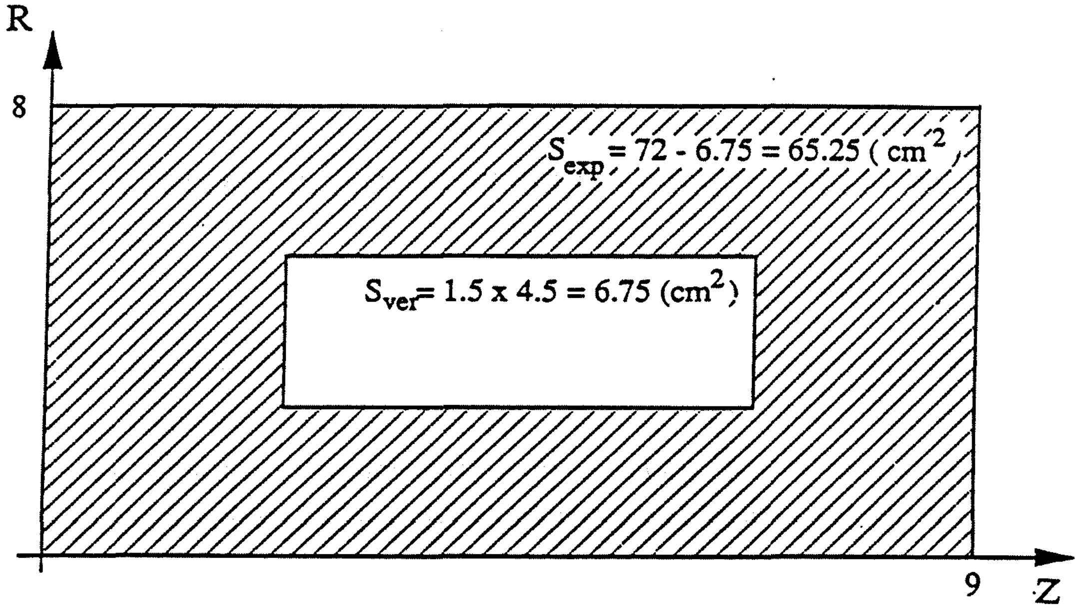

Figure 5.18: Schematic display of S_{exp} and S_{ver}.

Before the cosmic veto, expanding the vertex region from R_{min} < 1.5 cm and $|Z_{min}|$ < 4.5 cm to R_{min} < 8.0 cm and $|Z_{min}|$ < 9.0 cm, N_{exp} = 812 and S_{exp}=65.25 cm^2 (see fig. 5.18) are found. This gives a $Density_{cosmic}$=12.44 cm^{-2}. Using the surface of the vertex region, which is 6.75 cm^2, 84 cosmic background events are estimated to contribute to this region. Considering that 42 cosmic muon background events were removed by using the OD timing information, as explained above, there are 42 remained cosmic muon background events in the original vertex region, which corresponds to (1.05 ± 0.16)% of the total muon sample.

5.10.4 Other Backgrounds

All other sources of background, such as the background from beam gas interactions, beam wall interactions, are expected to be negligible. The background coming from $e^+e^- \rightarrow Z^0 \rightarrow q\bar{q}$ is also expected to be negligible from Monte Carlo simulation studies.

5.11 Summary and Corrected Event Numbers

In total 4002 $\mu^+\mu^-$ events collected during the 1990 runs are selected. Their distribution over the seven different e^+e^- centre-of-mass energies is given in the second column of table 5.3.

$\sqrt{s}$ (GeV)	$\mu^+\mu^-$ Events Detected	Corrected Number of Events ($20^o \leq \theta \leq 160^o$) statistical errors only	Total Corrected Number of Events over 4π statistical errors only
88.222	59	60.2 ± 8.0	71.0 ± 9.4
89.216	147	153.7 ± 12.8	181.3 ± 15.1
90.217	315	343.2 ± 19.3	395.8 ± 22.2
91.213	2871	3098.29 ± 63.19	3508.07 ± 71.55
92.208	290	308.2 ± 18.2	348.7 ± 20.7
93.211	180	190.3 ± 14.3	215.8 ± 16.2
94.203	140	146.5 ± 12.5	167.4 ± 14.3

Table 5.3: Number of Muon-pair candidate events at seven centre-of -mass energies

At each energy point, all events are corrected by the following factors based on the efficiencies determined in this chapter:

- 1.0057 ± 0.0012 for muon identification.
- 1.0038 ± 0.0009 for track reconstruction in the active space of the detector.
- 1.0291 ± 0.0025 for trigger efficiency averaged over the whole year.
- 1.0550 ± 0.0023 for the combined efficiency arising mainly from inefficiencies due to dead spaces of the detector.

- 1.1310± 0.0051 for the cut on the two highest momentum particles, the acollinearity and the polar angle acceptance.
- 0.9831± 0.0014 for the tau background.
- 0.9895± 0.0016 for the cosmic background.

For the trigger efficiency, the appropriate corrections for the different data taking periods have been used. Column 3 of table 5.3 displays the number of muon-pairs at seven different centre-of-mass energies after applying all above corrections except the correction for the cut on the two highest momentum particles, the acollinearity and the polar angle acceptance. The latter cuts are explicitly incorporated in the final analysis using the ZFITTER routine.

By combining all the efficiencies listed above, the systematic error on the numbers quoted in column 3 of table 5.3 is estimated to be 0.43% and on the numbers quoted in column 4 of table 5.3 is 0.66%.

Before extrapolating the results from the polar angle region $20^o \leq \theta \leq 160^o$ to 4π, a fit of the $|cos\theta|$ distribution to the function $1+cos^2\theta$ where θ is the polar angle of the μ^- particle is the best check on the validity of the angular distribution measured, as it is insensitive to the forward backward asymmetry.

One notices that the inefficiencies caused by dead spaces are localised in restricted ϕ regions (See fig. 5.14). A subsample is used to study the $|cos\theta|$ distribution which consists of those events in which both of the two highest momentum particle tracks fall in the following azimuthal 'acceptance region' (well outside the dead space from the TPC and the forward cross):

$$4^o < \phi < 26^o; \quad 34^o < \phi < 86^o; \quad 94^o < \phi < 146^o;$$
$$154^o < \phi < 206^o; \quad 214^o < \phi < 266^o; \quad 274^o < \phi < 326^o;$$
$$334^o < \phi < 356^o.$$

This technique removes the θ-dependent inefficiencics caused by dead spaces. Fig. 5.19 shows the distribution of $|cos\theta|$ after implementing all the correction factors except the cosmic and τ background corrections. Although they may be θ dependent as well, the contamination from the cosmic and τ background to the $|cos\theta|$ distribution is negligible for the present purpose. The data are found to be in good agreement (χ^2/n.d.f= 0.3432) with a $1+cos^2\theta$ distribution.

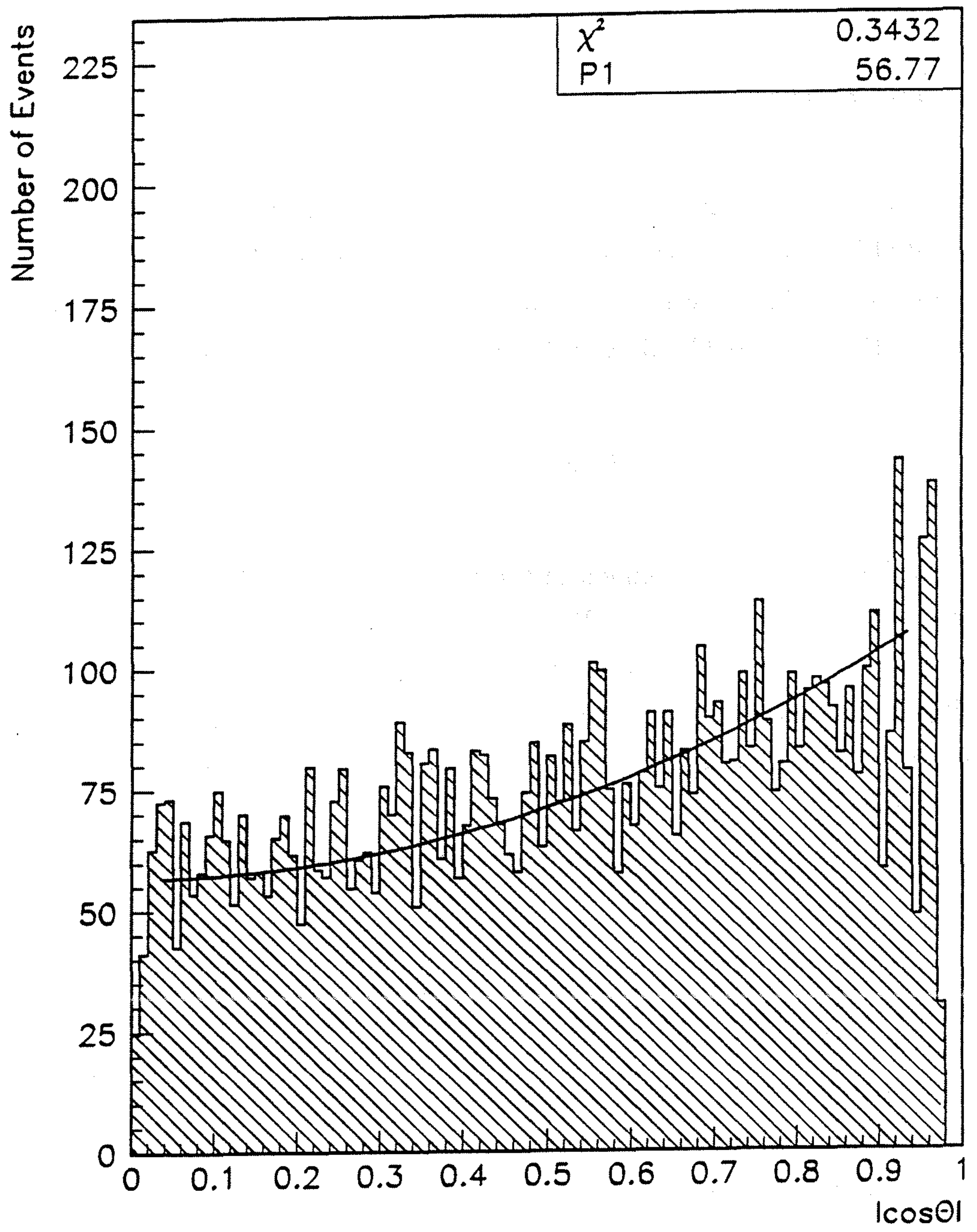

Figure 5.19: The distribution of | $cos\theta$ |, all the corrections having been applied, and result of a fit to a function P1(1 + $cos^2\theta$).

Column 4 of table 5.3 shows the number of muon-pairs at each beam energy after all the correction factors have been applied, including a $1+cos^2\theta$ extrapolation of the observed polar angle region.

5.12 Luminosity

Before calculating the muon cross section, it is necessary to determine the total time integrated luminosity. In this section, this problem is handled as follows:

The expected number of events N in a given reaction with production cross section σ, is related to the integrated luminosity $\int \mathcal{L}$dt and the total detection efficiency ϵ_{total}:

$$\int \mathcal{L}dt = \frac{N}{\sigma\epsilon_{total}} \tag{5.13}$$

In e^+e^- colliders, the measurement of the Bhabha($e^+e^- \rightarrow e^+e^-$) events at very small angles whose theoretically (QED) cross section is well known is the common method to determine the machine luminosity. The luminosity monitors are placed at very small polar angle covering a few degrees relative to the beam line. This method also offers the advantage that the strictly weak radiative corrections are very small in this angular region.

The lowest order pure QED Bhabha scattering cross section is given by the expression:

$$(\frac{d\sigma}{d\Omega})_{QED} = \frac{\alpha^2}{4s}[(1+c^2) + 2\frac{(1+c)^2+4}{(1-c)^2} - 2\frac{(1+c)^2}{(1-c)}] \tag{5.14}$$

where s = $4E^2_{beam}$ is the centre of mass energy, c = $\cos\theta$ where θ is the scattering angle of the electron and α is the QED coupling constant.

Three contributions, γ-annihilation(s-channel), γ-exchange(t-channel) and their interference(s-t) correspond to each of the three terms in Eq.(5.14). Fig. 5.20 illustrates the corresponding pure QED lowest order Bhabha diagrams.

The Eq.(5.14) can be written more compactly as:

$$(\frac{d\sigma}{d\Omega})_{QED} = \frac{\alpha^2}{4s}(\frac{(3+c^2)}{1-c})^2 \tag{5.15}$$

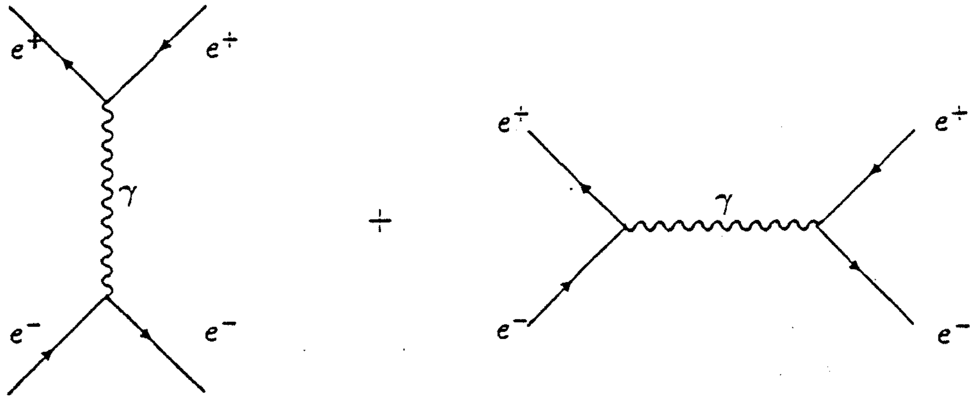

Figure 5.20: The lowest order QED diagrams contribution to the Bhabha scattering $e^+e^- \to e^+e^-$: t-channel (left) and s-channel (right).

The radiative correction to the cross section from the initial and final state radiation as well as interference bewteen the two should be taken into account as described in ref.[58].

At the Z^0 resonance, the Z^0 propagator terms have to be included, and the cross section should be written as:

$$\frac{d\sigma}{d\Omega} \simeq \frac{d\sigma}{d\Omega}_{QED}(1+\delta_w) \tag{5.16}$$

where the correction δ_w includes all electroweak contributions, weak corrections to the vertex and to the propagator. At the small angles ($\theta \ll 1$ mradian), where the luminosity monitoring takes place, due to the pole in the t-channel exchange, the QED approximation to the total cross section is usually sufficient. The interference between Z^0 and γ diagrams in the range of the Z^0 resonance is very small and the correction is negligible.

The total accepted Bhabha cross section is:

$$\sigma_{QED} = \int_{\theta_{min}}^{\theta_{max}} \frac{d\sigma}{d\Omega} \tag{5.17}$$

where $\theta_{min}, \theta_{max}$ define the angular region of acceptance for the detector.

By using the integrated cross section σ, the luminosity L can be obtained as:

$$L = \frac{N - N_{bg}}{\sigma\epsilon} \tag{5.18}$$

where N is the number of detected luminosity events, N_{bg} is the number of background events, ϵ is the luminosity detection efficiency in the acceptance region.

5.12.1 Luminosity Measurement

The Luminosity is measured with the Small Angle Tagger(SAT) in the small angle region. The geometrical description of the SAT is presented in section 3.6.

The description of Bhabha event triggers can be found in section 3.8. The Bhabha selection criteria are the same as described in [57].

At the 90% confidence level, the Bhabha trigger efficiency is greater than 99.8% and the total experimental uncertainty is 0.8% [57]. The total theoretical uncertainty is 0.5% [58].

Table 5.4 shows the integrated luminosity taken at each beam energy point during the 'accepted' runs[57].

$\sqrt{s}$ (GeV)	Number of Bhabha events	Integrated Luminosity $(nb)^{-1}$
88.222	9129	$320.1 \pm 3.3 \pm 3.0$
89.216	11401	$406.8 \pm 3.8 \pm 3.8$
90.217	10404	$379.8 \pm 3.7 \pm 3.6$
91.213	63329	$2380.6 \pm 9.5 \pm 22.4$
92.208	8090	$312.4 \pm 3.5 \pm 2.9$
93.211	9507	$377.8 \pm 3.9 \pm 3.6$
94.203	10404	$419.3 \pm 4.1 \pm 3.9$

Table 5.4: The integrated luminosity collected during the runs (see 5.5.4) in this analysis. The systematic error includes 0.8% experimental error and 0.5% theoretical error.

5.13 Determination of the Dimuon Cross Section

The physical observable which can be extracted from the muon and Bhabha data samples is the dimuon cross section.

$\sqrt{s}$ (GeV)	Uncorrected Number of $\mu^+\mu^-$ events	σ_μ (nb) $20^o < \theta < 160^o$	σ_μ (nb) 4π
88.222	59	0.19 ± 0.03	0.22 ± 0.03
89.216	147	0.38 ± 0.03	0.45 ± 0.04
90.217	315	0.91 ± 0.05	1.04 ± 0.06
91.213	2871	1.301 ± 0.027	1.474 ± 0.030
92.208	290	0.99 ± 0.06	1.12 ± 0.07
93.211	180	0.50 ± 0.04	0.57 ± 0.04
94.203	140	0.35 ± 0.03	0.40 ± 0.03

Table 5.5: Number of selected events and cross-section σ_μ for $e^+e^- \rightarrow Z^0/\gamma \rightarrow \mu^+\mu^-$ for different centre-of-mass energies. The errors are statistical only.

The muon pair cross-section σ_μ is then determined by:

$$\sigma_\mu(\sqrt{s}) = \frac{N_{\mu corr}(\sqrt{s})}{L} \tag{5.19}$$

where $N_{\mu corr}$ $(\sqrt{s})$ is the corrected number of muons detected at each centre-of-mass energy (see table 5.3) and the L is the sum over all accepted runs of the integrated luminosity collected at each energy (see table 5.4).

Table 5.5 shows the cross-sections after the corrections. The error is statistical only. In column 3, the results are for the events unweigthed for the selection criteria that both muon momenta are > 15 GeV/c, the polar angle of the negative muon satisfies $20^o < \theta < 160^o$ and that the acollinearity angle is $< 10^o$. The system uncertainties is 0.42%. In column 4, the results corrected to all the corrections and acceptance over 4π detection are presented. The systematic error then is 0.7% as discussed in the section 5.11.

The cross sections obtained by this analysis are in agreement with the DELPHI results obtained within the restricted polar angle acceptance $43^o < \theta < 137^o$ [62] and $32.9^o < \theta < 147.1^o$ [63].

In the next chapter we will extract estimates of some electroweak parameter values obtained in the extended $20^o < \theta < 160^o$ polar angle interval studied in this work.

Chapter 6

Determination of the Z^0 Parameters and Interpretation of the Results in the Framework of the Standard Model

In this chapter Γ_l, M_Z and Γ_Z are determined by fitting the cross section formula of eqs. 2.17 and 2.19 described in Chapter 2 to the experimental di-muon line shape obtained in Chapter 5 for data taken in 1990 within the polar angle range $20^o < \theta < 160^o$. The ratio R_l between Γ_{hadron} and Γ_l is computed. Finally, the number of light neutrino species is derived. Furthermore, we combine the observed cross sections for the 1990 data with the cross sections for the 1991 data obtained from ref. [66], which have been calculated in the same polar angle range as for 1990, and reperform the same fits and calculations as for the 1990 data alone.

6.1 Program Used to Determine the Z^0 Parameters from the Dimuon Line Shape

The program used to fit the Z^0 parameters is ZFITTER[11, 69]. The discussion about the formula used in the program can be found in chapter 2 and ref [69, 70]. It is based on a semi-analytical approach to fermion pair production in e^+e^- annihilation and Bhabha scattering. The program allows for model-independent and Standard

Model fits to the data. For a 'model independent' fit, the only assumption is a Breit-Wigner form of the Z line shape and the validity of QED for the calculation of the radiator function. Thus, apart from numerically unimportant contributions from the Z-γ interference, and from non-photonic radiative corrections, the procedure leads to a determination of the Z line shape parameters (independent of the S.M.) and leads to the best values of free input parameters such as M_Z, Γ_Z and Γ_l, etc. In this thesis only the 'model independent' fits are presented. The formula used to fit the data can be found in section 2.3.2 (eqs. 2.17 and 2.19). The ZFITTER program works in a way which relies on formulae that are analytically integrated over a finite angular region with respect to the scattering angle. The program directly calculates predictions for observable quantities.

The ZFITTER program allows for cuts on the energies and acollinearity of the final-state fermions. However, the energy cut has to be the same for both. For the fits in which the data of 1990 and 1991 are combined, a simultaneous fit is carried out taking into account the respective systematic errors on luminosity and event selection (see Chapter 5 for all the cuts for event selection).

6.2 Fit of the Measured Cross Section

The theoretical cross section expression used in the program ZFITTER discussed in section 6.1, depending on the parameters M_Z, Γ_Z and $(\Gamma_e\Gamma_\mu)^{1/2}$ (assuming e-μ universality $\Gamma_l = (\Gamma_e\Gamma_\mu)^{1/2}$) has been fitted to the cross section values for the process $e^+e^- \rightarrow Z^0/\gamma \rightarrow \mu^+\mu^-$ corrected for experimental cuts (see chapter 5) measured in 1990 at 7 centre of mass energies around the Z^0 peak displayed in table 5.5. This three parameters fit gave the following results where only systematic errors not arising from uncertainties in beam energies have been taken into account:

M_Z=91.110 ± 0.053(stat)± 0.002(sys) GeV,

Γ_Z=2.509 ± 0.091(stat) ± 0.003(sys) GeV,

$\Gamma_l=(\Gamma_e\Gamma_\mu)^{1/2}$=84.05 ± 2.63(stat) ± 0.45(sys) MeV,

χ^2/d.o.f.=5.30/(7-3)=1.33

The results of the fit are shown in fig. 6.1.

For the mass of Z^0, an extra error of ± 20 MeV [68] must be added due to the LEP beam energy calibration error. A systematic error of 4.5 MeV should also be added to Γ_Z due to the relative point-to-point uncertainty on the collision energy. This gives:

$$M_Z = 91.110 \pm 0.053(\text{stat}) \pm 0.020(\text{sys}) \text{ GeV},$$

$$\Gamma_Z = 2.509 \pm 0.091(\text{stat}) \pm 0.005(\text{sys}) \text{ GeV}.$$

These values agree with the average results obtained from the four LEP experiments[71] for M_Z=(91.187±0.007) GeV and Γ_Z=(2.492±0.007) GeV. The values of $m_t = 141$ GeV and $m_H = 300$ GeV were used as input to the ZFITTER program.

However, as the number of hadronic events is much bigger than the number of $\mu^+\mu^-$ events, the parameters M_Z and Γ_Z can be determined with much better precision from the hadronic events than from the muon data. One can fix the Z^0 mass M_Z and width Γ_Z from the results of the fits to the hadronic line shape[65] and only leave $(\Gamma_e\Gamma_\mu)^{1/2}$ free. Using the average results M_Z=(91.187±0.007) GeV and Γ_Z=(2.492±0.007) GeV from the four LEP experiments[71], we get:

$$\Gamma_l = (\Gamma_e\Gamma_\mu)^{1/2} = 83.77 \pm 0.71(\text{stat}) \pm 0.44(\text{sys}) \text{ MeV}$$

$$\chi^2/\text{d.o.f.} = 7.54/(7\text{-}1) = 1.26$$

where the systematic error is due to the event selection and the systematic error on the luminosity.

The fitted $e^+e^- \rightarrow Z^0/\gamma \rightarrow \mu^+\mu^-$ line shape with only $(\Gamma_e\Gamma_\mu)^{1/2}$ as a free parameter is shown in fig. 6.2. The χ^2/d.o.f. of the fitted line shape to the data is good (χ^2/d.o.f.= 1.26).

The systematic error on the leptonic partial width due to the uncertainty on M_Z(±0.007 GeV) has been estimated by refitting with M_Z=91.194 GeV and 91.18 GeV. The fitted leptonic partial width varied by ±0.02 MeV. The estimated systematic error on $(\Gamma_e\Gamma_\mu)^{1/2}$ due to the uncertainty on Γ_Z(±0.007 GeV) is ±0.195 MeV. Between these two, the error due to the uncertainty on Γ_Z is the absolute dominated one. Combining the systematic error due to the event selection and the systematic error on the luminosity and the error raised from the uncertainty on Γ_Z, the final result is:

$$\Gamma_l = (\Gamma_e\Gamma_\mu)^{1/2} = 83.77 \pm 0.71(\text{stat}) \pm 0.48 \text{ (sys) MeV}$$

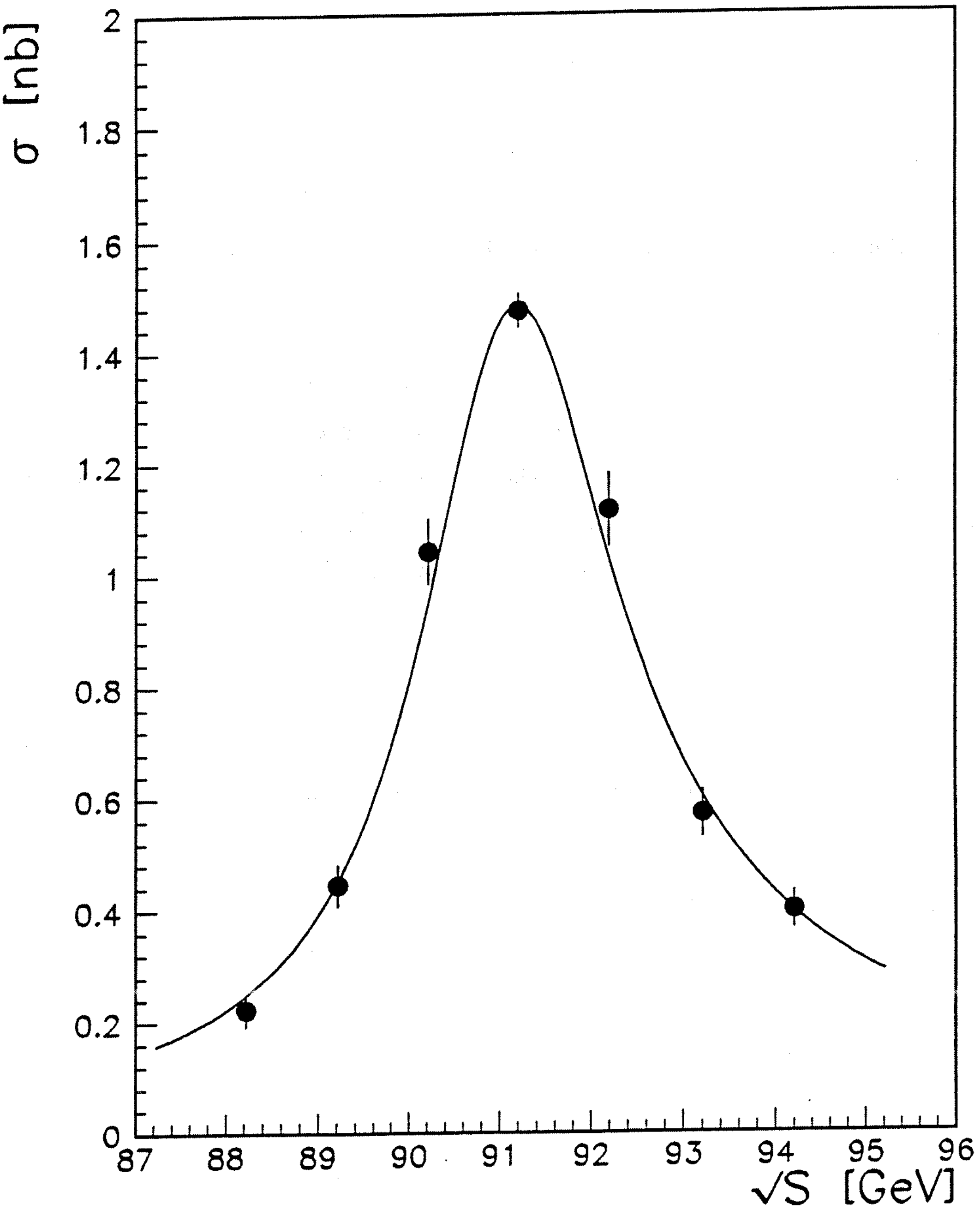

Figure 6.1: The $\mu^+\mu^-$ line shape obtained by fitting $\sigma_\mu(s)$ using the ZFITTER program with M_Z, Γ_Z and $(\Gamma_e\Gamma_\mu)^{1/2}$ as free parameters. See table 5.5 for the experimental values.

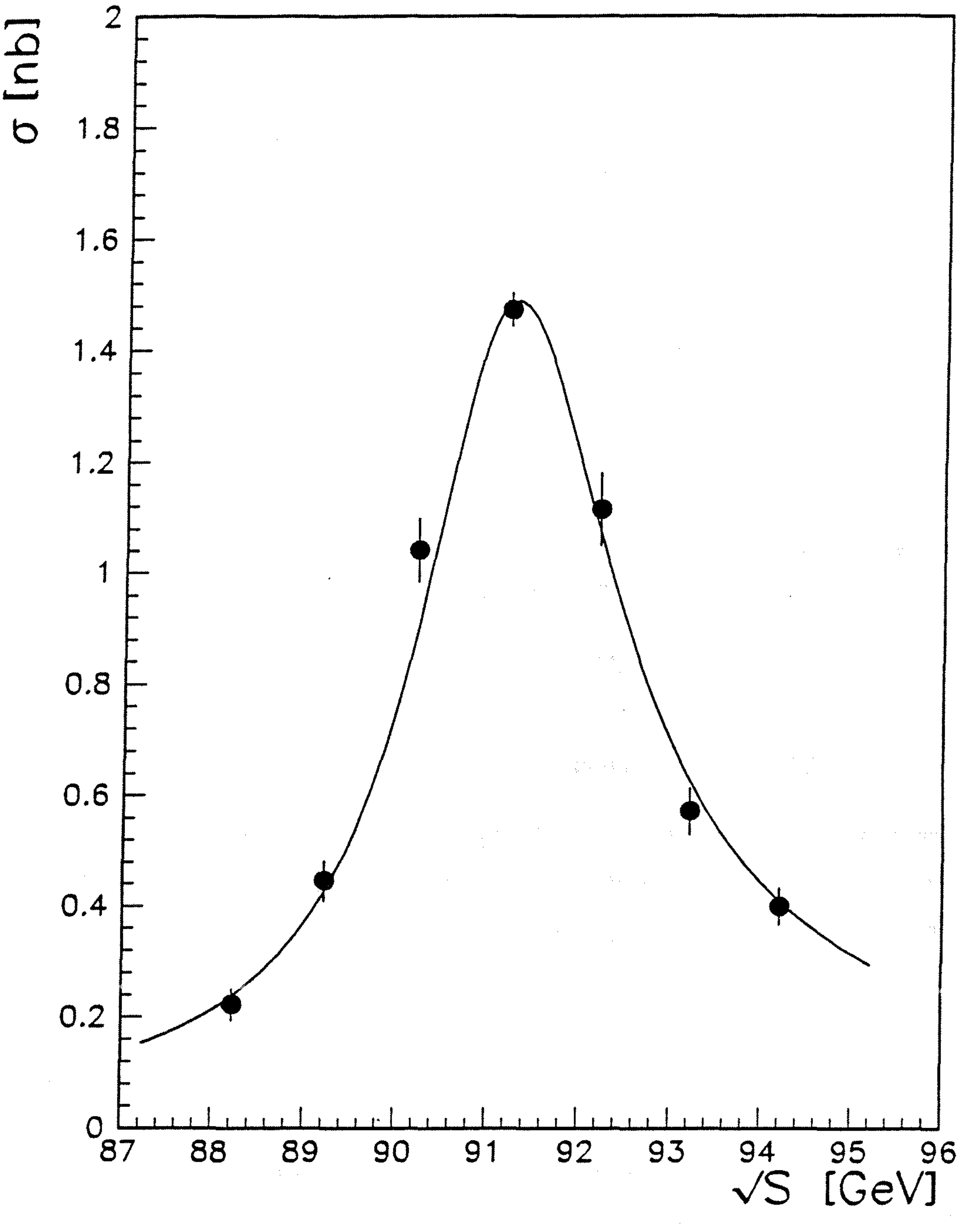

Figure 6.2: The $\mu^+\mu^-$ line shape obtained by fitting $\sigma_\mu(s)$ using the ZFITTER program with only $(\Gamma_e\Gamma_\mu)^{1/2}$ as a free parameter.

6.2.1 Estimation of the Effective Weak Mixing Angle $sin^2\theta_w^{eff}$

As discussed in chapter 2, $sin^2\theta_w^{eff}$ can be computed from the following expression:

$$sin^2\theta_w^{eff} = \frac{1}{4}[1 \pm \sqrt{\frac{4\Gamma_l}{\rho_{eff}(1+\frac{3\alpha}{4\pi})(\frac{G_\mu M_Z^3}{6\pi\sqrt{2}})} - 1}\ ] \tag{6.1}$$

with

$$\rho_{eff} = \rho_0(1 + \frac{3\sqrt{2}G_F}{16\pi^2}m_t^2) \tag{6.2}$$

Taking ρ_0=1 as predicted by the Standard Model and m_t=141 ±27 GeV [67], we estimate the value of the $sin^2\theta_W^{eff}$ from eq. 6.1 to be:

$sin^2\theta_W^{eff}$=0.239 $\pm$ 0.029

or

$sin^2\theta_W^{eff}$=0.261 $\pm$ 0.029

The error due to the uncertainty on the Γ_l is the dominant one and has a contribution of 0.024 in the error of $sin^2\theta_w^{eff}$. The value of $sin^2\theta_W^{eff}$=0.239 $\pm$ 0.029 agrees with the world average value $sin^2\theta_W^{eff}$=0.2324 $\pm$ 0.0011 [67].

6.3 Checking the Number of Light Neutrino Species

Fig. 6.3 shows the muon cross sections obtained in chapter 5 compared to the Z^0 muon line shape derived from the Standard Model by assuming the number of light neutrino species to be equal to two, three and four respectively. The partial widths were taken from the Standard Model with α_s=0.12, m_t=141 GeV and a m_H=300 GeV[67]. It is clear that only the line shape with three light neutrino species fits the data and the experimental results rule out the possibility to have a fourth light ($m_\nu < M_Z/2$) neutrino within the standard model.

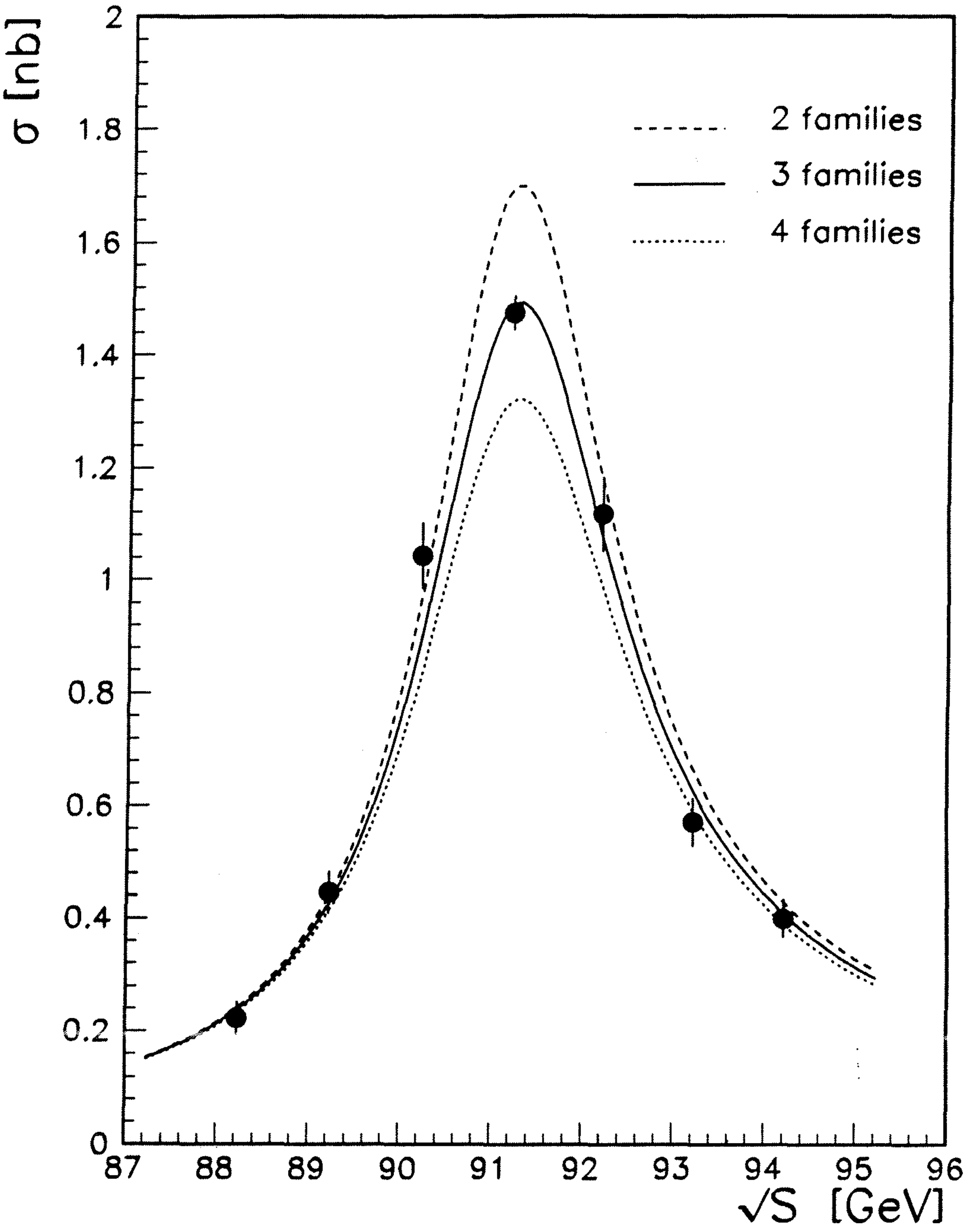

Figure 6.3: The $\mu^+\mu^-$ line shape. The solid line corresponds to the Standard Model predictions for three neutrino species and the dashed and dotted lines are for two and four light neutrino species. The data are the dimuon cross sections obtained in chapter 5.

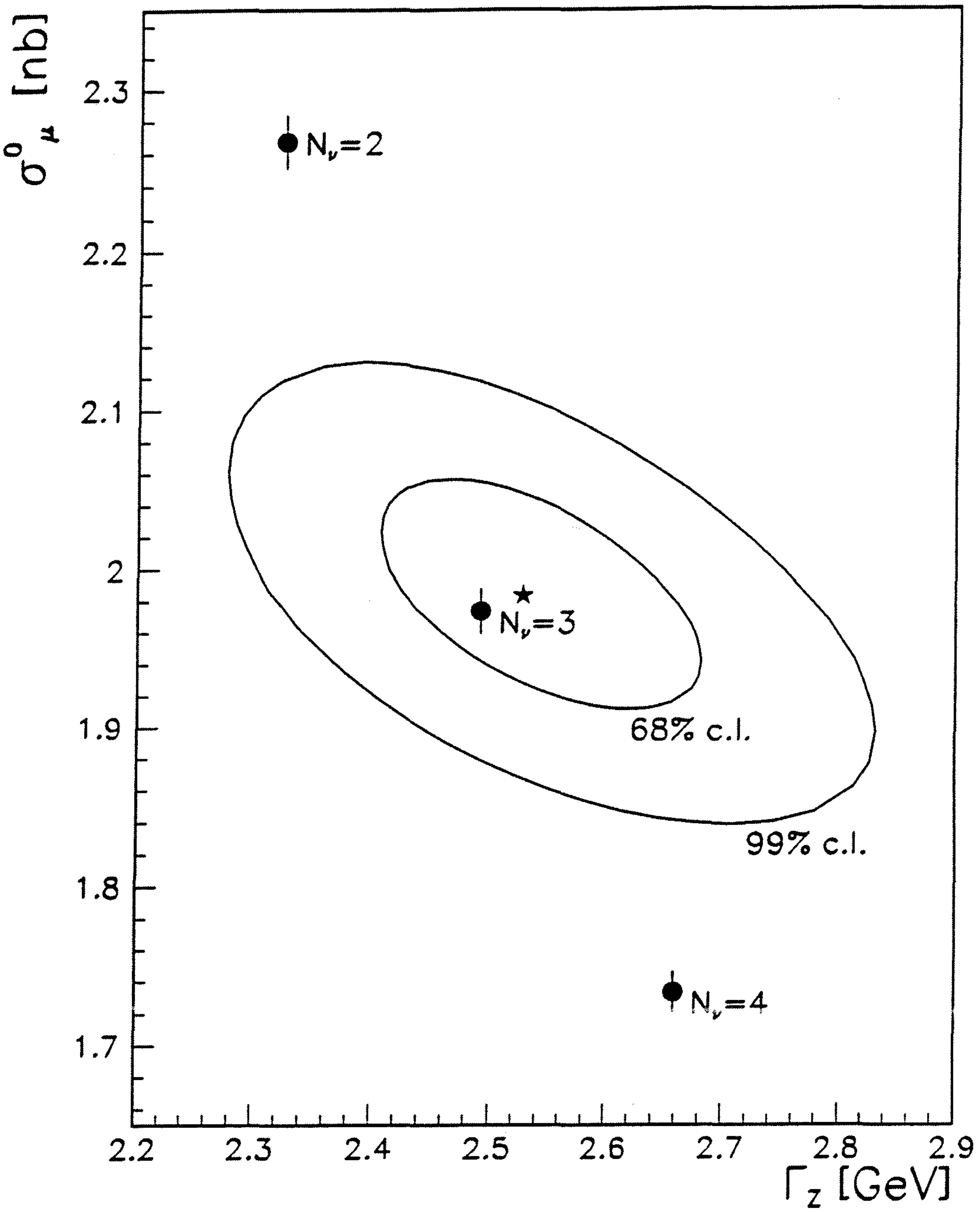

Figure 6.4: The 68% and 99% confidence level contours in the Γ_Z, σ^0_μ plane for the two parameter fit to the experimental muon line shape. The predictions for two, three and four light neutrino species from the Standard Model are also shown (black points).

6.3.1 Simultaneous Fit of Γ_Z and σ_μ^0, the Born Peak Cross Section

After correcting for the initial state radiation and assuming e-μ universality, the Born peak cross section σ_μ^0 can be determined from the relation:

$$\sigma_\mu^0 = \frac{12\pi\Gamma_e\Gamma_\mu}{M_Z^2\Gamma_Z^2} = \frac{12\pi\Gamma_l^2}{M_Z^2\Gamma_Z^2} \tag{6.3}$$

The advantage of introducing σ_μ^0 in the fit rather than $(\Gamma_e\Gamma_\mu)^{1/2}$ is that σ_μ^0 depends on the ratio Γ_l/Γ_Z which is insensitive to the top mass.

Using the 'model independent' fit from the ZFITTER program again and expressing eq. 2.19 as the function of σ_μ^0 instead of Γ_l (see eq. 6.3), fixing the mass of the Z^0 to the average value M_Z=(91.187±0.007) GeV[67] determined from the four LEP experiments and leaving Γ_Z and σ_μ^0 free in the fit, we obtain:

Γ_Z=2.528 ± 0.090(stat)±0.003(sys) GeV,
σ_μ^0=1.984 ± 0.048(stat)±0.021(sys) nb
χ^2/d.o.f.=7.38/(7-2)=1.48

This provides a detailed way to check and display the effect of the number of light neutrino species on the predictions of the Standard Model. Fig. 6.4 shows the correlation between the fitted Γ_Z and σ_μ^0 with 68% and 99% confidence level contours, along with the predictions of the Standard Model for two, three and four neutrino species respectively. The following parameter values were used when computing the Standard Model prediction, M_Z=(91.187±0.007) GeV, Γ_Z=2.492 GeV, α_s=0.12±0.006, m_t=141±27 GeV and 50 $GeV < m_H <$ 1000 GeV, Γ_ν=166.7±0.56 MeV and Γ_l=83.6±0.32 MeV [67, 71]. The top mass and its variation and the lower limit of m_H are based on [67].

The fitted parameters deviate by less than one standard deviation from the standard model expectations for three neutrino species.

Taking both M_Z and Γ_Z from the average results of the four LEP experiments, only leaving σ_μ^0 as a free parameter, we obtain the result of a one parameter fit:

σ_μ^0=1.995 ± 0.040(stat) ± 0.021(sys) nb
χ^2/d.o.f.=7.54/(7-1)=1.26

The uncertainty of the σ_μ^0 due to the uncertainty on M_Z and Γ_Z are 0.0002 and 0.001 respectively. This gives the finial result:

σ_μ^0=1.995 ± 0.040(stat) ± 0.021(sys) nb

6.3.2 Quantitative Estimates of the Number of Light Neutrino Species

From the Z^0 line shape measurement one can extract the number of "light" ($m_\nu < M_Z/2$) neutrino species present in the Standard Model, and hence infer the number of quark and lepton generations. If there are extra contributions to the invisible decay within of the Z^0, a quantitative estimate of the number of neutrino species could lead to a result different from 3 [72].

There are several ways to determine the number of neutrino species. The following have been used in this thesis:

In the framework of the Standard Model, the total width of the Z^0 is given by:

$$\Gamma_Z = \Gamma_h + 3\Gamma_l + \Gamma_{inv} \tag{6.4}$$

where Γ_h, Γ_l and Γ_{inv} are the partial widths of hadron, lepton and "invisible" respectively. The most straightforward way to determine the 'number of light neutrino species' is:

$$N_\nu = \frac{\Gamma_{inv}}{\Gamma_\nu} = \frac{\Gamma_Z - \Gamma_h - 3\Gamma_l}{\Gamma_\nu} \tag{6.5}$$

where N_ν is the number of light neutrino species and Γ_ν is the partial width for a neutrino.

Introducing N_ν from eq. 6.5 to eq. 2.19 in the ZFITTER program and fixing the partial widths to the value from the Standard Model, one can use the dimuon cross section alone to directly check the number of light neutrino species. Taking again M_Z=(91.187±0.007) GeV, α_s=0.120±0.006, m_t=141±27 GeV and with the value 50 GeV < m_H < 1000 GeV[67], the partial widths predicted by the Standard Model are:

Γ_h=1.74±0.01GeV, Γ_l=83.64±0.32 MeV and Γ_ν=166.7±0.56 MeV.

The number of neutrino species obtained from the fit is:

N_ν=3.00±0.17

Despite the fact that Γ_Z is not very sensitive to the muon data due to the small statistics in the $\mu^+\mu^-$ channel (thus the corresponding error on N_ν is quite large), the possibility that N_ν = 2,4 is again clearly ruled out.

From eq. 6.3, Γ_Z can be written as

$$\Gamma_Z = \frac{\Gamma_l}{M_Z}\sqrt{\frac{12\pi}{\sigma_\mu^0}} \tag{6.6}$$

so the number of neutrino species eq. 6.5 can be derived as follows:

$$N_\nu = \frac{\frac{\Gamma_l}{M_Z}\sqrt{\frac{12\pi}{\sigma_\mu^0}} - \Gamma_h - 3\Gamma_l}{\Gamma_\nu} \tag{6.7}$$

In analogy to eq. 6.3,

$$\sigma_h^0 = \frac{12\pi\Gamma_e\Gamma_h}{M_Z^2\Gamma_Z^2} = \frac{12\pi\Gamma_l\Gamma_h}{M_Z^2\Gamma_Z^2}$$

so that:

$$N_\nu = \frac{\Gamma_l}{\Gamma_\nu}(\frac{1}{M_Z}\sqrt{\frac{12\pi}{\sigma_\mu^0}} - \frac{\sigma_h^0}{\sigma_\mu^0} - 3) \tag{6.8}$$

The advantage in doing so is that the ratio of σ_h^0/σ_μ^0 is practically independent of m_t due to an almost complete cancellation of m_t dependent terms. Moreover, instead of taking Γ_ν from the Standard Model, the ratio Γ_ν/Γ_μ is used. The ratio of Γ_ν/Γ_μ is particularly insensitive to the radiative corrections and has only a weak dependence on m_t and m_H. Therefore N_ν determined in this way has a small uncertainty.

Taking the ratio Γ_l/Γ_ν=0.502±0.001 and σ_h^0=41.45± 0.031 nb from the Standard Model, which corresponds to m_t=141±27 GeV and 50 GeV< m_H <1000 GeV, and using M_Z=91.187±0.007 GeV from the average of the four experiments [71], and $\sigma_\mu^0 = 1.995 \pm 0.045$ nb obtained by this analysis in section 6.3.1, the number of light neutrino species N_ν is found to be :

N_ν=2.99 ± 0.06

Although the Standard Model does not predict the number of generations as such, one can attempt to determine N_ν in a way which is less dependent on its validity by taking σ_h^0 = 41.84 ±0.45 nb as obtained by DELPHI in 1990[65] and σ_μ^0 from our measured value $\sigma_\mu^0 = 1.995 \pm 0.045$ nb. The number of light neutrino species N_ν is then found to be :

N_ν=2.99 ± 0.08

The major uncertainty on N_ν comes from the overall normalisation uncertainty on σ_μ^0 and σ_h^0 although the cancellation of the uncertainty on the luminosity measurement is taken into account already.

Finally, in order to decrease the uncertainty on σ_h^0 we use the average result of the four LEP experiments, σ_h^0=41.16±0.18 nb[71]. The number of light neutrino species N_ν obtained in this way is:

N_ν=3.07 ± 0.08

The calculation of the number of neutrino species with σ_h^0=41.16±0.18 nb from the four LEP experiments gives an equaly precise estimate of the number of light neutrino species compared to the value obtained by using the DELPHI 1990 σ_h^0 result due to the higher statistics, even if in the latter case there is cancellation of the uncertainty on the luminosity. Moreover, using the theoretical value of σ_h^0 gives a still more precise estimate of the number of light neutrino species N_ν.

In conclusion the four estimates of N_ν obtained in this section are in excellent agreement with N_ν=3, excluding $N_\nu \neq 3$ within the framework of the Standard Model and leave little room for non Standard Model contributions to the invisible decay width of the Z^0.

6.4 Ratio of the Partial Widths

The ratio R_l of hadronic partial width over the leptonic partial width assuming e-μ universality, can be defined as: $R_l = \frac{\Gamma_{had}}{\Gamma_l}$.

From eq. 6.3 and

$$\sigma_h^0 = \frac{12\pi\Gamma_e\Gamma_h}{M_Z^2\Gamma_Z^2} \tag{6.9}$$

one derives alternatively the ratio $R_l = \frac{\sigma_h^0}{\sigma_\mu^0}$.

Taking σ_h^0 from the average of the four LEP experiments $\sigma_h^0 = 41.16 \pm 0.18$ nb[71] and $\sigma_\mu^0 = 1.995 \pm 0.045$ from the result of this analysis, one finds:

$$R_l = \frac{\Gamma_h}{\Gamma_l} = \frac{\sigma_{had}^0}{\sigma_\mu^0} = 20.63 \pm 0.47$$

6.5 Combination of the 1990 and 1991 Data

In order to reduce the statistical error on the muon data, we combined the 1990 muon cross sections obtained from Chapter 5 and the DELPHI 1991 muon cross section results [66] for which the polar angle acceptance also covered the interval $20^o \leq \theta \leq 160^o$.

As before, only the 'model independent' fits provided by the ZFITTER program will be used. The ZFITTER program also allows a simultaneous fit of different data samples taking into account the respective systematic error on the luminosity and event selection.

Combining the 1990 and 1991 data and reperforming all the fits and calculations described in the previous sections, we obtain the following results:

Fitting M_Z, Γ_Z and $(\Gamma_e\Gamma_\mu)^{1/2}$ to the combined line shape data (see section 6.2 for the fit of the 1990 data only), we obtain the results:

M_Z=91.172 ± 0.030(stat) ± 0.002(sys) GeV,
Γ_Z=2.483 ± 0.058(stat) ± 0.003(sys) GeV,
$\Gamma_l=(\Gamma_e\Gamma_\mu)^{1/2}$=82.80 ± 1.60(stat) ± 0.29(sys) MeV,
χ^2/d.o.f.=13.08/(14-3)=1.19

An extra error of ± 6.3 MeV [67] must be added to M_Z due to the LEP beam energy calibration error and a systematic error of 4.5 MeV should be added to Γ_Z due to the relative point-to-point uncertainty on the collision energy. This gives the following results:

M_Z=91.172 ± 0.030(stat) ± 0.007(sys) GeV,

Γ_Z=2.483 ± 0.058(stat) ± 0.005(sys) GeV,

The systematic errors on M_Z, Γ_Z and Γ_l are smaller compared to the results of the fit of the 1990 data due to the fact that the error on the luminosity of the 1991 runs is much smaller than that of 1990.

The results of the fit are shown in fig. 6.5.

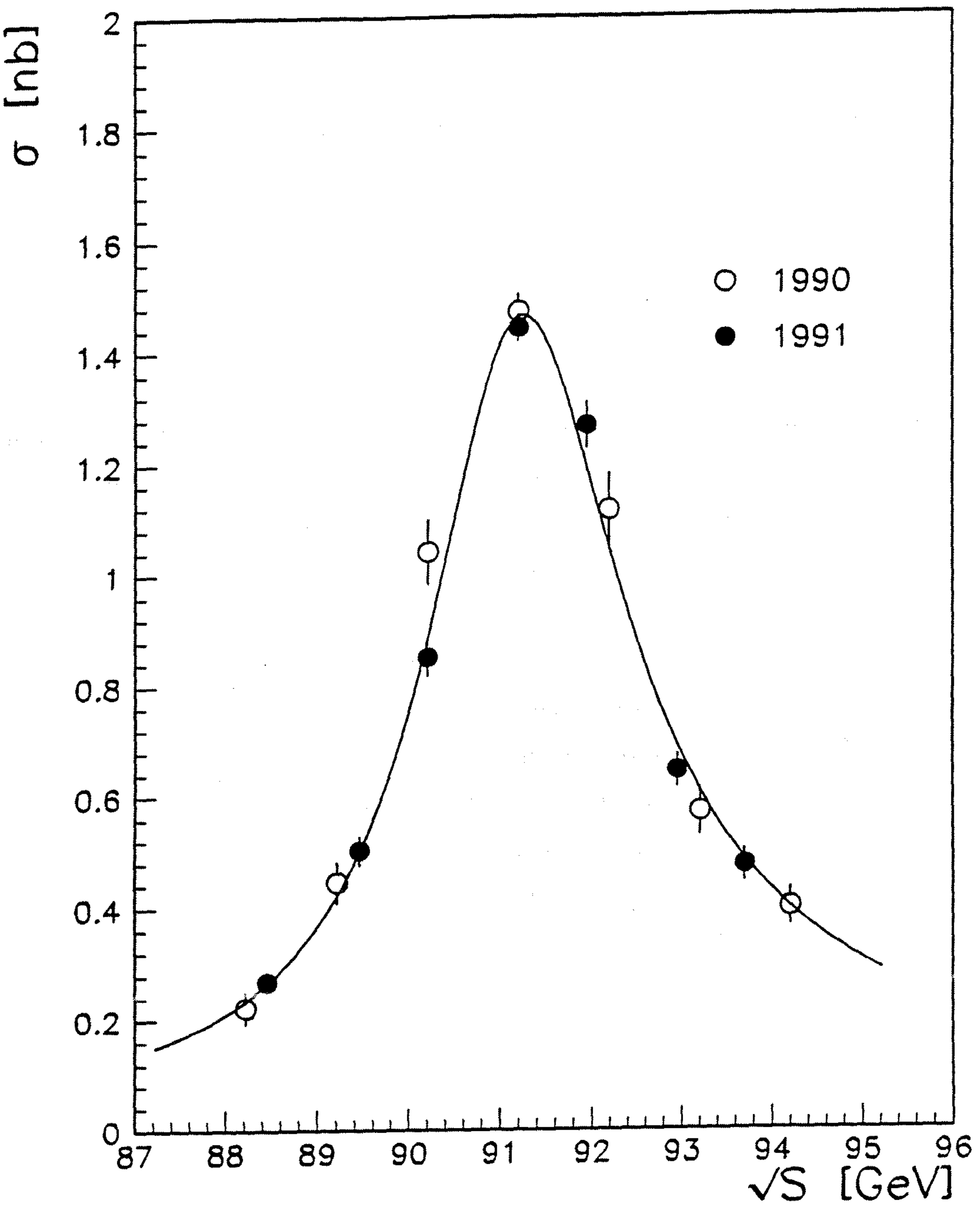

Figure 6.5: The $\mu^+\mu^-$ line shape obtained by fitting $\sigma_\mu(s)$ with M_Z, Γ_Z and Γ_μ as free parameters using ZFITTER to the combined 1990 and 1991 results.

By doing the fit with the 1990 and 1991 data simultaneously the uncertainties on M_Z and Γ_Z are reduced from 0.057 GeV (for 1990 data) to 0.030 GeV and from 0.091 GeV to 0.058 GeV respectively where the uncertainty on Γ_l is reduced from 2.67 MeV to 1.63 MeV. However the uncertainties on M_Z and Γ_Z are still high as compared to the results obtained by only using the DELPHI 1990 hadronic data [65]. In order to get a more precise result on Γ_l, a fit was carried out with only Γ_l as a free parameter and M_Z and Γ_Z taken from the average of the four LEP experiments. The result is:

$$\Gamma_l=(\Gamma_e\Gamma_\mu)^{1/2}= 83.09 \pm 0.46(\text{stat}) \pm 0.28(\text{sys})\ \text{MeV}$$

$$\chi^2/\text{d.o.f.}= 13.35/(14\text{-}1)=1.03$$

An additional error of 0.195 MeV must be added to Γ_l due to the uncertainty on Γ_Z (see section 6.2 for 1990 data fit alone and the discussion of the error). This gives:

$$\Gamma_l=(\Gamma_e\Gamma_\mu)^{1/2}= 83.09 \pm 0.46(\text{stat}) \pm 0.34(\text{sys})\ \text{MeV}$$

The results of the fit are shown in fig. 6.6.

We recall the discussion in chapter 2 about the fact that the measurement of a lower limit on mass of the top quark $m_t > 91$ GeV by the CDF experiments implies $\Gamma_l \geq 83.30$ MeV. As the combined fit leads to the result Γ_l=83.09 ± 0.57 MeV, the central value of Γ_l is less than the lower limit. One can hence not use eq. 6.1 to directly calculate $sin^2\theta_W^{eff}$.

However, the result of the combined fit agrees with the lower limit on Γ_l derived from the CDF experiments. Assuming that Γ_l follows a gaussian distribution G(Γ_l), using the "classical" statistical techniques used by the "Review of Particle Properties", one can very well give an upper limit for Γ_l at the 90% confidence level by the following procedure:

1. renormalize the gaussian probability distribution for Γ_l such that the integral of G(Γ_l) over Γ_l from 83.30 MeV to infinity is equal to 1.0

2. find the value Γ_l(limit) such that the integral over Γ_l of the renormalized distribution from 83.30 MeV to Γ_l(limit) is equal to 90%

3. set Γ_l(limit) to be the desired upper limit with confidence level 90%

i.e.

$$\frac{\int_{83.3}^{\Gamma_l(limit)} G(\Gamma_l)d\Gamma_l}{\int_{83.3}^{\infty} G(\Gamma_l)d\Gamma_l} = 0.9$$

The result is:

$$\Gamma_l(\text{limit}) = 84.122 \text{ MeV}$$

Taking ρ_0=1 as predicted by the Standard Model, m_t = 141 ± 27 GeV, and M_Z= 91.187 ± 0.007 GeV [67], we find:

$$0.2241 \leq sin^2\theta_W^{eff} \leq 0.25$$

or

$$0.25 \leq sin^2\theta_W^{eff} \leq 0.2597$$

at the 90% confidence level.

The interval $0.2241 \leq sin^2\theta_W^{eff} \leq 0.25$ agrees with the world average value $sin^2\theta_W^{eff}$=0.2324 ± 0.0011 [67].

The correlation between the fitted Γ_Z and σ_μ^0 for 1990 data alone, shown in fig. 6.4, strongly favours a number of light neutrino species N_ν = 3. The results of the simultaneous fit of Γ_Z and σ_μ^0 to the 1990 and 1991 data are:

$$\Gamma_Z=2.486 \pm 0.057(\text{stat}) \pm 0.004(\text{sys}) \text{ GeV},$$

$$\sigma_\mu^0=1.964 \pm 0.029(\text{stat}) \pm 0.013(\text{sys}) \text{ nb}$$

$$\chi^2/\text{d.o.f.}=13.34/(14-2)=1.11$$

Fig. 6.7 shows the correlation between the fitted Γ_Z and σ_μ^0 with 68% and 99% confidence level contours, alone with the predictions of the Standard Model for two,

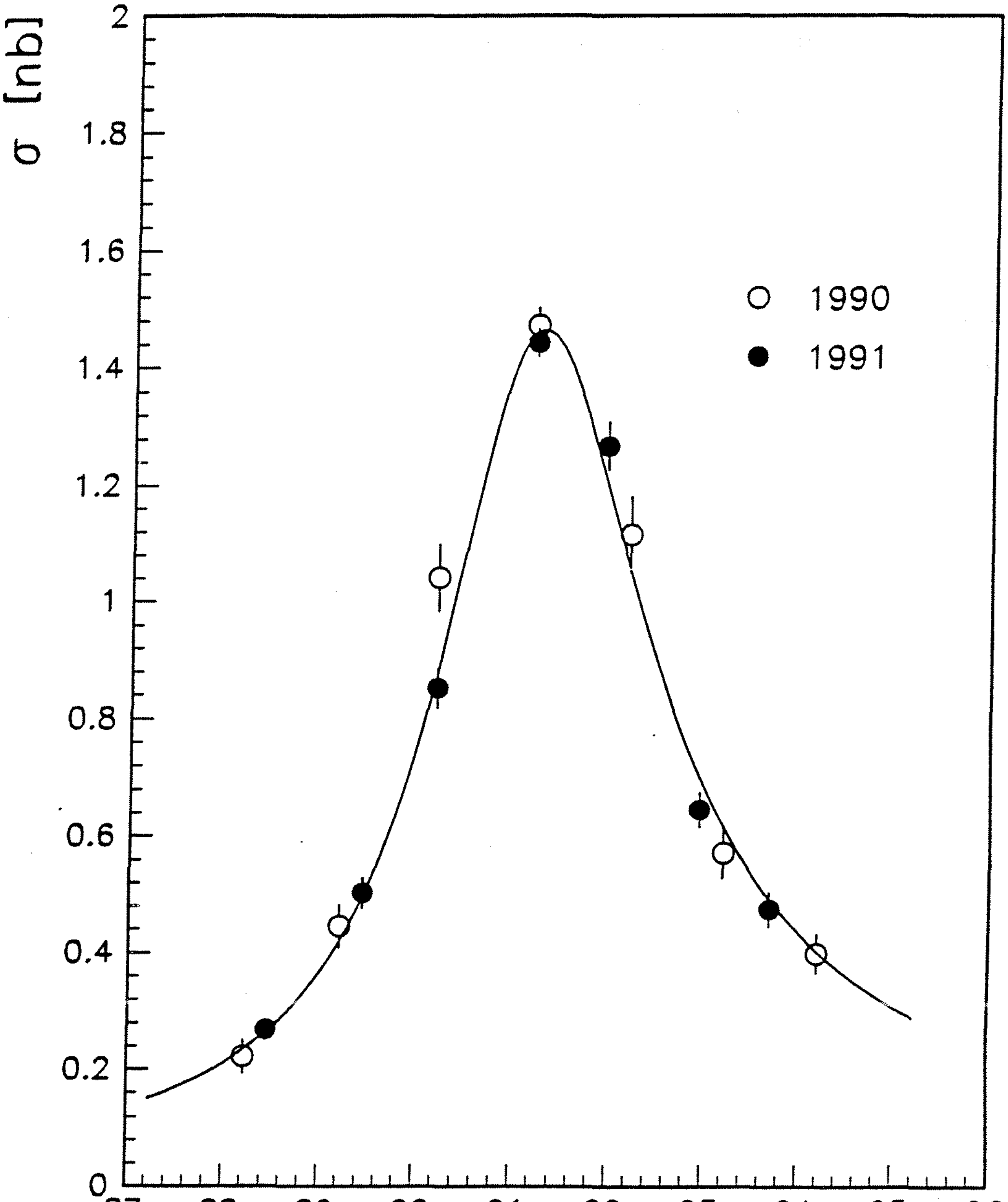

Figure 6.6: The $\mu^+\mu^-$ line shape obtained by fitting $\sigma_\mu(s)$ with only Γ_μ as free parameter using ZFITTER with 1990 and 1991 results.

three and four neutrino species respectively. For the standard Model, the following values were used, M_Z=(91.187±0.007) GeV, Γ_Z=2.492 GeV, α_s=0.12±0.006, m_t=141 ± 27 GeV and 50 GeV < m_H < 1000 GeV, Γ_ν=166.7±0.56 MeV and Γ_l=83.6±0.32 MeV [67]. Compared to fig. 6.4, fig. 6.7 puts the limitation on the number of light neutrino species much closer to three.

Taking Γ_z=2.492 ± 0.007 GeV from the average of the four LEP experiments and leaving σ^0_μ as a free parameter in the fit, one gets:

σ^0_μ=1.962 ± 0.022(stat) ± 0.013(sys) nb

Additional error of 0.002 should be added to σ^0_μ due to the uncertainty on Γ_Z. This gives:

σ^0_μ=1.962 ± 0.022(stat) ± 0.013(sys) nb

Taking σ^0_h from the average of the four LEP experiments $\sigma^0_h = 41.16 \pm 0.18$ nb[71] and $\sigma^0_\mu = 1.962 \pm 0.026$ nb from the result of this analysis, one obtains for the ratio of the partial widths:

$$R_l = \frac{\Gamma_h}{\Gamma_l} = \frac{\sigma^0_h}{\sigma^0_\mu} = 20.98 \pm 0.28$$

Taking Γ_l/Γ_ν=0.502±0.001 and σ^0_h=41.45± 0.031 nb from the Standard Model (see section 6.3.2) and M_Z=91.187±0.007 GeV from the average of the four experiments[67] and $\sigma^0_\mu = 1.962 \pm 0.026$ nb obtained by this analysis in this section from the 1990 and 1991 data, using eq. 6.8 to calculate the number of neutrino species, one gets:

N_ν=2.94 ± 0.04.

Taking σ^0_h from the four LEP average, we find (using eq. 6.8):

N_ν=3.02 ± 0.06.

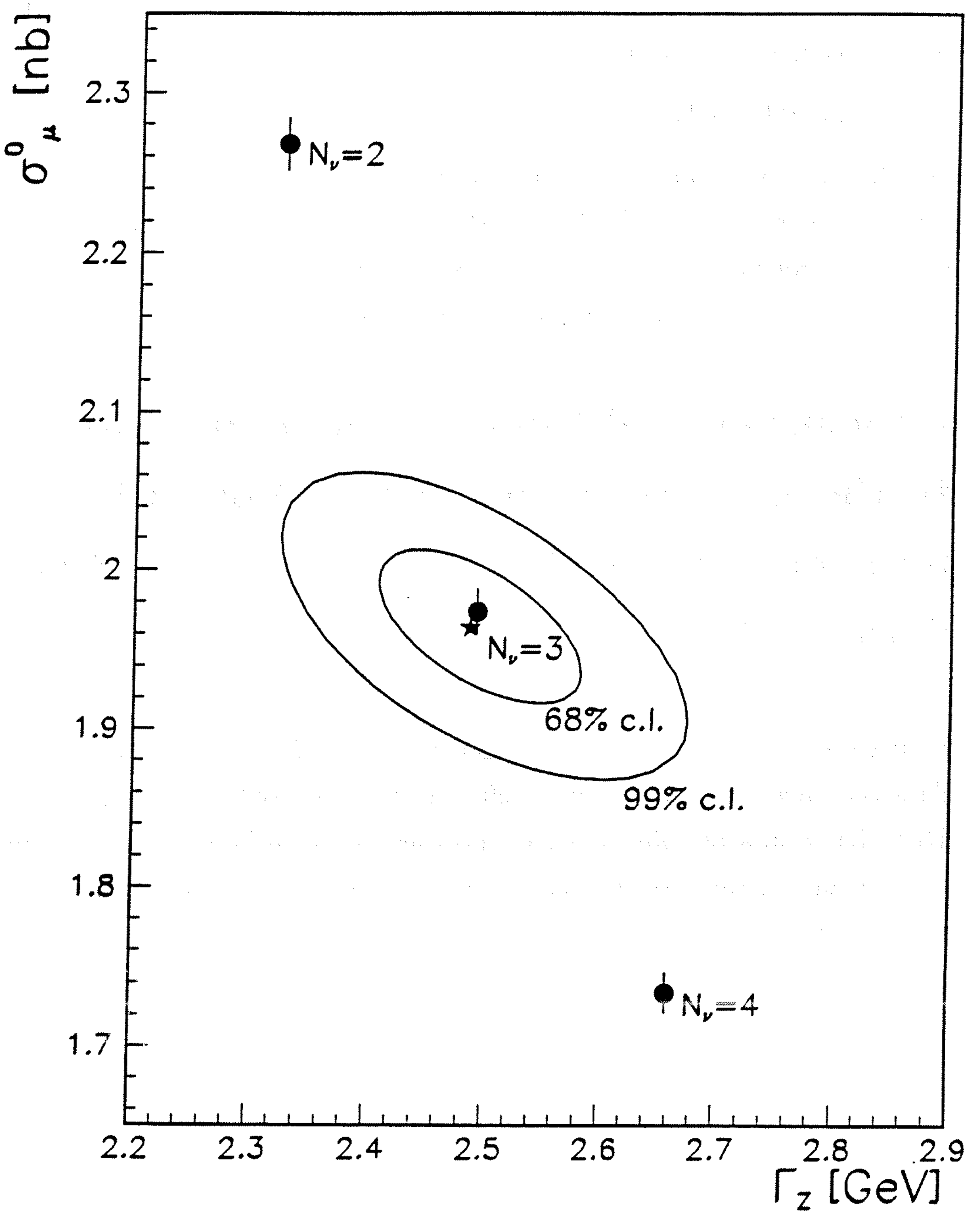

Figure 6.7: The 68% and 99% confidence level contours in the Γ_Z, σ^0_μ plane for the two parameter fit to the experimental muon line shape for the 1990 and 1991 data. The predictions for two, three and four light neutrino species from the Standard Model are also shown.

Again, the average value of M_Z from the four LEP experiments was used for the calculation.

Taking $\sigma_h^0 = 41.223 \pm 0.16$ nb[66] from the DELPHI results of 1990 and 1991 the fitted number of neutrino species is:

$$N_\nu = 3.00 \pm 0.05$$

Using the DELPHI value for σ_h^0 gives a smaller error on N_ν than the one obtained when using the average σ_h^0 from the four LEP experiments due to the cancellation of the luminosity error in the ratio $\frac{\sigma_h^0}{\sigma_\mu^0}$ in eq. 6.8. This is not true for the 1990 data alone as the error on σ_μ^0 is the dominant one in that case.

6.6 Conclusions and Comparison of Our Results to the Average Result of the Four LEP Experiments and to the Predictions of the Standard Model

Combining the measured cross sections for $e^+e^- \rightarrow Z^0/\gamma \rightarrow \mu^+\mu^-$ in the polar angle acceptance region $20^o \leq \theta \leq 160^o$ for 1990 data obtained in chapter 5 and the DELPHI results of 1991 based on measurements performed in the same interval of polar angles, some electroweak parameters of the Z^0 vector boson have been determined with good precision.

The $e^+e^- \rightarrow Z^0/\gamma \rightarrow \mu^+\mu^-$ cross sections determined either from 1990 data alone or combined with the 1991 data, have been used to measure the mass and width of the Z^0. The muon partial decay width Γ_μ and the muon pair pole cross section σ_μ^0 have also been obtained.

The parameter $sin^2\theta_w^{eff}$ was computed and the number of light neutrino species N_ν was examined. The results are only compatible with $N_\nu = 3$ with little room for possible non standard contributions to the invisible decay width of the Z^0.

The Standard Model parameters measured in this thesis are summarised in table 6.1 in which these results are also compared to the corresponding average for the four LEP experiments [67] and to Standard Model predictions for $N_\nu = 3$. The Standard Model predictions were computed for $\alpha_s = 0.120 \pm 0.006$, $m_t = 141 \pm 27$ GeV and 50 GeV< m_H <1000 GeV. All the results derived from the line shape analysis using either 1990 results alone or combining 1990 and 1991 data agree very well with the average of the together four LEP experiments as well as the Standard Model predictions.

Parameter	Experiment 90	Experiment 90,91	LEP Average	Standard Model
M_Z (GeV)	91.110 ± 0.057	91.172 ± 0.030	91.187 ± 0.007	
Γ_Z (GeV)	2.509 ± 0.091	2.483 ± 0.058	2.492 ± 0.007	
Γ_l (MeV)	83.77 ± 0.86	83.09 ± 0.57	83.33 ± 0.30	$83.64^{+0.34}_{-0.22}$
$\mathrm{Sin}\theta_w^{eff}$	0.239 ± 0.029	[0.224, 0.25] at 90% C.L.	0.2324 ± 0.0011	0.2323 ± 0.034
N_ν	2.99 ± 0.06	2.94 ± 0.04	3.00 ± 0.037	3
R_l	20.63 ± 0.47	20.98 ± 0.28	20.85 ± 0.07	$20.75^{+0.039}_{-0.016}$

Table 6.1: Comparison of our measured values with the average results of the four LEP experiments and the Standard Model predictions for $N_\nu = 3$.

Summary and Conclusions

This work was carried out in the framework of an international collaboration using the DELPHI detector installed at the LEP collider of CERN. It mainly contains two parts, respectively discribing our contribution to the Forward Muon detector system (MUF) of DELPHI and a measurement of the $e^+e^- \rightarrow Z^0/\gamma \rightarrow \mu^+\mu^-$ line shape. The Z^0 mass, the Weinberg angle $sin^2\theta_w$ as well as the ratio of the hadronic to muon partial decay widths are determined. These measurements allow direct checks of the number of lepton and quark generations and of the validity of the Standard Model.

The performance of the on-line drift velocity monitoring system of the DELPHI Forward Muon Chambers has been studied and optimized in test setups and during data taking. Detector dependent software has been written in order to monitor the drift velocity through the DELPHI slow control system. A series of functions has been added to the standard DELPHI Elementary Process running on a VAX computer and to the Skeleton program running on a Motorola 6809 processor. It was shown that with the on-line drift velocity monitoring system, the uncertainty in the drift velocity of the Forward Muon Chambers could in principle be reduced to about 1%, representing the limitation from the mechanical or electrical tolerances of these chambers.

The s-dependence of the $e^+e^- \rightarrow Z^0/\gamma \rightarrow \mu^+\mu^-$ cross section has been studied with the DELPHI detector at seven different center-of-mass energies ranging from 88.22 GeV to 94.22 GeV around the Z^0 peak for the data taken during 1990. A first analysis of these 1990 data has already been published [63]. However, for the present analysis the polar angle acceptance has been extended from $32.9^o < \theta < 147.1^o$ to $20^o < \theta < 160^o$. Such an extension was mainly possible by the improvement in track reconstruction which was achieved in the forward region since reference [63] was published. A total of 4002 $\mu^+\mu^-$ events have been selected from the data taken in 1990, corresponding to an integrated luminosity of 4596.8 nb^{-1}.

The muon event selections have been described in detail. The track reconstruction is performed using the Time Projection Chamber (TPC), Inner Detector (ID) and Outer Detector (OD) in the barrel region and the FCA and FCB chambers in the forward region. During most of the running periods the efficiencies of the tracking chambers outside the region $20^o < \theta < 160^o$ were so low that any further extension of this polar angle interval was judged to be unsafe.

Events are selected as muon pair candidates using the following sequence of criteria:

- The number of tracks N_{TK} produced by charged particles is small with $1 < N_{TK} < 6$.
- The acollinearity angle θ_{acol} between the tracks produced by the two particles with highest momentum is less than 10^o.
- To reduce the background arising from τ-decays in events with $N_{TK} > 2$, we either require that $\theta_{acol} < 1^o$ or that at least one of the two highest momentum particles is identified as muons by the muon chambers.
- The two most energetic particles each have momentum above 15 GeV/c.
- The tracks of the two most energetic particles emerge from a cylindrical vertex region defined as r < 1.5 cm and $|z| < 4.5$ cm where r and $|z|$ are the projected distances, respectively perpendicular to - and along the beam axis, between the e^+e^--interaction point and the point of closest approach of the track.
- Both highest momentum particles should be identified as muons by at least one of the following detectors: MUB, MUF, HPC, FEMC or HCAL.
- Events for which $\theta_{acol} > 1^o$ and the deposited energy in HCAL is greater than a cut-off value are rejected as τ-decays.
- Finally, the negative particle with the highest momentum should be emitted with a polar angle $20^o < \theta < 160^o$.

In order to correct for inefficiencies and backgrounds, the number of events selected at each energy point has to be weighted. These weighting factors are obtained from the data and from a sample of 10000 simulated $\mu^+\mu^-$ and 9000 simulated $\tau^+\tau^-$ events. The background arising from e^+e^- final states was found to be negligible. Luminosity measurements are based on the observation of Bhabba events recorded by the small angle tagger SAT.

The measurement of the mass and the total width of the Z^0 has been carried out by fitting the energy dependence of the cross section around the Z^0-pole in a model independent way. The lepton partial decay width $\Gamma_l = (\Gamma_e\Gamma_\mu)^{1/2}$, assuming e-$\mu$ universality, and the muon pair pole cross section σ_μ^0 have been obtained in the same way. The ratio $R_l = \Gamma_h/\Gamma_l$ of the hadronic partial width to the leptonic partial width has been computed and the number of light neutrino species N_ν has been extracted.

The main experimental results are as follows:

- **The mass and width of the Z^0 are:**

  $$M_Z = 91.110 \pm 0.053(\text{stat}) \pm 0.020(\text{sys})\ \text{GeV},$$
  $$\Gamma_Z = 2.509 \pm 0.091(\text{stat}) \pm 0.005(\text{sys})\ \text{GeV},$$

  in good agreement with the average values of the four LEP experments.

- **By fixing M_Z=(91.187±0.007) GeV and Γ_Z=(2.492±0.007) GeV to the average values of the four LEP experiments[71], the lepton partial decay width and the muon pair pole cross section are found to be:**

  $$\Gamma_l = (\Gamma_e\Gamma_\mu)^{1/2} = 83.77 \pm 0.71(\text{stat}) \pm 0.48\ (\text{sys})\ \text{MeV}$$
  $$\sigma_\mu^0 = 1.995 \pm 0.040(\text{stat}) \pm 0.021(\text{sys})\ \text{nb}$$

- **Taking σ_h^0 = 41.16 ±0.18 nb[71] from the average of the four LEP experiments, the ratio R_l of the hadronic partial width to the leptonic partial width assuming e-μ universality, was obtained as:**

  $$R_l = \frac{\Gamma_h}{\Gamma l} = \frac{\sigma_{had}^0}{\sigma_\mu^0} = 20.63 \pm 0.47$$

- **The effective Weinberg angle parameter $sin^2\theta_w^{eff}$ was computed from Γ_l and the mass of the top quark m_t = (141 ± 27) GeV [67], the value is:**

  $$sin^2\theta_W^{eff} = 0.239 \pm 0.029$$

- **The number of light neutrino species N_ν has been extracted as:**

$$\boldsymbol{N_\nu = 2.99 \ \pm 0.06}$$

in agreement with 3 lepton and quark generations.

Similar results are obtained when combining the $e^+e^- \rightarrow Z^0/\gamma \rightarrow \mu^+\mu^-$ cross section values obtained in this analysis for the 1990 data with those published by DELPHI for the 1991 data within the same polar angle region.

All the results derived from these analyses agree very well with the average of the four LEP experiments as well as the Standard Model predictions.

Appendix A

DELPHI Slow Control System

The design of the DELPHI slow control system was based on the following criteria:

- Configurable software for use by the different subdetectors;
- Compatibility with the DELPHI data acquisition system via the use of common software packages and VAX computers;
- Use of available hardware and software components where possible.

The slow control software consists of three layers:

- **State Model** This is the top layer. It is a hierarchically ordered state model in which subdetectors are treated as objects which must be in one of a set of pre-defined states. Below this, each subdetector is similarly treated until a set of elementary objects is reached, each of which corresponds to a subsystem of the subdetector.
- **Elementary Processes (EP)** One elementary process controls and monitors the hardware of each subsystem of a subdetector and sets the state of the corresponding elementary object in the state model description.
- **G64 crates** These form the interface between the VAX-based elementary process and the hardware. They receive commands from the elementary processes and return information back to them.

The code of the EP interacts with the user, handles errors, displays graphs and plots of the state of its apparatus. The EP communicates with the G64 crates to get monitored data and possibly to control equipment operation. The EP makes *Remote Procedure Calls (RPCs)*[46] to the G64 crates to exchange this information.

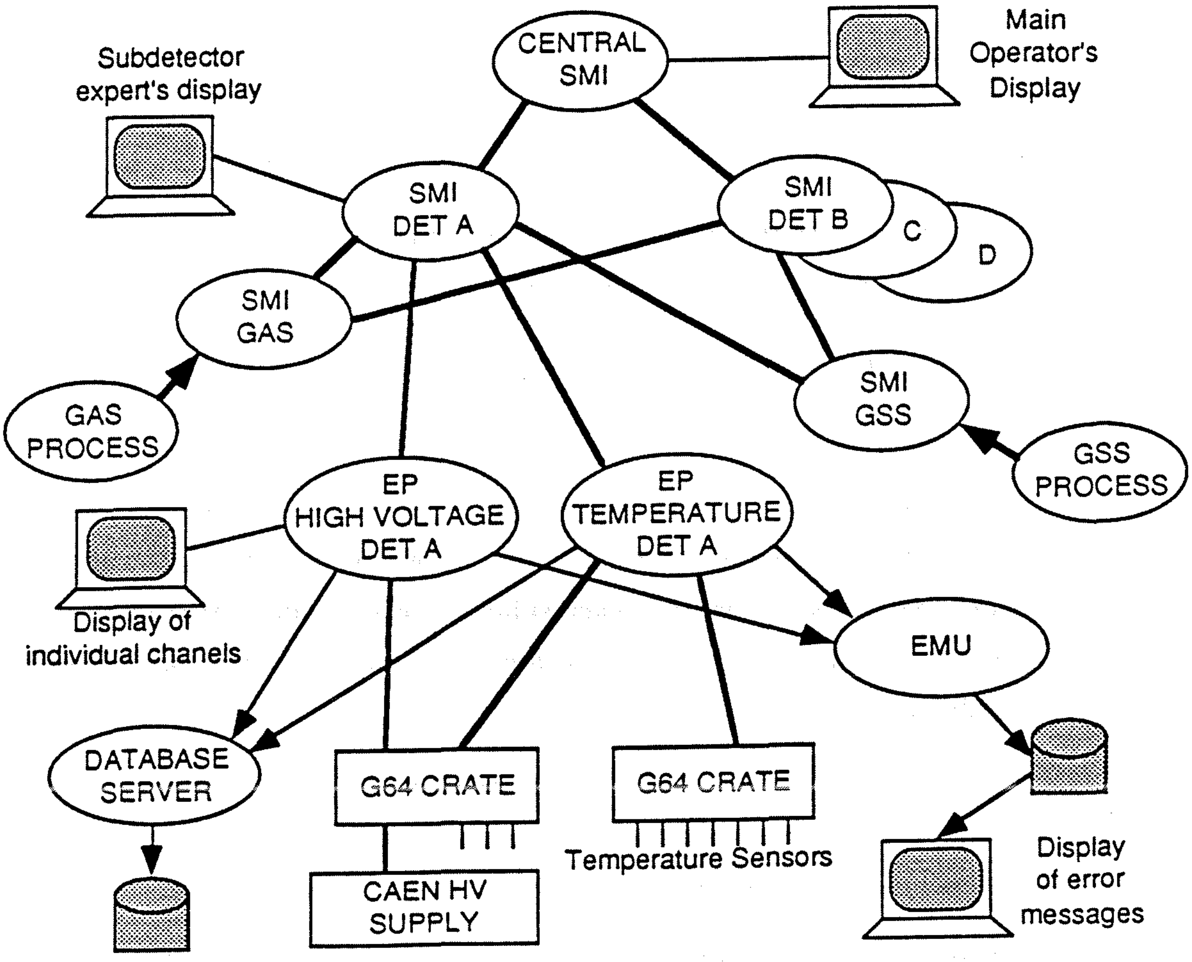

Figure 6.8: The structure of the DELPHI slow controls software

There are several additional systems providing the human interface for the central operator, i.e. links to the gas and safety systems, and logging of parameter values to a database.

The state model used for the upper levels of the control software is implemented using the CERN Model State Management Interface (SMI)[48]. There are two levels of processes or SMI domains. In the top level, each subdetector is represented by an object that is allowed to be in one of a set of states which are e.g. 'ready to take data', 'not ready', and 'in error'. Underneath there is a SMI domain for each subdetector containing objects for each of the subsystems within the subdetector. Fig. 6.8 shows the structure of the DELPHI slow controls software. The top level SMI domain implements control logic relating to entire subdetectors and takes the action automatically if necessary. The subdetector domains contain logic that allows interaction between the subsystems of the subdetector. It receives commands from the upper level and transmits them to the appropriate subsystems.

Elementary Process

The elementary process is the interface between the hardware and the following functions[45]:

- EMU (Error Message Utility): All the error messages will be sent here. EMU Sends information to the operators, writing down the error message in a logfile.
- Slow Controls database: accessed via SCAP, Slow Controls Access Package.
- Calibration database: accessed via DDAP, Detector Description Access Package.
- Global Data: inter-process data sharing.
- HIPE (Human Interface to Elementary Process)
- SMI (State Management Utility): EP will change the SMI state of the detectors if required. It can also execute the commands from the operator to change the parameters and the state of the monitored channels.

The elementary processes (EPs) set the state of elementary objects. The EP performs the following functions to control and monitor a hardware subsystem:

- Receiving commands from the detector's SMI domain and transmitting them to the G64 system.
- Receiving messages from the G64 indicating changes in hardware conditions and making appropriate changes to the state of the elementary object to which the EP corresponds.
- Monitoring the state of the hardware via the G64 system either at request from the higher level or at timed intervals.
- Updating a database with changes in those parameters needed for data analysis.
- Injecting messages into a distributed message system when appropriate.
- Communicating with a user via a VMS global section, permitting reading and setting of individual channels. A configurable, interactive program is provided to enable the user to manipulate the global section and is intended for use during diagnostic sessions.

The EP is a standard program configured from a database file when it starts. It is written in FORTRAN.

G64 Skeleton

The G64 system is the low level monitoring system based on the G64 bus. Double height MAC-64 crates designed at the CERN-ECP division are used. The configurable G64 program receives RPCs from the elementary processes to read or set the hardware. The program loop continuously monitors the apparatus, reporting changes via RPC to the EPs. The program is written in PASCAL.

The G64 skeleton program[44] loops perform the following operations:

- Accepts RPC calls. These will usually come from an elementary process running in an equipment computer. The call may:
  1. Define the channel to be monitored or set. Any request to the skeleton program must address the hardware channel by referring to a crate, slot and channel number. This channel number is referred to as the physical address of the channel. The slot number is the number of the slot in the MAC-64 card frame. A maximum of 32 slots may be defined. The channel

number is the number of the channel within the slot. The skeleton software allows a variable number of channels to be defined for each slot.

2. Following receipt of such a call it may set up some initial parameters (such as error limits; switch limits; event counting limits, etc.) in the G64 processor memory. The hardware is initialised corresponding to the channels defined.
3. Request a read or write of a particular channel. Any requested values are returned to the caller.
4. Define the EP number.
5. Define the address of an alarm server on the VAX.

- Reads any channel that is to be monitored. This is compared with error and switch limits. If the error condition has changed, a specified error routine will be called. An error message is sent to the VAX.
- Sends possible alarm messages to the elementary process.
- Takes commands from a keyboard attached to the system. These are then processed as if they were RPC requests from the equipment computer, but any response is sent back to the attached terminal.

Remote Procedure Call (RPC)

Basically, Remote Procedure Call allows a programme on one machine to call a subroutine on the other machine without knowing that it is remote.

In the RPC, the client stub uses a routine, called Run-Time System (RTS), to send the message from the client processor to the server processor and waits for a reply message to be sent back. When the reply arrives, the stub marshals the returned parameters and puts them into the variables in the calling programme. Then the client stub returns to the calling programme just like a normal subroutine.

The server stub is located on the remote machine. It is called by the RPC run-time system when the message arrives from the client. The server stub performs the operations complementary to those of the client stub: unmarshalling the parameters passed to the subroutine, calling the subroutine, and marshalling the return parameters.

Because all the communication details are handled by the RPC run-time system already, the stubs contain only the code which is specific to the application involved.

The DELPHI slow control system contains a series of auxiliary systems. They are: central operator's display system, links to the safety systems and GAS system, updates to the database system and error messages display system.

Central operator's display system is a configurable, Motif-based X-windows program. It displays the states of the objects in a SMI domain and allows commands to be sent to those objects. The same program can be used either to control the top level domain or those of the subdetectors. Displaying the top level domain allows the operator to see the overall state of DELPHI slow controls as well as that of environmental parameters in the vicinity of the detector. The display also provides a summary of the state of related systems in the experiment such as the trigger, the data acquisition system and the LEP machine. Commands can be issued to subdetectors. This display is the operator's main method of interacting with the slow controls system.

The link from the safety systems to the GAS system provide the link from the DELPHI gas system and the independent general safety and surveillance system to the DELPHI slow control system. This interaction is provided by means of textual messages and SMI objects. The messages allow detailed information to be exchanged, while SMI is used to enable DELPHI to trigger actions on the receipt of signals from the gas or safety systems. In addition to these software links, hardwired interlocks from both the General Surveillance and Security system (GSS) and the gas systems ensure that potentially dangerous systems are switched off in the event of an alarm.

The updates to the database system use a purpose-written hierarchical database manager to update the values of various parameters required for the analysis of the data from the DELPHI experiment. All access to the database is made via a single database server process. The server process itself is accessed by the elementary process using Remote Procedure Calls running over DECnet.

The Error messages display system uses CERN Model Error Message Utility (EMU)[49] to inject, route and log the error messages. The error messages can be routed to different log files by using various tags associated with the messages. A configurable display program, based on X-windows, allows both the central operator to see current messages from all subdetectors on a central display and subdetector experts to read messages previously logged by their EPs.

GSS: The General Safety and Surveillance (GSS) provided from LEP is a system to incorporate with detectors for gas, smoke and flood, etc. The GSS and DELPHI computers keep each other informed of safety problems via the local-area network.

Appendix B

The Nitrogen Laser System

The nitrogen laser, used for the calibration of the monitoring chamber, was developed and built in NIKHEF (Nationaal Instituut voor Kern en Hoge Energie Fysica, Amsterdam, the Netherlands) for the calibration of the DELPHI Inner Detector and the TPC.

The nitrogen laser pulses UV light at a wave length of 337 nm. One of the advantages of the nitrogen laser is that it can produce a light pulse of very short duration (≈ 1 ns) which is sufficiently short compared to the drift time of the electrons in the drift chamber. This light pulse is able, for a moderate pulse energy, to produce a track of sufficient ionization clusters in the chamber gas. The nitrogen laser can produce straight and reproducible ionization tracks over an area which is limited by the aperture of the entrance window of the chambers.

The Electrical and Optical Setup of the Laser System

Fig. 6.9 shows the electrical and optical setup of the laser system. It consists of four thick copper plates P1, P2 and P3, P4 which are charged to 18 kV. The cavity that generates the laser light is the gap between the plates. It is filled with nitrogen gas at atmospheric pressure. The plates P1 and P3 are connected by a metal strip to a triggered spark gap, acting as a fast switch.

Once the spark gap has fired, the voltage on P1 and P3 drops rapidly while the voltage on P2 and P4 remains unaffected because of the relatively high impedance of the connections to the high voltage supply. This leads to a fast rising of the electrical field in the cavity. Immediately, a gas discharge starts to develop over the full length of the cavity ending in the formation of a highly conductive plasma. The collisions of the electrons with the gas molecules result, at the end of the discharge, in a population

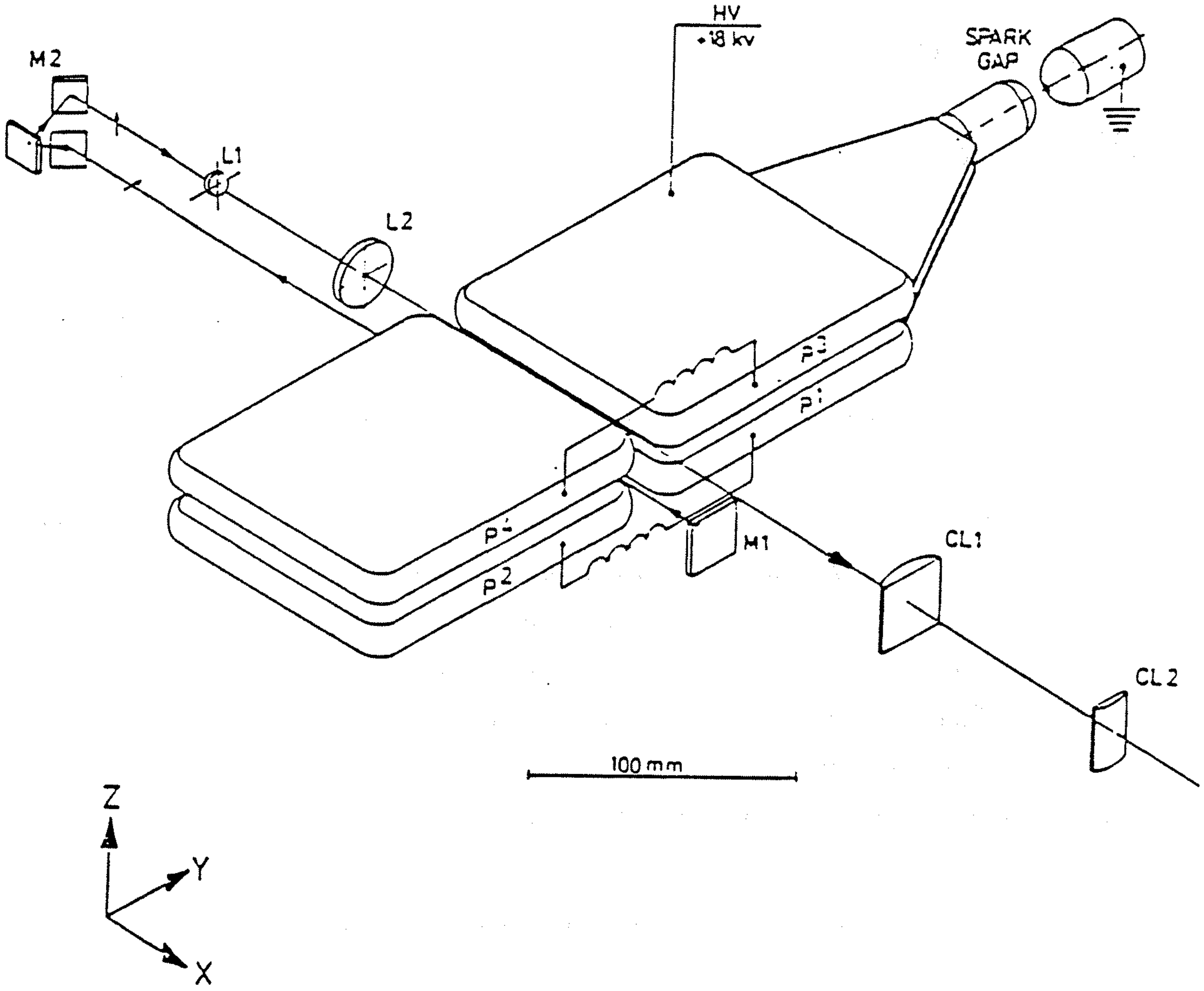

Figure 6.9: Artists view of the optical setup of the laser system. See text for the meaning of the symbols.

inversion. The light generated from the cavity is emitted over a fairly large angle and is only limited by the exit window.

Because the development time of the discharge depends on the magnitude of the electric field, the oscillator cavity, which has the smallest width, lases first. The light emitted at the start of the light pulse is reflected against the mirror M1 and passes the cavity again where it is amplified. Since the life time of the excited states is limited to a few ps, there is no use for a second, semi-transparent mirror to form an optical resonator.

The oscillator beam is directed by the three-mirror-assembly M2 into the amplifier cavities. The difference in width between the oscillator and amplifier cavity is adjusted in such a way that the resulting time difference just compensates for the path length between the two cavities. As a result the incoming light is strongly amplified.

The telescope formed by the positive lenses L1 and L2 can expand the beam in front of the amplifier by a factor of 20. As a consequence, the divergence is reduced by the same factor and a nicely parallel beam is obtained. The expansion of the beam also implies a significant reduction in the intensity of the incoming light. However, since the light gain in the amplifier cavity is largely saturated, the energy reduction of the exiting beam amounts only to a factor of 2.

The final laser beam has a divergence which is close to the diffraction limit and has fairly good isotropy. The energy per pulse amounts to about 100 μJ, which in combination with the pulse duration of 1 ns results in a peak power of the order of 100 kW at a wavelength of 337 nm.

Bibliography

[1] "Summary of the 1990 data processing on the FARM", DELPHI 90-48 PROG 156.

[2] S.L. Glashow, Nucl. Phys. **22** (1961) 579.

[3] A. Salam, Phys. Rev. **127** (1962) 331.

[4] S. Weinberg, Phys. Rev. Lett **19** (1967) 1264.

[5] L. Rolandi, XXVI International Conference in High Energy Physics, Dallas, Texas, p.56, August 5-12 1992, CERN-PPE/92-175

[6] G.Arnison et al. (UA1 Collab.), Phys. Lett. **126B** (1983) 398.

[7] M. Banner et al. (UA2 Collab.), Phys. Lett. **129B** (1983) 130.

[8] Chris Quigg, Gauge theories of strong-weak and electromagnetic Ineractions(1983). ed. D. Pines.

[9] C.Altarelli et al., Z physics at LEP 1, CERN 89-08, Vol 1.

[10] R.D. Peccei, Electroweak Interaction, The Standard Model and Beyond, Chateau Lake Louise, 18-24 February 1990.

[11] D.Bardin et al., ZFITTER, An Analytic Program for Fermion pair production in e^+e^- Annihilation CERN-TH . 6443/92.

[12] D.Bardin et al., Z. Phys. C44(1989) 493; Comput. Phys. Commun. 29 (1989) 185, CERN-TH. 6443/92

[13] D.Bardin et al., Nucl. Phys. **B351** (1991)1 and Phys. Lett. **B255** (1991) 290.

[14] M. Consoli and W.Hollik, Z physics at LEP 1, CERN 89-08, Vol 1.

[15] F.Berends, Z physics at LEP 1, CERN 89-08, Vol 1.

[16] F.Dydak, 25th International Conference on High Energy Physics, Singapore, 2-8 Aug. 1990 p.3

[17] D.Bardin et al., Nucl. Phys. **B276** (1986) 1.

[18] M. Contreras, Joint International Lepton-Photon Symposium and Europhysics Conference on High Energy Physics, Geneva, Swizerland, 25 July-1 August 1991, p.366.

[19] DELPHI Collaboration, P.ABREU et al. 'Parameters of the Z^0 Resonance from Combined Preliminary Data of the LEP Experiments', Dallas, Texas, DELPHI 92-113 PHYS 219.

[20] L. Okun et al., 'Electroweak Radiative Corrections and Top Quark Mass', CERN-Th.6053/91

[21] "LEP Design Report" CERN-LEP/84-01 (1984)

[22] M.Sands 'Introduction to the Physics of Electron Storage Rings' SLAC-121 UC-28 Nov. 1970.

[23] P.Aarnio et al., DELPHI Collab., 'DELPHI Progress Report', DELPHI 84-60(1984).

[24] P.Aarnio et al., DELPHI Collavoration, Nucl. Instr. Meth. **A303** (1991) 233.

[25] M.Ellila, Acta Polytechnica Scandinavica Appl. Phys. Series 159 (1988);
N.A.Filatova, Nucl. Instr. Meth. **A243** (1986) 91;
G.D.Alekseev et al., Nucl. Instr. Meth. **A269** (1988) 652.

[26] J.Vaz, Ph.D Thesis, Universidade Técnica de lisboa, Nov.1990.

[27] 'DELPHI Data Analysis Program (DELANA) user's Guide', DELPHI note 87-95 PROG 98 (1989).

[28] 'ZEBRA - Data Structure Management System', CERN Program Library, Q100 (1987).

[29] 'DELSIM DELPHI EVENT GENERATION AND DETECTOR SIMULATION -user's Guide', DELPHI note 89-67 PROG 142 (1989).

[30] J.E. Campagne and R. Zitoun, Zeit. Phys **C43** (1989) 469, and Proc. of the Brighton Workshop on Radiative Corrections, Suses, July 1989.

[31] S.Jadach, B. Ward, Z. Was, R. Stuart, W. Hollik, in Z Physics at LEP 1, ed. G. Altarelli et al., Vol.3, CERN 89-08 (1989) 69-77.

[32] F.A Berends, W. Hollik, and R. Kleiss, Nucl. Phys. **B304** (1988) 712; M. Bohm, R. Kleiss and W. Hollik, Nucl. Phys. **B304** (1988) 469.

[33] 'TANAGRA - Track Analysis and Graphics Package', DELPHI note 87-95 (1987).

[34] F.Sauli, 'Principles of operation of multiwire proportional and drift chambers', CERN 77-09,GENEVA, 1977.

[35] G.D Alekseev et al., Nucl. Instr. Meth. **177** (1980) 385.

[36] V.Palladino and B.Sadoulet Nucl. Instr. Meth. **128** (1975) 323.

[37] R.C.Fernow, 'Introduction to experimental particle physics', Cambridge University, 1986.

[38] P.Aarnio et al., DELPHI collaboration, Nucl. Instr. Meth. **A303** (1991) 233.

[39] C.De Clercq et al., Nucl. Instr. Meth. **A243** (1986) 77.

[40] E.Daubie et al. Nucl. Instr. Meth. **A252** (1986) 435.

[41] F.Stichelbaut et al., Nucl. Instr. Meth. **A283** (1989) 792.

[42] J.Buytaert et al., Nucl. Instr. Meth. **A310** (1991) 596.

[43] E.Daubie, 'Etude de chambres à dérive d'électrons exploitées en mode "streamer" limité avec une distance de dérive maximale de 10 cm', Ph.D. Thesis, Universite de L'Etat Mons, 1991.

[44] G.Smith, 'Delphi Slow Controls G64 Microcomputers Skeleton Program,Version 3.0', CERN, 25th Feb. 1990.

[45] T.Adye, 'The Slow Controls Elementary Process', Rutherford Appleton Laboratory, 17th May 1989.

[46] T.J. Berners-Lee, 'Introduction to Remote Procedure Call', CERN, Data Handling Division, Online Group,June 1988.

[47] T. Adye et al., Proceedings of the conference on 'Computing in high energy physics', Annecy, France, 1992.

[48] A. Defendini et al., 'The MODEL state manager user manual', CERN ECP-DS.

[49] P. Burkimsher, EMU, The MODEL Error Message Utility, Version 2.1, CERN ECP, Dec. 1990.

[50] F. Hartjes, Ph. D. thesis. NIKHEF, Nederland.

[51] F. Stichelbaut, Ph. D. thesis. Universite Liber de Bruxelles, Belgium.

[52] W. Van Doninck, Private communication.

[53] 'Summary of the 1990 data processing on the FARM', DELPHI 90-48 PROG 156.

[54] M. Winter, private communication.

[55] N. Crosland, Ph.D Thesis, St. John's College, Oxford.

[56] P. ABREU et al., DELPHI Collaboration, Phys. Lett. **B241** (1990) 435.

[57] From LUMINOSITY90 file maintained by the DELPHI AST Group.

[58] DELPHI Collaboration, DELPHI91-08 PHYS 84, 'Theoretical uncertainty on the luminosity measurement', DELPHI91-104 PHYS 147.

[59] CORPUS, PROG175, DELPHI91-67. PHYS121, 23 JUL 91.

[60] EMMASS Muon Identification Within DELPHI, DELPHI 92-17 phys 157.

[61] D. BARDIN et al., CERN-TH. 6443/92.

[62] P. ABREU et al., DELPHI Collaboration, phys. Letters. **B260** (1991) 240.

[63] P. ABREU et al., DELPHI Collaboration, Nucl. Phys **B367** (1991) 511.

[64] P. ABREU et al., DELPHI Collaboration, Z. Phys. C - particles and Field 53, 567-580(1992).

[65] P. ABREU et al., DELPHI Collaboration, Nucl. Phys. **B367** (1991) 511.

[66] P.ABREU et al., DELPHI Collaboration, To be published.

[67] L. Rolandi, XXVI International Conference in High Energy Physics, Dallas, Texas, p.56, August 5-12 1992, CERN-PPE/92-175.

[68] The LEP callaborations, ALEPH,DELPHI.L3 AND OPAL, Phys. Letters **B276** (1992) 247.

[69] D. Bardin et al., Z. Phys. C44(1989) 493; Comput. Phys. Commun. 29 (1989)185, CERN-TH. 6443/92.

[70] D. Bardin et al., Nucl. Phys. **B351** (1991) 1 and Phys. Letters **B255** (1991) 290.

[71] The LEP electroweak working Group, 'Parameters of the Z^0 Resonance from Combined Preliminary Data of the LEP Experiments', XXVI International Conference in High Energy Physics, Dallas, Texas, August 5-12 1992, DELPHI 92-113 PHYS 219.

[72] C. Jarlskog, CERN preprint, Orchids to the Standard Model, CERN-TH/90-5918 (1990).